SYNTHESIS, SOLUTION ASSEMBLY, AND CHARACTERIZATION OF AMPHIPHILIC BLOCK POLYMERS

by

Elizabeth G. Kelley

A dissertation submitted to the Faculty of the University of Delaware in partial fulfillment of the requirements for the degree of Doctor of Philosophy in Chemical Engineering

Spring 2014

ProQuest LLC.
789 East Eisenhower Parkway
P.O. Box 1346
Ann Arbor, MI 48106 - 1346

SYNTHESIS, SOLUTION ASSEMBLY, AND CHARACTERIZATION OF AMPHIPHILIC BLOCK POLYMERS

by

Elizabeth G. Kelley

Approved: _____
Abraham M. Lenhoff, Ph.D.
Chair of the Department of Chemical and Biomolecular Engineering

Approved: _____
Babatunde A. Ogunnaike, Ph.D.
Dean of the College of College Engineering

Approved: _____
James G. Richards, Ph.D.
Vice Provost for Graduate and Professional Education

I certify that I have read this dissertation and that in my opinion it meets the academic and professional standard required by the University as a dissertation for the degree of Doctor of Philosophy.

Signed: _____

Thomas H. Epps, III, Ph.D.
Professor in charge of dissertation

I certify that I have read this dissertation and that in my opinion it meets the academic and professional standard required by the University as a dissertation for the degree of Doctor of Philosophy.

Signed: _____

Millicent O. Sullivan, Ph.D.
Professor in charge of dissertation

I certify that I have read this dissertation and that in my opinion it meets the academic and professional standard required by the University as a dissertation for the degree of Doctor of Philosophy.

Signed: _____

Eric M. Furst, Ph.D.
Member of dissertation committee

I certify that I have read this dissertation and that in my opinion it meets the academic and professional standard required by the University as a dissertation for the degree of Doctor of Philosophy.

Signed: _____

Darrin J. Pochan, Ph.D.
Member of dissertation committee

To Mom and Dad

For always believing in me and my dreams

ACKNOWLEDGMENTS

I would like to begin by thanking by advisors, Thomas Epps and Millicent Sullivan, for inspiring me to think creatively, challenging me to do my best work, and helping me to become an independent researcher.

I would also like to thank my committee members, Eric Furst and Darrin Pochan, for their support over the past several years. Their suggestions provided important insights into my work and inspired many of the recommendations for future work in this dissertation.

I owe a great debt of gratitude to the Epps and Sullivan group members, both past and present. They have not only been inspiring colleagues but absolutely amazing friends. In particular, I would like to thank Julie Albert, Kory Blocker, John Larsen, Pete Millili, Meghan Reilly, and Maëva Tureau for their patience and answering all of my many questions when starting this research. I would especially like to thank Owen Young for all of his suggestions and reminding me to "don't be angry" when things didn't go the way I planned. To the current group members, Jill Emerson, Chad Greco, Angela Holmberg, Wei-Fan Kuan, Ming Luo, Kai Mayeda, Melody Morris, Erik Munsell, Abbygail Palmer, Nikki Ross, Cameron Shelton, and Moran Urello, thank you for all of your help, support, and encouragement. I would especially like to thank Sarah Mastroianni for being my 'partner in crime' whether synthesizing 6 polymers at once or figuring out how to travel by train across England.

Additionally, I would like to thank a number of people for their help in my research including Frank Kriss and Chaoying Ni for help with microscopy

experiments, Steve Bai for help with NMR experiments, and John Dykins and Leila Choe for help with mass spectrometry experiments. I owe a great debt of gratitude to several scientists at NIST including Paul Butler, Yun Liu, Matthew Wasbrough, Katie Weigandt, and especially Andrew Jackson. I would like to thank Yuri Melnichenko and Lilin He at ORNL for their help with SANS experiments, and Simon Rogers and Michelle Calabrese for their help with the Flow SANS experiments. I thank Doug Nixon for his help designing glassware and quick repairs when things broke, and Gary Wellmaker and George Whitmyre for all of their help in keeping the labs running. I would especially like to thank Kathie Young for all of her help and support over the years.

I would also like to thank the 'solutions' group, including Christina Marino, Tom Smart, Jon Seppala, and Matt Green for their helpful suggestions and late night laughs while purging a reactor or sitting by the beamline. I also thank Sarah Hann for teaching me that science can be fabulous.

I especially would like to thank Ryan Murphy. His critical thinking, creativity, and enthusiasm inspired many aspects of this work, and he was an invaluable sounding board for many of my crazy ideas. I also thank him for reminding me of why I became a scientist.

Most importantly, I would like to thank my friends and family. I thank my friends for always believing me and for forgiving me for being awful at keeping in touch over the past 6 years. I thank all of my family for their support over the years, especially my Chachi and Uncle Denis for their encouragement and understanding what it means to be a graduate student. I would also like to thank my Grammy and my Meme, two of the strongest women I have had the honor of knowing. These women

inspired me to never give up on my dreams, no matter what obstacles life threw my way. I also thank my brother. Professionally, I thank him for his creative genius and for turning my stick figures into beautiful cover art. More importantly, I thank him for always being able to make me laugh and reminding me to not take myself too seriously.

Finally, I would like to thank my parents. I cannot begin to thank them for everything that they have done for me. I would not be the person I am today without their love and encouragement.

TABLE OF CONTENTS

LIST OF TABLES xv
LIST OF FIGURES xvii
ABSTRACT xxxii

Chapter

1 INTRODUCTION 1

1.1 Amphiphiles 2
1.2 Block Polymer Amphiphiles 9
1.3 Emerging Applications of Solution Assemblies 22

1.3.1 Aqueous Nanoreactors 22
1.3.2 Nanomedicines 25

1.4 Thesis Overview 36

REFERENCES 38

2 MATERIAL SYNTHESIS AND CHARACTERIZATION 49

2.1 Macromolecule Synthesis 49

2.1.1 Anionic Polymerization 49
2.1.2 Fmoc Solid Phase Peptide Synthesis (SPPS) 60

2.2 Chemical Characterization 66

2.2.1 Chromatography Techniques 67

2.2.1.1 Size Exclusion Chromatography (SEC) 67
2.2.1.2 Reverse Phase High Performance Liquid Chromatography (RP-HPLC) 71

2.2.2 Matrix-Assisted Laser Desorption/Ionization Time of Flight (MALDI-TOF) Mass Spectrometry 74
2.2.3 Proton Nuclear Magnetic Resonance (^{1}H NMR) Spectroscopy .. 81

2.3 Summary 85

REFERENCES 86

3 CHARACTERIZATION TECHNIQUES 89

3.1 Scattering Techniques 89

3.1.1 Dynamic Light Scattering (DLS) 93
3.1.2 Small Angle X-ray and Neutron Scattering (SAXS and SANS) 99

3.2 Cryogenic Transmission Electron Microscopy (cryo-TEM) 110
3.3 Summary 117

REFERENCES 118

4 COMPLEMENTARY METHODS FOR CHARACTERIZING SOLUTION ASSEMBLED STRUCTURES 121

4.1 Introduction 121
4.2 Experimental 123

4.2.1 Materials 123
4.2.2 Micelle Preparation 123
4.2.3 Micelle Characterization 124

4.2.3.1 Dynamic Light Scattering (DLS) 124
4.2.3.2 Cryogenic Transmission Electron Microscopy (cryo-TEM) 124
4.2.3.3 Cryo-TEM Image Analysis 124
4.2.3.4 Small Angle Neutron Scattering 126
4.2.3.5 SANS Form Factor Model and Data Analysis 127

4.3 Results 130

4.3.1 Radial Density Profile Analysis Using Cryo-TEM 130
4.3.2 Micelle Density Profile Analysis Using SANS 133

4.4 Discussion 135
4.5 Conclusions 138

REFERENCES 140

5 STRUCTURAL CHANGES IN BLOCK POLYMER MICELLES INDUCED BY COSOLVENT MIXTURES 144

5.1 Introduction 144
5.2 Experimental 146
5.2.1 Materials and Polymer Synthesis 146
5.2.2 Solution Preparation 147
5.2.3 Micelle Characterization 147
5.2.3.1 Contact Angle 147
5.2.3.2 Dynamic Light Scattering (DLS) 148
5.2.3.3 Cryogenic Transmission Electron Microscopy (cryo-TEM) 149
5.2.3.4 Small Angle X-ray Scattering (SAXS) 149
5.2.3.5 Proton Nuclear Magnetic Resonance (^{1}H NMR) Spectroscopy 150
5.2.3.6 Small Angle Neutron Scattering (SANS) 150
5.2.3.7 SANS Form Factor Model and Data Fitting 150
5.3 Results 155
5.3.1 PB-Cosolvent Interfacial Tension 155
5.3.2 Effects of Interfacial Tension on Micelle Size 156
5.3.3 Detailed SANS Data Modeling of Micelles in Cosolvent Mixtures 160
5.4 Discussion 170
5.5 Conclusions 174
REFERENCES 176
6 EFFECTS OF COSOLVENT MIXTURES ON BLOCK POLYMER MICELLE DYNAMICS 180
6.1 Introduction 180
6.2 Experimental 183
6.2.1 Materials 183
6.2.2 Solution Preparation 183
6.2.3 Time-Resolved Small Angle Neutron Scattering (TR-SANS) .. 185
6.2.4 TR-SANS Data Analysis 185
6.3 Results 189
6.3.1 TR-SANS Studies of Micelles in Cosolvent Mixtures 189
6.3.2 Chain Exchange Kinetics in Low Interfacial Tension Systems 194

6.4 Discussion 196
6.5 Conclusions 200

REFERENCES 201

7 CONSQUENCES OF COSOLVENT REMOVAL ON THE STABILITY OF BLOCK POLYMER MICELLES 204

7.1 Introduction 204
7.2 Experimental 207

7.2.1 Materials 207
7.2.2 Micelle Solution Preparation 208
7.2.3 Dynamic Light Scattering (DLS) 209
7.2.4 Small Angle X-ray Scattering (SAXS) 209
7.2.5 Cryogenic Transmission Electron Microscopy (cryo-TEM) 210
7.2.6 Small Angle Neutron Scattering (SANS) 211

7.2.6.1 Chain Exchange Sample Preparation 211
7.2.6.2 Size Distribution Sample Preparation 211
7.2.6.3 SANS Experiments 212

7.3 Results 212

7.3.1 Effects of Cosolvent Removal on Micelle Size 212
7.3.2 Investigation into Micelle Growth Mechanism 217
7.3.3 Size Evolution Concentration Dependence 221
7.3.4 Size Evolution through a Bimodal Pathway 225

7.4 Discussion 227
7.5 Conclusions 229

REFERENCES 231

8 INFLUENCE OF MIXING ON CHAIN EXCHANGE IN HIGHLY AMPHIPHILIC BLOCK POLYMER MICELLES 235

8.1 Introduction 235
8.2 Experimental Section 238

8.2.1 Materials 238
8.2.2 Micelle Solution Preparation and Mixing 239

8.2.2.1 Solution Preparation 239
8.2.2.2 Micelle Solution Mixing 240

8.2.3 Small Angle Neutron Scattering (SANS) 241
8.2.3.1 Flow SANS 241
8.2.3.2 Static SANS 241
8.3 Results 242
8.3.1 Effects of Mixing on Chain Exchange 242
8.3.2 Mixing-Induced Chain Exchange Kinetics 248
8.4 Discussion 252
8.5 Conclusions 257
REFERENCES 258
9 DESIGN AND SYNTHESIS OF AMPHIPHILIC POLYMER-PEPTIDE CONJUGATES 262
9.1 Introduction 262
9.2 Experimental 267
9.2.1 Materials 267
9.2.2 Hydrophobic Block Synthesis and Functionalization. 268
9.2.2.1 Poly(ethyl ethylene) Synthesis *via* Chemical Hydrogenation 268
9.2.2.2 Synthesis of Azide-Functionalized PEE 270
9.2.3 Hydrophilic Block Synthesis 271
9.2.3.1 Solid Phase Peptide Synthesis (SPPS) 271
9.2.3.2 Dye Labeled Peptide for Förster Resonance Energy Transfer (FRET) Experiments 271
9.2.3.3 On-resin Polymer Conjugation 274
9.2.3.4 Peptide Synthesis using Pre-functionalized Resin 276
9.2.4 Polymer-Peptide Conjugation using Copper-Catalyzed Azide-Alkyne Cycloaddition Reactions 277
9.2.5 Material Characterization 278
9.2.5.1 Size Exclusion Chromatography (SEC) 278
9.2.5.2 Proton Nuclear Magnetic Resonance (^{1}H NMR) Spectroscopy 279
9.2.5.3 High Performance Reverse Phase Liquid Chromatography (RP-HPLC) 279

9.2.5.4 Matrix Assisted Laser Desorption Ionization Time of Flight Mass Spectrometry (MALDI-TOF MS) 279
9.2.5.5 FRET Experiments 280
9.2.5.6 Thin Layer Chromatography (TLC) 280
9.2.5.7 Attenuated Total Reflection Fourier Transform Infrared Spectroscopy (ATR-FTIR) 281

9.3 Results 282

9.3.1 Hydrophobic Block Synthesis and Functionalization 282
9.3.2 Hydrophilic Block Design and Synthesis 286
9.3.3 Amphiphilic Polymer-Peptide Conjugate Synthesis 295

9.4 Discussion 298
9.5 Conclusions 300

REFERENCES 301

10 THESIS SUMMARY AND RECOMMENDATIONS FOR FUTURE WORK 306

10.1 Thesis Summary 306

10.1.1 Developing Complementary Methods for Characterizing Solution Assembled Structures 307
10.1.2 Understanding Effects of Common Processing Conditions on Block Polymer Assemblies 308
10.1.3 Designing Amphiphilic Polymer-Peptide Conjugates 311

10.2 Recommendations for Future Work 312

10.2.1 Exploring Block Polymer Micelle Dynamics 312

10.2.1.1 Polymer Properties and Solution Additive Effects 313
10.2.1.2 Kinetically-Controlled Agitation Effects 315

10.2.2 Developing Libraries of Amphiphilic Polymer-Peptide Conjugates 319

10.2.2.1 Controlling Peptide Location 319
10.2.2.2 Exploring Other Block Chemistries 321
10.2.2.3 Targeting Different Morphologies 326

10.2.3 Probing Structure-Property Relationships in Targeted Drug Delivery Vehicles 327

10.2.3.1 Understanding Nanostructure Morphology in Biologically Relevant Environments 328
10.2.3.2 Determining the Ligand Location within Targeted Drug Delivery Vehicles 329

10.2.4 Summary of Future Directions 333

REFERENCES 334

Appendix

A RADIAL CORONA PROFILE FOR SANS DATA MODEL 342
B CODE FOR MICELLE FORM FACTOR MODEL 344
C SANS DATA AND FITS FOR BLOCK POLYMER MICELLES IN COSOLVENT MIXTURES 355
D PB HOMOPOLYMER SOLUBILITY IN COSOLVENT MIXTURES 365
E COMPARISON OF SANS DATA FITTING RESULTS FOR A BIMODAL DISTRIBUTION OF MICELLE SIZES 367
F POLYMER END-GROUP CHEMISTRIES 369
G POLYMER-PEPTIDE CONJUGATION CHEMISTRIES 379
H COPYRIGHT PERSMISSIONS 388

LIST OF TABLES

Table 1.1 **CMC of common small molecule and macromolecular amphiphiles** 18

Table 2.1 **Summary of PB-OH and PB-PEO polymers** 60

Table 2.2 **Standard side chain protecting groups used in SPPS** 63

Table 2.3 **MALDI 'recipes' for common polymers** 76

Table 4.1. **Amphiphilic homopolymer characterization data** 123

Table 4.2 **Summary of amphiphilic homopolymer micelle characterization data** 131

Table 4.3 **Corona chain stretching in amphiphilic homopolymer micelles calculated using dimensions from SANS data modeling** 137

Table 5.1 **Viscosity and refractive index values for water/THF cosolvent mixtures used to analyze DLS data** 149

Table 5.2 **Density and scattering length density values for the materials used in this study** 152

Table 5.3 **Summary of micelle characterization data determined by DLS, SAXS, cryo-TEM, and SANS, in which Q is aggregation number, Rc is core radius, σRc is core polydispersity, σint is interfacial width, Rh is hydrodynamic radius, Rm is micelle radius, H is corona thickness estimated as H = Rm – Rc using Rm (SAXS) and Rc (cryo-TEM), and Rg is radius of gyration of the PEO chains. Note that Rm from SANS was estimated based on corona density profile where the volume fraction of PEO < 0.02** 158

Table 6.1 **Solvent mixture compositions for TR-SANS experiments** 184

Table 6.2 **Input and fit parameters for fitting TR-SANS data for 30 vol% THF PB-PEO micelle solution at 55 °C** 196

Table 6.3 **Estimated χ values for the different H_2O/THF mixtures at 25 °C** .. 199

Table 7.1 **Micelle solution concentrations before and after dialysis.** 209

Table 8.1 **Summary of SANS data modeling results for the post-mixed, pre-mixed, and vortexed samples in Figure 8.2** 246

Table 9.1 **Summary of unprotected peptide, PEO, and PEE solubility in common solvents used for copper-catalyzed azide-alkyne cycloaddition reactions*** 296

Table C1 **SANS model fit parameters for micelle corona profile** 364

Table G1 **Summary of DLS characterization results for functionalized micelles** 386

LIST OF FIGURES

Figure 1.1 **Schematic representation of nanoscale structures formed by amphiphilic molecules in aqueous solutions. The hydrophobic portions of the molecule (red) aggregate and are shielded from the aqueous environment by the hydrophilic portions of the molecule (blue). Adapted from reference 9.** 2

Figure 1.2 **Schematic representation of unimer and micelle concentration as a function of total amphiphile concentration in solution. At the CMC, the unimers assemble into micelles. Above this concentration, further addition of amphiphile leads to the formation of new micelles and the concentration of free unimers in solution is equal to the CMC value. Adapted from reference 9.** 4

Figure 1.3 **Schematic representation of the amphiphilic packing parameter that dictates the self-assembled structure. The drive to reduce the hydrophobic interface area favors growth of the assembly, while repulsions between the hydrophilic headgroups limit the micelle size. The balance between these opposing interactions determines the optimal interfacial area, a_0.** 7

Figure 1.4 **Representation of structures formed by block polymer amphiphiles. The structure depends on the molecular curvature, as described by the packing parameter (P). The scale bar in cryogenic transmission electron microscopy images (cryo-TEM) is 100 nm, and the image of cylindrical micelles was reproduced from Jain and Bates, *Science*, 2003, 300, 460-464. The image was reprinted with permission from AAAS.** 10

Figure 1.5 **Phase diagram for dilute solutions of poly(butadiene-*b*-ethylene oxide) block polymer amphiphiles. The polymer forms various morphologies including bilayer vesicles (B), cylindrical micelles (C), spherical micelles (S), and networks (N), depending on the molecular curvature of the amphiphile. The molecular curvature is controlled by the degree of polymerization of the hydrophobic block (N_{PB}) and hydrophilic weight fraction (w_{PEO}), and the desired solution morphology can be targeted by tuning the block polymer molecular weight and composition. The figure was reproduced from Jain and Bates, *Science*, 2003, 300, 460-464. The figure was reprinted with permission from AAAS.** 11

Figure 1.6 **Schematic representation of crew-cut and star-like micelles as considered by scaling theories. In crew-cut micelles, the degree of polymerization of the hydrophobic block (N_B) >> degree of polymerization of the hydrophilic block (N_A). Micelle at the opposite limit, $N_A >> N_B$, are referred to as star-like.** 15

Figure 1.7 **Schematic representation of dynamics processes in block polymer micelles. (a) Single chain exchange and (b) fusion/fission events are both thought to contribute to micelle formation and relaxation.** 20

Figure 1.8 **Design requirements for an idealized polymeric drug delivery vehicle. Adapted from review by Allen *et al.*[5]** 26

Figure 1.9 **Schematic representative of passive and active targeting in nanomedicine, adapted from a review by Farokhzad and Langer.[113] In passive targeting, nanoparticles pass through the leaky vasculature and selectively accumulate in solid tumors due to the EPR effect. In active targeting, targeting groups interact with cell surface receptors and facilitate cellular internalization of the drug carrier.** 28

Figure 2.1 **Regioisomers of polybutadiene. 1,2 addition is favored in polar solvents, while 1,4 addition is favored in apolar solvents.** 54

Figure 2.2 **Synthetic scheme for synthesis of poly(butadiene-*b*-ethylene oxide) (PB-PEO).** 56

Figure 2.3 **Schematic representation of solid phase peptide synthesis (SPPS) principle.** 61

Figure 2.4 **Reaction scheme for Fmoc removal using piperdine.** 65

Figure 2.5 **Reaction scheme for amino acid coupling *via* carboxylic acid activation using HBTU and subsequent amide bond formation.** 65

Figure 2.6 **SEC chromatogram and corresponding calibration curve for four low dispersity polystyrene standards.** 69

Figure 2.7 **Representative SEC chromatogram for a PB-PEO block polymer and corresponding PB-OH macroinitiator. Both polymers show a single low dispersity peak. Importantly, there is no peak corresponding to the PB-OH homopolymer in the PB-PEO trace.** .. 71

Figure 2.8 **Schematic representation of RP-HPLC separation. The analyte adsorbs to the hydrophobic column and remains there until the mobile phase is hydrophobic enough to elute the peptide. The more hydrophobic the analyte, the later it elutes off of the column.** 72

Figure 2.9 **Representative RP-HPLC data for characterization of PEO-peptide conjugates. (a) The standard solvent gradient used for analysis of peptides and PEO-peptides in this dissertation in which solvent B is 0.1 vol% TFA in acetonitrile. (b) Representative RP-HPLC traces for peptide, PEO-peptide conjugates, and PEO. The retention time increase with the hydrophobicity of the material, PEO > PEO-peptide > peptide.** 74

Figure 2.10 **Schematic representation of matrix-assisted laser desorption/ionization (MALDI) process.** 75

Figure 2.11 **Representative MALDI-TOF MS trace for a 3.2 kg mol^{-1} PB-OH polymer. The peak-to-peak spacing corresponds to the PB repeat unit molecular weight.** 78

Figure 2.12 **Comparison of different operation modes in MALDI-TOF MS (a) linear mode is more sensitive but has a lower resolution compared to (b) reflectron mode. Both spectra are for a 9.6 kg mol^{-1} PB-OH.** 79

Figure 2.13 **Representative mass spectra from salt doping experiments. Either sodium chloride (Na^+) or potassium chloride (K^+) was added to the sample to confirm which higher molecular weight peaks due to cations associating with the peptide.** 80

Figure 2.14 **Representative ^{1}H NMR spectra for PB-OH homopolymer. (a) Full spectra showing protons used to determine the relative ratios of 1,2 and 1,4 PB regioisomers and (b) zoomed in spectra showing the downfield shift of protons adjacent to the hydroxyl group after treating the samples with TFAA.** 84

Figure 2.15 **^{1}H NMR spectrum for a poly(butadiene-*b*-ethylene oxide) (PB-PEO) block polymer, with the peak assignments shown above. Note that the PEO peak at 3.7 ppm was clipped vertically.** 85

Figure 3.1 **Schematic representation of (a) Bragg scattering and (b) constructive and deconstructive wave interference. Adapted from Higgins and Benoit.[3]** 91

Figure 3.2 **Relationship between wavevectors and scattering vector (q) in elastic scattering.** 92

Figure 3.3 **Schematic representation of a dynamic light scattering (DLS) experiment. The diffusive motions of the particles lead to fluctuations in the measured intensity (I_t) about its average ($<I_t>$). These fluctuations are related mathematically through the time autocorrelation function.** 93

Figure 3.4 **Comparison of correlation functions for small and large particles. The larger particles diffuse slower, leading to longer correlation times and a slower decay of the correlation function.** 95

Figure 3.5 **Schematic representation of laser light scattering instrument.** 98

Figure 3.6 **Schematic representation of the effects of contrast variation on the measured structure of a core-shell particle in a SANS experiment.** 101

Figure 3.7 **Schematic representation of a small angle scattering experiment. (a) Diagram of instrument in which the incident beam is scattering by the sample and the scattering is measured by a 2-D detector. (b) The 2-D scattering data are reduced and integrated azimuthally to yield the 1-D scattered intensity *vs.* q.** 103

Figure 3.8 **Representative scattering data for a solid sphere with a radius, R = 5 nm.** 105

Figure 3.9 Schematic of the important optical components in a conventional TEM instrument. The condenser lenses and aperture focus and align the beam. The objective lens and aperture refocus and filter the beam after it passes through the sample. 112

Figure 3.10 Common artifacts in cryogenic transmission electron microscopy (cryo-TEM): (a-c) poorly vitrified samples (d) ethane crystals (e) beam damage to the sample and (f) hexagonally-packed spherical structures. 116

Figure 3.11 Schematic representation of size segregation of particles due to sample preparation, with larger particles at the edges of the holes and smaller particles in the center. 116

Figure 4.1 Characterization of micelles formed by sample 4c using cryo-TEM. (a) Cryo-TEM micrograph and (b) corresponding gray scale profile from cryo-TEM micrograph analysis and fit for sample 4c, supporting the PNIPAM chains form a diffuse, hydrated corona. Contrast shown in (a) was enhanced by 5% in ImageJ for clarity; the contrast was not adjusted for the profile analysis. Scale bar is 100 nm. The gray scale profile in (b) was averaged over 50 micelles. 132

Figure 4.2 Characterization of the amphiphilic homopolymer micelles using SANS. (a) SANS data (symbols) and fits with a spherical micelle form factor (lines) for 4a, 4b, and 4c in D_2O and (b) micelle corona profiles from the SANS data fits. 134

Figure 4.3 Comparison of normalized corona profiles for sample 4c from cryo-TEM micrograph analysis and SANS data modeling. Shaded area represents the range of dimensionless volume fraction profiles that gave similar fits to the gray scale profile from cryo-TEM. Solid line is the dimensionless profile from the SANS data modeling. R is the radius at which the respective corona profile decreased to 0. 138

Figure 5.1 Schematic representation of (a) block polymer micelle and (b) micelle density profile used to model SANS data. 151

Figure 5.2 PB-cosolvent interfacial tension as a function of THF content. Error bars represent the range of calculated values due to variability in the contact angle measurements. 156

Figure 5.3 **Representative DLS and cryo-TEM data for PB-PEO micelles in water/THF cosolvent mixtures. Plots of the decay constant (Γ) *vs.* q^2 determined from lights scattering for PB-PEO micelles in 0% (a) and 20% THF (b) cosolvent mixtures. Insets are the corresponding cryo-TEM micrographs (scale bar = 100 nm). Note that only the PB cores are visible in the micrographs due to minimal electron density contrast between PEO and water.** 157

Figure 5.4 **(a) DLS, SAXS, and cryo-TEM data showing the micelle hydrodynamics radius R_H, micelle radius R_m, and micelle core radius R_c, vs THF content in H_2O/THF mixtures. Error bars represent range in measured radii.** 157

Figure 5.5 **Experimentally determined micelle core radii (R_c) and corona thickness (H) for PB-PEO micelles in H_2O/THF cosolvent mixtures. Error bars for R_c represent the range of measured values. Error bars for H represent the range in calculated values. Solid lines are the theoretical scaling relationships for star like micelles.** 159

Figure 5.6 **SANS data (symbols) and fits (solid lines) for PB-PEO and PB-*d*PEO micelles in D_2O/THF-d_8 mixtures, where the labels indicate the volume percent of THF-d_8 in the cosolvent mixtures. Error bars represent the standard deviation in the measured intensity.** 161

Figure 5.7 **Fraction of free chains in the micelle solutions determined from the SANS data modeling. Error bars represent the range of values that gave the same goodness of fit.** 162

Figure 5.8 **SANS data (symbols) and fits (solid lines) for PB-PEO (a) and PB-*d*PEO (b) micelles in D_2O/THF-d_8 mixtures, where the labels indicate the volume percent of THF-d_8 in the cosolvent mixtures. Error bars represent the standard deviation in the measured intensity.** 163

Figure 5.9 **Micelle aggregation number (Q) and solvent fraction in the core ($\varphi_{solvent}$) determined from the SANS data analysis. Error bars in Q represent the range of fit values with similar goodness of fits. Error bars for $\varphi_{solvent}$ represent the range of calculated values due to uncertainty in the fit parameters used in the calculation. Dashes lines are to guide the eye.** 164

Figure 5.10 **Radial composition profile in the PEO corona in PB-PEO micelles in D_2O/THF-d_8 mixtures as determined from SANS data analysis.** 166

Figure 5.11 **Radius of gyration (R_g) of PEO homopolymer (6 kDa) in D_2O/THF-d_8 cosolvent mixtures determined from SANS measurements. SANS data were fit with a Debye function to determine the** Rg**. Error bars represent the range in fit values for** Rg **with similar goodness of fits.** 167

Figure 5.12 **(a) ^{1}H NMR spectra of PB-PEO micelles in D_2O/THF-d_8 mixtures, boxed regions highlight the peaks associated with the PB and PEO blocks, and (b) fraction of mobile PB chains in PB-PEO micelles calculated from (a). Error bars in (b) represent standard deviation in values from three experiments.** 169

Figure 6.1 **Schematic representation of single chain exchange mechanism, showing (1) extraction of the core block, (2) diffusion of the chain through the solvent, and (3) reinsertion of the chain into another micelle. Extraction of the core block (step 1) is assumed to the rate-limiting step.** 187

Figure 6.2 **Schematic representation of chain exchange experiments. At t= 0, PB-PEO and PB-*d*PEO micelles are mixed. Single chain exchange leads to randomization of the PEO/*d*PEO chains in the micelle corona, which contrast matches the solvent.** 190

Figure 6.3 **TR-SANS curves for mixtures of PB-PEO and PB-*d*PEO micelles in 30 vol% THF-d_8 cosolvent mixtures in D_2O/H_2O at 30 °C (top), 10 vol% THF-d_8 at 30 °C (middle), and 10 vol% THF-d_8 at 50 °C (bottom).** 191

Figure 6.4 **TR-SANS curves for mixtures of PB-PEO and PB-*d*PEO micelles in 30 vol% THF-d_8 cosolvent mixtures at 30 °C (top), 55 °C (middle), and 60 °C (bottom).** 193

Figure 6.5 **(a) Relaxation function for the 30 vol% THF-d_8 micelle solution as a function of temperature. (b) Time-temperature superposition of TR-SANS data and fit for T_{ref} = 55 °C. Empirical shift factors for time-temperature superposition are given in inset of (b).** 195

Figure 6.6 **Estimated relaxation functions for PB-PEO micelles in H_2O/THF cosolvent mixtures at 25 °C.** 199

Figure 7.1 **(a) DLS data showing the effects of stirring on the change in $<R_H>$ following dialysis to H_2O (Day 0 to Day 120). The THF content and polymer concentration prior to dialysis were 43 vol% and 10 mg mL^{-1}, respectively. The agitated sample was stirred at 200 rpm. (b) DLS data showing the change in $<R_H>$ before (Day -1) and after (Day 0 to 90) THF cosolvent removal as a function of THF content in stirred samples. The polymer concentration was 2 mg mL^{-1} before dialysis to water. In all cases, the solutions were stirred at 200 rpm. The variability in $<R_H>$ was 1 to 3 nm.** 214

Figure 7.2 **SAXS data for micelles prepared in various water/THF mixtures (0 - 50 vol% THF) before (Day -1) and after (Day 3 and Day 30) dialysis to pure water. The concentration before dialysis was 2 mg mL^{-1} and all samples were stirred after dialysis. Black diamonds mark the peak location before dialysis to water. SAXS curves were shifted vertically for clarity.** 216

Figure 7.3 **SANS curves for mixtures of PB-PEO and PB-*d*PEO micelles (open and gray circles) and pre-mixed PB-PEO/PB-*d*PEO micelles (black circles) in D_2O/H_2O at 25 °C. The t= 10 d sample was gently stirred at 200 rpm.** 218

Figure 7.4 **Cryo-TEM studies of PB-PEO micelle size evolution following cosolvent removal. Micelle solutions were prepared at a polymer concentration of 2 mg mL^{-1} with 0-50 vol% THF in water. Day -1 analyses were performed in the cosolvent mixtures prior to dialysis against pure water. Subsequently, on Day 0, solutions were dialyzed against pure water to remove the THF. Day 7, Day 8, and Day 90 correspond to the number of days following dialysis. Note that images at different magnifications were scaled for ease of comparison. Scale bars represent 100 nm.** 220

Figure 7.5 **Cryo-TEM micrographs showing changes in PB-PEO micelle core radii between Day 0 and Day 20 for several polymer concentrations. The initial polymer concentrations were 2 mg mL^{-1}, 5 mg mL^{-1}, and 10 mg mL^{-1}. After dialysis, the concentrations followed the same trend but were approximately half the initial concentration (Section 7.2.2). In each case, the THF content was 43 vol% prior to dialysis into water. Scale bars are 100 nm.** 222

Figure 7.6 **(top) SANS data (points) and fits (solid lines) for micelle solutions at different concentrations. (bottom) Corresponding number frequency distribution of core radii from fits to SANS data. The initial polymer concentrations were 2 mg mL^{-1}, 5 mg mL^{-1}, and 10 mg mL^{-1}. After dialysis, the concentrations followed the same trend but were approximately half the initial concentration (Section 7.2.2). Samples for the SANS experiments were prepared in 43 vol% THF and dialyzed against D_2O, and SANS experiments were performed at Day 11 post dialysis to D_2O. The sensitivity of the number frequencies from the SANS data modeling was approximately ± 5% for the 2 mg mL^{-1} data and ± 15% for the 5 mg mL^{-1} and 10 mg mL^{-1} data.** 224

Figure 7.7 **(a) Cryo-TEM images showing changes in PB-PEO core radii 21 days post-dialysis. The polymer concentration was initially 10 mg mL^{-1} and the THF content was 43 vol% before dialysis. Scale bars represent 100 nm. (b) Corresponding histograms of micelle sizes obtained from analysis of cryo-TEM images. Sample size for each histogram ranged from 450 and 3000 micelles.** 226

Figure 8.1 **Effects of common mixing types on chain exchange in block polymer micelles. PB-PEO micelles were (a) sheared in a Couette cell at γ = 5000 s^{-1} for 90 min (b) sparged with N_2 for 60 min or (c) vortexed at approximately 3000 rpm for up to 20 min. All solutions contained 5 mg mL^{-1} polymer in D_2O/H_2O mixtures. Scattering data were collected at 25 °C.** 244

Figure 8.2 **Effects of mixing on micelle structure. SANS data (points) and form factor fits (red lines) for the post-mixed, pre-mixed, and vortexed micelle samples. The data sets were analyzed with a form factor model for block polymer micelles.** 246

Figure 8.3 **Effects of vial headspace (amount of air) on mixing induced chain exchange. Each solution was vortex-mixed in a 1 dram vial; however, the volume of sample within the vial was varied. Increasing the sample volume (decreasing the headspace) significantly reduced the rate of chain exchange. Both solutions contained 5 mg mL^{-1} polymer in D_2O/H_2O mixtures and were vortex mixed for 15 min. Scattering data were collected at 25 °C.** 248

Figure 8.4 **Effects of micelle concentration on vortex-induced chain exchange in block polymer micelles. SANS data for (a) 2.5 mg mL^{-1} (b) 7.5 mg mL^{-1} (c) 10 mg mL^{-1} and (d) 15 mg mL^{-1} samples vortex-mixed for varying times.** 249

Figure 8.5 **Chain exchange kinetics plotted as R(t) *vs.* vortex mix time for PB-PEO micelles at varying concentrations.** 251

Figure 8.6 **Vortex-induced chain exchange kinetics in block polymer micelles. Kinetics of chain exchange for different concentration micelles plotted as the concentration of exchanged chains. The kinetics for the low concentration micelle solutions are linear with mix time; however, the rate constant appears to decrease with increasing concentration. The kinetics for the highest concentration sample (15 mg mL^{-1}) are the slowest and deviate from linearity.** 252

Figure 8.7 **Schematic representation of block polymer micelle adsorption to the air/water interface. The hydrophobic block is exposed to air and is surrounded (laterally and underneath) by the hydrophilic block in water.** 254

Figure 9.1 **Schematic representation of the contradictory need for shielded ligand (stars) during circulation to take advantage of passive targeting yet accessible ligands to bind to cells and take advantage of active targeting.** 264

Figure 9.2 **Schematic representation of enzyme-responsive polymer-peptide conjugate design. The micelles accumulate in the tumor by passive targeting. Within the tumor, the peptide linkage is cleaved by the MMP proteases, exposing the targeting ligand and facilitating cellular uptake by receptor-mediated endocytosis.** 266

Figure 9.3 **Synthesis scheme for the hydrophobic PEE-N_3 block via (1) chemical hydrogenation using a diimide and (2) end-group functionalization.** 282

Figure 9.4 **SEC traces for PB-OH precursor and PEE-OH polymer. THF was used as an eluent, and the recorded intensity was the differential refractive index. Dispersities were calculated based on polystyrene standards.** 284

Figure 9.5 **^{1}H NMR spectra confirming the complete hydrogenation of PB-OH to yield PEE-OH.** 284

Figure 9.6 **^{1}H NMR spectra of end-functionalized PEE. The PEE-OH and PEE-mesyl samples contained residual *p*-tolyl mercaptan (TDS, < 5 wt%) from the chemical hydrogenation reaction. The presence of the TDS did not affect the end-functionalization reactions, and TDS was removed by the methanol precipitations during the PEE-N_3 purification.** 285

Figure 9.7 **Schematic representation of hydrophilic PEO-peptide block synthesis.** 286

Figure 9.8 **Probing peptide sensitivity to enzymatic cleavage using FRET. (a) Schematic representation of FRET experiments and (b) fluorescence data showing increased fluorescence in peptide samples incubated with active enzyme (collagenase + Ca^+ ions) compared to inhibited enzyme (collagenase), supporting that the peptide linkage is enzyme sensitive.** 288

Figure 9.9. **Characterization of crude 'interface' peptide. (a) RP-HPLC trace indicating the peptide was synthesized to high purity and (b) MALDI-TOF MS data showing the majority product was the desired sequence. Sequence: N-GEPQGI↓WGQKGGRGDSPGG(alkyne)-C.** 290

Figure 9.10 **Characterization of PEO-peptide conjugates synthesized on resin. Crude RP-HPLC traces (a and b) and MALDI-TOF mass spectrum (c and d) for the end and interface conjugates, respectively. The expected and observed molecular weight for the PEO-peptide conjugates were ~4200 g mol^{-1}.** 292

Figure 9.11 **Characterization of PEO-peptide conjugate synthesized by first functionalizing the resin with a heterobifunctional PEO and then growing the peptide from the polymer chain. (a) Schematic representation of the synthetic scheme. (b) RP-HPLC data of the crude reaction product containing a peak at 27 min and 32 min corresponding to the PEO-peptide and unreacted PEO, respectively. (c) MALDI-TOF MS confirming PEO-peptide synthesis. Expected molecular weight: 2474 g mol^{-1}, observed molecular weight: 2602 g mol^{-1}. The discrepancy between the expected and observed molecular weights likely was due to incomplete deprotection of the peptide.** 294

Figure 9.12 **Schematic representation of amphiphilic polymer-peptide conjugate synthesis.** 295

Figure 9.13 Monitoring PEE-N_3 + peptide-alkyne coupling with ATR-FTIR. The peak at 2100 cm^{-1} in the PEE-N_3 spectrum corresponded to the azide stretches. This peak was not seen in the PEE-peptide conjugate spectrum, suggesting complete coupling between the blocks. 297

Figure 10.1 Schematic representation of amphiphilic polymer-peptide conjugate library with location of the functional peptide linkage (stars) varied throughout the hydrophilic backbone. 320

Figure 10.2 Schematic representation of polymer-peptide conjugate synthesis with the peptide linkage embedded within the hydrophilic backbone. First, the resin is functionalized with a heterobifunctional hydrophilic polymer, then the peptide linkage is synthesized using solid phase peptide synthesis (SPPS), and finally a second hydrophilic polymer is coupled to the N-terminus of the peptide. 321

Figure 10.3 Schematic representation of materials library synthesized using the modular chemistries described in this dissertation. 325

Figure 10.4 Schematic representation of controlling self-assembled morphology by varying the hydrophobic to hydrophilic block ratio in amphiphilic polymer-peptide conjugates. 327

Figure 10.5 Schematic representation of synthesis, self-assembly, and characterization of amphiphilic polymer-peptide conjugates using anomalous small angle X-ray scattering (ASAXS). For ASAXS experiments, selenium-labeled amino acids are incorporated into the targeting ligand, and then ASAXS experiments are performed at multiple X-ray energies above and below the Se K-edge. The scattered intensity can then be decomposed into the non-resonant and resonant scattering from the entire micelle structure and anomalous scatterer (Se), respectively, facilitating precise determination of the ligand location with the self-assembled structure. 330

Figure 10.6 Energy dependent real (f') and imaginary (f'') parts of X-ray scattering factor for selenium. The K-edge (12.658 keV) is accessible at synchrotron radiation sources for ASAXS experiments. 331

Figure C1 SANS data (points) and fits (lines) for PB-PEO and PB-*d*PEO micelles in a 0 vol% THF cosolvent mixture (pure water). 356

Figure C2 **SANS data (points) and fits (lines) for PB-PEO and PB-*d*PEO micelles in a 2.5 vol% THF cosolvent mixture.** 356

Figure C3 **SANS data (points) and fits (lines) for PB-PEO and PB-*d*PEO micelles in a 5 vol% THF cosolvent mixture.** 357

Figure C4 **SANS data (points) and fits (lines) for PB-PEO and PB-*d*PEO micelles in a 10 vol% THF cosolvent mixture.** 357

Figure C5 **SANS data (points) and fits (lines) for PB-PEO and PB-*d*PEO micelles in a 15 vol% THF cosolvent mixture.** 358

Figure C6 **SANS data (points) and fits (lines) for PB-PEO and PB-*d*PEO micelles in a 20 vol% THF cosolvent mixture.** 358

Figure C6 **SANS data (points) and fits (lines) for PB-PEO and PB-*d*PEO micelles in a 30 vol% THF cosolvent mixture.** 359

Figure C7 **SANS data (points) and fits (lines) for PB-PEO and PB-*d*PEO micelles in a 40 vol% THF cosolvent mixture.** 359

Figure C8 **SANS data (points) and fits (lines) for PB-PEO and PB-*d*PEO micelles in a 50 vol% THF cosolvent mixture.** 360

Figure C9 **SANS data (points) and fits (lines) for PB-PEO and PB-*d*PEO micelles in a 60 vol% THF cosolvent mixture.** 360

Figure C10 **SANS data (points) and fits (lines) for PB-PEO and PB-*d*PEO micelles in a 70 vol% THF cosolvent mixture.** 361

Figure C11 **SANS data (points) and fits (lines) for PB-PEO and PB-*d*PEO micelles in a 72 vol% THF cosolvent mixture.** 361

Figure C12 **SANS data (points) and fits (lines) for PB-PEO and PB-*d*PEO micelles in a 75 vol% THF cosolvent mixture.** 362

Figure C13 **SANS data (points) and fits (lines) for PB-PEO and PB-*d*PEO micelles in a 77 vol% THF cosolvent mixture.** 362

Figure C14 **SANS data (points) and fits (lines) for PB-PEO and PB-*d*PEO micelles in an 80 vol% THF cosolvent mixture.** 363

Figure C15 **SANS data (points) and fits (lines) for PB-PEO and PB-*d*PEO micelles in a 90 vol% THF.** 363

Figure C16 **SANS data (points) and fits (lines) for PB-PEO and PB-*d*PEO micelles in pure THF cosolvent mixture.** 364

Figure D1 **Absorbance measurements for PB homopolymer in H_2O/THF mixtures. Error bars represent the standard deviation of measurements from three different polymer solutions.** 366

Figure E1 **SANS data and fits using a monomodal or bimodal distribution. SANS data (points) and monomodal or bimodal fits (solid lines) for micelle solutions at initial polymer concentrations of (a) 2 mg mL^{-1}, (b) 5 mg mL^{-1}, and (c) 10 mg mL^{-1}. Insets correspond to number frequency distributions of core radii for a monomodal (left) and bimodal (right) Schulz distribution of spheres. For each solution, THF content was 43 % by volume prior to dialysis into pure D_2O, and data were collected 11 d following dialysis. Arrows highlight distinguishing features between the monomodal and bimodal fits to the scattering curve.** 368

Figure F1 **Synthetic scheme for PB-PEO-COOH.** 369

Figure F2 **Representative ^1H NMR spectrum confirming successful synthesis of PB-PEO-COOH. Note that the PEO peak was clipped for clarity.** 371

Figure F3 **Synthetic scheme for PB-PEO-Br.** 372

Figure F4 **^1H NMR spectra confirming successful synthesis of PB-PEO-Br. Note that the PEO peak was clipped for clarity.** 373

Figure F5 **Scheme for two-step synthesis of PB-PEO-N_3.** 374

Figure F6 **^1H NMR of PB-PEO-OH, PB-PEO-mesyl intermediate, and PB-PEO-N_3 final product. Note that the PEO peak was clipped for clarity.** 376

Figure F7 **SEC trace for PB-PEO-N_3. Calculated dispersity is based on polystyrene standards.** 377

Figure G1 **Schematic representation of PB-PEO-peptide synthesis *via* on-resin conjugation.** 379

Figure G2 **Images from the TNBS assay of the peptide-loaded resin beads (a) before and (b) after reaction with PB-PEO-COOH.** 381

Figure G3 **Schematic representation of micelle functionalization using an aqueous copper-catalyzed azide-alkyne cycloaddition (click) reaction.** 382

Figure G4 **SEC data for PB-PEO-N_3 precursor and PB-PEO-peptide conjugates. SEC experiments were performed using THF as a mobile phase.** 384

Figure G5 **UV-Vis spectra from the TNBS assay of the PB-PEO-N3 precursor and the PB-PEO-peptide conjugate. The trinitrophenyl derivative control was prepared by incubating TNBS with a 200 μM glycine solution.** 385

ABSTRACT

Analogous to small molecule lipids and surfactants, amphiphilic block polymers self-assemble into well-defined nanostructures in aqueous solutions such as spherical micelles, cylindrical micelles, and vesicles. Their macromolecular architecture leads to several advantages compared to small molecule amphiphiles, including increased chemical versatility, explicit control over the size and structure of solution assemblies, extremely low critical aggregation concentrations, and exceptionally slow chain exchange. These attractive advantages have motivated significant research efforts towards developing polymeric surfactants for emerging nanotechnologies including aqueous nanoreactors and drug delivery vehicles. To take full advantage of block polymer materials in these applications, a comprehensive understanding of the factors that influence self-assembly behavior as well as robust methods for controlling the chemical functionality of polymeric assemblies must continue to be developed. Accordingly, this dissertation demonstrates the synthesis, solution assembly, and characterization of amphiphilic block polymers towards the goal of creating well-defined nanoassemblies. The first objective of this dissertation was to systematically investigate the effects of common processing conditions on the structure, dynamics, and long-term stability of block polymer micelles. The pronounced effects of organic cosolvent addition and subsequent removal were studied using a combination of cryogenic transmission electron microscopy and small angle neutron scattering. Notably, solution agitation was found to have unexpected consequences on the dynamics and stability of the resulting assemblies. A growing

number of works indicate that in addition to the structure, the chemical functionality of polymeric assemblies plays a critical role in determining the *in vivo* fate of drug delivery vehicles. Thus, the second objective of this research was to establish a tunable method for controlling the display of peptide groups within polymeric assemblies to target specific diseased tissues. A modular synthetic strategy was developed for creating well-defined polymer-peptide conjugates that allowed control over both the peptide sequence and peptide location within the polymer backbone. Together, the efforts in this dissertation provide the foundation for the rational design of novel materials by enabling greater control over both the structure and functionality of polymer-based nanoassemblies.

Chapter 1

INTRODUCTION

Amphiphilic molecules play an important role in everyday life. The cell membrane is composed of more than 100 structurally unique amphiphilic lipids that self-assemble into a well-defined bilayer which separates the cell from its surrounding environment and maintains a delicate balance of nutrients essential to life.[1] In fact, some theories hypothesize that this compartmentalization by self-assembled amphiphiles was essential to the origins of life.[2] Synthetic amphiphiles, also referred to as surfactants, are integral components in diverse chemical products ranging from motor oils in cars, drilling muds used to recover petroleum, and personal care and cleaning products in our homes.[3] There is also growing interest in developing these versatile materials for applications in nanotechnologies including biosensors, medical imaging, drug delivery, and aqueous nanoreactors.[4-8] Innovate macromolecular amphiphiles have a distinct advantage over small molecules for these applications given their synthetic versatility, tunable self-assembly, and favorable solution properties. Accordingly, the aims of this work were to improve the fundamental understanding of factors that influence macromolecular solution assembly and to develop robust methods for controlling the surface functionality of polymeric nanostructures. Together the results in this dissertation enable control of the structure and surface chemistry of polymeric assemblies and advance the development of these promising materials for emerging nanotechnologies.

1.1 Amphiphiles

The versatility of amphiphilic materials comes from their unique chemical structure and associated self-assembly behavior. Amphiphilic molecules are composed to two chemically distinct regions: a hydrophilic (water-loving) portion and a hydrophobic (water-hating) portion. As a result of this dual nature, amphiphilic molecules spontaneously self-assemble in aqueous solutions as depicted in Figure 1.1. In these nanoscale structures, the hydrophobic portions of the molecules (usually hydrocarbon chains) aggregate and are shielded from the aqueous environment by the hydrophilic portions of the molecules, which form a protective outer layer that is referred to as a corona.

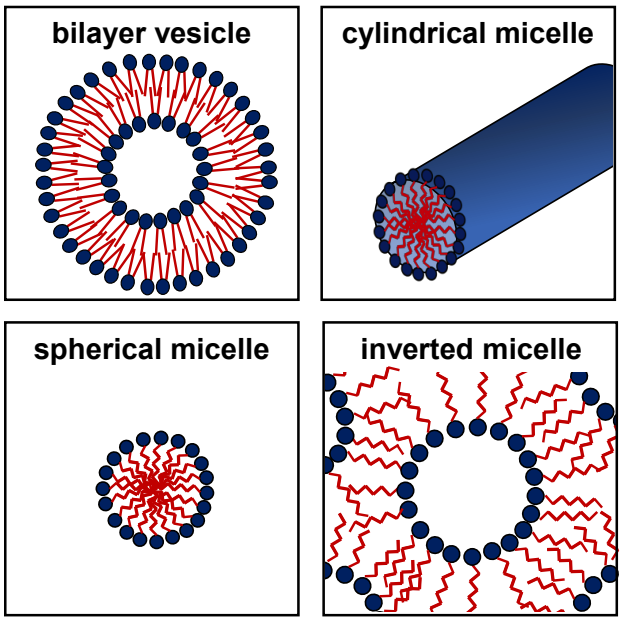

Figure 1.1 Schematic representation of nanoscale structures formed by amphiphilic molecules in aqueous solutions. The hydrophobic portions of the molecule (red) aggregate and are shielded from the aqueous environment by the hydrophilic portions of the molecule (blue). Adapted from reference 9.

Thermodynamics of Micelle Formation

The tendency for hydrophobic regions of a molecule to avoid contact with the water is termed the hydrophobic effect.[9,10] While this effect is driven in part by the enthalpically unfavorable interactions between the hydrophobic portion of the molecule and water, solution self-assembly is primarily an entropically driven process. In the absence of salts or organic molecules, hydrogen-bonding leads to a tetrahedral arrangement of water molecules.[10] Adding unassociated hydrocarbon chains to water disrupts this hydrogen-bonding and forces a local ordering in the water molecules that is entropically unfavorable.[9-11] Subsequent assembly of the amphiphiles reduces the order of the water molecules and therefore is energetically favorable.

Because of the hydrophobic effect, amphiphilic molecules form a variety of nanoscale structure in aqueous solutions. The amphiphiles spontaneously self-assemble above a critical concentration, referred to as the critical micelle concentration (CMC) or more generally as the critical aggregation concentration (CAC), as depicted in Figure 1.2.[9-11] The amphiphiles are dispersed in solution below the CMC, and the unassociated molecules are often referred to as unimers. Above this concentration, further addition of amphiphiles leads to the formation of new assemblies, and the concentration of unimers in solution remains essentially constant at the CMC value.

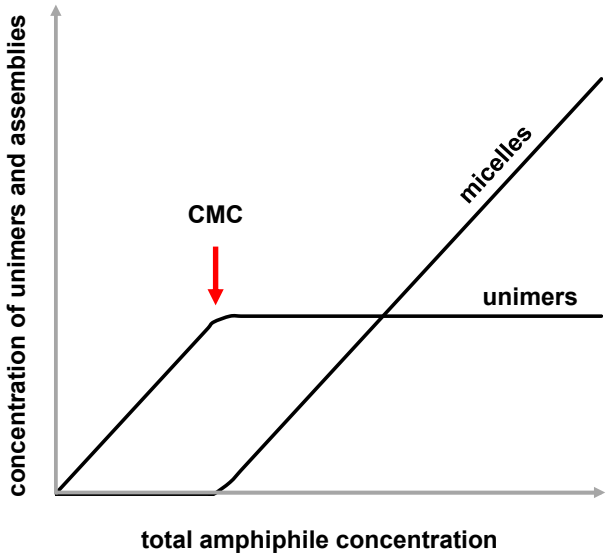

Figure 1.2 Schematic representation of unimer and micelle concentration as a function of total amphiphile concentration in solution. At the CMC, the unimers assemble into micelles. Above this concentration, further addition of amphiphile leads to the formation of new micelles and the concentration of free unimers in solution is equal to the CMC value. Adapted from reference 9.

The CMC is an important characteristic of amphiphilic molecules, and knowing this value is crucial to understanding the self-assembly and solution properties. Many solution properties, such as the surface tension[12,13] and electrical conductivity,[13] show an abrupt change at the CMC and provide a convenient means of determining the CMC. Other techniques to measure the CMC, such as dynamic light scattering (DLS)[14] and diffusion-ordered nuclear magnetic resonance spectroscopy (DOSY),[15] are sensitive to the diffusion of the amphiphilic molecules. Another common method for determining the CMC relies on changes in the spectroscopic properties of dyes, as these measurements are readily made using common equipment

in most laboratories; however, a downside of this approach is that the presence of the dye also may influence the self-assembly behavior.[14,16-18]

In general, the CMC is a function of the amphiphile structure and solvent selectivity. [3,9,11] For a spherical assembly, the CMC is described by

$$CMC = \exp(-4\pi r^2 \gamma / kT) \quad (1)$$

in which r is the effective radius of the molecule and γ is the interfacial tension between the hydrophobe and the solvent.[9] Consequently, increasing the molecular weight of the hydrophobic portion of the molecule or altering the solvent selectively (increasing γ) decreases the CMC. The CMC also depends on the hydrophilic portion of the molecule and the addition of salts. Ionic surfactants typically have higher CMCs compared to nonionic surfactants, as electrostatic interactions between the headgroups must be overcome to form a micelle from ionic surfactants.[3,11] Accordingly, adding salts decreases the CMC of ionic surfactants by shielding the headgroup repulsions. The CMC is affected by temperature; however, these effects are quite complex.[3] Increasing the temperature decreases the hydration of the hydrophilic portion of the molecule, which favors micelle formation; however, higher temperatures also disrupt the water structure around the hydrophobic portion of the molecule, which decreases the driving force for micellization.

Micelle formation above the CMC can be described as a cooperative process, as it requires simultaneous participation of numerous amphiphilic molecules.[10] The hydrophobic effect dictates a lower size limit, as an assembly formed by two or three amphiphilic molecules cannot eliminate the unfavorable hydrophobic/water interface.

Accordingly, several molecules must come together to create a stable assembly. At the same time, repulsive interactions between the amphiphilic molecules impose an upper size limit and restrict the micelle growth. These opposing interactions ultimately dictate the resulting size and structure of the aggregate, and the number of molecules per assembly is referred to as the aggregation number.

Equilibrium Structures

As suggested in Figure 1.1, amphiphiles form a variety of structures in aqueous solutions ranging from spherical micelles to elongated rod-like or cylindrical micelles to bilayer vesicles. Understanding these morphologies requires an understanding of not only the self-assembly process described above, but also the intramolecular forces within the structure. Unfavorable interactions between the hydrocarbon chain and the solvent minimize the interfacial area per molecule, while steric repulsions between the hydrophilic head groups tend to increase the interfacial area (Figure 1.3). Consequently, the final morphology is dictated by a delicate balance between these opposing interactions, which is described by the packing parameter,*P*

$$P = \frac{v}{l_c a_0} \tag{2}$$

in which v is the volume of the hydrophobic tail, l_c is the maximum hydrophobic tail length, and a_0 is the area between the hydrophobic tail and hydrophilic head group. Amphiphiles with small packing parameters (*i.e.* large interfacial areas) form structures with large interfacial curvature such as spheres, whereas amphiphiles with

large values of the packing parameter (small interfacial areas) form structures with less curvature such as cylinders or bilayers.

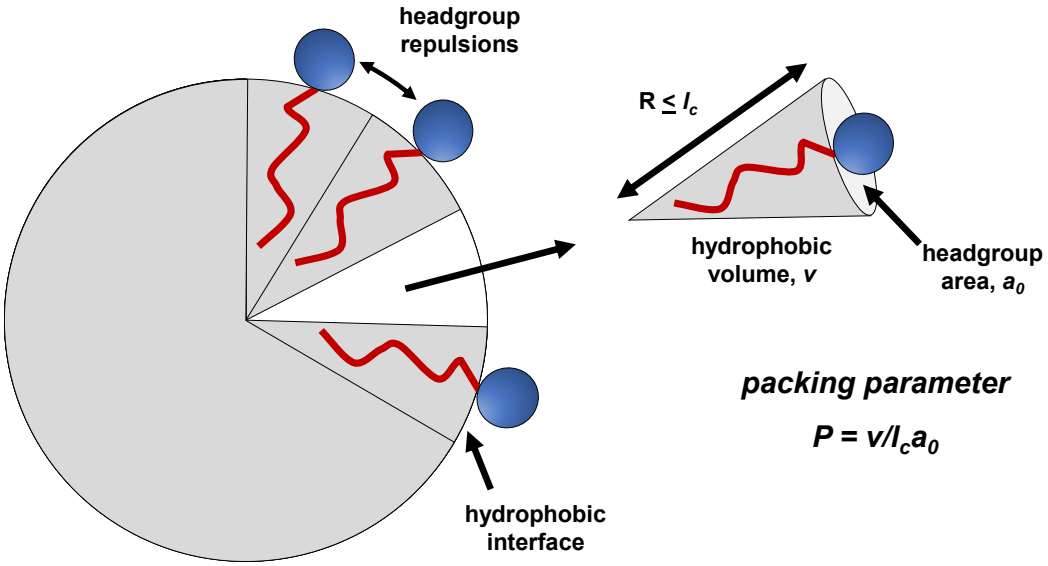

Figure 1.3 Schematic representation of the amphiphilic packing parameter that dictates the self-assembled structure. The drive to reduce the hydrophobic interface area favors growth of the assembly, while repulsions between the hydrophilic headgroups limit the micelle size. The balance between these opposing interactions determines the optimal interfacial area, a_0.

At higher amphiphile concentrations, intermolecular interactions between assemblies further influences the assembled structure.[3,11] Depending on the shape of the individual assemblies, they pack together into three-dimensional structures that are referred to as liquid crystals. For example, spherical micelles form cubic structures while cylindrical micelles from hexagonal structures.[9,11] The long-range order of

these assemblies is appealing for applications in templating inorganic materials for catalysis and molecular separations.[19-21]

Equilibrium Dynamics

The field of solution assembly originates from the study of small molecule surfactants and lipids. As suggested by Figure 1.2, free unimers coexist with the micelles in solution, and the constituent molecules are redistributed continuously between equilibrium surfactant assemblies on time scales ranging from μs to ms.[22] However, accessing the necessary length scales and time scales to understand these rapid equilibrium dynamics in small molecule amphiphiles is experimentally challenging. Early studies indirectly probed the dynamics by perturbing the system using a temperature or pressure jump and watching the system relax back to equilibrium. In the 1970s, Aniansson and Wall first theoretically described, and later experimentally demonstrated, that these *near* equilibrium dynamics are dominated by single exchange events, in which an individual surfactant molecules transfers from one micelle to another,[23-26]

$$S_n + S_m \leftrightarrow S_{n-1} + S_{m+1}$$

The relaxation was described by two time constants. The first time constant was used to fit the fast relaxation due to changes in the unimer concentration, and did not account for changes in the number density of micelles. The second, slower time constant then was associated with the change in the number of micelles due to exchange of chains between the micelles. Importantly, this chain exchange between assemblies allows amphiphilic small molecules to achieve an equilibrium structure.

1.2 Block Polymer Amphiphiles

An amphiphilic block polymer consists of covalently bonded hydrophobic and hydrophilic polymer segments. Akin to small molecule amphiphiles, these macromolecules also self-assemble into classic nanostructures in aqueous solutions, such as spherical micelles, cylindrical micelles, and vesicles. The resulting morphology can be controlled by varying the molecular curvature, and specific nanostructures and sizes can be targeted by controlling the block polymer molecular weight and composition as suggested in Figures 1.4 and 1.5. Moreover, the seemingly limitless combinations of polymer chemistries, chain architectures, and block polymer compositions provide access to complex morphologies not attainable with small molecule systems. For example, the solution self-assembly of an ABC triblock terpolymer in which block A is hydrophilic and blocks B and C are different hydrophobic blocks leads to elaborate multicompartment nanostructures with segregated B and C domains within the hydrophobic core.[27,28] While the synthetic versatility block polymer systems creates a wealth of elegant nanostructures, it also introduces a complex parameter space for controlling their self-assembly. The self-assembly of many block polymer amphiphiles is characterized in literature; however, certain aspects of their intricate self-assembly have remained elusive and the ability to take full advantage of these promising materials requires a comprehensive understanding of the factors that influence their structure, dynamics, and long-term stability.

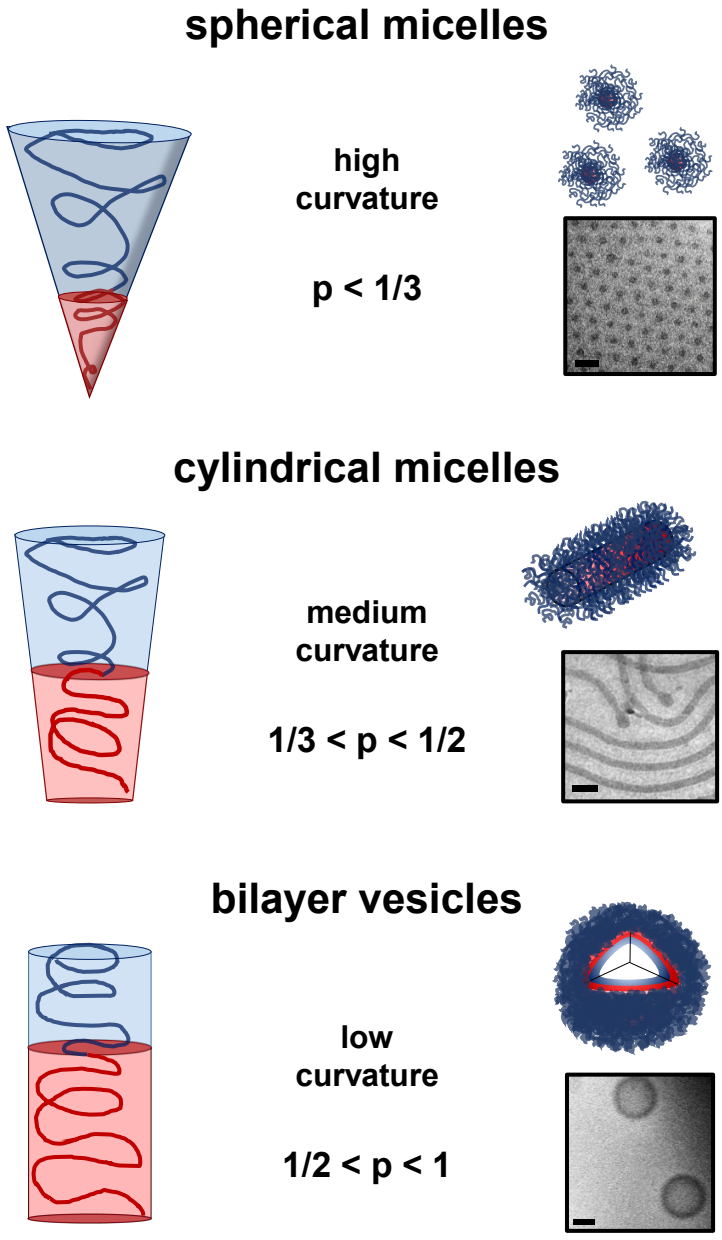

Figure 1.4 **Representation of structures formed by block polymer amphiphiles. The structure depends on the molecular curvature, as described by the packing parameter (P). The scale bar in cryogenic transmission electron microscopy images (cryo-TEM) is 100 nm, and the image of cylindrical micelles was reproduced from Jain and Bates, *Science*, 2003, 300, 460-464. The image was reprinted with permission from AAAS.**

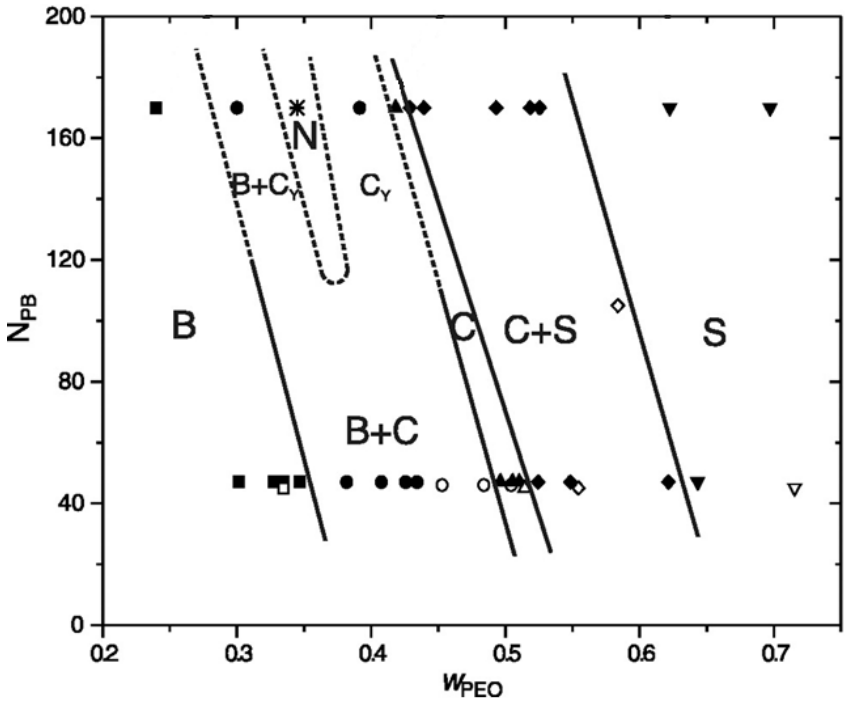

Figure 1.5 Phase diagram for dilute solutions of poly(butadiene-*b*-ethylene oxide) block polymer amphiphiles. The polymer forms various morphologies including bilayer vesicles (B), cylindrical micelles (C), spherical micelles (S), and networks (N), depending on the molecular curvature of the amphiphile. The molecular curvature is controlled by the degree of polymerization of the hydrophobic block (N_{PB}) and hydrophilic weight fraction (w_{PEO}), and the desired solution morphology can be targeted by tuning the block polymer molecular weight and composition. The figure was reproduced from Jain and Bates, *Science*, 2003, 300, 460-464. The figure was reprinted with permission from AAAS.

Structure and Thermodynamics

Decades of fundamental research provide a framework for understanding and controlling several factors that influence the self-assembled morphology in polymeric amphiphiles.[29] Many of the early studies focused on the solution assembly of the commercially available 'Pluronics' (BASF), which are amphiphilic diblock and

triblock copolymers based on poly(ethylene oxide) and poly(propylene oxide). [30-41] Growing interest in macromolecular surfactants has inspired synthesis of numerous other amphiphilic block polymer systems.[42,43] Of particular interest are spherical block polymer micelles, which are composed of a well-defined hydrophobic core surrounded by a hydrophilic corona. Small molecule hydrophobic cargoes readily are loaded into the micelle cores, which has inspired the development of these materials for applications in drug delivery, templating metal nanoparticles, separation processes, and aqueous nanoreactors.[42] Controlling the properties of polymeric micelles is especially desirable because their loading capacity and performance in the abovementioned applications is directly correlated to their size. The following sections describe theoretical efforts to relate the block polymer properties, such as the overall molecular weight, relative composition, and polymer-solvent interactions, to the resulting micelle structure.[43-45]

As in small molecule systems, the final morphology of a block polymer assembly is dictated by a balance of hydrophobic interactions and intramolecular interactions within the structure. In general, the micelle free energy ($F_{micelle}$) is composed of three terms:

$$F_{micelle} = F_{interface} + F_{core} + F_{corona} \quad (3)$$

in which $F_{interface}$, F_{core} and F_{corona} are the free energy contributions of the interface, core, and corona, respectively. The balance of these terms in a block polymer micelle at equilibrium is described by two classes of theories in literature: mean-field theories and scaling theories.[44,45]

Mean field theories reduce a multibody problem into simplified, effective interaction terms by replacing the local potentials with an effective field.[44] Using this approach, several works have provided insights into the dependence of the micelle aggregation number, core size, and corona dimensions on the degree of polymerization of the hydrophobic and hydrophilic blocks, as well as the polymer-polymer and polymer-solvent interaction parameters in the equilibrium assemblies.[45-55] Mean field theories support that a narrow interface exists between the core and corona of the micelle, and this interfacial profile was used in subsequent theoretical analyses.[45] Mean field theories are in reasonably good agreement with experimental data;[56] however, these theories work best for systems with weak polymer-solvent interactions and excluded volume interactions.[44]

Systems with strong excluded volume interactions are better described by scaling theories that take into account the spatial correlations within the structure.[44,45] In these theories, complicated structural and thermodynamic features in the micelle are described by simple geometrical and physical arguments.[45,57-60] Scaling theories for polymer micelles describe the corona density profile in terms of correlation blobs,[45] as pioneered by de Gennes.[61]

In all theories, micelle formation is driven by the minimization of the interfacial free energy, $F_{interface}$, which is proportional to the interfacial area per chain,

$$F_{interface} = \frac{4\pi {R_c}^2 \gamma}{Q} \quad \sim \quad Q^{-1/3}\gamma \tag{4}$$

in which R_c is the micelle core radius, γ is the interfacial tension, and Q is the micelle aggregation number.

In scaling theories, F_{core} is due chain stretching in the micelle core to maintain a constant melt density if the micelle radius is greater than the root-mean-square end-to-end distance of the hydrophobic block,

$$\frac{F_{core}}{k_B T} = \frac{{R_c}^2}{N_B {l_B}^2} \sim Q^{2/3} \tag{5}$$

in which l_B segment length of the hydrophobic monomer.

Finally, F_{corona} is due to stretching of the chains that are attached to the curved surface of the core,

$$\frac{F_{corona}}{k_B T} \sim Q^{1/2} \ln R/R_{core} \tag{6}$$

in which R is the overall micelle radius.

Scaling theories distinguish between the two limiting cases of micelle structures formed by block polymers presented in Figure 1.6. Crew-cut micelles are characterized by having the degree of polymerization of the hydrophobic block (N_B) greater than that of the hydrophilic block (N_A) (*i.e.* $N_B >> N_A$), while the opposite case is considered for star-like micelles ($N_A >> N_B$).[44,58]

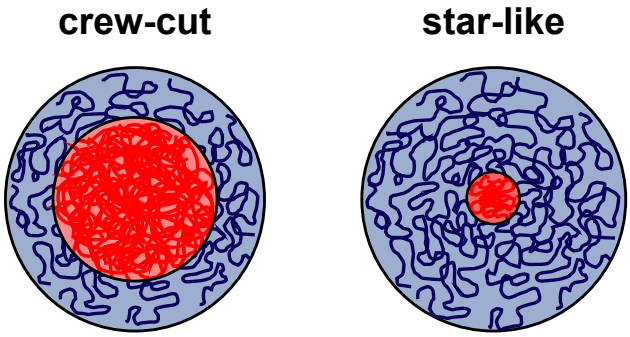

Figure 1.6 Schematic representation of crew-cut and star-like micelles as considered by scaling theories. In crew-cut micelles, the degree of polymerization of the hydrophobic block (N_B) >> degree of polymerization of the hydrophilic block (N_A). Micelle at the opposite limit, N_A>>N_B, are referred to as star-like.

In crew-cut micelles, the free energy contributions from the corona are assumed to be negligible compared to the free energy contributions from the core. Thus, substituting the expressions for F_{core} (Equation 5) and $F_{interface}$ (Equation 4) into the overall micelle free energy expression (Equation 3) and minimizing with respect to aggregation number yields[44,58]

$$Q \approx (\gamma {l_B}^2/kT)N_B \tag{7}$$

and

$$R_c \approx {N_B}^{2/3} l_b \tag{8}$$

Finally, because the corona thickness is small compared to the core radius, the overall micelle size scales as

$$R \approx R_c \approx {N_B}^{2/3} l_b, \tag{9}$$

In the opposite limit for star-like micelles, the dominant free energy contribution is from the corona chain stretching. Substituting F_{corona} and $F_{interface}$ into $F_{micelle}$ and minimizing with respect to aggregation number as above yields

$$Q \approx \left(\gamma {l_B}^2/kT\right)^{6/5} {N_B}^{4/3} \quad (10)$$

and

$$R_c \approx {N_B}^{3/5} l_b \quad (11)$$

and the overall micelle radius scales with the corona thickness:

$$R \approx {N_B}^{4/5} {N_A}^{3/5} l_b \quad (12)$$

These scaling analyses highlight several important parameters for controlling the block polymer micelle size. In the case of both crew-cut and star-like micelles, the aggregation number and size are highly dependent on the degree of polymerization of the core block (N_B), which is in qualitative agreement with experimental studies of several block polymer systems.[62,63] The scaling analyses further suggest that the micelle aggregation number and size are highly sensitive to the interfacial tension, implying that the micelle structure can be tuned by controlling the solvent selectivity, as reported in Chapter 5 of this dissertation.[64-67] The analyses described above provide basic guidelines for tuning the size and structure of equilibrium assemblies; however, as discussed below, many block polymer solution assemblies are not at equilibrium and instead are long-lived metastable structures. Thus, achieving control over the

block polymer solution assembly requires a detailed understanding of both the thermodynamic and kinetic driving forces in these systems.

Extremely Low Critical Micelle Concentration

In contrast to small molecule amphiphiles, macromolecular amphiphiles consist of tens to hundreds of hydrophobic repeat units. Equation 1 implies that the CMC exponentially decreases with increasing length of the hydrophobic block. Consequently, the CMC in polymeric amphiphiles is much lower than that in small molecule amphiphiles (Table 1.1) and oftentimes is experimentally inaccessible by common measurement techniques.[17,68]

The extremely low CMC values of block polymer amphiphiles are an attractive advantage of these materials for certain applications, motivating theoretical and experimental research into the effects of polymer structure on the CMC. For example, studies by Eisenberg and coworkers demonstrated that increasing the molecular weight of the hydrophobic block at a constant corona block molecular weight decreased the CMC due to the increasing hydrophobicity of the material, [69,70] whereas keeping the core block molecular weight constant and increasing the hydrophilic block molecular weight slightly increased the CMC. [39,40,70] Theoretical predictions suggest that the block polymer architecture[55] and molecular weight distribution (dispersity)[71,72] also affect the CMC of these materials. For example, adding a third polymer block and creating an ABA triblock copolymer decreases the CMC of the material.[17,73] These reports demonstrate that the CMC of the material is effectively tuned by controlling the polymer molecular weight, composition, and chain architecture, providing an additional level of control over the self-assembly behavior. However,

these results also highlight the complex parameter space for exploring and understanding block polymer solution assembly.

Table 1.1 CMC of common small molecule and macromolecular amphiphiles

amphiphile*	CMC (g L^{-1})
SDS[74,75]	2 to 2.7
Brij nonionic surfactants[76]	~ 1×10^{-3} to 0.7
PEP-PEO-PEO (Pluronic)[77]	~ 10 to 20
PS-PEO[17,78]	1×10^{-3} to 6×10^{-3}
PB-PEO[14,68]	< 10^{-3} to 4×10^{-3}

*SDS = sodium dodecyl sulfate;
PEP-PEO-PEO = poly(propylene oxide-*b*-ethylene oxide-*b*-propylene oxide);
PS-PEO = poly(styrene-*b*-ethylene oxide);
PB-PEO = poly(butadiene-*b*-ethylene oxide)

Arrested or 'Frozen' Dynamics

Another consequence of the macromolecular hydrophobic block is the extremely high energy barrier to dynamic exchange processes. Over the past decade, it has become increasing apparent that these processes are exceedingly slow and seemingly non-existent in block polymer assemblies.[29,44,79-83] Because of the extraordinarily slow dynamics, the self-assembled structure depends on the assembly pathway, and the "final" morphology is often a kinetically-trapped or long-lived metastable state.[83] Therefore, a single block polymer can form multiple structures depending on the solution preparation method, and careful optimization of the preparation conditions as well as an understanding of the driving forces for structural rearrangement are necessary to produce well-defined, uniform, and reproducible solution assemblies.[83]

To take full advantage of block polymer amphiphiles and intelligently use them in desired applications, the assembly kinetics and pathways must be understood. A great deal of theoretical,[84-89] computational,[85,90-93] and experimental[18,66,81,94-101] research over the past decade has been devoted to understanding these phenomena. Small angle scattering methods, in particular, have provided valuable insights into the assembly processes[98] and equilibrium chain exchange[18,66,81,94-101] in these materials. However, a cohesive understanding of polymeric micelle dynamics is still lacking and the dominant dynamic processes during micelle formation and structural transitions remain unclear. Gaining this understanding is complicated further by the complex dependence of micelle dynamics on numerous coupled factors that can depend upon how far removed the assemblies are from their equilibrium configuration (*e.g.* aggregation number, size, and shape).[84,102-104] Accordingly, it is important to distinguish between the different types of kinetic processes in polymer assemblies. The phrase 'relaxation kinetics' is used to describe micelle-to-micelle relaxation processes in response to a perturbation (*i.e.* solvent switch or pressure/temperature jump), while 'equilibrium dynamics' or 'equilibrium chain exchange' refers to dynamic processes in an assembly that has not been perturbed. Finally, 'micellization kinetics' refers to micelle formation (*i.e.* unimer to micelle formation).

In general, two mechanisms are considered key for facilitating changes in micelle size and structure in all of the scenarios described above: single chain exchange and micelle fusion/fission (Figure 1.7). In single chain exchange, a chain is expelled from one micelle, diffuses through solution, and then reinserts into another micelle. A fusion event occurs when two micelles collide, leading to a deformation of their coronas, and the cores subsequently merge to form a larger micelle. A fission

event is the reverse process in which a larger micelle divides into two smaller micelles.

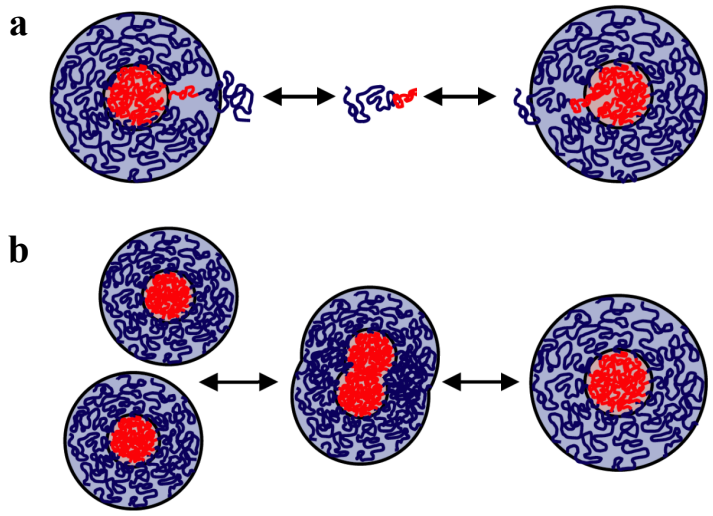

Figure 1.7 Schematic representation of dynamics processes in block polymer micelles. (a) Single chain exchange and (b) fusion/fission events are both thought to contribute to micelle formation and relaxation.

Near equilibrium, single chain exchange events dominate the dynamics in both small molecule surfactant and block polymer micelles.[81,89,95-97] However, the energetic barrier to chain exchange in macromolecular systems normally is much higher due to the long-chain hydrophobic block, and this barrier is highly dependent on the solvent selectivity for each of the polymer blocks.[82,83,89] Chain exchange events are imperceptibly slow in highly selective solvents,[79,81,82] yet occur readily in mildly selective solvents.[95-97]

Meanwhile, far from equilibrium, the dominant dynamic process in macromolecular assemblies is unclear.[102,104-107] Dormidontova used scaling analysis to suggest that fusion is the preferred growth mechanism in micelles during micellization, as opposed to the single chain events that are prevalent near equilibrium.[84] Fusion events also have been noted during micelle relaxation and sphere-to-cylinder morphological transitions.[108-110] However, recent experimental work by Rharbi suggested that fusion events also may occur in equilibrium assemblies, although these events are much slower than single chain exchange.[106]

In contrast, other reports argue that the energetic barrier to deform block polymer micelle coronas is too high to permit fusion in macromolecular systems, and therefore that only single chain events are favored.[89,92] Thus, despite the growing importance of understanding dynamics in macromolecular assemblies, the mechanisms governing structural evolution in highly perturbed systems remain unresolved. Decoupling the thermodynamic and kinetic constraints in block polymer assemblies is an essential step in the successful application of these materials.

1.3 Emerging Applications of Solution Assemblies

The flexibility in molecular architecture and block polymer composition allow the properties of macromolecular surfactants to be tailored to the specific application. As a result, several amphiphilic block polymers are produced on an industrial scale and are widely used as emulsifiers, detergents, and stabilizers in personal care and cosmetic products, inks, separation processes, and oil recovery.[38,41] The well-defined and tunable self-assembly coupled with the synthetic versatility of these materials also has motivated significant research efforts towards developing block polymer assemblies for emerging nanotechnologies including aqueous nanoreactors[7,8,111] and drug delivery vehicles.[4,6,112-114] The work presented in this dissertation explores polymeric materials for both of these emerging applications in which macromolecular amphiphiles have a distinct advantage over small molecules given their synthetic versatility, tunable self-assembly, and low CMC values. Described below is the detailed motivation and background for developing designer amphiphilic macromolecules and controlling their self-assembly behavior.

1.3.1 Aqueous Nanoreactors

Organic solvents constitute the majority of waste in the chemical environment; thus, there are both economic and environmental incentives for performing organic reactions in water.[115] However, most industrially-used organic reactions are not possible in water due to the limited solubility of the reagents and the decomposition and/or deactivation of the substrates in aqueous environments.[7,115] Amphiphile self-assembly presents an attractive solution to these contradictory needs in waste management *vs.* reagent solubility. Hydrophobic substrates and catalysts can be efficiently encapsulated into the hydrophobic cores of polymeric assemblies,

solubilizing the reagents while protecting them from degradation. These novel nanoreactors combine the benefits of both homogeneous and heterogeneous catalysis by increasing the local concentrations of reagents while also simplifying product recovery.[7,8,111]

The synthetic versatility of amphiphilic macromolecules allows for the direct incorporation of transition metal catalysts[111,116-119] into the micelle core or the polymerization of organocatalysts.[120-122] Recent work by O'Reilly and coworkers developed polymeric nanoreactors based on the organocatalyst 4-dimethylaminopyridine (DMAP), in which the catalytic DMAP functionality was immobilized within the polystyrene core of self-assembled micelles.[120,121] The tethered catalyst improved the reactions rates up to 100-fold compared to the rates when using unsupported catalysts in organic solvents,[120] and the tethered catalyst also improved the selectivity of the reaction towards the hydrophobic substrate.[121] Moreover, the hydrophilic block of these materials was made from a thermoresponsive polymer, poly(N-isopropylacrylamide) (PNIPAM), and hence the catalyst could be recovered by simply heating the solution to cause the polymer to precipitate. The catalytic performance of these nanoreactors was not affected by multiple recycling steps, demonstrating the immense potential for polymeric nanoreactors for not only improved reaction rates and selectivity, but also simplified catalyst recovery.[120]

In addition to the synthetic versatility afforded by polymeric systems, the low CMC and slow chain exchange inherent to macromolecular assemblies is advantageous in nanoreactor applications. Work by Thayumanavan and Ramamurthy demonstrated that the arrested chain exchange in polymeric nanoreactors reduced the hydrolysis of the substrate and improved the product selectivity compared to small

molecule surfactant assemblies.[123] Moreover, water often is not present in the core of highly hydrophobic polymer-based assemblies, which further improves the selectivity of aqueous nanoreactors.[124]

Remaining Challenges in Nanoreactor Development

Amphiphilic macromolecules have tremendous potential for developing aqueous nanoreactors to reduce the use of organic solvents in industrial processes, increase reaction yields and selectivity, and simplify product and catalyst recovery. However, further advancing these technologies requires not only developing new materials, but also understanding the effects of the nanoreactor structure on its catalytic properties. For example, studies of nanoreactors assembled from small molecule surfactants demonstrated that the nanoreactor structure influences the reaction rates and that the optimal nanoreactor morphology may depend on the type of the reaction.[115,125,126] The exact relationships between the nanoreactor structure and catalytic efficiency are not well understood in small molecule systems and have not been explored at all in polymeric nanoreactors. Developing these relationships requires detailed *in situ* characterization of the nanoscale structure and a strong fundamental understanding of the factors that influence the structure and dynamics of macromolecular assemblies. The tunable self-assembly, slow dynamic process, and synthetic versatility inherent to polymeric amphiphiles are key to further developments of nanoreactor technologies.

1.3.2 Nanomedicines

Over 100 years ago, Nobel Laureate Paul Ehrlich coined the phrase 'magic bullet' to describe an idealized therapeutic that went specifically to diseased cells and did not affect the surround tissues.[127] The past 100 years have seen great advances in identification of therapeutics to treat devastating diseases[113,114] as well as development of nanodelivery structures with improved targeting potential, both fueling progress towards the creation of these magic bullets.[6,112,127] Today, more than 40 nanomedicines are used clinically to treat diseases such as anemia, chronic pain, cancer, and hepatitis.[6]

Some of the earliest nanomedicines were based on self-assembled liposomes, in which proteins and drugs were encapsulated within the hydrophilic core. Encapsulating therapeutics within liposomes increased their circulation times and improved their pharmacokinetic profiles while also reducing toxic side effects, and today liposomal-based chemotherapeutics are routinely used to treat cancer.[6] Pioneering work by Kabanov and Kataoka extended the use of amphiphilic block polymers to the development of drug delivery vehicles.[5,6,128-134] These polymeric systems combined the advantages of nanoscale self-assembly with the synthetic versatility of polymeric materials. However, despite their promise, no block polymer-based therapeutics have advanced to clinical use.[6] Multiple research efforts have begun to reveal the complex and sometimes contradictory design requirements for developing these materials for use in biomedical applications such as drug delivery, summarized in Figure 1.8. The unique advantages of polymeric assemblies in drug delivery and the current understanding of the physicochemical properties that affect their performance in biomedical applications are discussed in more detail below.

nanostructure 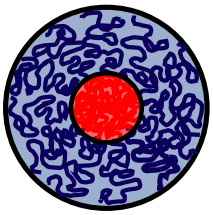	• tunable *size* between 10 to 100 nm • tailored *morphology* • high kinetic *stability* (low CMC)
core 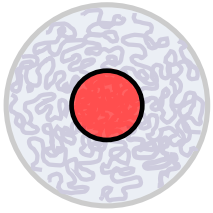	• high *loading capacity* • *compatible* with therapeutic ➢ increase loading ➢ control release profile
corona 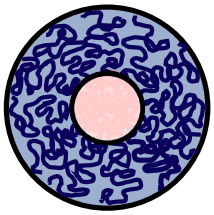	• *biocompatible* • *serum stability* ➢ prevent micelle aggregation ➢ minimize protein binding
targeting group 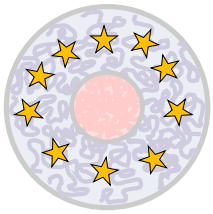	• highly *specific* • controlled *display* ➢ shielded to prolong circulation times ➢ accessible to targeted receptors

Figure 1.8 Design requirements for an idealized polymeric drug delivery vehicle. Adapted from review by Allen *et al.*[5]

Block Polymer Assemblies

The exquisite control over the size and structure of amphiphilic block polymer assemblies as well as the slow chain exchange inherent to these materials are particularly attractive for drug delivery. The synthetic versatility of macromolecular assemblies enables the design of specific nanocarrier sizes and shapes while the kinetic stability ensures that the nanocarrier is stable upon injection into the body. These advantageous properties of block polymer assemblies and examples from literature are described in the following section.

Literature suggests the optimal nanoparticle size range for cancer treatment is 10 – 100 nm, length scales readily achieved by block polymer assemblies.[135,136] The lower size limit is set by the need to avoid renal clearance, as particles <10 nm are rapidly filtered by the kidneys.[135,137] The upper size limit is governed by multiple factors, as nanoparticle size affects biodistribution (*e.g.* partitioning/filtration by the liver and/or spleen *vs.* tumors), diffusion through solid tumors, and cellular internalization.[138-143]

A major advantage of nanomedicines for the treatment of cancer is the concept of 'passive targeting' due to the enhanced permeability and retention (EPR) effect. The EPR effect is a phenomenon unique to solid tumors and is caused by defects in the vasculature surrounding a tumor that lead to extensive leakage of blood and plasma components, including nanoparticles, into the tumor.[138-140] As a result, nanoparticles administered intravenously have been found to selectively accumulate in tumors. While the size of the assemblies allows passive targeting of tumors by the EPR effect, it also limits their transport through the tumor due to their low diffusivity.[141,142] Accordingly, the ideal assembly must be large enough to selectively

accumulate within tumors, but not so large that that it cannot effectively diffuse through the tumor interstitium. Once within the tumor, the drug carrier must be internalized by the cancer cells, and carrier size also influences the cellular internalization pathway. Large particles (>1 μm) are taken up by phagocytosis whereas particles ranging from ~10 to 300 nm typically are internalized by clathrin mediated endocytosis.[143] Together, these coupled and demanding size effects suggest that nanoparticles on the order of <100 nm are able to selectively accumulate in tumors, effectively diffuse through the tumor, and be internalized by cells.

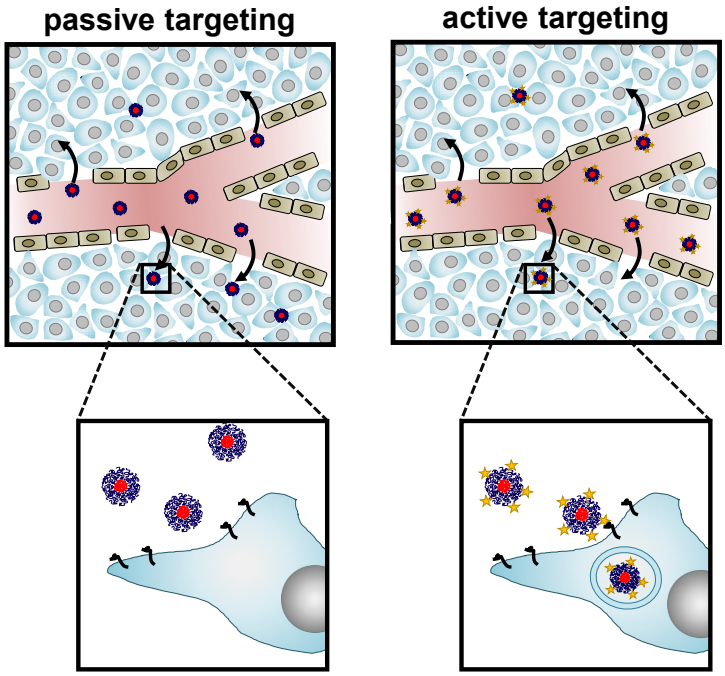

Figure 1.9 Schematic representative of passive and active targeting in nanomedicine, adapted from a review by Farokhzad and Langer.[113] In passive targeting, nanoparticles pass through the leaky vasculature and selectively accumulate in solid tumors due to the EPR effect. In active targeting, targeting groups interact with cell surface receptors and facilitate cellular internalization of the drug carrier.

In addition to enabling improved control of the assembly size as compared with small molecule amphiphiles, amphiphilic block polymers provides access to a variety of nanostructure morphologies simply by tuning the block polymer composition.[5,43,144] Literature reports have demonstrated that the nanoparticle structure is also very important in designing materials for biomedical applications. For example, studies of polystyrene nanoparticles showed that rigid, elongated particles were not recognized by macrophages due to their large surface area.[145] Work by Discher *et al*. expanding on these finding and showed that flexible cylindrical micelles (also referred to as filomicelles) also were not internalized by macrophages, thereby enhancing their circulation times *in vivo* for up to 1 week.[146] The elongated micelles showed unprecedented circulation times that were 10-fold longer than the times reported for spherical micelles.[146] These results demonstrate that the shape of nanoparticles can be tuned to further influence the pharmacokinetic profile of the therapeutics.

Another important advantage of macromolecular assemblies is their larger payload capacity compared to small molecule assemblies, enabling the encapsulation of greater amounts of therapeutics. Also, their low CMC and exceptionally slow chain exchange helps retain encapsulated cargoes *in vivo*. There are approximately 5 L of blood in the human body. Accordingly, the drug delivery vehicles are diluted by approximately 1000-fold upon injection. Most small molecule assemblies are not stable upon these dilutions, as their CMCs are typically ~1 g L^{-1}; however, the low CMCs inherent to polymeric assemblies (Table 1.1) ensure that these nanocarriers are more stable and retain their encapsulated cargo upon extreme dilution.[37,54,55,147] Moreover, studies of block polymer assemblies also suggest that physically

encapsulating a hydrophobic drug within a micelle can increase the kinetic stability of the assembly.[133]

Hydrophobic Core

A key function of a drug delivery vehicle is to encapsulate and protect a therapeutic within the hydrophobic core. However, even with the larger core volumes in polymeric assemblies, the total hydrophobic volume within a micelle formulation is small. Assuming a typical micelle formulation contains ~1 vol% polymer in solvent, and the core constitutes <0.5 vol% of the micelle, the total core volume in 1 mL of solution is ~5 μL.[5] Accordingly, maximizing the drug loading capacity and efficiency is crucial to the successful development of delivery vehicles.

Interactions between the core block and the hydrophobic cargo have been shown to influence both the drug encapsulation efficiency and release profile.[148-150] For example, nuclear magnetic resonance spectroscopy studies suggested that the core block dynamics affect the encapsulation efficiency of hydrophobic compounds, and hydrophobic polymers with a lower glass transition temperature (T_g) were able to solubilize more drugs.[151] Also, fluorescence studies revealed that dye release from a glassy core (high T_g) was very slow.[150] Polymer-drug interactions also are important for determining the encapsulation efficiency as well as release profile. For example, studies of pyrene solubilization in block polymer micelles demonstrated that the pyrene partition coefficient was two orders of magnitude higher in polystyrene cores[5,78,152] [poly(styrene-*b*-ethylene oxide) and poly(styrene-*b*-acrylic acid)] as compared to the hydrophobic poly(propylene oxide) core in Pluronics.[129] These results suggest that the more hydrophobic polystyrene cores are better able to

solubilize the aromatic dye and indicate that tuning the specific drug-polymer interactions increases both the encapsulation efficiency and loading-capacity.[153] Similarly, studies by Ansell *et al.* showed that drug release kinetics could be tuned by varying the hydrophobicity of paclitaxel and therefore its partition coefficient in aqueous lipid assemblies.[148] Increasing the hydrophobicity of the drug by incorporating an alkane tail increased its partition coefficient and significantly improved its pharmacokinetic profile.[148]

The physical state of the drug as well as its distribution within the micelle core further affects the encapsulation efficiency, drug release kinetics, and pharmacokinetic profile.[148,149,154] For example, work by Langer and coworkers demonstrated that crystalline drugs were released more slowly from polymeric nanoparticles.[154] Studies of the release kinetics of hydrophobic dyes suggested that the molecules were uniformly distributed throughout the core.[150] This result is consistent with recent anomalous small angle X-ray scattering (ASAXS) experiments that directly demonstrated that hydrophobic small molecules were uniformly distributed throughout the micelle core.[155] In contrast, release studies by Eisenberg *et al.* indicated that amphiphilic small molecule dyes containing both hydrophobic and hydrophilic regions were solubilized at the micelle core-corona interface and that the encapsulation efficiency was a function of the surface area of the micelle core.[156] These studies further suggest that the drug release profile is a complex function of the polymer-drug interactions and that the drug carrier may need to be optimized for the therapeutic of interest.

The majority of drug delivery vehicles rely on physically incorporating the hydrophobic molecule within the nanocarrier. An alternative strategy is to covalently

attach the drug to the hydrophobic polymer in an effort to overcome the limitations to drug loading efficiency of physical encapsulation approaches.[133,134,157-159] Pioneering work by Kataoka and coworkers covalently attached the anticancer drug Adriamycin to the hydrophobic block in poly(aspartic acid-*b*-ethylene glycol) micelles.[133,134,157] Subsequent work has extended this approach to other chemotherapeutics such as doxorubicin[158] and paclitaxel.[160] Moreover, polymer drugs developed by Uhrich and coworkers are promising materials for drug delivery, in which therapeutics such as morphine,[161] aspirin,[162] and coumaric acid[163] are directly incorporated into the polymer backbone. Using these polymer drugs in amphiphilic block polymer architectures could increase the drug loading within the assemblies compared to physical encapsulation approaches and eliminate the need for complex drug-loading procedures. The synthetic versatility in polymer chemistry and continued advances in new materials present exciting opportunities for effectively incorporating therapeutic molecules into polymeric nanocarriers.

Hydrophilic Corona

The micelle corona serves as a protective barrier for the therapeutic cargo, and along with carrier size, is a key determinant of the biodistribution. Importantly, the micelle corona must reduce nonspecific interactions with serum components, referred to as opsonization, which leads to rapid clearance of the delivery vehicle from the body.[164] This ability to avoid immune system recognition and prolong circulation times is referred to as 'stealthiness.' A growing number of studies have demonstrated the extreme influence of the surface chemistry and charge on the performance of polymeric materials in biological applications.[5,113,114,135,136]

Materials with a positive surface charge have a high affinity for the negatively charged proteoglycans expressed on the cell surface, but also are highly toxic.[143,165-172] For example studies by Millili *et al.* showed that removing excess polyethylenimine (PEI), a cationic polymer, from PEO functionalized gene delivery vehicles both improved the cellular internalization efficiency and reduced the cytotoxicity of the materials.[171] Similarly, studies by Blanazs *et al.* showed that polymersomes that were surface-functionalized with the cationic polymer poly[2-dimethylamino)ethylmethacrylate] (PDMA) showed rapid cellular accumulation *in vitro* at short time scales (*e.g.* < 1 h).[173] The authors also noted reduced uptake after longer exposures (*e.g.* 48 h) due to increasing toxic effects of the cationic polymer.[173] Anionic polymers have been shown to be significantly less toxic than cationic polymers, as they are repelled by negatively charged cellular membranes as well as negatively charged residues within extracellular matrix; however, their use on the surface of biomedical materials is limited due to significant protein binding that occurs under physiological conditions.[143,165] Nonionic or zwitterionic polymers such as poly(ethylene oxide) (PEO) or poly(ethylene glycol) (PEG), polysaccharides, and poly(2-methacryloyloxyethyl phosphorylcholine) (PMPC) have found the most success in biomedical applications.[143,174-176] Work by Reineke and coworkers demonstrated that polymer micelles containing polysaccharides were stable in full serum conditions for more than 14 h with minimal protein interactions.[177]

PEO (which is structurally equivalent to PEG) is by far the most commonly used hydrophilic polymer in biomedical applications.[164,178,179] PEO has been shown to increase the *in vivo* circulation times of peptides, proteins, inorganic nanoparticles, liposomes, and polymeric assemblies,[164,178,179] and is a key component of several

nanomedicines used clinically.[6,112] In fact, the first polymer-based therapeutics to reach the clinic were PEO-protein conjugates.[112]

The widespread use of PEO is due to its well-known ability to increase the colloidal stability of nanoparticles in physiologically relevant conditions as well as decrease protein binding *in vivo*.[164,178,179] PEO is highly water soluble and several reports show that 3 water molecules can associate with each PEO unit.[180-184] SAXS studies by Smart *et al*. revealed that the PEO corona in polymersomes were fully stretched and maintained their highly hydrated nature.[180] The steric repulsions that result from this dense chain configuration prevents foreign objects from absorbing onto the nanoparticle due to the unfavorable loss of conformation entropy of the PEO chains.[132] This extraordinary physiological advantage of PEO, coupled with its other benefits including non-toxicity, nonimmunogenicity, and FDA-approval have led to its widespread use in numerous biomaterials.

Targeting Groups

The first 'targeted' drug delivery vehicles were developed in the early 1980's.[185,186] Antibody fragments were incorporated into liposomes and these systems showed significantly enhanced binding to specific cell types.[185,186] The potential benefits in cellular specificity of these targeted systems motivated significant research interest in attaching targeting ligands to various other nanocarriers to create Ehrlich's magic bullets. However, the past 30 years of research has revealed that attaching targeting groups often does not alter the biodistribution of the carrier, although in some cases, it can enhance phagocytic clearance. The main benefit of most

ligand-targeted carriers is that they can stimulate enhanced cellular uptake in target cells by receptor-mediated endocytosis.[136]

Remaining Challenges in Delivery Vehicle Development

Despite challenges in the development of delivery vehicles, these systems continue to command attention due to the pressing clinical need for improved drug targeting. Literature precedent clearly demonstrates that both the nanocarrier structure and surface functionality are essential determinants of the *in vivo* performance of delivery vehicles, and block polymer assemblies enable exquisite control over both of these design requirements. Fundamentally understanding the effects of drug-loading procedures and solution processing conditions on the resulting assembly is essential to controlling both the structure and stability of the nanocarrier. Moreover, an effective drug delivery vehicle must balance the stealthiness required for prolonged circulation and bioaccumulation with the display of targeting ligands. Work by Gu *et al.* elegantly demonstrated that a delicate balance between ligand display and stealth properties achieves maximal drug carrier uptake *in vitro* and *in vivo*.[187] However, achieving this balance is challenging and robust chemistries that allow control over the ligand display clearly are needed. Optimizing both the structure and surface chemistry of block polymer assemblies will meet the demanding design requirements for holistic drug delivery vehicles.

1.4 Thesis Overview

This dissertation presents the synthesis, self-assembly, and solution characterization of amphiphilic block polymers. The first aim of this work was to develop complementary methods for characterizing block polymer solution assemblies and subsequently use these methods to understand the effects of common processing condition on the structure, dynamics, and long-term stability of block polymer assemblies. Specifically, key results demonstrated that cosolvent addition led to a marked decrease in micelle size and increased the rate of chain exchange in the assemblies, while subsequent cosolvent removal had unforeseen consequences on the micelle stability. Following cosolvent removal, the micelles grew through a distinct bimodal pathway separated by multiple fusion events, and detailed investigation into the growth mechanism revealed that this unexpected growth critically depended on solution agitation. Most notably, this work demonstrated that solution agitation led to dynamic processes not seen in the bulk solution and emphasized the importance of selecting and controlling processing conditions when preparing block polymer solution assemblies. The improved understanding of factors that influence block polymer solution assembly are applicable to materials design for emerging applications such as nanoreactors and drug delivery vehicles, leading to significant synergies in, and streamlined optimization of, the development of these nanotechnologies.

A growing number of works demonstrate that both the structure and surface functionality of nanomaterials dictate their performance in biomedical applications. Thus, second aim of this work was to develop a method to control the surface functionality of polymeric assemblies for drug delivery applications. A modular synthetic strategy was developed for creating well-defined polymer-peptide conjugates

that allowed control over both the peptide sequence and peptide location within the polymer backbone. This level of control over conjugate architectures is not possible with common polymer-peptide conjugation strategies in literature, yet is essential to understand the intimate structure-property relationships inherent to polymeric materials in biological environments. Altogether, the results presented in this dissertation will enable greater control over the structure and functionality of polymeric assemblies for applications in emerging nanotechnologies.

Descriptions of the synthesis and chemical characterization techniques used to create the well-defined macromolecules necessary for this work are described in Chapter 2. Chapter 3 presents an overview of *in situ* characterization techniques for solution assemblies, and Chapter 4 demonstrates the powerful combination of cryogenic transmission electron microscopy (cryo-TEM) and small angle neutron scattering (SANS) for obtaining detailed structural information on nanometer length scales. The effects of cosolvent addition on the structure and dynamics of block polymer micelles are explored in Chapters 5 and 6, respectively, and Chapter 7 investigates the unexpected consequences of cosolvent removal on the long-term stability of these assemblies. The effects of routine laboratory mixing on chain exchange in block polymer assemblies are examined Chapter 8. Chapter 9 develops a modular and highly tunable synthetic strategy for controlling the display of targeting ligands within polymeric assemblies. Finally, Chapter 10 summarizes the main results of this dissertation and recommends future work towards the rational design and detailed characterization of designer amphiphilic block polymers.

REFERENCES

1 Gennis, R. B. *Biomembranes Molecular Structure and Function*. Springer-Verlag, 1989.

2 Szostak, J. W., Bartel, D. P. & Luisi, P. L. (2001), *Nature* **409**, 387-390

3 Rosen, M. J. *Surfactants and Interfacial Phenonmena*. 3rd edn, Wiley-Interscience, 2004.

4 Kelley, E. G., Albert, J. N. L., Sullivan, M. O. & Epps, T. H. (2013), *Chemical Society Reviews* **42**, 7057-7071

5 Allen, C., Maysinger, D. & Eisenberg, A. (1999), *Colloids and Surfaces B: Biointerfaces* **16**, 3-27

6 Duncan, R. & Gaspar, R. (2011), *Molecular Pharmaceutics* **8**, 2101-2141

7 Cotanda, P., Petzetakis, N. & O'Reilly, R. K. (2012), *MRS Communications* **2**, 119-126

8 Lu, A. & O'Reilly, R. K. (2013), *Current Opinion in Biotechnology* **24**, 639-645

9 Israelachvili, J. N. *Intermolecular & Surface Forces*. 9th edn, Elsevier Science Imprint, 2002.

10 Tanford, C. *The Hydrophobic Effect: Formation of Micelles and Biological Membranes*. 2nd edn, Wiley-Interscience, 1979.

11 Hamley, I. W. *Introduction to Soft Matter: Synthetic and Biological Self-Assembling Materials*. Revised edn, John Wiley & Sons, 2007.

12 Kunieda, H. & Shinoda, K. (1976), *The Journal of Physical Chemistry* **80**, 2468-2470

13 Muñoz, M., Rodríguez, A., Graciani, M. d. M. & Moyá, M. L. (2004), *Langmuir* **20**, 10858-10867

14 Topel, Ö., Çakır, B. A., Budama, L. & Hoda, N. (2013), *Journal of Molecular Liquids* **177**, 40-43

15 Bakkour, Y., Darcos, V., Li, S. & Coudane, J. (2012), *Polymer Chemistry* **3**, 2006-2010

16 Ringsdorf, H., Venzmer, J. & Winnik, F. M. (1991), *Macromolecules* **24**, 1678-1686

17 Zhao, C. L., Winnik, M. A., Riess, G. & Croucher, M. D. (1990), *Langmuir* **6**, 514-516

18 Mok, M. M., Thiagarajan, R., Flores, M., Morse, D. C. & Lodge, T. P. (2012), *Macromolecules* **45**, 4818-4829

19 Antonietti, M. (2001), *Current Opinion in Colloid & Interface Science* **6**, 244-248

20 Beck, J. S. *et al.* (1992), *Journal of the American Chemical Society* **114**, 10834-10843

21 Kresge, C. T., Leonowicz, M. E., Roth, W. J., Vartuli, J. C. & Beck, J. S. (1992), *Nature* **359**, 710-712

22 Wennerstrom, H. & Lindman, B. (1979), *Physics Reports-Review Section of Physics Letters* **52**, 1-86

23 Aniansso.Ea & Wall, S. N. (1974), *Journal of Physical Chemistry* **78**, 1024-1030

24 Aniansson, E. A. G. & Wall, S. N. (1975), *Journal of Physical Chemistry* **79**, 857-858

25 Aniansson, E. A. G. *et al.* (1976), *Journal of Physical Chemistry* **80**, 905-922

26 Wall, S. N. & Aniansson, G. E. A. (1980), *Journal of Physical Chemistry* **84**, 727-736

27 Liu, C., Hillmyer, M. A. & Lodge, T. P. (2008), *Langmuir* **24**, 12001-12009

28 Moughton, A. O., Hillmyer, M. A. & Lodge, T. P. (2011), *Macromolecules* **45**, 2-19

29 Jain, S. & Bates, F. S. (2003), *Science* **300**, 460-464

30 Kositza, M. J., Bohne, C., Alexandridis, P., Hatton, T. A. & Holzwarth, J. F. (1999), *Macromolecules* **32**, 5539-5551

31 Kositza, M. J., Bohne, C., Alexandridis, P., Hatton, T. A. & Holzwarth, J. F. (1999), *Langmuir* **15**, 322-325

32 Pedersen, J. S. & Gerstenberg, M. C. (2003), *Colloids and Surfaces a-Physicochemical and Engineering Aspects* **213**, 175-187

33 Alexandridis, P., Zhou, D. L. & Khan, A. (1996), *Langmuir* **12**, 2690-2700

34 Svensson, B. & Olsson, U. (2000), *Macromolecules* **33**, 7413-7419

35 Svensson, B., Olsson, U. & Alexandridis, P. (2000), *Langmuir* **16**, 6839-6846

36 Wanka, G., Hoffmann, H. & Ulbricht, W. (1990), *Colloid and Polymer Science* **268**, 101-117

37 Zhou, D. L., Alexandridis, P. & Khan, A. (1996), *Journal of Colloid and Interface Science* **183**, 339-350

38 Alexandridis, P. & Alan Hatton, T. (1995), *Colloids and Surfaces A: Physicochemical and Engineering Aspects* **96**, 1-46

39 Alexandridis, P., Athanassiou, V., Fukuda, S. & Hatton, T. A. (1994), *Langmuir* **10**, 2604-2612

40 Alexandridis, P., Holzwarth, J. F. & Hatton, T. A. (1994), *Macromolecules* **27**, 2414-2425

41 Alexandridis, P. & Lindman, B. *Amphiphilic block copolymers: self assembly and applications*. Elsevier, 2000.

42 Riess, G. (2003), *Progress in Polymer Science* **28**, 1107-1170

43 Mai, Y. Y. & Eisenberg, A. (2012), *Chemical Society Reviews* **41**, 5969-5985

44 Lund, R., Willner, L. & Richter, D. (2013), *Advances in Polymer Science* **259**, 51-158

45 Zhulina, E. B. & Borisov, O. V. (2012), *Macromolecules* **45**, 4429-4440

46 Balsara, N. P., Tirrell, M. & Lodge, T. P. (1991), *Macromolecules* **24**, 1975-1986

47 Leibler, L., Orland, H. & Wheeler, J. C. (1983), *Journal of Chemical Physics* **79**, 3550-3557

48 Lund, R., Willner, L., Lindner, P. & Richtert, D. (2009), *Macromolecules* **42**, 2686-2695

49 Nagarajan, R. (1986), *Advances in Colloid and Interface Science* **26**, 205-264

50 Nagarajan, R. & Ganesh, K. (1989), *Journal of Chemical Physics* **90**, 5843-5856

51 Nagarajan, R. & Ganesh, K. (1989), *Macromolecules* **22**, 4312-4325

52 Noolandi, J. & Hong, K. M. (1982), *Macromolecules* **15**, 482-492

53 Whitmore, M. D. & Noolandi, J. (1985), *Macromolecules* **18**, 657-665

54 Nagarajan, R. & Ruckenstein, E. (1991), *Langmuir* **7**, 2934-2969

55 Linse, P. (1993), *Macromolecules* **26**, 4437-4449

56 Greenall, M. J., Buzza, D. M. A. & McLeish, T. C. B. (2009), *Macromolecules* **42**, 5873-5880

57 Zhulina, E. B., Adam, M., LaRue, I., Sheiko, S. S. & Rubinstein, M. (2005), *Macromolecules* **38**, 5330-5351

58 Halperin, A., Tirrell, M. & Lodge, T. P. (1992), *Advances in Polymer Science* **100**, 31-71

59 Halperin, A. (1987), *Macromolecules* **20**, 2943-2946

60 Daoud, M. & Cotton, J. P. (1982), *Journal De Physique* **43**, 531-538

61 de Gennes, P. G. *Scaling concepts in polymer physics*. Cornell University Press, 1979.

62 Forster, S., Zisenis, M., Wenz, E. & Antonietti, M. (1996), *Journal of Chemical Physics* **104**, 9956-9970

63 Qin, A. *et al.* (1994), *Macromolecules* **27**, 120-126

64 Kelley, E. G., Smart, T. P., Jackson, A. J., Sullivan, M. O. & Epps, T. H. (2011), *Soft Matter* **7**, 7094-7102

65 Seo, Y. S., Kim, M. W., Ou-Yang, D. H. & Peiffer, D. G. (2002), *Polymer* **43**, 5629-5638

66 Lund, R. *et al.* (2011), *Soft Matter* **7**, 1491-1500

67 Lund, R., Willner, L., Stellbrink, J., Radulescu, A. & Richter, D. (2004), *Macromolecules* **37**, 9984-9993

68 Pispas, S. & Hadjichristidis, N. (2003), *Langmuir* **19**, 48-54

69 Astafieva, I., Zhong, X. F. & Eisenberg, A. (1993), *Macromolecules* **26**, 7339-7352

70 Astafieva, I., Khougaz, K. & Eisenberg, A. (1995), *Macromolecules* **28**, 7127-7134

71 Linse, P. (1994), *Macromolecules* **27**, 6404-6417

72 Gao, Z. & Eisenberg, A. (1993), *Macromolecules* **26**, 7353-7360

73 Bonné, T. B., Lüdtke, K., Jordan, R. & Papadakis, C. M. (2007), *Macromolecular Chemistry and Physics* **208**, 1402-1408

74 da Silva, R. C., Loh, W. & Olofsson, G. (2004), *Thermochimica Acta* **417**, 295-300

75 Regalado, E. J., Selb, J. & Candau, F. (1999), *Macromolecules* **32**, 8580-8588

76 Hait, S. & Moulik, S. (2001), *J Surfact Deterg* **4**, 303-309

77 Lopes, J. R. & Loh, W. (1998), *Langmuir* **14**, 750-756

78 Wilhelm, M. *et al.* (1991), *Macromolecules* **24**, 1033-1040

79 Jain, S. & Bates, F. S. (2004), *Macromolecules* **37**, 1511-1523

80 Lund, R. *Small Angle Neutron Scattering as a Tool to Study Kinetics of Block Copolymer Micelles*. Vol. 161 Springer-Verlag Berlin, 2010.

81 Lund, R., Willner, L., Richter, D. & Dormidontova, E. E. (2006), *Macromolecules* **39**, 4566-4575

82 Won, Y. Y., Davis, H. T. & Bates, F. S. (2003), *Macromolecules* **36**, 953-955

83 Hayward, R. C. & Pochan, D. J. (2010), *Macromolecules* **43**, 3577-3584

84 Dormidontova, E. E. (1999), *Macromolecules* **32**, 7630-7644

85 Li, Z. L. & Dormidontova, E. E. (2010), *Macromolecules* **43**, 3521-3531

86 Esselink, F. J., Dormidontova, E. & Hadziioannou, G. (1998), *Macromolecules* **31**, 2925-2932

87 Esselink, F. J., Dormidontova, E. E. & Hadziioannou, G. (1998), *Macromolecules* **31**, 4873-4878

88 Halperin, A. (2011), *Macromolecules* **44**, 5072-5074

89 Halperin, A. & Alexander, S. (1989), *Macromolecules* **22**, 2403-2412

90 Dormidontova, E. E. & Li, Z. L. (2010), *Abstracts of Papers of the American Chemical Society* **240**

91 Li, Z. L. & Dormidontova, E. E. (2011), *Soft Matter* **7**, 4179-4188

92 Nyrkova, I. A. & Semenov, A. N. (2005), *Macromolecular Theory and Simulations* **14**, 569-585

93 Nyrkova, I. A. & Semenov, A. N. (2005), *Faraday Discussions* **128**, 113-127

94 Choi, S. H., Bates, F. S. & Lodge, T. P. (2011), *Macromolecules* **44**, 3594-3604

95 Choi, S. H., Lodge, T. P. & Bates, F. S. (2010), *Physical Review Letters* **104**, 047802

96 Lu, J., Bates, F. S. & Lodge, T. P. (2013), *ACS Macro Letters* **2**, 451-455

97 Lu, J., Choi, S., Bates, F. S. & Lodge, T. P. (2012), *ACS Macro Letters* **1**, 982-985

98 Lund, R. *et al.* (2009), *Physical Review Letters* **102**, 188301

99 Lund, R. *et al.* (2007), *Journal of Applied Crystallography* **40**, S327-S331

100 Lund, R., Willner, L., Stellbrink, J., Lindner, P. & Richter, D. (2006), *Physical Review Letters* **96**, 068302

101 Zinn, T., Willner, L., Lund, R., Pipich, V. & Richter, D. (2012), *Soft Matter* **8**, 623-626

102 Denkova, A. G., Mendes, E. & Coppens, M. O. (2010), *Soft Matter* **6**, 2351-2357

103 Meli, L., Santiago, J. M. & Lodge, T. P. (2010), *Macromolecules* **43**, 2018-2027

104 Nicolai, T., Colombani, O. & Chassenieux, C. (2010), *Soft Matter* **6**, 3111-3118

105 Meli, L. & Lodge, T. P. (2009), *Macromolecules* **42**, 580-583

106 Rharbi, Y. (2012), *Macromolecules* **45**, 9823-9826

107 Repollet-Pedrosa, M. H. & Mahanthappa, M. K. (2013), *Soft Matter*, 7684-7687

108 Burke, S. E. & Eisenberg, A. (2001), *Langmuir* **17**, 6705-6714

109 Denkova, A. G., Mendes, E. & Coppens, M. O. (2009), *Journal of Physical Chemistry B* **113**, 989-996

110 Landazuri, G., Fernandez, V. V. A., Soltero, J. F. A. & Rharbi, Y. (2012), *Journal of Physical Chemistry B* **116**, 11720-11727

111 Vriezema, D. M. *et al.* (2005), *Chemical Reviews* **105**, 1445-1490

112 Duncan, R. (2003), *Nature Reviews Drug Discovery* **2**, 347-360

113 Farokhzad, O. C. & Langer, R. (2009), *ACS Nano* **3**, 16-20

114 Shi, J., Votruba, A. R., Farokhzad, O. C. & Langer, R. (2010), *Nano Letters* **10**, 3223-3230

115 Lipshutz, B. H. in *Transition Metal-Catalyzed Couplings in Process Chemistry* 299-312 Wiley-VCH Verlag GmbH & Co. KGaA, 2003.

116 Nuyken, O., Persigehl, P. & Weberskirch, R. (2002), *Macromolecular Symposia* **177**, 163-174

117 Liu, Y. *et al.* (2011), *Journal of the American Chemical Society* **133**, 14260-14263

118 Gall, B., Bortenschlager, M., Nuyken, O. & Weberskirch, R. (2008), *Macromolecular Chemistry and Physics* **209**, 1152-1159

119 Persigehl, P., Jordan, R. & Nuyken, O. (2000), *Macromolecules* **33**, 6977-6981

120 Cotanda, P., Lu, A., Patterson, J. P., Petzetakis, N. & O'Reilly, R. K. (2012), *Macromolecules* **45**, 2377-2384

121 Cotanda, P. & O'Reilly, R. K. (2012), *Chemical Communications* **48**, 10280-10282

122 Lu, A., Cotanda, P., Patterson, J. P., Longbottom, D. A. & O'Reilly, R. K. (2012), *Chemical Communications* **48**, 9699-9701

123 Arumugam, S., Vutukuri, D. R., Thayumanavan, S. & Ramamurthy, V. (2005), *Journal of the American Chemical Society* **127**, 13200-13206

124 Lu, A., Moatsou, D., Longbottom, D. A. & O'Reilly, R. K. (2013), *Chemical Science* **4**, 965-969

125 Lipshutz, B. H. *et al.* (2011), *The Journal of Organic Chemistry* **76**, 4379-4391

126 Lipshutz, B. H., Ghorai, S., Leong, W. W. Y., Taft, B. R. & Krogstad, D. V. (2011), *The Journal of Organic Chemistry* **76**, 5061-5073

127 Strebhardt, K. & Ullrich, A. (2008), *Nat. Rev. Cancer* **8**, 473-480

128 Kabanov, A., Zhu, J. & Alakhov, V. in *Advances in Genetics* Vol. Volume 53 (eds Mien-Chie Hung Leaf Huang & Wagner Ernst) 231-261 Academic Press, 2005.

129 Kabanov, A. V. *et al.* (1995), *Macromolecules* **28**, 2303-2314

130 Harada, A. & Kataoka, K. (1998), *Macromolecules* **31**, 288-294

131 Kwon, G. S., Yokoyama, M., Okano, T., Sakurai, Y. & Kataoka, K. (1993), *Pharmaceutical Research* **10**, 970-974

132 Otsuka, H., Nagasaki, Y. & Kataoka, K. (2003), *Advanced Drug Delivery Reviews* **55**, 403-419

133 Yokoyama, M. *et al.* (1998), *Journal of Controlled Release* **50**, 79-92

134 Yokoyama, M. *et al.* (1991), *Cancer Research* **51**, 3229-3236

135 Davis, M. E., Chen, Z. & Shin, D. M. (2008), *Nature Reviews Drug Discovery* **7**, 771-782

136 Heidel, J. & Davis, M. (2011), *Pharmaceutical Research* **28**, 187-199

137 Choi, H. S. *et al.* (2007), *Nat. Biotechnol.* **25**, 1165-1170

138 Fang, J., Nakamura, H. & Maeda, H. (2011), *Advanced Drug Delivery Reviews* **63**, 136-151

139 Iyer, A. K., Khaled, G., Fang, J. & Maeda, H. (2006), *Drug Discovery Today* **11**, 812-818

140 Maeda, H., Wu, J., Sawa, T., Matsumura, Y. & Hori, K. (2000), *Journal of Controlled Release* **65**, 271-284

141 Dreher, M. R. *et al.* (2006), *J. Natl. Cancer Inst.* **98**, 335-344

142 Nomura, T., Koreeda, N., Yamashita, F., Takakura, Y. & Hashida, M. (1998), *Pharmaceutical Research* **15**, 128-132

143 Canton, I. & Battaglia, G. (2012), *Chemical Society Reviews* **41**, 2718-2739

144 Blanazs, A., Armes, S. P. & Ryan, A. J. (2009), *Macromolecular Rapid Communications* **30**, 267-277

145 Champion, J. A. & Mitragotri, S. (2006), *Proceedings of the National Academy of Sciences of the United States of America* **103**, 4930-4934

146 Geng, Y. *et al.* (2007), *Nature Nanotechnology* **2**, 249-255

147 Torchilin, V. P. (2001), *Journal of Controlled Release* **73**, 137-172

148 Ansell, S. M. *et al.* (2008), *Journal of Medicinal Chemistry* **51**, 3288-3296

149 Kumar, V., Adamson, D. H. & Prud'homme, R. K. (2010), *Small* **6**, 2907-2914

150 Teng, Y., Morrison, M. E., Munk, P., Webber, S. E. & Procházka, K. (1998), *Macromolecules* **31**, 3578-3587

151 Rekatas, C. J. *et al.* (2001), *Physical Chemistry Chemical Physics* **3**, 4769-4773

152 Zhao, J., Allen, C. & Eisenberg, A. (1997), *Macromolecules* **30**, 7143-7150

153 Schulz, A. *et al.* (2014), *ACS Nano* **8**, 2686-2696

154 Gref, R. *et al.* (1994), *Science* **263**, 1600-1603

155 Sanada, Y. *et al.* (2013), *Journal of the American Chemical Society* **135**, 2574-2582

156 Choucair, A. & Eisenberg, A. (2003), *Journal of the American Chemical Society* **125**, 11993-12000

157 Bae, Y. *et al.* (2004), *Bioconjugate Chemistry* **16**, 122-130

158 del Rosario, L. S., Demirdirek, B., Harmon, A., Orban, D. & Uhrich, K. E. (2010), *Macromolecular Bioscience* **10**, 415-423

159 Rosario-Melendez, R., Yu, W. L. & Uhrich, K. E. (2013), *Biomacromolecules* **14**, 3542-3548

160 Gu, Y. *et al.* (2013), *Biomacromolecules* **14**, 2772-2780

161 Rosario-Melendez, R., Harris, C. L., Delgado-Rivera, R., Yu, L. & Uhrich, K. E. (2012), *Journal of Controlled Release* **162**, 538-544

162 Erdmann, L. & Uhrich, K. E. (2000), *Biomaterials* **21**, 1941-1946

163 Ouimet, M. A., Stebbins, N. D. & Uhrich, K. E. (2013), *Macromolecular Rapid Communications* **34**, 1231-1236

164 Knop, K., Hoogenboom, R., Fischer, D. & Schubert, U. S. (2010), *Angewandte Chemie International Edition* **49**, 6288-6308

165 Vonarbourg, A., Passirani, C., Saulnier, P. & Benoit, J.-P. (2006), *Biomaterials* **27**, 4356-4373

166 Hunter, A. C. & Moghimi, S. M. (2010), *Biochimica Et Biophysica Acta-Bioenergetics* **1797**, 1203-1209

167 Mislick, K. A. & Baldeschwieler, J. D. (1996), *Proceedings of the National Academy of Sciences of the United States of America* **93**, 12349-12354

168 Xia, T. *et al.* (2006), *Nano Letters* **6**, 1794-1807

169 Xia, T., Kovochich, M., Liong, M., Zink, J. I. & Nel, A. E. (2008), *ACS Nano* **2**, 85-96

170 Millili, P. G. *et al.* (2010), *Microscopy Research and Technique* **73**, 866-877

171 Millili, P. G., Yin, D. H., Fan, H., Naik, U. P. & Sullivan, M. O. (2010), *Bioconjugate Chemistry* **21**, 445-455

172 Chollet, P., Favrot, M. C., Hurbin, A. & Coll, J.-L. (2002), *The Journal of Gene Medicine* **4**, 84-91

173 Blanazs, A., Massignani, M., Battaglia, G., Armes, S. P. & Ryan, A. J. (2009), *Advanced Functional Materials* **19**, 2906-2914

174 Lemarchand, C., Gref, R. & Couvreur, P. (2004), *European Journal of Pharmaceutics and Biopharmaceutics* **58**, 327-341

175 Lowe, A. B. & McCormick, C. L. (2002), *Chemical Reviews* **102**, 4177-4190

176 Liu, S. & Armes, S. P. (2002), *Angewandte Chemie International Edition* **41**, 1413-1416

177 Yin, L., Dalsin, M. C., Sizovs, A., Reineke, T. M. & Hillmyer, M. A. (2012), *Macromolecules* **45**, 4322-4332

178 Gref, R. *et al.* (2000), *Colloids and Surfaces B-Biointerfaces* **18**, 301-313

179 Veronese, F. M. & Pasut, G. (2005), *Drug Discovery Today* **10**, 1451-1458

180 Smart, T. P., Mykhaylyk, O. O., Ryan, A. J. & Battaglia, G. (2009), *Soft Matter* **5**, 3607-3610

181 Kjellander, R. & Florin, E. (1981), *Journal of the Chemical Society-Faraday Transactions I* **77**, 2053-2077

182 Lusse, S. & Arnold, K. (1996), *Macromolecules* **29**, 4251-4257

183 Shikata, T., Takahashi, R. & Sakamoto, A. (2006), *Journal of Physical Chemistry B* **110**, 8941-8945

184 Wang, R. L. C., Kreuzer, H. J. & Grunze, M. (2000), *Physical Chemistry Chemical Physics* **2**, 3613-3622

185 Heath, T. D., Fraley, R. T. & Papahadjopoulos, D. (1980), *Science* **210**, 539-541

186 Leserman, L. D., Barbet, J., Kourilsky, F. & Weinstein, J. N. (1980), *Nature* **288**, 602-604

187 Gu, F. *et al.* (2008), *Proceedings of the National Academy of Sciences* **105**, 2586-2591

Chapter 2

MATERIAL SYNTHESIS AND CHARACTERIZATION

This chapter describes experimental procedures for the synthesis of well-defined block polymers and peptides as well as techniques to characterize the resulting materials. These procedures allow for the accurate control over the polymer and peptide composition that is necessary to develop these materials for drug delivery applications.

2.1 Macromolecule Synthesis

Development and optimization of macromolecular assemblies requires materials with well-defined compositions, controlled molecular weights, low dispersities, and high purities. The following sections describe synthetic approaches for creating block polymers and peptides that meet these demands.

2.1.1 Anionic Polymerization

Introduction

In the 1950's, Michael Szwarc demonstrated that 'living' carbanionic polymers could be synthesized under carefully controlled conditions.[1,2] Today, anionic polymerization is used on an industrial scale to synthesize materials for tires, shoe soles, and adhesives.[3-5] An important advantage of anionic polymerization is the absence of an inherent termination mechanism, meaning that the polymer chains will continue to grow until all of the available monomer is consumed or the reaction is

intentionally terminated. This 'living' nature of the polymerization allows for precise control over the polymer molecular weight and composition.

There are two kinetically controlled steps in anionic polymerization: initiation and propagation,

$$\text{Initiation:} \qquad I + M \xrightarrow{k_i} P_1^*$$

$$\text{Propagation:} \qquad P_1^* + M \xrightarrow{k_p} P_2^*$$

$$P_n^* + M \xrightarrow{k_p} P_{n+1}^*$$

in which k_i and k_p are the initiation and propagation rate constants, respectively. As suggested by the propagation expression, the reaction will continue to proceed until the monomer is consumed. Subsequently, the reaction is terminated by adding a proton donor (in this work, acidic methanol).

Typically, the initiation step is fast (*i.e.* $k_i > k_p$) and hence the concentration of active chain ends is equal to the initiator concentration. Assuming all of the monomer is consumed, then the number average degree of polymerization (N_n) is given by

$$N_n = K\frac{[M]_o}{[I]_o} \tag{1}$$

in which $[M]_o$ and $[I]_o$ are the initial monomer and initiator concentrations, respectively, and K is the functionality of chain growth ($K = 1$ for organometallic compounds used in this dissertation).

For a living polymerization, the distribution of chain lengths (dispersity, Đ) is described by a Poisson distribution,

$$Đ = \frac{N_w}{N_n} = 1 + \frac{1}{N_n} \tag{2}$$

Accordingly, the dispersity approaches unity as the degree of the degree of polymerization increases, and narrow molecular weight distributions are achieved even at low molecular weights.[5,6]

When used under appropriate reaction conditions, living anionic polymerization is a powerful synthetic approach; however, it is important also to be aware of the limitations of this technique. The high reactivity and low concentration of active chain ends makes anionic polymerization highly sensitive to trace impurities (*e.g.* H_2O and O_2).[6] Accordingly, all reactions must be carried out under inert conditions and all reagents must be meticulously purified. The organometallic reagents used to initiate the polymerization reactions and purify the monomers also are also highly sensitive to air and must be handled with extreme care. Finally, anionic polymerization of polar or functional monomers often is not possible due to side reactions.[5,6] Polar groups, such as the carbonyl group found in methyl methacrylate, are reactive toward the nucleophilic chain end, which leads to chain termination and complex polymer structures.[5,6] Despite these challenges, the ability to produce well-defined polymers, and more importantly block polymers, makes anionic polymerization ideal for synthesizing carefully designed and well-defined materials needed in this dissertation.

The following sections describe the reagents, polymerization conditions, and protocols used to synthesize the polymers studied throughout this dissertation. The two-step synthesis of poly(butadiene-*b*-ethylene oxide) (PB-PEO) is based on the method described by Hillmyer and Bates.[7]

Materials

Anionic polymerizations require rigorously purified reagents to avoid termination. Accordingly, all reagents were purified extensively using the air-free techniques described below.

Initiator

In this work, two different initiators were used. Anionic polymerization of butadiene was initiated with commercially available *sec*-butyllithium (1.4 M in cyclohexane, Sigma Aldrich). The anionic ring opening polymerization of ethylene oxide (EO) was accomplished using potassium naphthalenide synthesized in-house. Prior to use, the naphthalene (99%, Sigma Aldrich) was purified by recrystallization from ethanol. Potassium naphthalenide was prepared by mixing potassium (98%, chunks in mineral oil, Sigma Aldrich) with a 10% molar excess of naphthalene (99%, Sigma Aldrich) in anhydrous tetrahydrofuran (THF) under argon. This dark green mixture was stirred for at least 24 h before use. The initiator degrades over time; however, knowing the exact concentration is not crucial because the polymerization is initiated by a colorimetric titration (see below). The starting concentrations typically ranged from 0.03 to 0.06 M. *Note that potassium naphthalenide reacts with Teflon, and hence glass stir bars must be used during initiator preparation and all subsequent reactions.*

Solvent

Choosing the appropriate solvent is essential to a successful anionic polymerization. The solvent must be able to dissolve the growing chain while remaining unreactive as a monomer, chain termination agent or chain transfer agent.[5,6,8] Moreover, the solvation of the counterion significantly affects the polymerization kinetics.[5,6] The ionic species are insoluble in apolar solvents, and the counterion is strongly associated with the carbanion. The separation between the counterion and the carbanion increases with counterion size, and as a result, the kinetics are faster for larger counterions ($K^+ > Li^+$). The opposite trend is seen in polar solvents (*e.g.* THF used in this dissertation). The smaller counterions (*e.g.* Li^+) are more solvated than the larger counterions, increasing the distance between the chain end and the counterion and thereby increasing the polymerization kinetics.

Especially important in this dissertation, the resulting polymer structure from polymerization of 1,3 dienes (*e.g. 1,3*-butadiene) depends on the solvent used during the reaction. Shown in Figure 2.1 are the two regioisomers of PB, and the relative composition of these structures influences the chemical and physical properties of the polymer.[9-11] The anionic polymerization of butadiene in apolar solvents results in high 1,4 addition, whereas the polymerization in polar solvents favors 1,2 addition.[5,12] In polar solvents, the anionic center is localized on carbon 2 and the polymerization occurs across carbons 1 and 2.[5] The resulting polymer contains carbons 1 and 2 in the backbone with a pendant double bond.[5,12] In this dissertation, the polymerization of butadiene was carried out in THF, resulting in >90% 1,2 addition. Anionic ring opening polymerizations of EO also were performed in THF.

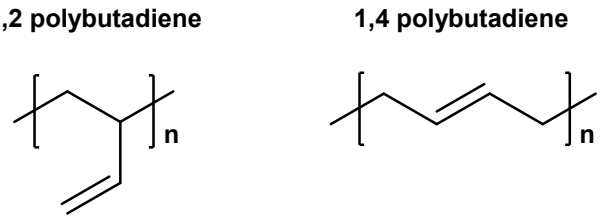

Figure 2.1 Regioisomers of polybutadiene. 1,2 addition is favored in polar solvents, while 1,4 addition is favored in apolar solvents.

Solvents for polymerization reactions were purified on an SG Waters solvent purification system. THF (Optima HPLC grade, Fisher Scientific) was degassed by sparging with argon for 30 min and then dried by passage through two alumina columns. The solvent was collected in a flask that was first heated with a gas torch (flame-treated) to remove any moisture and then evacuated and backfilled with argon 5 times.

Monomer

Inhibitors and trace impurities in the monomers were removed by rigorous air-free purification methods. Butadiene (≥ 99%, Sigma Aldrich) was purified by distillation over *n*-butyllithium salts. *Note butadiene monomer can contain trace butene impurities that will terminate the polymerization; therefore it is essential to purchase high purity monomers from the manufacturer*. The *n*-butyllithium salts (2.5 M in heptane, Acros Organics) were dried under reduced pressure. Typically ~ 0.15 to 0.20 mL of purification agent were used per gram of monomer. The butadiene monomer was vacuum distilled into the flask containing the purification agent, which was kept on liquid nitrogen. The flask was warmed to ~0 °C on an ice

bath and stirred for 10 min. Then, the monomer was vacuum distilled into a second salt flask. Again, the monomer was stirred over the purification agent for ~10 min on an ice bath. Finally, the desired amount of purified butadiene was distilled into a flame-treated burette. The monomer was stored in liquid nitrogen until use. EO ($\geq$ 99.5%, Sigma Aldrich) was purified in a similar manner. Specifically, EO was purified by successive distillations over butylmagnesium chloride salts (2.0 M in THF, Sigma Aldrich). Typically ~ 0.10 to 0.20 mL of purification agent were used per gram of EO. The desired amount of EO monomer was transferred to a flame-treated burette and stored in liquid nitrogen until use.

Extreme care must be taken when working with butadiene and ethylene oxide monomers. Both monomers are highly toxic and exist as gasses at room temperature. All distillations must be performed cold and the purified monomers must be stored below 0 °C. The volumetric size of the burettes should be at least twice the volume of monomer. All purification flasks must be equipped with a pressure relief valve as the heat of reaction with the purification reagents can cause a sufficient increase in temperature to lead to an explosion. Excess monomer should only be vented into the chemical fume hood after all work is complete, and venting should be performed for at least 2 h.

Synthesis

The PB-PEO diblock copolymers studied in this dissertation were synthesized via two sequential anionic polymerizations.[7] First, a hydroxyl-terminated polybutadiene (PB-OH) was synthesized and then used as a macroinitiator of EO to

create PB-PEO (Figure 2.2). The two-step synthesis is necessary because PB-PEO cannot be polymerized in a single step, as the living EO chain ends strongly associate with lithium counterions in polar solvents which prevents chain propagation.[13-15] However, a major advantage of the two-step synthesis was that multiple PB-PEO block copolymers and their deuterated analogs [(polybutadiene-*b*-ethylene oxide-d_4) (PB-*d*PEO)] could be synthesized from the same macroinitiator, allowing for direct comparison between the different polymers. The synthesis of PB-OH and PB-PEO are described in the following sections.

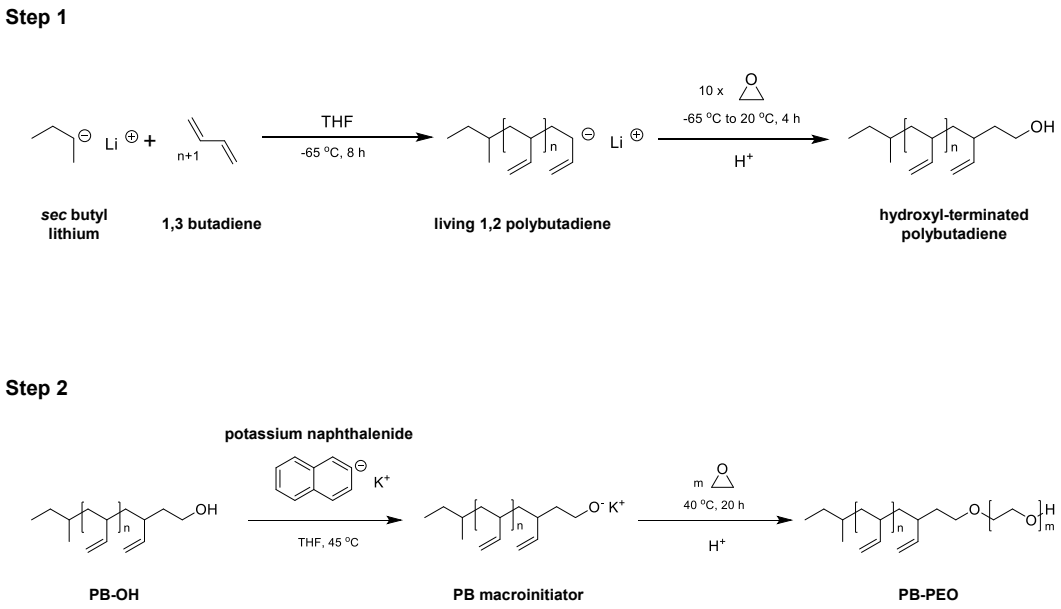

Figure 2.2 Synthetic scheme for synthesis of poly(butadiene-*b*-ethylene oxide) (PB-PEO)

Hydroxyl-terminated Polybutadiene (PB-OH) Synthesis

Polymerization of butadiene was performed in THF using *sec*-butyl lithium as an initiator. In this reaction, the strong association in lithium alkoxides was exploited to quantitatively react the PB chain ends with a single EO repeat unit, yielding a fully hydroxyl-functionalized polymer.

Before starting the polymerization, the custom-built glass reactor was flame-treated to remove any residual moisture and then evacuated and backfilled with argon 5 times. After the last purge, the reactor was pressured to ~3 psi with argon. The reactor also was equipped with a pressure gauge and a pressure relief valve to monitor the pressure as the gaseous monomers were added to the reactor and to prevent an explosion. THF (~ 20 to 30 mL solvent/g of polymer) was added to the reactor and then cooled to - 65°C using a dry ice/isopropanol bath. The reactor pressure was maintained at ~1 psi by adding argon. The desired amount of *sec*-butyl lithium was then injected into the reactor, upon which the solvent turned pale yellow. The amount of monomer required to initiate all the chain ends was calculated and added to the reactor to begin the polymerization. Subsequently, the remaining monomer was slowly added to ensure that the pressure in the reactor did not exceed 6 psi. The reaction was allowed to proceed for 8 h. The reaction progress also was determined by monitoring the reactor pressure to ensure that all of the butadiene was consumed. At the end of the reaction, the dry ice was removed from the bath and the reactor pressure was reduced to <1 psi before adding 10 molar equivalents of EO per living chain end. Upon EO addition, the reaction mixture turned clear and was allowed to stir for an additional 2 h. After 2 h, the reaction was terminated by adding

acidic methanol (~1 M, 25 mL total). The reaction was stirred for an additional 30 min and then the reactor was vented for 2 h to remove the excess EO.

The reaction solvent was removed by rotary evaporation and the polymer was redissolved in methylene chloride. Subsequently, the polymer was washed with a saturated sodium bicarbonate solution to neutralize the excess acid from the termination step, and then the polymer was washed with water until the aqueous phase was neutral. The methylene chloride was removed by rotary evaporation and the polymer was freeze-dried from benzene. The PB-OH polymer was characterized using size exclusion chromatography (SEC), matrix-assisted laser desorption/ionization mass spectrometry (MALDI-TOF MS) and proton nuclear magnetic resonance (^{1}H NMR) spectroscopy before use in subsequent reactions. Importantly, the molecular weights determined from MALDI-TOF MS and end-group analysis in ^{1}H NMR were compared to ensure all of the chain ends were functionalized with a hydroxyl group before the PB-OH was used as a macroinitiator in PB-PEO synthesis.

Poly(butadiene-b-ethylene oxide) (PB-PEO) Synthesis

PB-PEO was synthesized by anionic ring opening polymerization of EO (Figure 2.2). *Note that the same procedures were used for EO and deuterated EO (ethylene oxide-d_4).* Before the start of the reaction, the reactor was flame-treated and purged as described above. After the last purge, the reactor was pressured to ~ 2 psi. The desired amount of PB-OH macroinitiator was dissolved in anhydrous THF in the glovebox (typically 1 to 3 g of PB-OH in ~300 mL of THF). The PB-OH solution was then added to the reactor, and the reactor was heated to 40 °C in a water bath. The

PB-OH polymer was reinitiated using potassium naphthalenide which acts as a strong base.[7,13,16] The PB-OH was titrated slowly with the potassium naphthalenide until a light green color persisted for at least 15 min. The large molar absorptivity of the potassium naphthalenide enabled precise determination of the titration end point.[7] Then, the amount of EO required to initiate all of the chains was calculated and added to the reactor, upon which the reaction mixture turned clear. The remaining EO was added slowly to ensure that the reactor pressure did not exceed 6 psi. Then, the reaction was allowed to proceed for 22 h and the reaction progress was determined by monitoring the reactor pressure. At the end of the reaction, the reaction mixture typically was light blue/gray in color. The reaction was terminated by adding acidic methanol (~1 M, 25 mL total), upon which the reaction mixture turned colorless. The reaction was stirred for an additional 30 min and then the reactor was vented for 2 h to remove any residual EO.

The resulting polymer was purified as described above and then characterized by SEC and ^{1}H NMR. *Note that the residual naphthalene in the polymer was not removed by the washes, but could be removed during the freeze-drying process as naphthalene sublimes.* The polymers studied in this dissertation are summarized in Table 2.1.

Table 2.1 Summary of PB-OH and PB-PEO polymers

Polymer	M_n (g mol^{-1})[a]	N_{PB}[b]	N_{PEO}[c]	w_{EO}[d]	Đ[e]
PB-OH	1,600	30	1	-	1.10
PB-OH	3,200	59	1	-	1.06
PB-PEO	11,200	59	178	0.71	1.06
PB-*d*PEO	11,100	59	163	0.71	1.05

[a] number average molecular weight determined by MALDI-TOF MS for the PB-OH precursors and calculated using the block polymer composition from ^{1}H NMR for the PB-PEO polymers
[b] number average degree of polymerization of the PB block
[c] number average degree of polymerization of the PEO block
[d] hydrophilic weight fraction determined from ^{1}H NMR spectroscopy
[e] dispersity determined from SEC with polystyrene standards

2.1.2 Fmoc Solid Phase Peptide Synthesis (SPPS)

Introduction

In 1963, Bruce Merrifield published his seminal work on the synthesis of a tetrapeptide using an innovative solid phase approach.[17] Within 10 years, more than 500 papers were published on solid phase peptide synthesis,[18] and Merrifield was awarded the 1984 Nobel Prize in chemistry for '*..his development of a simple and ingenious method for obtaining peptides and proteins.*'[19]

SPPS has revolutionized peptide chemistry. This approach enables exquisite control over the amino acid sequence while facilitating facile synthesis of peptides and small proteins. Excess reagents can be used to drive the reactions to completion, and then residual reagents are easily removed from by washing the solid support.[18] Moreover, the chemistries are amenable to automation technologies, which are now routinely used in industry for the development of new peptide therapeutics.[20-22]

The principles of SPPS are outlined in Figure 2.3. First, the C-terminal amino acid is attached to an insoluble resin *via* its carboxyl group. Then, a temporary protecting group is removed from the α-amino group. The second amino acid then is

coupled to the first amino acid via amide bond formation. After the coupling, all excess reagents are washed away from the resin. These general steps are repeated, building the desired peptide sequence one amino acid at a time. Finally, the completed peptide is removed from the resin.

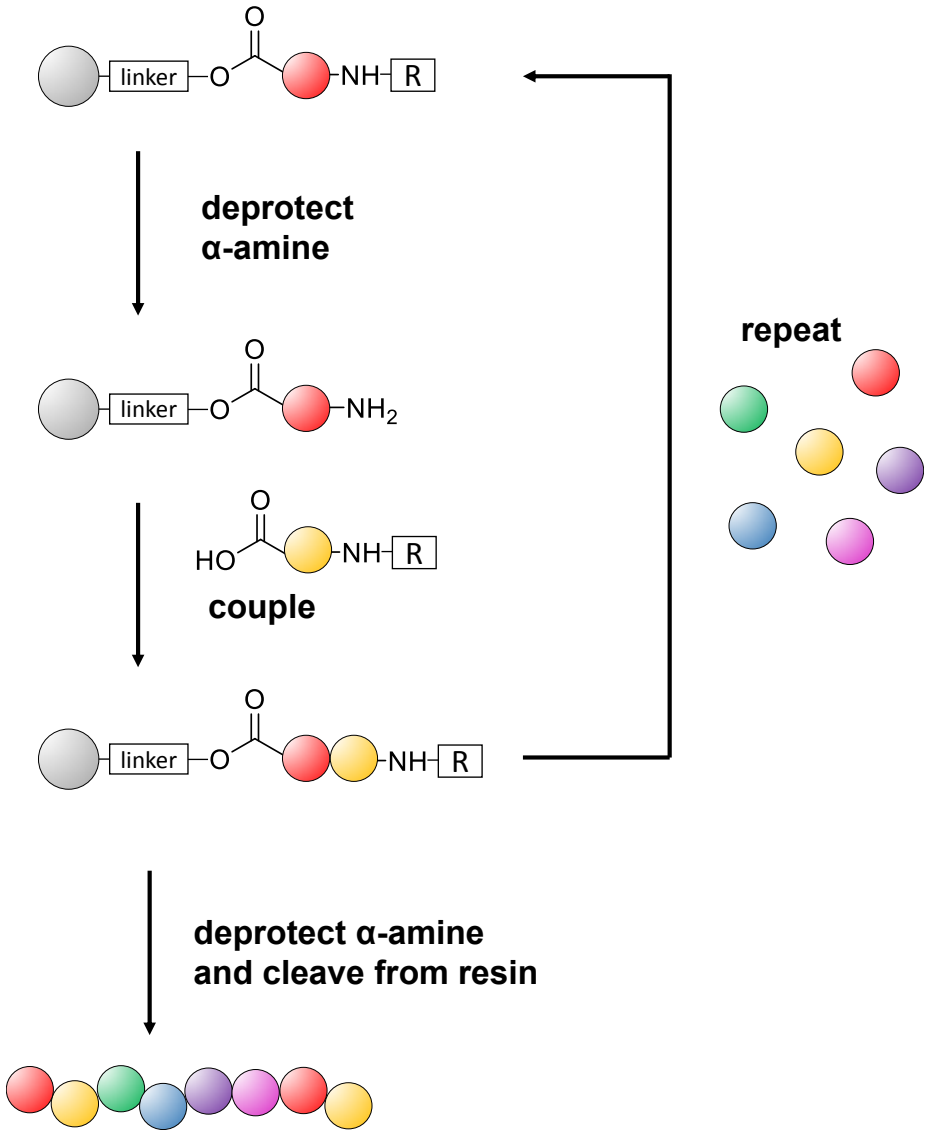

Figure 2.3 Schematic representation of solid phase peptide synthesis (SPPS) principle.

While SPPS is incredibly powerful, it is important also to be aware of its limitations. As a consequence of the sequential amino acid additions, the final peptide purity is significantly affected by the efficiency of each coupling step. For example, if each coupling step were 95% efficient (as is typical in the case of amide bond formation), the overall yield of a 10 amino acid peptide would be only ~65% and the yield of a 20 amino acid peptide would be <40%. Obviously, these low yields are undesirable, and hence care must be taking to minimize side reactions and ensure high coupling efficiencies.

Merrifield's original SPPS method utilized tert-butoxycarbonyl (Boc) groups to temporarily protect the α-amine and relied on side chain protecting groups with different sensitivities to acidolysis.[17,23,24] While Merrifield SPPS creates well-defined peptides, it requires hydrofluoric acid (HF) and a specially designed vessel to cleave the final peptide product from the resin. Fortunately, developments in fully orthogonal protecting group chemistries that require mild cleavage conditions have made SPPS more accessible to both academic and industrial labs alike.[18] Most peptides, including the peptides employed in this dissertation, are now synthesized using fluorenylmethyloxycarbonyl (Fmoc)-based protection chemistries. The α-amino group is protected with a base-labile Fmoc group, while the amino acid side chain groups are protected with acid labile-protecting groups and the peptide is attached to the resin *via* and acid-sensitive linker.[18] Using this approach, the Fmoc group can be removed from the α-amino group during the synthesis without affecting any of the side chain protecting groups, and the final peptide (and all side chain protecting groups) is removed from the resin with an acidic cleavage 'cocktail'.[18]

The following sections describe in detail the reagents and protocols used in the Fmoc SPPS reported in Chapter 9.

Materials and Reagents

High purity Fmoc-protected amino acids and 2-(1H-benzotriazole-1-yl)-1, 1, 3, 3-tetramethyluronium hexafluorophosphate (HBTU) were purchased from NovaBiochem (EMD Biosciences). A series of standard side chain protecting groups were used for amino acids with functional side chains (Table 2.2). Low loading H-Rink Amide ChemMatrix resin (0.27 mmol/g) was purchased from PCAS BioMatrix Inc. *Note that the rink amide linker yields a peptide with C-terminal amide.* Piperidine (ReagentPlus, 99%) and 4-methylmorpholine (ReagentPlus, 99%) were purchased from Sigma Aldrich. All other reagents were purchased from Sigma Aldrich and used as received.

Table 2.2 Standard side chain protecting groups used in SPPS

Amino acid (abbreviation)	Side chain protecting group (abbreviation)
arginine (R)	2,2,4,6,7-pentamethyldihydrobenzofuran-5-sulfonyl (Pbf)
aspartic acid (D)	t-butyl ester (OtBu)
glutamine (Q)	triphenylmethyl (Trt)
glutamic acid (E)	t-butyl ester (OtBu)
lysine (K)	tert-butyl carbonyl (Boc)
serine (S)	t-butyl ether (tBu)
tryptophan (W)	tert-butyl carbonyl (Boc)

All SPPS reagents were prepared before beginning each synthesis. The Fmoc deprotection solution contained 20 vol% piperidine in dimethylformamide (DMF) and the amino acid dissolution solvent contained 0.4 M methylmorpholine in DMF. The amino acid and HBTU for each coupling step were weighed into a vial and sealed with a septum.

Synthesis

Peptides were synthesized on a 0.1 mmol scale using Fmoc SPPS using a Protein Technologies, Inc. Tribute Automated Peptide Synthesizer. At the start of the synthesis, the resin was weighed into the reaction vessel, rinsed with dimethylformamide (DMF), and then swelled with dichloromethane (DCM) for 30 min. *Note that the resin must be handled carefully to prevent the beads from fracturing.* The Fmoc protecting group on the amine-functionalized resin then was cleaved using the standard deprotection reaction conditions as depicted in Figure 2.4.

Importantly, the cleaved Fmoc group forms an adduct with piperidine that strongly absorbs UV light, and the progress of the deprotection reaction can be monitored by measuring the UV absorbance of this adduct.[18] The Tribute synthesizer is equipped with inline UV-monitoring and a feedback control system to ensure efficient Fmoc removal. Typically the Fmoc group was removed after 5 min of treatment with the piperidine solution; however, the deprotection step was repeated until the UV absorbance dropped below a threshold value. Following Fmoc removal, the resin was rinsed with DMF.

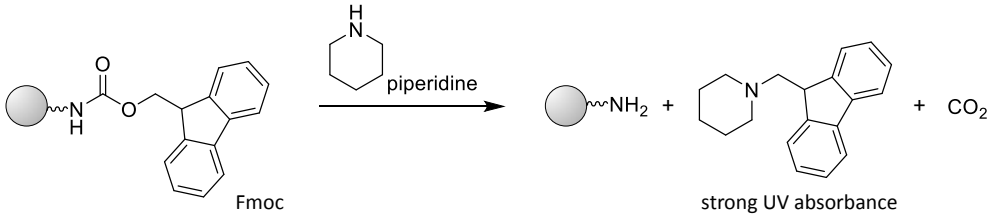

Figure 2.4 Reaction scheme for Fmoc removal using piperdine.

After removing the Fmoc group from the resin, the first amino acid was coupled to the resin using standard HBTU/methylmorpholine coupling conditions. Amino acid couplings were performed using 6 equivalents of both the amino acid and HBTU dissolved in 3 mL of DMF containing 0.4 M methylmorpholine. The solids were allowed to dissolve for 2 min to activate the carboxylic acid group (Figure 2.5), and then the amino acid solution was added to the resin. The coupling reaction was mixed for 2 h, and the reagents were removed. Finally, the resin was rinsed thoroughly with DMF, and the Fmoc group was removed from the α-amine group as described. The coupling and deprotection steps were repeated until the desired sequence was complete.

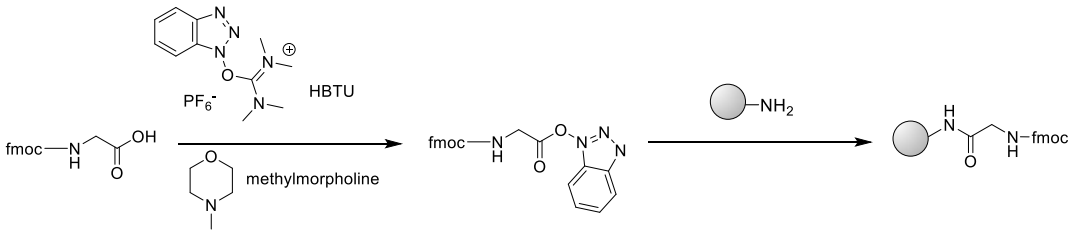

Figure 2.5 Reaction scheme for amino acid coupling *via* carboxylic acid activation using HBTU and subsequent amide bond formation.

Following addition of the final amino acid, the N-terminal Fmoc protecting group was removed using the standard conditions. The resin was rinsed with DMF and then DCM, and subsequently, the resin was dried under a nitrogen stream. If the peptide was not going to be used immediately, the dried resin was stored at 4 °C. Otherwise, the final peptide was removed from the resin using a trifluoroacetic acid (TFA)-based cleavage 'cocktail'.[18] This final step also removes the acid-labile side chain protecting groups. Water and triisopropylsilane (TIS) were added as scavengers to quench the highly reactive cations produced during the cleavage reaction.[18] The final cleavage mixture contained 95:2.5:2.5 v/v TFA: TIS: H_2O. The cleavage was performed for 3 h and the cleaved product was separated from the resin beads by filtration. Then, the solution was concentrated under a nitrogen stream and peptide was precipitated into cold diethyl ether to remove the cleaved side chain protecting groups. The peptide was recovered by centrifugation at 4000 rpm for 5 min at 4 °C, and the resulting pellet was dissolved in $H_2O$and lyophilized. The synthesized peptide then was characterized using reverse phase high performance liquid chromatography (RP-HPLC) and mass spectrometry as described in subsequent sections.

2.2 Chemical Characterization

Methods used to determine the molecular weight, purity, and chemical composition of the synthesized macromolecules are described in the following sections. Polymers were characterized using SEC, MALDI-TOF MS, and ^{1}H NMR spectroscopy. Peptides were characterized using a combination of RP-HPLC and MALDI-TOF MS.

2.2.1 Chromatography Techniques

Chromatography techniques are an important tool for characterizing synthetic macromolecules and provide essential information on their distribution and purity. In general, the macromolecule is dissolved in a solvent (mobile phase) and then passed over a porous stationary phase. Separation is based on the differential partitioning of the molecules between the stationary and mobile phases.[25] There are several types of chromatography that exploit different types of interactions between the macromolecules and the stationary phase, and it is important to utilize the appropriate technique that provides the best separation of the sample. Two different types of chromatography were used in this dissertation. The distribution and purity of the polymers were determined with SEC and the purity of synthetic peptides was characterized with RP-HPLC. These techniques are described in more detail in the following sections.

2.2.1.1 Size Exclusion Chromatography (SEC)

SEC is a powerful technique routinely used to characterize synthetic polymers.[6,8] SEC provides information on the complete molecular weight distribution and can be used to calculate the polymer molecular weight, confirm successful block polymer synthesis, and monitor the purity of the polymeric sample.[8]

Theory

As the name implies, SEC separates molecules based on their size (*i.e.* hydrodynamic volume).[6] A dilute polymer solution (mobile phase) flows through a column packed with beads of a porous gel (stationary phase) with pore sizes ranging from 50 – 10^6 Å.[6] The solvent carries the polymer molecules through the pores and

the smallest polymers are able to pass through most of the pores. As a result, the smallest polymer chains have the longest flow path the column, while the largest chains cannot fit through most of the pores and have a shorter flow path. Accordingly, the polymer chains elute from the column in order of decreasing size.

The concentration of polymer in the eluent is monitored continuously using a differential refractive index detector, giving a quantitative indication of the polymer molecular weight distribution. However, the polymers are separated based on their hydrodynamic volume and not molecular weight; therefore, the columns must be calibrated with polymer standards of known molecular weight. Typically, a series of low dispersity polystyrene standards are run to calibrate the SEC columns. A calibration curve is constructed by plotting the standard molecular weight (M) as a function of elution volume ($V_e = V_t \times flowate$), which correlates the time spent on the column with the polymer molecular (Figure 2.6). Note that log(M) is linear with V_e, which is consistent with theoretical predications for the size-based separation.[6]

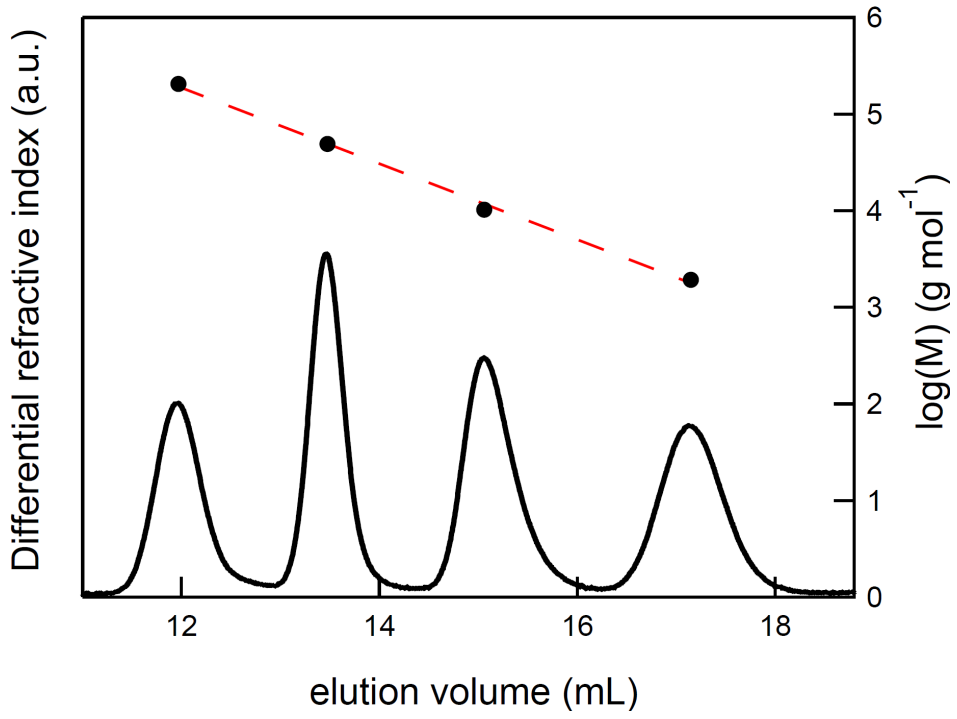

Figure 2.6 SEC chromatogram and corresponding calibration curve for four low dispersity polystyrene standards.

The number average (M_n) and weight average (M_w) molecular weight also can be directly calculated from the SEC chromatogram. The measured differential refractive index (DRI) is proportional to the mass concentration of polymer in solvent (g L^{-1}),[26] and thus

$$M_n = \frac{\sum DRI_i}{\sum \frac{DRI_i}{M_i}} \tag{3}$$

$$M_w = \frac{\sum DRI_i M_i}{\sum DRI_i} \tag{4}$$

in which the M_i is the molecular weight and DRI_i is the corresponding measured intensity. The molecular weight dispersity ($Đ$) then can be calculated as $Đ = M_w/M_n$.

It is important to note that unless the unknown sample is the same polymer as the standards, the M_n and M_w calculated from SEC are not the absolute molecular weights of the sample and instead are referred to as the *relative* molecular weight and dispersity.

Application

In this dissertation, SEC was used to determine the dispersity of all synthesized polymers, confirm successful block polymer synthesis, and ensure that any post-polymerization modification chemistries did not degrade or crosslink the polymers. All experiments were run with THF as the mobile phase at a flow rate of 1 mL min^{-1}. The polymers were analyzed using Styragel HR1 and HR4 columns, which are packed with cross-linked poly(styrene-*co*-divinylbenzene) particles. Some of the more polar polymers (such as PEO homopolymers or PB-PEO) interacted with the divinylbenzene-based column packing, as evidenced by the tail that was seen at longer elution times as well as the artificially broadened SEC chromatograms. The reported relative dispersities were calculated based on polystyrene standards.

Shown in Figure 2.7 are representative SEC chromatograms for a PB-PEO block polymer and corresponding PB-OH macroinitiator. Both polymers showed a single low dispersity peak (Đ = 1.05 for both polymers). The PB-PEO peak shifted to shorter retention times compared to the PB-OH macroinitiator, consistent with the diblock polymer having a higher molecular weight. Also, there was no peak

corresponding to the PB-OH macroinitiator in the PB-PEO trace, confirming that the PB-PEO polymer was a pure diblock.

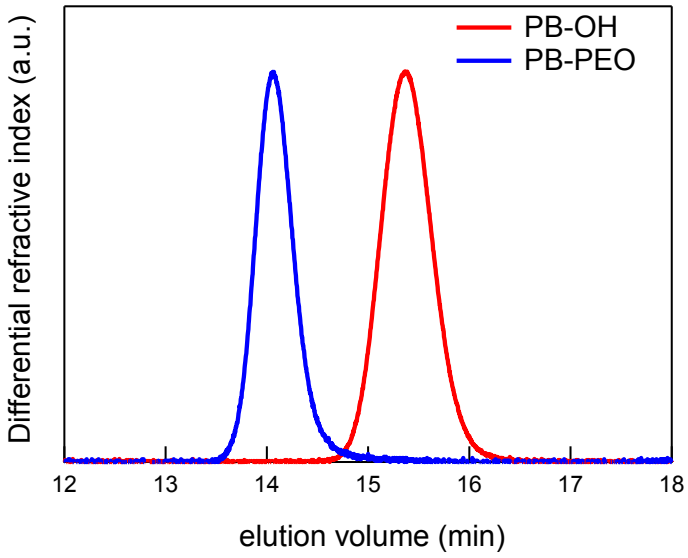

Figure 2.7 Representative SEC chromatogram for a PB-PEO block polymer and corresponding PB-OH macroinitiator. Both polymers show a single low dispersity peak. Importantly, there is no peak corresponding to the PB-OH homopolymer in the PB-PEO trace.

2.2.1.2 Reverse Phase High Performance Liquid Chromatography (RP-HPLC)

RP-HPLC is the standard method for both determining and controlling the purity of synthetic peptides.[18]

Theory

Reverse phase chromatography is a form of partition chromatography in which the separation is based on differential analyte partitioning between the mobile and stationary phase. The column packing is hydrophobic, and the samples are eluted off

of the column with a solvent gradient that increases in hydrophobicity over time (Figure 2.8). The more hydrophobic the sample, the later it will elute off of the column.

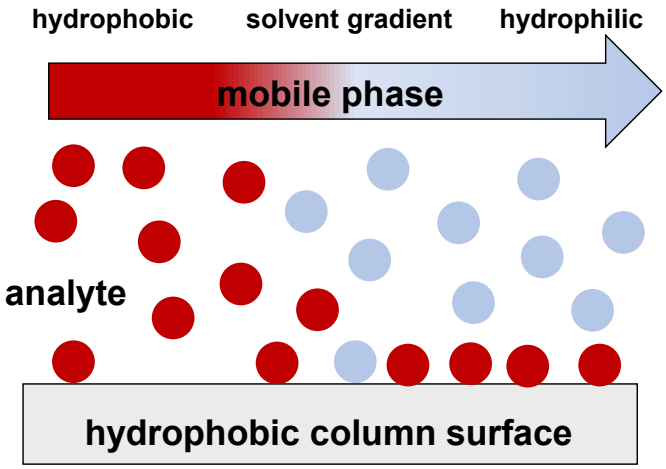

Figure 2.8 Schematic representation of RP-HPLC separation. The analyte adsorbs to the hydrophobic column and remains there until the mobile phase is hydrophobic enough to elute the peptide. The more hydrophobic the analyte, the later it elutes off of the column.

Application

RP-HPLC analysis was used in this dissertation to determine the purity of synthesized peptides, confirm synthesis of PEO-peptide conjugates, and separate PEO-peptide conjugates from unreacted peptide (Chapter 9). All analyses were performed using an octadecyl silica column (*i.e.* C18, silica gel packing decorated with 18 carbon chains).[18,27] The mobile phase consisted of a linear gradient between solvent A and solvent B, in which A is 0.1 vol% trifluoroacetic acid (TFA) in water, and B is 0.1 vol% TFA acetonitrile. The TFA was added to the solvents to increase

the affinity of the analyte to the mobile phase. The elution of the peptides of the column was monitored by UV-Vis absorbance at 210 nm and 280 nm, corresponding to the intrinsic absorbance of the peptide backbone and tryptophan residues, respectively. The purity of the crude peptides was determined using an analytical column, and larger quantities of material were purified using a semi-prep C18 column, as the greater amounts of material could be loaded onto the larger column. The purified peptide was recovered by collecting fractions of the eluent.

Shown in Figure 2.9 is the standard solvent gradient used in this dissertation. The solvent gradient was a linear AB gradient from 5 vol% B to 65 vol% B over 48 min. At the end of each run, the solvent composition was increased to 95 vol% B to flush the column and then decreased to 5 vol% B to equilibrate the column before starting the next sample run. Also shown in Figure 2.9 are representative RP-HPLC traces for a peptide, PEO-peptide conjugate, and PEO, in which the retention time increased with hydrophobicity of the material (PEO > PEO-peptide > peptide).

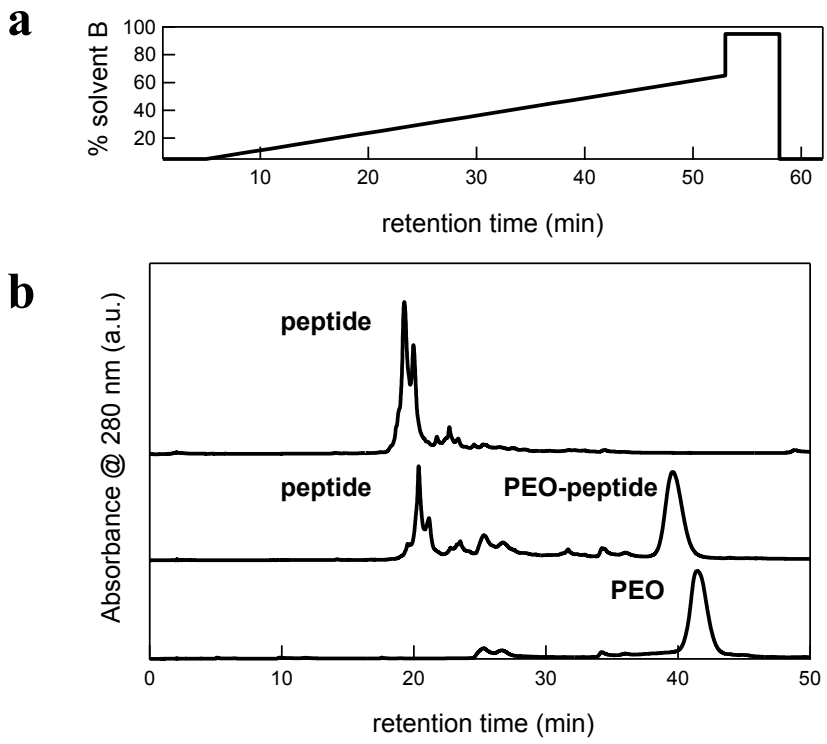

Figure 2.9 Representative RP-HPLC data for characterization of PEO-peptide conjugates. (a) The standard solvent gradient used for analysis of peptides and PEO-peptides in this dissertation in which solvent B is 0.1 vol% TFA in acetonitrile. (b) Representative RP-HPLC traces for peptide, PEO-peptide conjugates, and PEO. The retention time increase with the hydrophobicity of the material, PEO > PEO-peptide > peptide.

2.2.2 Matrix-Assisted Laser Desorption/Ionization Time of Flight (MALDI-TOF) Mass Spectrometry

MALDI-TOF mass spectrometry has become an important tool in characterizing both polypeptides/proteins and synthetic polymers.[28-35] In particular, MALDI-TOF MS is a powerful method for determining the *absolute* molecular weight of the sample as well as providing valuable information on the molecular weight distribution, composition, and end-group functionality of polymers.[29,31-33,35,36]

Theory

MALDI is referred to as a 'soft' ionization method because it does not fragment the polymer upon ionization. To prepare samples for analysis, the sample is mixed with a large excess of matrix and the mixture is co-crystallized onto a sample target (Figure 2.10). Matrices are usually an organic acid with a chromophore that absorbs the majority of energy from the laser pulse and then transfers a proton to the sample.[37] The matrix is essential for both the desorption and ionization processes, and finding the appropriate matrix for a polymer sample is key for obtaining a good mass spectrum.[37] Many polymer samples also require a cationizing agent, such as Na^+ or Ag^+ salt, to help ionize the sample.[30] Matrices and cationizing salts used for common polymers are summarized in Table 2.3.[38]

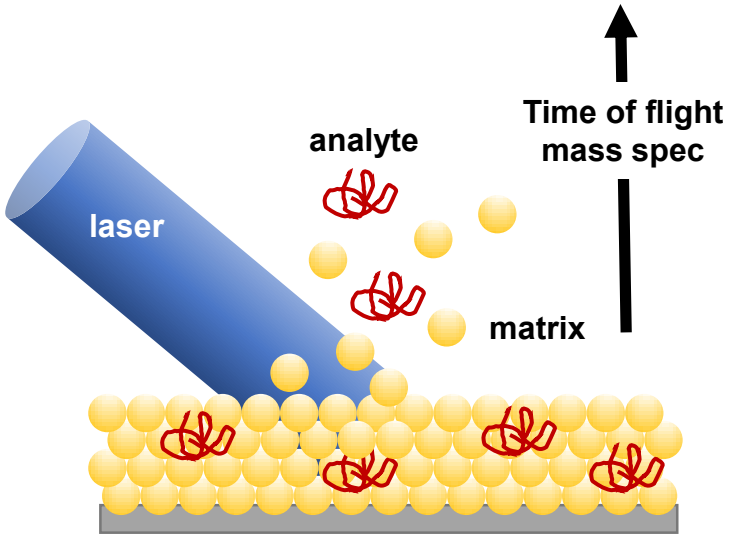

Figure 2.10 Schematic representation of matrix-assisted laser desorption/ionization (MALDI) process.

Table 2.3 MALDI 'recipes' for common polymers

Polymer*	Matrix	Cationizing salt	Recipe
PEO	α-Cyano-4-hydroxycinnamic acid (HCCA)	-	30 mg mL^{-1} matrix in 1:1 (v/v) acetonitrile/water 1 mg mL^{-1} polymer in H_2O spot layer of matrix and dry, then polymer and dry, then matrix
PB, PS, PI, PMMA	dithranol	silver trifluoroacetate (AgTFA)	20 mg mL^{-1} matrix 10 mg mL^{-1} salt 10 mg mL^{-1} polymer all solutions in THF mix 10:1:2 (v/v) matrix: salt: polymer and spot on target

*poly(ethylene oxide) [PEO], polybutadiene [PB], polystyrene [PS], polyisoprene [PI], and poly(methyl methacrylate) [PMMA]

Following ionization, the ions are accelerated down the time-of-flight (TOF) mass analyzer by an electric potential. Importantly, MALDI primarily produces singly charged species; therefore, all of the ions have the same kinetic energy and the velocity only depends on the sample mass.[37] The lighter ions hit the detector at the end of the mass analyzer before the heavier ions, and hence recording the intensity as a function of time gives the mass spectrum.

A representative mass spectrum for a 3.2 kg mol^{-1} PB-OH polymer is shown in Figure 2.11. Note that the x-axis is the mass to charge (m/z) ratio; however, for this ionization method m/z corresponds directly to mass because the polymers are singly

charged. The peak-to-peak spacing corresponds to the repeat unit molecular weight, and the recorded mass (M) is given by

$$M = M_{cation} + M_{end-groups} + nM_o \tag{5}$$

in which M_{cation}, $M_{end\text{-}group}$, and M_o are the masses of the cation, chain end-groups, and repeat unit, respectively, and n is the degree of polymerization. The measured signal is proportional to the number concentration of chains; therefore, the number average (M_n) and weight average (M_w) molecular weights can be calculated according to

$$M_n = \frac{\sum IM_i}{\sum I} \tag{6}$$

$$M_w = \frac{\sum IM_i^2}{\sum I\, M_i} \tag{7}$$

in which I and M_i are the measured intensity and mass, respectively.

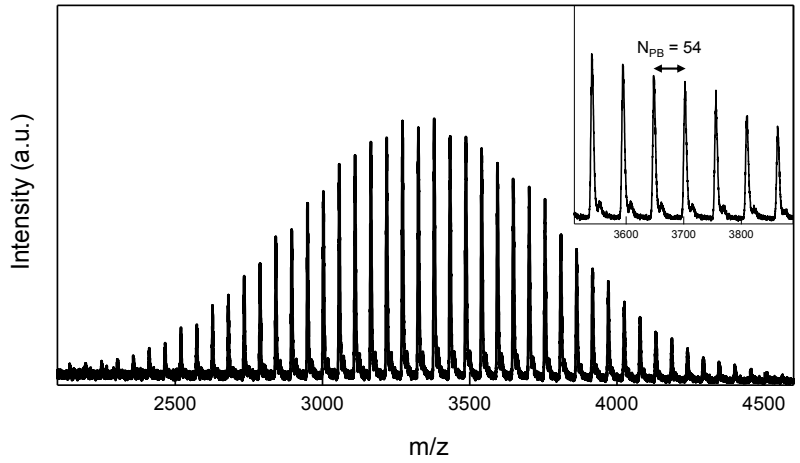

Figure 2.11 Representative MALDI-TOF MS trace for a 3.2 kg mol^{-1} PB-OH polymer. The peak-to-peak spacing corresponds to the PB repeat unit molecular weight.

Application

Throughout this dissertation, MALDI-TOF MS was used to determine the molecular weight of end-functionalized polymers, peptides, and polymer-peptide conjugates.

Importantly, MALDI-TOF MS was used to determine the absolute molecular weight of all PB-OH precursors, both to confirm that all of the chains were successfully end-capped with hydroxyl groups and to calculate the absolute molecular weight of the block polymers studied. While the literature reports the successful ionization of polymer samples with molecular weights on the order of 100 kg mol^{-1},[28] in practice it is difficult to obtain a mass spectrum for polymers with molecular weights >10 kg mol^{-1}. There also are two different modes of operation for MALDI-TOF MS, as compared in Figure 2.12. Linear mode is more sensitive, making it better for analysis of high molecular weight polymers; however, linear mode

has a lower resolution (~ 100 m/z). Conversely, reflectron mode (also referred to as reflector mode) is less sensitive but has much higher mass resolution, making it ideal for characterizing low molecular weight polymers and peptides.

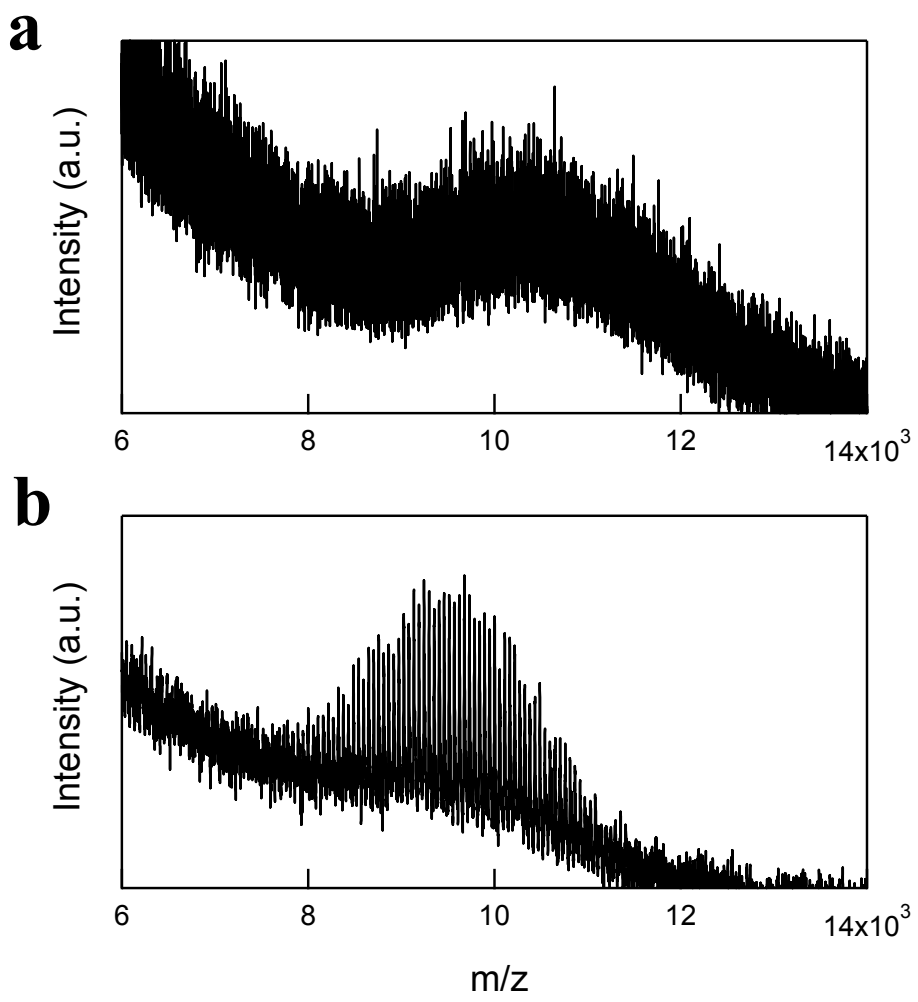

Figure 2.12 Comparison of different operation modes in MALDI-TOF MS (a) linear mode is more sensitive but has a lower resolution compared to (b) reflectron mode. Both spectra are for a 9.6 kg mol^{-1} PB-OH.

MALDI-TOF MS is also an invaluable technique for characterizing synthesized peptides and polymer-peptide conjugates. It is essential to confirm the molecular weight of the desired peptides and identify any potential impurities. Accordingly, it is important to note that peptides often interact with cations (most often Na^+ and K^+) or the matrix, resulting in additional high molecular weight peaks in the mass spectrum (Figure 2.13). These peaks readily are distinguished from other impurities by using a different matrix or performing salt doping experiments, in which a saturated salt solution is added to the analyte solution before depositing the samples onto the target. As seen in Figure 2.13, specific high molecular weight peaks were more pronounced after salt addition, confirming that these peaks were due to salt association with the sample.

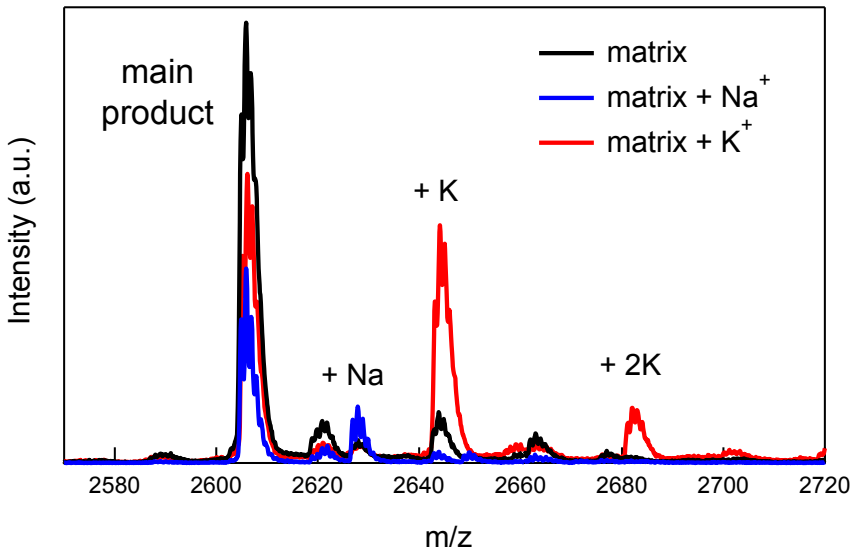

Figure 2.13 Representative mass spectra from salt doping experiments. Either sodium chloride (Na^+) or potassium chloride (K^+) was added to the sample to confirm which higher molecular weight peaks due to cations associating with the peptide.

2.2.3 Proton Nuclear Magnetic Resonance (^{1}H NMR) Spectroscopy

Nuclear magnetic resonance spectroscopy is an invaluable technique for determining the chemical composition, structure, and end-functionality of polymers.

Theory[39,40]

Nuclear magnetic resonance spectroscopy relies on the magnetic properties of atomic nuclei. In particular, nuclei with a spin quantum number I = ½, such as ^{1}H, ^{13}C, ^{9}F and ^{31}P, are important for NMR spectroscopy. When placed in an external magnetic field, these nuclei align either with or against the magnetic field. Nuclei aligned with the magnetic field are in a low-energy state while nuclei aligned against the magnetic field are in a high-energy state. The fundamental resonance frequency (υ_o) of a nucleus is proportional to the strength of the magnet and corresponds to the amount of energy required to flip a nucleus from the low-energy state to the high-energy state,

$$\upsilon_o = \frac{\gamma B_o}{2\pi} \tag{8}$$

in which γ is the strength of the nuclear magnet (magnetogyric ratio) and B_o is the strength of the applied magnet. The resonant frequency not only depends on the type of nucleus, but also on the position of the nucleus within the molecule. Adjacent nuclei locally modify the magnetic field, giving rise to unique resonant frequencies for each nucleus in the molecule and providing detailed information on the molecular structure.

In a ^{1}H NMR experiment, the nuclei are subjected to strong pulse of radio frequencies near υ_o that aligns all of the nuclei with the magnetic field. The nuclei are

then allowed to relax back to their low energy state and this process is recorded over time. The resulting signal as a function of time is called the free induction decay (FID) and is subjected to a Fast Fourier Transform to convert the data from the time domain to a plot of intensity as a function of frequency (frequency domain). The resulting spectrum contains a peak for each resonant frequency (nucleus) in the sample. Importantly, the measured intensity in a ^{1}H NMR spectrum directly corresponds to the number of protons, allowing for accurate calculations of the molecular composition.

The individual resonant frequencies are described by a chemical shift (δ),

$$\delta = 10^{6}\,(\nu^{sample} - \nu^{ref})/\nu^{ref} \tag{9}$$

in which ν^{sample} and ν^{ref} are the resonant frequencies of the sample and reference, respectively. The value for δ has units of ppm and is independent of the spectrometer used in the experiment, allowing all data to be compared. Typically, chemical shifts are reported relative to the reference compound tetramethylsilane (TMS).

From an application standpoint, note that the signal-to-noise ratio (S/N) in an NMR spectrum is a function of the number of sample scans (NS) [$S/N \propto NS^{1/2}$] and the magnetic field strength (B_0), [$S/N \propto {B_O}^{3/2}$]. Therefore, increasing either of these experimental parameters can improve the signal-to-noise ratio in the resulting spectrum.

Application

In this dissertation, ^{1}H NMR spectroscopy was used to determine the composition of the PB-OH homopolymer and PB-PEO block polymer, as well as to determine the efficiencies of chain-end functionalization reactions (Chapter 9). ^{1}H NMR spectroscopy samples were prepared at a concentration of ~10 mg mL^{-1} in deuterated chloroform containing 0.03 vol% TMS. Proton spectra typically were averaged over 16 scans; however, more scans were used when necessary to increase the signal-to-noise ratio.

Shown in Figure 2.14 is an example ^{1}H NMR spectrum for a PB-OH macroinitiator. The peaks between 4.8 and 5.0 ppm correspond to the protons adjacent to the double bonds. Based on the peak assignments in Figure 2.14, the relative composition of the 1,2 and 1,4 PB regioisomers can be determined. Also, the peak at ~3.6 ppm corresponds to the protons adjacent to the hydroxyl end-group, and often overlaps with trace amounts of THF in the sample. To reliably integrate this peak for end-group analysis, PB-OH was treated with trifluoroacetic anhydride (TFAA), which shifts the peak to 4.4 ppm.[41-43] The degree of polymerization calculated from ^{1}H NMR was compared with the results from MALDI-TOF MS to confirm that the hydroxyl end-capping reaction was essentially 100% efficient.

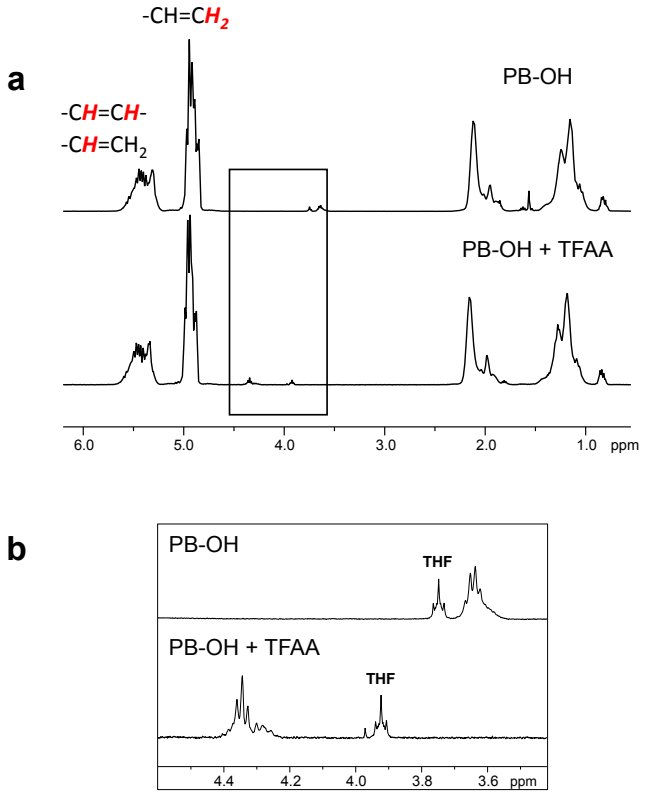

Figure 2.14 Representative ^{1}H NMR spectra for PB-OH homopolymer. (a) Full spectra showing protons used to determine the relative ratios of 1,2 and 1,4 PB regioisomers and (b) zoomed in spectra showing the downfield shift of protons adjacent to the hydroxyl group after treating the samples with TFAA.

^{1}H NMR spectroscopy also was used to determine the composition of the PB-PEO polymers (Figure 2.15) by comparing the peak integrations at ~3.6 ppm corresponding to the PEO backbone with the peak integrations corresponding to double bonds within the PB. The composition of the PB-*d*PEO polymer could not be directly determined from ^{1}H NMR, so a known mass of the block polymer was blended with a known mass of PEO homopolymer and the PB-*d*PEO composition was back-calculated from the composition of the blend measured by ^{1}H NMR.

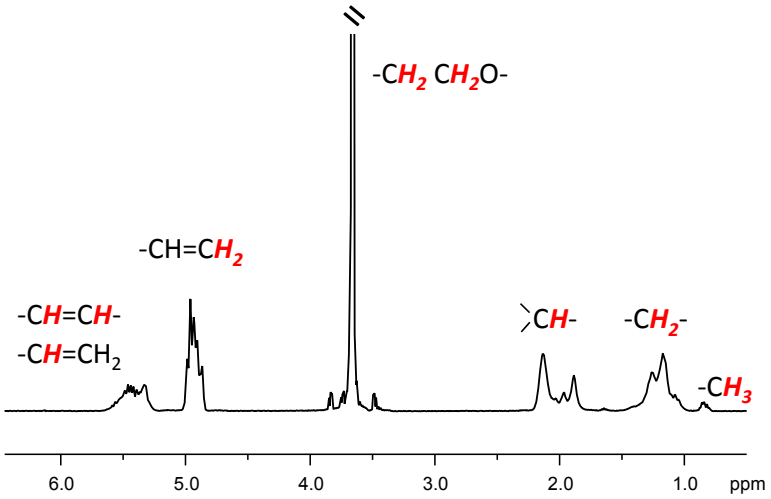

Figure 2.15 **^{1}H NMR spectrum for a poly(butadiene-*b*-ethylene oxide) (PB-PEO) block polymer, with the peak assignments shown above. Note that the PEO peak at 3.7 ppm was clipped vertically.**

2.3 Summary

This chapter provided an overview of macromolecular synthesis techniques to create well-defined block polymers and peptides with controlled compositions and high purities. These materials were characterized using complementary analysis methods to ensure accurate determinations of the molecular compositions and purities. The ability to control the block polymer molecular weight and composition with such accuracy was essential for synthesizing PB-PEO and corresponding PB-*d*PEO polymers necessary for studying the structure and dynamics of solution assemblies described in the following chapters (Chapters 5 through 8). Moreover, the synergistic use of the synthesis and chemical characterization methods described here provided the foundation for synthesizing novel polymer-peptide conjugates with controlled chain architectures presented in Chapter 9.

REFERENCES

1 Szwarc, M. (1956), *Nature* **178**, 1168-1169

2 Szwarc, M., Levy, M. & Milkovich, R. (1956), *Journal of the American Chemical Society* **78**, 2656-2657

3 Hsieh Henry, L. in *Applications of Anionic Polymerization Research* Vol. 696 *ACS Symposium Series* Ch. 2, 28-33 American Chemical Society, 1998.

4 http://www.kraton.com/about/history.php.

5 Odian, G. *Principles of Polymerization*. 4th edn, John Wiley & Sons, Inc, 2004.

6 Young, R. J. & Lovell, P. A. *Introduction to Polymers*. 2nd edn, CRC Press, 1991.

7 Hillmyer, M. A. & Bates, F. S. (1996), *Macromolecules* **29**, 6994-7002

8 Hiemenz, P. C. & Lodge, T. P. *Polymer Chemistry*. 2nd edn, CRC Press, 2007.

9 Fetters, L. J., Lohse, D. J., Richter, D., Witten, T. A. & Zirkel, A. (1994), *Macromolecules* **27**, 4639-4647

10 Won, Y.-Y., Brannan, A. K., Davis, H. T. & Bates, F. S. (2002), *The Journal of Physical Chemistry B* **106**, 3354-3364

11 Lotti, L., Coiai, S., Ciardelli, F., Galimberti, M. & Passaglia, E. (2009), *Macromolecular Chemistry and Physics* **210**, 1471-1483

12 Morton, M., Falvo, L. A. & Fetters, L. J. (1972), *Journal of Polymer Science Part B: Polymer Physics* **10**, 561-&

13 Cabasso, I. & Zilkha, A. (1974), *Journal of Macromolecular Science-Chemistry* **A 8**, 1313-1324

14 Quirk, R. P. & Ma, J. J. (1988), *Journal of Polymer Science Part A: Polymer Chemistry* **26**, 2031-2037

15 Young, R. N., Quirk, R. P. & Fetters, L. J. (1984), *Advances in Polymer Science* **56**, 1-90

16 Gee, G., Higginson, W. C., Taylor, K. J. & Trenholm, M. W. (1961), *Journal of the Chemical Society*, 4298-4303

17 Merrifield, R. B. (1963), *Journal of the American Chemical Society* **85**, 2149-2154

18 Chan, W. C. & White, P. D. *Fmoc Solid Phase Peptide Synthesis*. Oxford University Press, 2000.

19 http://www.nobelprize.org/nobel_prizes/chemistry/laureates/1984/press.html.

20 Verlander, M. (2007), *Int J Pept Res Ther* **13**, 75-82

21 Marder, O. & Albericio, F. (2003), *Chimica Oggi-Chemistry Today* **21**, 35-40

22 Kaspar, A. A. & Reichert, J. M. (2013), *Drug Discovery Today* **18**, 807-817

23 Merrifield, R. B. (1964), *Biochemistry* **3**, 1385-1390

24 Merrifield, R. B. (1964), *Journal of the American Chemical Society* **86**, 304-305

25 Harris, D. C. *Quatitative Chemical Analysis*. 7th edn, W. H. Freeman and Company.

26 Rubinstein, M. & Colby, R. H. *Polymer Physics*. Oxford, 2008.

27 Byrnes, M. in *Peptide Analysis Protocols* Vol. 36 *Methods in Molecular Biology* (eds BenM Dunn & MichaelW Pennington) Ch. 4, 37-52 Humana Press, 1994.

28 Aksenov, A. A. & Bier, M. E. (2008), *Journal of the American Society for Mass Spectrometry* **19**, 219-230

29 Arnould, M. A., Polce, M. J., Quirk, R. P. & Wesdemiotis, C. (2004), *International Journal of Mass Spectrometry* **238**, 245-255

30 Choi, S.-S. & Ha, S.-H. (2008), *Macromol. Res.* **16**, 108-112

31 Danis, P. O., Karr, D. E., Xiong, Y. S. & Owens, K. G. (1996), *Rapid Communications in Mass Spectrometry* **10**, 862-868

32 Hoteling, A. J., Erb, W. J., Tyson, R. J. & Owens, K. G. (2004), *Analytical Chemistry* **76**, 5157-5164

33 Nielen, M. W. F. (1999), *Mass Spectrometry Reviews* **18**, 309-344

34 Quirk, R. P., Gomochak, D. L., Wesdemiotis, C. & Arnould, M. A. (2003), *Journal of Polymer Science Part A: Polymer Chemistry* **41**, 947-957

35 Quirk, R. P., Kim, Y. J., Guo, Y., Wesdemiotis, C. & Arnould, M. A. (2006), *Journal of Polymer Science Part A: Polymer Chemistry* **44**, 2684-2693

36 Quirk, R. P., Gomochak, D. L., Wesdemiotis, C. & Arnould, M. A. (2002), *Abstracts of Papers of the American Chemical Society* **224**, U489-U489

37 Gibson, D. & E. Costello, C. in *Separation Science and Technology* Vol. Volume 2 (ed Ahuja Satinder) 299-327 Academic Press, 2000.

38 http://maldi.nist.gov/.

39 Jacobsen, N. E. *NMR Spectroscopy Explained*. John Wiley & Sons, Inc., 2007.

40 Ibbett, R. N. *NMR Spectroscopy of polymers*. Blackie Academic & Professional 1993.

41 Goldwasser, J. M. & Adolph, H. G. (1986), *Polymer Engineering and Science* **26**, 1510-1513

42 Skutnik, J. M., Assink, R. A. & Celina, M. (2004), *Polymer* **45**, 7463-7469

43 Wang, Y. B. & Hillmyer, M. A. (2000), *Macromolecules* **33**, 7395-7403

Chapter 3

CHARACTERIZATION TECHNIQUES

This chapter describes the characterization techniques used to study the solution assembly of amphiphilic block polymers. The concepts underlying these techniques are described here and the detailed results are presented in the following chapters. Importantly, the complementary use of the techniques described in this chapter provided valuable insights into the structure and dynamics of block polymer solution assemblies.

3.1 Scattering Techniques

Scattering techniques are an invaluable tool for characterizing solution assemblies.[1-3] Scattering methods describe a change in the direction of a traveling wave due to a change in the properties of the surrounding medium.[4] The changes in the surrounding medium may be due to changes in refractive index (light), electron density (X-rays), or nuclei (neutrons) of the sample; however, the basic principles of scattering apply to all types of radiation. This dissertation utilized two main scattering methods: dynamic light scattering (DLS) and small angle scattering. DLS was accessible in the laboratory and quickly provided quantitative information on the micelle sizes and size distributions.[5] DLS was a crucial technique for screening the effects of processing techniques on block polymer assemblies and was used to select samples for more in-depth studies. More detailed nanostructure characterizations then were performed using both small angle X-ray scattering (SAXS) and small angle

neutron scattering (SANS) experiments completed at several national laboratories including the Advanced Photon Source at Argonne National Laboratory (APS in Lemont, IL), the National Institute of Standards and Technology Center for Neutron Research (NCNR in Gaithersburg, MD), and the High Flux Isotope Reactor at Oak Ridge National Laboratory (HFIR in Oak Ridge, TN).

The Scattering Vector (q)

When an incident beam of radiation (light, X-rays, or neutrons) interacts with an ordered crystal lattice, two phenomena occur: (1) scattering of the incident wavevectors and (2) interference among the waves caused by the scattering events.[3] These events are illustrated by the classic Bragg diffraction experiment (Figure 3.1a). The wave scattered from the bottom plane (B), has to travel further to the detector than the wave scattered from the top plane (A).[3,4] Based on geometry, this extra distance is 2d sin (θ/2). The scattered waves will only be in phase if the extra distance traveled is an integer number of wavelengths, nλ, a phenomenon referred to as constructive interference (Figure 3.1b). If the waves are out of phase, their scattered amplitudes will cancel and thus not contribute to the measured scattering, which is referred to as destructive interference. Accordingly, the measured scattering must be related to the spacing between the planes,

$$n\lambda = 2d\sin(\theta/2) \quad (1)$$

in which n is an integer and θ is the scattered angle. Equation 1 also directly illustrates how scattered waves can be related to a structural property of the sample, *i.e.* the crystal lattice spacing.

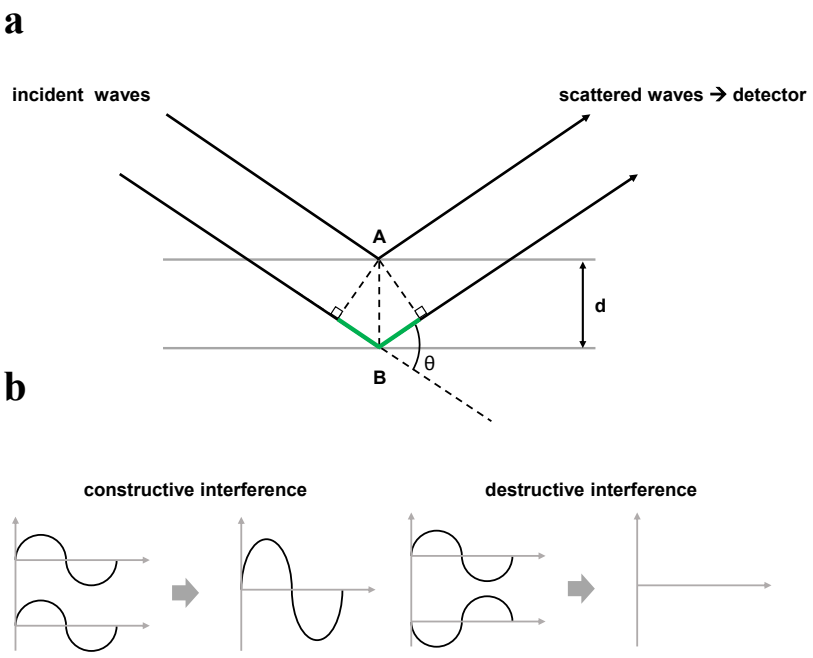

Figure 3.1 Schematic representation of (a) Bragg scattering and (b) constructive and deconstructive wave interference. Adapted from Higgins and Benoit.[3]

The Bragg scattering event in Figure 3.1 is presented in the form of wavevectors in Figure 3.2, in which an incident wavevector, $\mathbf{k}_i$, with magnitude $2\pi/\lambda$ is scattered by the sample. Assuming elastic scattering (*i.e.* the radiation wave does not exchange energy with the sample), the magnitude of the wavevector is unchanged and only the direction is altered. Accordingly, the final wavevector, $\mathbf{k}_f$, has the same

magnitude as $\mathbf{k_i}$. The wavevector change, $\boldsymbol{q} = \mathbf{k}_f - \mathbf{k}_i$, is referred to as the scattering vector or momentum transfer and can be described by,

$$|\boldsymbol{q}| = q = \frac{4\pi}{\lambda}\sin(\theta/2) \tag{2}$$

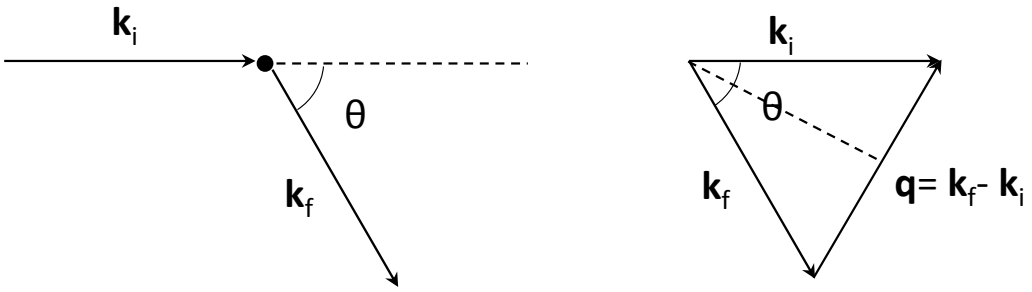

Figure 3.2 Relationship between wavevectors and scattering vector (q) in elastic scattering.

Substituting the expression for q into the Bragg's law (Equation 1) illustrates that the scattering vector is inversely related to the spacing of the planes,

$$2\pi/q = d/n \tag{3}$$

meaning larger objects scatter at smaller q. Accordingly, the length scales probed by the scattering experiment are dictated by the choice of q (which is determined by choice of λ and θ), and all scattering equations are described in terms of q. Scattering that is independent of q is referred to as incoherent scattering, while scattering that

depends on q is referred to as coherent scattering (*i.e.* the scattering waves are in phase) and provides information on the spatial correlations within the sample.[4]

3.1.1 Dynamic Light Scattering (DLS)

Theory

The instantaneous scattered intensity is a function of the particle arrangement in solution. As the particles diffuse through solution, the scattered intensity fluctuates over time (Figure 3.3). These fluctuations in intensity are mathematically related through the intensity autocorrelation function $G_2(\tau)$,

$$G_2(\tau) = \frac{1}{t'}\int_0^{t'} I(t)I(t+\tau)\,d\tau \tag{4}$$

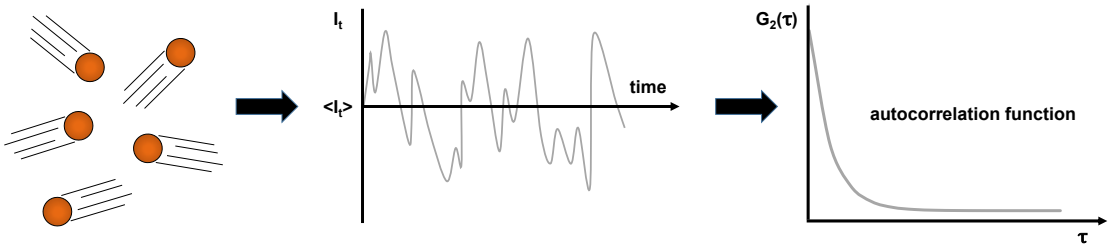

Figure 3.3 Schematic representation of a dynamic light scattering (DLS) experiment. The diffusive motions of the particles lead to fluctuations in the measured intensity (I_t) about its average ($<I_t>$). These fluctuations are related mathematically through the time autocorrelation function.

The experimentally measured intensity correlation function [$G_2(\tau)$] can be related to the electric field correlation function, $G_1(\tau)$ by the Siegert relationship

$$G_2(\tau) = B[1 + \beta|G_1|^2] \tag{5}$$

in which B is the baseline and β is an instrument-specific constant.[6] The electric field correlation function [$G_1(\tau)$] describes the correlation particle movements, and decays exponentially in time with a decay constant, Γ

$$G_1(\tau) = \exp(-\Gamma t) \tag{6}$$

For particles undergoing Brownian motion, the decay constant is related to the diffusivity ($\mathcal{D}$) according to

$$\Gamma = -\mathcal{D}q^2 \tag{7}$$

in which q^2 is the scattering vector modulus and is reflective of the distance traveled by the particles. In light scattering, the scattering vector accounts for solvent-induced changes in the wavelength by incorporating the refractive index of the solvent as

$$q = \frac{4\pi n}{\lambda}\sin(\theta/2) \tag{8}$$

in which n is the refractive index of the solvent.[4]

Assuming the particles are monodisperse and spherical, the diffusivity is then related to the particle radius according to the Stokes-Einstein equation

$$\mathcal{D} = \frac{kT}{6\pi\eta R} \tag{9}$$

in which k is the Boltzmann constant, T is temperature, η is the solvent viscosity and R is the particle radius. Accordingly, larger particles diffuse more slowly and the correlation function decays more slowly, as depicted in Figure 3.4.

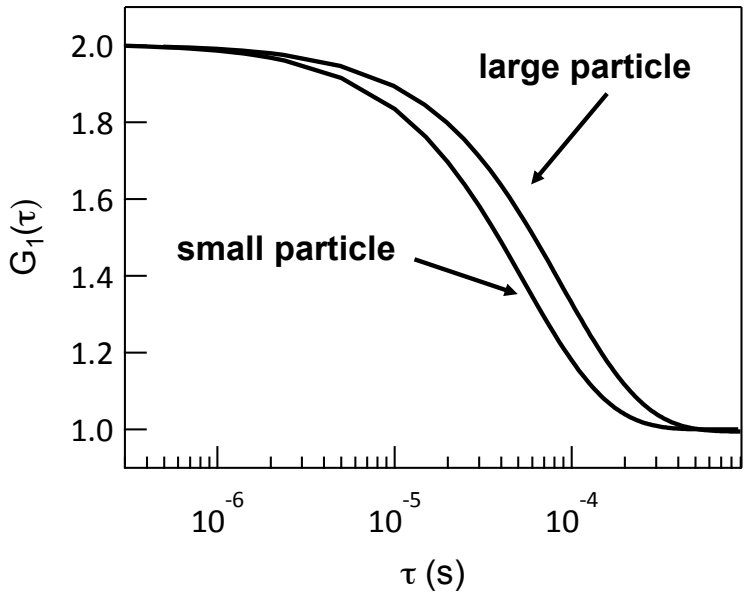

Figure 3.4 Comparison of correlation functions for small and large particles. The larger particles diffuse slower, leading to longer correlation times and a slower decay of the correlation function.

However, in most experimental systems, the particles are not perfectly monodisperse and the measured decay is the ***intensity-weighted*** sum of the individual particle decay functions,

$$G_1(\tau) = \sum_i A_i \exp(-\Gamma_i \tau) \tag{10}$$

in which A_i is the intensity-weight coefficient, and $A_i \propto c_i M_i P_i$ in which c_i and M_i are the concentration and molecular weight of the species, respectively, and P_i is the form factor of the particle (related to the shape; see Section 3.1.2). There are several models to account for polydispersity in DLS data One of the simplest models is the cumulant expansion which assumes that there is a monomodal distribution of particles that can be described by a Gaussian-like distribution,[7,8]

$$G_1(\tau) = \exp(-\bar{\Gamma}\tau)\left(1 + \frac{\mu_2}{2!}\tau^2 + \cdots\right) \tag{11}$$

in which $\bar{\Gamma}$ is the average decay constant (used to calculate the average hydrodynamic radius $<R_h>$) and the second term is related to the polydispersity of the sample. While higher order terms can be included into the cumulant expansion, the second order expansion usually captures the decay in a correlation function and provides valuable information on the size and size distribution of particles in solution.

For samples with a broad distribution of sizes or multimodal distributions, more complex fitting functions are required. One function is the CONTIN method available in commercial DLS software packages which selects the distribution that best fits the correlation function through numerical methods.[9-11] While this fitting

method can be very powerful, it is an ill-posed problem meaning that there is not a unique solution and multiple distributions can provide the same quality of fit to the data. As a result, the fitted size distribution does not always provide an accurate representation of the actual size distribution of the particles in solution.[5]

Application

DLS was used throughout this dissertation to understand the effects of common processing conditions on the size and size distribution in block polymer micelles. Experiments were performed using either a 488, 513, or 633 nm (blue, green, or red, respectively) laser coupled with a goniometer (Figure 3.5). The temperature of the sample was maintained at 25 °C. Data were typically collected at a scattering angle of 90°. In some experiments, the scattering angle was varied from 20° to 140° to determine whether or not the particles in a given sample were spherical (Equation 7).

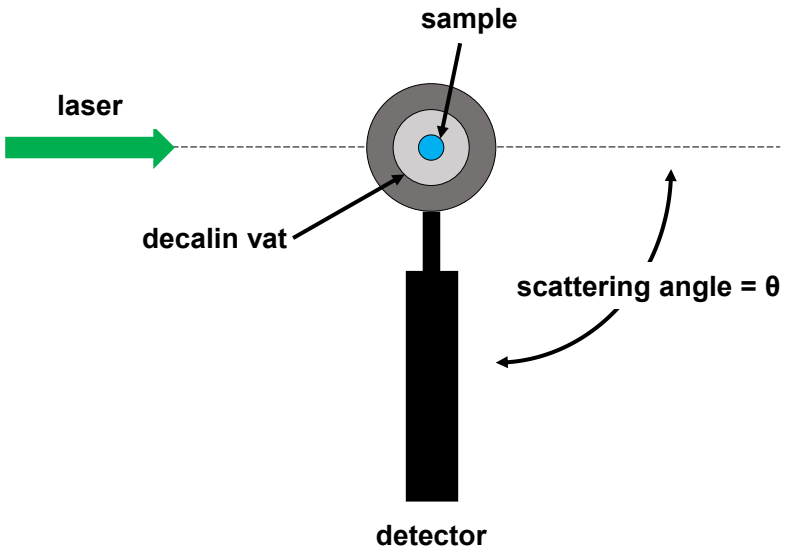

Figure 3.5 Schematic representation of laser light scattering instrument.

In properly designed experiments, DLS provides reliable quantitative information on the micelle size; however, there are several things to consider during sample preparation as well as data collection and analysis. The DLS theory described above assumes that all of the scattering events are independent (*i.e.* no multiple scattering); accordingly, DLS analyses were always performed on dilute samples. Also, it is important to note that the theories described above are for Rayleigh scattering, which assumes that the particles are much smaller than the wavelength of light. DLS does not provide accurate size information for large particles with radii approaching the wavelength of the laser $R \approx \lambda$.[1]

As depicted in Figure 3.4, a correlation function should plateau at short and long correlation times. Accordingly, the range of correlation times (τ) was selected to capture the entire relaxation function during the DLS experiment. The measured correlation functions were analyzed with either the second order cumulant or CONTIN

method described above. Both analysis methods provided the average hydrodynamic radii $\langle R_h \rangle$ of the micelles; however, the exact size distributions could not be determined using DLS. Importantly, DLS measured the *intensity-weighted* size, which made the results highly sensitive to a small number of large particles or aggregates in solution. This sensitivity further complicated efforts to determine the exact size distribution from DLS, particularly in Chapter 7 that studied a bimodal distribution of micelle sizes. DLS analysis was not sufficiently sensitive to the bimodal distribution and necessitated additional characterization methods to effectively capture the changing sizes in the micelle population.

3.1.2 Small Angle X-ray and Neutron Scattering (SAXS and SANS)

Theory

Probing the detailed structural characteristics of block polymer assemblies on length scales ranging from 1 to 100 nm requires very small scattering angles ($\theta < 5°$), making small angle scattering methods an ideal tool for probing solution assemblies.[2,3,12] The measured scattered intensity is a function of

$$I(q) = \phi \Delta\rho^2 P(q) S(q) \tag{12}$$

in which ϕ is the volume fraction of scatterer, $\Delta\rho$ is the scattering contrast, $P(q)$ is the form factor, and $S(q)$ is the structure factor. The form factor describes scattering interference between different parts of the same particle and hence provides information on the shape of that particle, whereas the structure factor describes scattering interference between different particles and hence provides information on

the particle-particle interactions in the system. In dilute solution with no interparticle interactions, such as the samples studied in this dissertation, $S(q) = 1$.

The basic scattering and interference effects apply to both X-ray and neutron scattering; however, the way radiation interacts with a material, and consequently, the scattering contrast ($\Delta\rho$) is different for the two methods.

Contrast in Scattering

X-rays interact with individual electrons and the scattering is due to the electron density distribution within the material. The X-ray scattering length density ρ_e of a material can be calculated according to

$$\rho_e = \frac{\sum_{i=1}^{n} Z_i r_e}{v_m} \tag{13}$$

in which Z_i is the atomic number of the ith element, $r_e = 2.81 \times 10^{-13}$ cm is the radius of the electron, and v_m is the molecular volume of the sample.[2] Accordingly, the scattering length density of a material increases with its atomic number. The X-ray scattering contrast is defined as the scattering length density difference between the sample and the surrounding solvent, $\Delta\rho = \rho_{e,\,sample} - \rho_{e,\,solvent}$.

Neutrons interact with the nucleus of the atom and the scattering is due to the distribution of nuclei within the sample.[2] Similar to above, the neutron scattering length density, ρ_n, can be calculated by

$$\rho_n = \frac{\sum_{i=1}^{n} b_c}{v_m} \tag{14}$$

in which b_c is the coherent nuclear scattering length. The nuclear scattering length varies randomly across the periodic table and also varies between isotopes of the same element. A particularly useful example of these isotopic variations is the difference between hydrogen and deuterium, which have coherent scattering lengths of -3.74×10^{-5} Å and 6.67×10^{-5} Å, respectively. These vastly different scattering lengths mean that the contrast in the system can be tuned by varying the hydrogen and deuterium content in the sample, a method referred to as contrast variation. Using this approach, parts of the structure can be matched to the surrounding solvent (Figure 3.6), proving detailed structural information on specific nanoscale features. The ability to hone in on specific structural details through contrast variation is a key advantage to neutron scattering *vs.* X-ray- or light-based methods.[3,12]

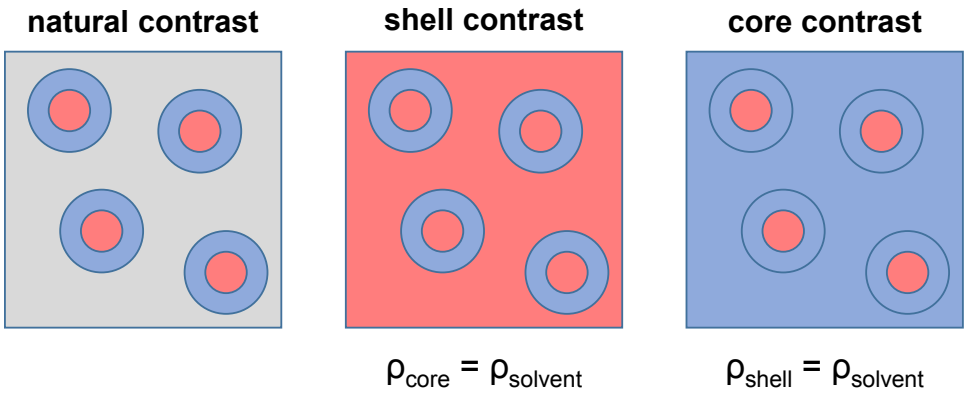

Figure 3.6 Schematic representation of the effects of contrast variation on the measured structure of a core-shell particle in a SANS experiment.

Experimental Set-up

A typical small angle scattering instrument is schematically represented in Figure 3.7. A monochromatic beam from the radiation source (either X-rays or neutrons) is collimated by a series of apertures. The incident beam then is scattered by the sample, and the scattered X-rays or neutrons are collected by a 2-D detector. Often times, the detector position can be moved to capture the scattering at different angles (*e.g.* length scales) of interest. Longer detector distances measure smaller scattering angles, which correspond to smaller q values (or larger structures). The 2-D scattering pattern then is azimuthally integrated, giving a 1-D scattering pattern that is plotted as the scattered intensity as a function of q.

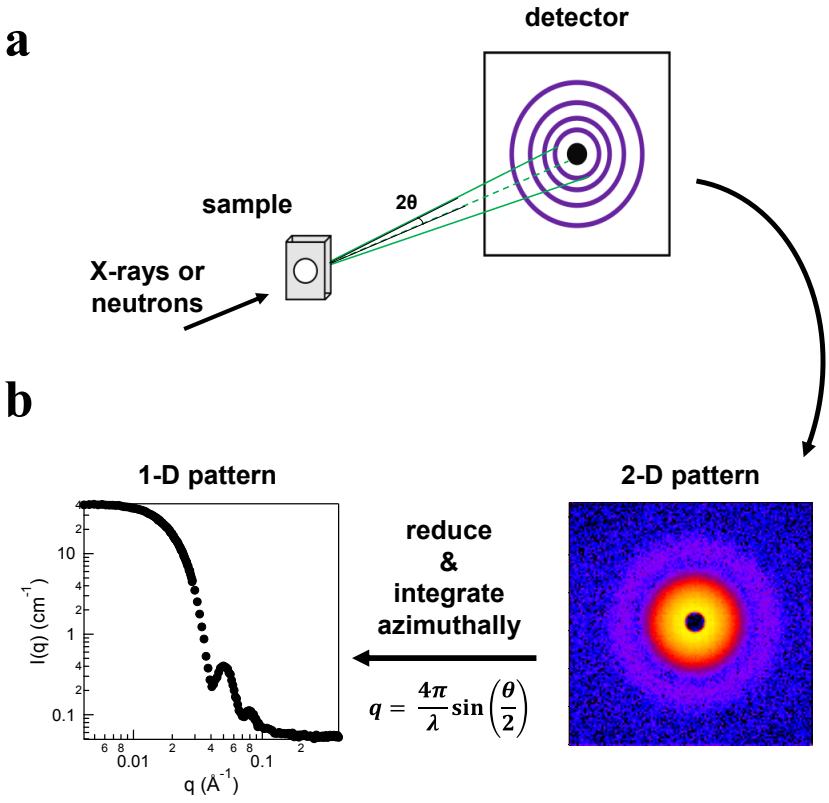

Figure 3.7 Schematic representation of a small angle scattering experiment. (a) Diagram of instrument in which the incident beam is scattering by the sample and the scattering is measured by a 2-D detector. (b) The 2-D scattering data are reduced and integrated azimuthally to yield the 1-D scattered intensity *vs. q*.

Data Analysis

The 1-D scattering data is analyzed to extract information regarding the sample's structure. There are two basic categories of scattering data analysis: model-independent and model-dependent. In model-independent analysis, the data are directly manipulated to yield structural information regarding the sample, while in model-dependent analysis, mathematical models that describe the sample structure are constructed and then used to fit the data.[2,3] In this dissertation, scattering data were

first analyzed with model-independent methods to obtain basic information on the size and structure of the sample, and this information was used to guide model-dependent analyses. It is important to obtain as much structural information about the sample as possible before beginning model-dependent analysis to ensure the fitting results are physically reasonable and to extract the most information from the scattering experiments.

A representative 1-D scattering plot for a sphere is presented in Figure 3.8 and discussed in the context of model-independent and model-dependent analyses.

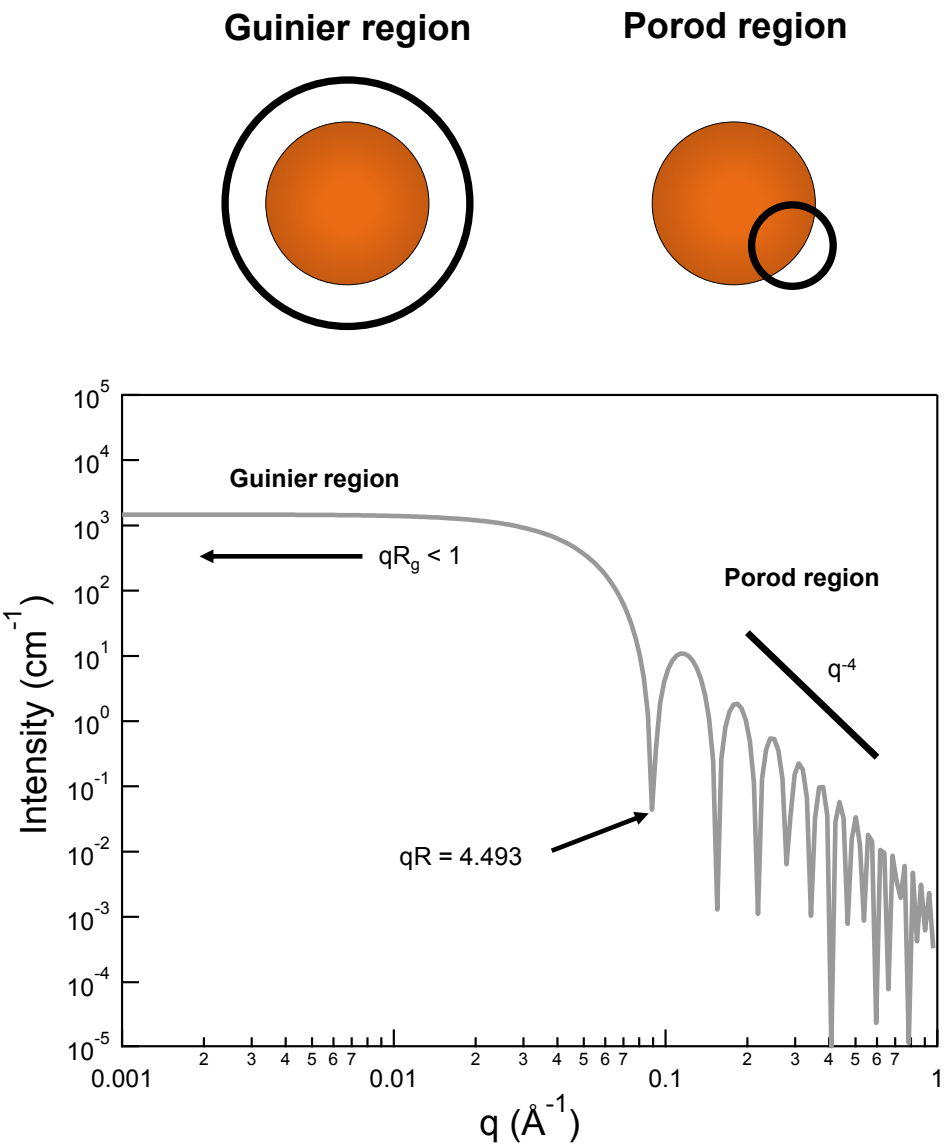

Figure 3.8 Representative scattering data for a solid sphere with a radius, R = 5 nm.

Model-independent Analysis

The Guinier and Porod analyses can be used to obtain information on the large and small length scales of the scattering object, respectively, as depicted in Figure 3.8. The Guinier approximation applies at low q in which the scattering is characteristic of the entire object,

$$I(q) = I_0 \exp\left(-\frac{q^2 {R_g}^2}{3}\right) \tag{15}$$

$$\ln[I(q)] = \ln[I_0] - \frac{q^2 {R_g}^2}{3} \tag{16}$$

in which I_0 is the absolute intensity extrapolated to $q \rightarrow 0$ and R_g is the radius of gyration of the scatterer. Accordingly, R_g can be determined directly by plotting the $\ln[I(q)]$ *vs.* q^2. Note that this assumption is only valid at $qR_g << 1$, such that the entire length scale of the object was probed by the scattering experiment.

According to the Porod Law, the scattering at high q is a function of the surface of the sample,

$$I(q) \propto q^{-n} \tag{17}$$

in which n is the Porod exponent. A Porod exponent of $n = 1$ corresponds to a 1-D object such as rigid cylinders, whereas $n = 2$ corresponds to a 2-D object such as large vesicles and $n = 4$ corresponds to a 3-D object such as spheres. A Porod plot is

constructed by plotting log[$I(q) - B$] *vs.* log(q), in which B is the incoherent background and the slope corresponds to the Porod exponent.

Model-dependent Analysis[2]

The amplitude of the scattered X-rays or neutrons [$A(q)$] is related to the distribution of scatters within the sample and can be described in terms of the scattering length density distribution $\rho(r)$

$$A(q) = \int_V \rho(r) e^{iqr} dr \tag{18}$$

For the solid sphere presented in Figure 3.8, the real-space radial scattering length density profile is defined as

$$\begin{aligned} \rho(r) &= \rho_0 \quad for\ r \leq R \\ \rho(r) &= 0 \quad for\ r > R \end{aligned} \tag{19}$$

Substituting the expression for the scattering length density distribution into Equation 18 and then evaluating the three-dimensional Fourier transform to transform from real-space to reciprocal space yields

$$\begin{aligned} A(q) &= \frac{\rho_0}{q} \int_0^R \rho(r) 4\pi r^2 \frac{\sin qr}{qr} dr \\ &= \rho_0 v \frac{3(\sin qR - qR \cos qR)}{(qR)^3} \end{aligned} \tag{20}$$

in which v is the volume of the sphere, and R is the sphere radius. The scattering intensity, $I(q)$, is given by the square of the scattering amplitude

$$I(q) = [A(q)]^2 = {\rho_0}^2 v^2 \frac{9(\sin qR - qR\cos qR)^2}{(qR)^6} \quad (21)$$

As seen in by Equation 21, the scattered intensity is a periodic function of q. The sphere radius then can be determined by the intensity minima in the 1-D scattering pattern (Figure 3.8), qR = 4.493, 7.725, 10.90…, which correspond to the zeroes of the $I(q)$ function. The general method for calculating the scattering amplitude described for a sphere can be extended to more complex scattering length density profiles, making model-dependent data analysis a powerful method for probing the structure of solution assemblies. A form factor model for spherical block polymer micelles is discussed in more detail in Chapters 4 and 5.

Application

SAXS

SAXS experiments were performed at the APS on either the 12-ID-C or DND-CAT beamlines. Samples were prepared in thin quartz capillaries (diameter = 1.5 mm), and scattering data were collected for 60 s. Micelle sizes were determined from the location of the first maxima in the scattering curve using the relationship qR = 5.763, in which R is the micelle radius derived from Equation 21.[2]

SANS

SANS experiments were performed at the NCNR on both the NG-3 and NG-7 30 m SANS lines. Samples generally were prepared in D_2O to minimize the incoherent background scattering from the solvent. Samples were loaded into 1 mm path length demountable cells for the scattering experiments. Typically, data were collected at three detector distances to cover an approximate q-range of 0.004 $Å^{-1} < q < 0.4$ $Å^{-1}$. Before running each experiment, data were collected for 5 min at the longest sample-to-detector distance determine the scattering count rate. The total run time for each detector distance was calculated based on the count rates, such that the total number of counts was approximately 10^6, 5×10^5, and 2.5×10^5 for the short, middle, and long detector distance, respectively. The transmission of each sample also was measured at the longest detector distance, as this value was needed to reduce the data.

All scattering data were reduced and converted to absolute intensity using the standard procedures provided by NIST.[13] The sample data were corrected for the background and empty cell scattering:

$$I_{corrected} = \left(I_{sample} - I_{bkgd} \right) - \frac{T_{sample}}{T_{empty}} \left(I_{empty} - I_{bkg} \right) \qquad (22)$$

in which $I_{corrected}$, I_{sample}, I_{bkgd}, and I_{empty} were the scattering data for the corrected sample, raw sample, background, and empty cell, respectively, and T_{sample} and T_{empty} were the measured transmission for the sample and empty cell, respectively. The data were further corrected for the detector sensitivity, converted to an absolute intensity based on the scattering from the attenuated open beam, and then azimuthally

integrated to yield the 1-D scattering patterns. Data were analyzed using the general methodology described above, and more detailed information on the form factor models are described in the following chapters.

3.2 Cryogenic Transmission Electron Microscopy (cryo-TEM)

Transmission electron microscopy (TEM) provides unparalleled insights into block polymer morphologies by enabling direct visualization of the nanoscale structures. TEM has long been used to visualize bulk block polymer morphologies on nanometer length scales, and the development of cryogenic transmission electron microscopy (cryo-TEM) has made this technique central to characterizing solution assemblies as well. Cryo-TEM provides detailed information on individual nanostructures, making it an invaluable technique for understanding coexisting structures or capturing short-lived intermediate structures that cannot be resolved with other characterization methods.[14-16]

Theory

In TEM, a monochromatic electron beam is focused onto the sample under high vacuum conditions to prevent scattering of the beam by air or other contaminants.[17] The beam is refined by a series of lenses and apertures, and the lenses control the focus and magnification. As the electron beam passes through the sample, some of the electron are scattered by the atoms in the sample. The scattered electrons are blocked by the objective aperture inserted below the focal plane of the sample, allowing only the direct beam to pass through.[17,18] More electrons are scattered by heavier atoms (based on atomic number) or by a thicker sample, resulting in a darker image. The contrast due to variations in the sample electron density or thickness is

referred to as mass-thickness or amplitude contrast. In polymeric samples, the mass-thickness contrast is usually low as the samples are composed of low molecular weight elements (H, C, O, and N). To improve the contrast in polymeric systems, bulk samples often are stained with heavy metal stains (OsO_4 or RuO_4);[19-21] however, the image contrast in cryo-TEM is enhanced by exploiting phase contrast.[14,15] Phase contrast is caused by interference between the electron waves from unscattered and elastically scattered electrons and is enhanced by imaging the sample at an underfocus.[14,18] However, imaging at an underfocus can change the contrast transfer function (CTF), which reduces the image resolution and leads to image artifacts.[22,23] Accordingly, most cryo-TEM imaging is performed at a nominal underfocus (2 – 10 μm) to enhance the phase contrast without distorting the image.[24-28]

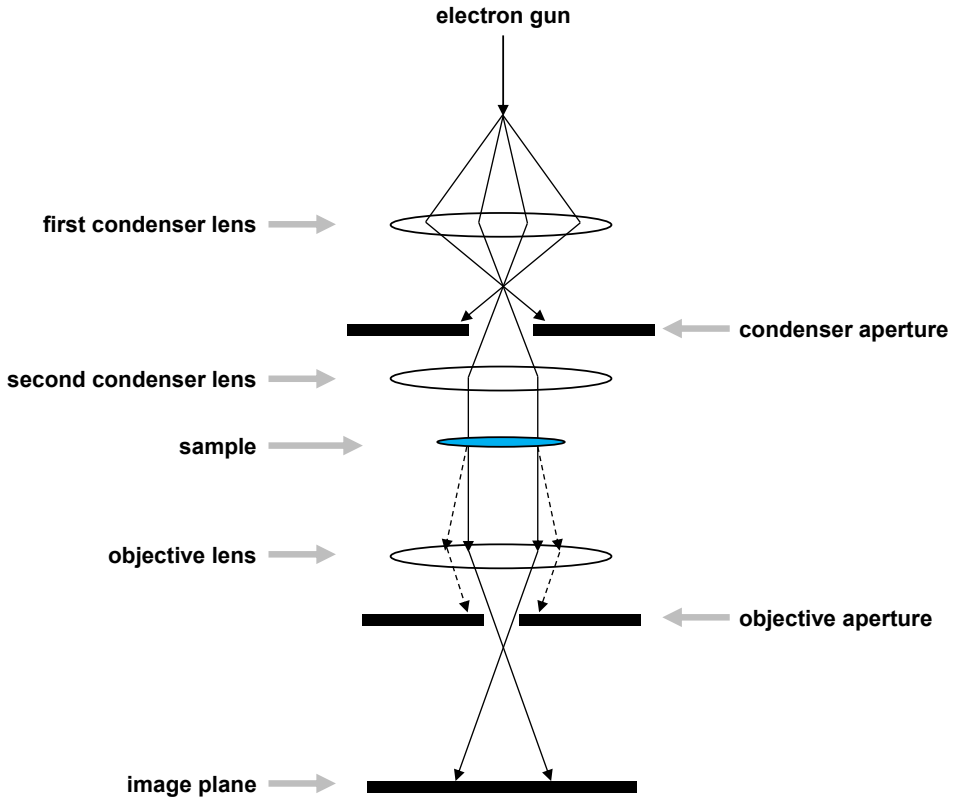

Figure 3.9 Schematic of the important optical components in a conventional TEM instrument. The condenser lenses and aperture focus and align the beam. The objective lens and aperture refocus and filter the beam after it passes through the sample.

Sample Preparation The high vacuum conditions required for TEM imaging are not directly amenable to liquid samples, and obtaining accurate images representative of the solution structure requires careful sample preparation. Most often, solution assembled structures are dried onto a TEM grid and then stained to enhance the contrast. However, the resulting images are not necessarily representative of the structure in solution. Drying and staining can influence the resulting morphology and in some cases, can even lead to misinterpretation of TEM-based data describing

solution assemblies.[14,15,29-31] Recent developments in the use of graphene oxide (GO)-based TEM supports facilitate the imaging of polymeric materials without the need for heavy staining agents.[32] These grids are an attractive alternative to heavy metal staining and enabled the discovery of a drying-induced phenomena in block polymer assemblies.[33]

Ideally, solution assemblies should be imaged in their native environment without compromising their structure. While developments in *in situ* liquid cell TEM holders have enabled direct imaging of block polymer micelles in solution, the polymers need to be covalently labeled with a heavy metal to provide sufficient contrast.[34] Cryo-TEM allows direct visualization of the solution assemblies without the need for a heavy metal stain. Cryo-TEM preserves the solution structure by ultra-fast freezing of the sample and enables direct visualization of the vitrified liquid sample. A droplet of the sample (~ 2 – 10 μL) is pipetted onto a perforated TEM grid. Excess solution then is removed by blotting the grid with a piece of filter paper, resulting in a thin liquid film (~100 to 300 nm) spanning the holes of the grid. The grid is plunged into liquid ethane, cooling the sample at a rate of 10^5 K s^{-1} and vitrifying the liquid.[14,15,35] The sample then is stored in liquid nitrogen until it is transferred to a cryo-holder for examination. The sample is imaged at cryogenic temperature (< -160 °C) and using a low accelerating voltage (typically 120 kV) to enhance the contrast.[14]

Application

Cryo-TEM was used throughout this dissertation to characterize block polymer assemblies and provide structural information that complemented the scattering methods described above. A powerful strategy is to use information extracted from cryo-TEM micrographs as the foundation for more quantitative analysis by SANS, described in Chapters 4 and 7.

Successful grid preparation is crucial to cryo-TEM; however grid preparation is a very tedious and delicate process. In this dissertation, all grids were prepared using an FEI Vitrobot to control the temperature and humidity during sample preparation. The Vitrobot also automates the grid blotting and then plunges the sample into the liquid ethane. Blotting is the most important step in grid preparation and automating this step helps improve the grid reproducibility. Typically, grids were blotted twice for 30 s each. If necessary, the blot number or blot time was adjusted to change the grid thickness. Thinner grids were obtained by increasing the blot number or the blot time. After blotting the sample, the sample was allowed to relax for 30 s (drain time on the Vitrobot) before plunging the grid into liquid ethane to mitigate any potential shear effects.[14]

Two types of grids were used in sample preparation: Quantifoil R2/1 and Quantifoil S7/2. The R2/1 grids have smaller grid holes and often were easier to vitrify, making them ideal for small (<100 nm) structures. The S7/2 have larger grid openings, which was better for imaging large (>200 nm) structures. Also, all grids were plasma cleaned before use to remove any contaminants and to increase the hydrophilicity of the grid.

Grids were transferred to a Gatan cryo holder and then imaged on a Tecnai G2 12 Twin TEM instrument operating at 120 kV. The microscope was allowed to thermally equilibrate for ~20 min after loading a new grid to prevent thermal drift while examining the sample. Initially, the grids were examined at low intensities to prevent beam damage to the sample. For imaging, the intensity was increased and the exposure time was set to 3 - 5 s to improve the image contrast.

There are several potential artifacts to be aware of while imaging cryo-TEM samples, and representative images are presented in Figure 3.10. Poorly vitrified grids (Figure 3.10 a-c) or ethane crystals (Figure 3.10 d) often are seen. Interactions between the electron beam and the sample can lead to radiolysis of the sample (also referred to as beam damage; see Figure 3.10 e). The grid preparation process produces a biconcave film which can lead to packing of the micelles (Figure 3.10 f) or size segregation (Figure 3.11) in which the largest particles are located at the edge of the hole where the ice is the thickest.

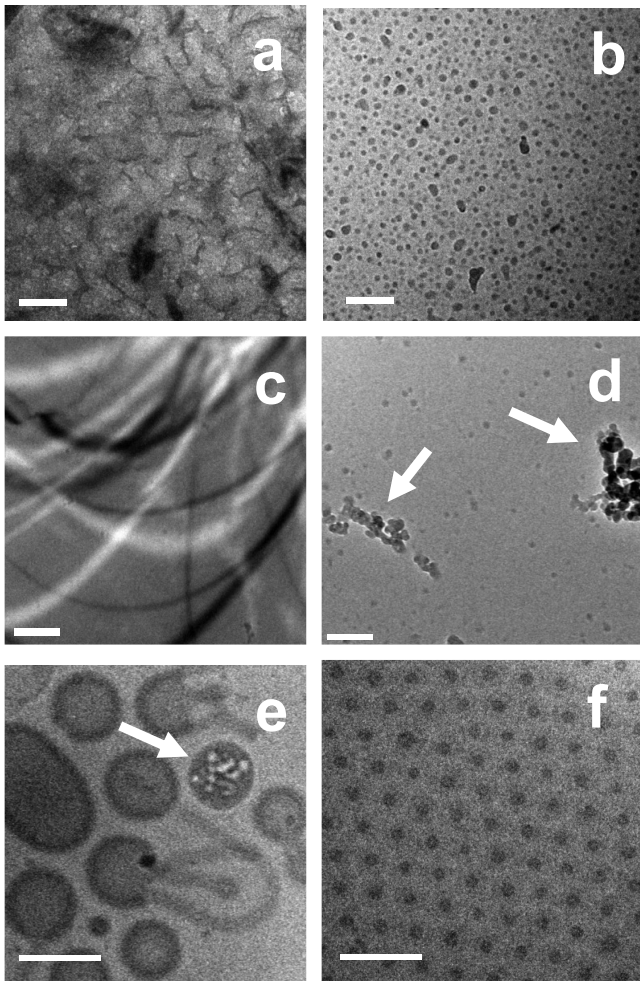

Figure 3.10 **Common artifacts in cryogenic transmission electron microscopy (cryo-TEM): (a-c) poorly vitrified samples (d) ethane crystals (e) beam damage to the sample and (f) hexagonally-packed spherical structures.**

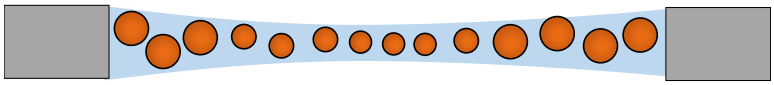

Figure 3.11 **Schematic representation of size segregation of particles due to sample preparation, with larger particles at the edges of the holes and smaller particles in the center.**

3.3 Summary

The complementary use of scattering and microscopy techniques described in this chapter provided valuable insights into the structure and dynamics of block polymer micelles not attainable through other methods. DLS was readily accessible and provided a rapid measure of the micelle sizes. Interesting samples identified using DLS were analyzed further with cryo-TEM to obtain particle-specific structural information. Finally, the structural information obtained from the DLS and cryo-TEM experiments provided the framework for detailed analysis of SAXS and SANS data. This powerful methodology was used to follow dynamic processes occurring over days or even months while simultaneously obtaining key structural information on nanometer length scales.

REFERENCES

1 *Neutron, X-ray, and Light Scattering: Introduction to an Investigative Tool for Colloidal and Polymeric Systems.* Elsevier, 1991.

2 Roe, R.-J. *Methods of X-ray and Neutron Scattering in Polymer Science*. Oxford University Press, 2000.

3 Higgins, J. S. & Benoit, H. C. *Polymers and Neutron Scattering.* Vol. 8 Oxford Science Pubblications, 1996.

4 Hiemenz, P. C. & Lodge, T. P. *Polymer Chemistry*. 2nd edn, CRC Press, 2007.

5 Rubinstein, M. & Colby, R. H. *Polymer Physics*. Oxford, 2008.

6 Berne, B. J. & Pecora, R. *Dynamic Light Scattering with Applications to Chemistry, Biology, and Physics*. Dover Publications, Inc. , 2000.

7 Koppel, D. E. (1972), *The Journal of Chemical Physics* **57**, 4814-4820

8 Frisken, B. J. (2001), *Applied Optics* **40**, 4087-4091

9 Provencher, S. W. (1979), *Makromolekulare Chemie-Macromolecular Chemistry and Physics* **180**, 201-209

10 Provencher, S. W. (1982), *Computer Physics Communications* **27**, 213-227

11 Provencher, S. W. (1982), *Computer Physics Communications* **27**, 229-242

12 Hamley, I. W. *Introduction to Soft Matter: Synthetic and Biological Self-Assembling Materials*. Revised edn, John Wiley & Sons, 2007.

13 Kline, S. R. (2006), *Journal of Applied Crystallography* **39**, 895-900

14 Danino, D. (2012), *Current Opinion in Colloid & Interface Science* **17**, 316-329

15 Cui, H. et al. (2007), *Soft Matter* **3**, 945-955

16 Weissman, H. & Rybtchinski, B. (2012), *Current Opinion in Colloid & Interface Science* **17**, 330-342

17 Williams, D. B. & Carter, C. B. *Transmission electron micrscopy: Basics*. Vol. 1 Springer, 1996.

18 Smith, M. F. & Langmore, J. P. (1992), *Journal of Molecular Biology* **226**, 763-774

19 Sawyer, L. C. & Grubb, D. T. *Polymer Microscopy*. 2nd edn, Chapman & Hall, 1996.

20 Tureau, M. S., Kuan, W.-F., Rong, L., Hsiao, B. S. & Epps, T. H. (2012), *Macromolecules* **45**, 4599-4605

21 Tureau, M. S. & Epps, T. H. (2012), *Macromolecules* **45**, 8347-8355

22 Crassous, J. J., Ballauff, M., Drechsler, M., Schmidt, J. & Talmon, Y. (2006), *Langmuir* **22**, 2403-2406

23 Crassous, J. J. et al. (2009), *Langmuir* **25**, 7862-7871

24 Won, Y.-Y., Brannan, A. K., Davis, H. T. & Bates, F. S. (2002), *The Journal of Physical Chemistry B* **106**, 3354-3364

25 Zheng, Y. et al. (1999), *The Journal of Physical Chemistry B* **103**, 10331-10334

26 Langmore, J. P. & Smith, M. F. (1992), *Ultramicroscopy* **46**, 349-373

27 Smith, M. F. & Langmore, J. P. (1992), *Journal of Molecular Biology* **226**, 763-774

28 Toyoshima, C. & Unwin, N. (1988), *Ultramicroscopy* **25**, 279-291

29 Kilpatrick, P. K., Miller, W. G. & Talmon, Y. (1985), *Journal of Colloid and Interface Science* **107**, 146-158

30 Talmon, Y. (1983), *Journal of Colloid and Interface Science* **93**, 366-382

31 Zhao, H. et al. (2011), *Macromolecular Chemistry and Physics* **212**, 663-672

32 Patterson, J. P. et al. (2012), *Soft Matter* **8**, 3322-3328

33 Petzetakis, N. et al. (2013), *ACS Nano* **7**, 1120-1128

34 Proetto, M. T. et al. (2014), *Journal of the American Chemical Society* **136**, 1162-1165

35 Siegel, D. P., Green, W. J. & Talmon, Y. (1994), *Biophysical Journal* **66**, 402-414

Chapter 4

COMPLEMENTARY METHODS FOR CHARACTERIZING SOLUTION ASSEMBLED STRUCTURES

This chapter demonstrates the complementary use of scattering and microscopy techniques to characterize nanostructures in aqueous solutions. Specifically, cryogenic transmission electron microscopy (cryo-TEM) image analysis and small angle neutron scattering (SANS) data modeling were used to determine the radial density profiles of amphiphilic homopolymer micelles. The structural analysis techniques described in this chapter provide the foundation for *in situ* nanostructure characterization used throughout this dissertation. Part of text and figures are reproduced and adapted with permission from Patterson, J. P., Kelley, E. G., *et al.* *Macromolecules* **2013**, 46, 6319-6325.

4.1 Introduction

As discussed in Chapter 1, the solution assembly of amphiphilic block polymers has attracted significant research attention given their utility in application including drug and gene delivery systems,[1,2] nanoreactors in separation science,[3] and nanoelectronics.[4] The solution self-assembly of another class of amphiphiles, so-called 'associative polymers' or 'amphiphilic homopolymers', also has been studied extensively.[5-26] Examples of these systems include homopolymers in which the monomer units contain both hydrophilic and hydrophobic moieties[6-8] or homopolymers end-functionalized with ionic head groups[12] or small hydrophobic groups, such as alkyl chains.[8,10,11,14,17,23-25] Like amphiphilic diblock or triblock

polymers, these amphiphilic homopolymers have been shown to self-assemble into well-defined structures, making them promising materials for applications that necessitate aqueous solution assembly.[10,22]

Cryo-TEM is a powerful tool for characterizing solution assembled nanostructures and has provided unique insights into nanoscale morphologies as well as self-assembly processes and phase transition behavior.[27-29] While cryo-TEM is used throughout literature to study solution assembled structures,[27-29] fewer reports have demonstrated the utility of this technique for analyzing the radial density distribution of polymeric nanoparticles.[30,31] The detailed density distribution of nanostructures is investigated more often using small angle neutron or X-ray scattering (SANS or SAXS) experiments.[30,32-36] However, as highlighted by Ballauff *et al.*, both cryo-TEM and small angle scattering methods are sensitive to the local density distribution of the sample.[30] By using both SAXS and cryo-TEM micrograph analysis, Ballauff *et al.* showed that quantitative structural information can be determined from cryo-TEM micrographs of colloidal particles.[30] Herein, a similar approach is used and both cryo-TEM micrograph analysis and SANS experiments are exploited to study the solution assembled structure of amphiphilic homopolymers.

This chapter reports a detailed study on the solution assembly behavior of a series of poly(N-isopropylacrylamide) amphiphilic homopolymers using a combination of scattering techniques and cryo-TEM. Importantly, these sulfur-carbon-sulfur (SCS) pincer-functionalized amphiphilic homopolymers are potential precursors to solution-assembled nanoreactors exhibiting catalytic activity. The current work focuses on characterizing the aqueous solution assembly of pincer-functionalized homopolymers with different molecular weights, as the ability to

understand and tailor the self-assembly of these materials will allow for more detailed studies of the effects of nanoreactor nanostructure on catalytic properties.

4.2 Experimental

4.2.1 Materials

Amphiphilic homopolymers end-functionalized with reactive centers for potential catalytic applications were prepared as described in literature.[37,38] The polymers examined in this chapter were synthesized by Dr. Joseph P. Patterson and Prof. Rachel K. O'Reilly at the University of Warwick and are summarized in Table 4.1.

Table 4.1. Amphiphilic homopolymer characterization data

Sample	M_n[a] (kDa)	M_n[b] (kDa)	M_w[c] (kDa)	N_{PNIPAM}[d]	Đ[a]	$f_{hydrophobic}$[e]
4a	11.8	14.2	15.8	120	1.12	0.04
4b	20.3	21.0	25.3	180	1.21	0.03
4c	23.8	30.6	38.5	270	1.24	0.02

[a] From SEC based on poly(methyl methacrylate) standards
[b] Based on end-group analysis from ^{1}H NMR spectroscopy
[c] Calculated from ^{1}H NMR and SEC according to
$M_w = (N_{PNIPAM} M_o + M_{pincer}) * Đ$
[d] Degree of polymerization of PNIPAM block from ^{1}H NMR end-group analysis
[e] Hydrophobic weight fraction calculated from ^{1}H NMR

4.2.2 Micelle Preparation

Micelle solutions were prepared by adding H_2O to the dried polymer powder and stirring overnight. The resulting solutions were filtered through a 0.45 μm nylon filter.

4.2.3 Micelle Characterization

4.2.3.1 Dynamic Light Scattering (DLS)

DLS experiments were performed using a Lexel Laser Inc. 488 nm, 100 mW laser coupled with a Brookhaven Instruments Corporation goniometer. The correlation function was recorded at 90° and analyzed using the quadratic cumulant method. All measurements were performed at 25 °C.

4.2.3.2 Cryogenic Transmission Electron Microscopy (cryo-TEM)

Micelle solutions for cryo-TEM experiments were prepared at concentrations ranging from 2.0 mg mL^{-1} to 5.0 mg mL^{-1}. Samples for cryo-TEM were prepared at 25 °C in a constant humidity environment using a FEI 110 Vitrobot. A 2 - 10 μL droplet of micelle solution was applied to a holey carbon-coated copper grid, and the grid was blotted to remove excess solution. Subsequently, the sample was vitrified by plunging the grid into liquid ethane. Grids were transferred to a Gatan cryo stage and imaged using a Tecnai G2 12 Twin TEM at an accelerating voltage of 120 kV. The temperature of the cryo stage was maintained below -170 °C while imaging the samples.

4.2.3.3 Cryo-TEM Image Analysis

The cryo-TEM micrographs were analyzed using methods adapted from literature.[30] The gray values, $G(r)$, were determined using the Radial Profile Plot plugin in ImageJ,[39] which azimuthally integrates the image intensity as a function of distance, *r*, from the center of the micelle. Profiles of multiple micelles were averaged together from different images (total sample size = 50 micelles). Error bars represent the 95% confidence interval for the averaged gray value at a given *r*. Images for the

profile analysis were acquired close to focus, thus contributions from the contrast transfer function (CTF) were assumed to be negligible.[30]

The profiles were fit according to Equation 1,

$$\frac{G(r)}{G_0} = exp\left(-2K\rho_{corona}(r)\sqrt{R^2 - r^2}\right) \quad (1)$$

in which G_0 is the background gray value, K is a fitting constant, $\rho_{corona}(r)$ is the radial density distribution of polymer in the micelle corona, R is the micelle radius, and r is the distance from the center of the micelle. The radially decreasing corona profile, $\rho_{corona}(r)$, was described by a linear combination of 2 b splines,[34,40]

$$\rho_{corona}(r) = \frac{\rho_1(r) + a\rho_2(r)}{1 + a} \quad (2)$$

in which a is a fitting parameter and ρ_1 and ρ_2 are given below,

$$\rho_1(r) = \frac{4(r - R_c - s)^3 - (r - R_c - 2s)^3}{4s^3} \quad for\ R_c \le r < R_c + s$$

$$\rho_1(r) = \frac{-(r - R_c - 2s)^3}{4s^3} \quad for\ R_c + s \le r < R_c + 2s \quad (3)$$

$$\rho_1(r) = 0 \quad elsewhere$$

and

$$\rho_2(r) = \frac{-(r - R_c - s)^3}{4s^3} \qquad for\ R_c \le r < R_c + s$$

$$\rho_2(r) = 0 \qquad elsewhere \tag{4}$$

in which r is the distance from the center of the micelle, R_c is the core radius, and s controls the width of the profile. Four parameters were fit during the cryo-TEM micrograph analysis: *R, K, s,* and the weighting of the *b* splines, a. The core radius was fixed at 2 nm.

Then, the gray values were scaled according to the total expected PNIPAM volume per micelle,

$$\alpha \int 4\pi \frac{G_o - G(r)}{G_o} r^2 dr = Q v_{corona} \tag{5}$$

α is the scaling constant, G_o is the background gray value, r is the distance from the center of the particle, Q is the aggregation number, and v_{corona} is the volume of the PNIPAM block.

4.2.3.4 Small Angle Neutron Scattering

SANS experiments were performed at the National Institute of Standards and Technology (NIST), Center for Neutron Research (NCNR, Gaithersburg, MD) on the NG-7 30 m SANS beamline. An incident wavelength of 6.0 Å with a wavelength spread ($\Delta\lambda/\lambda$) of 0.12 was used with sample-to-detector distances of 1.0 m, 4.0 m, and

13.5 m to access a scattering vector (q) range of 0.004 $Å^{-1} < q < 0.6$ $Å^{-1}$. The scattering vector modulus is defined as $q = 4\pi/\lambda \sin(\theta/2)$, in which θ is the scattering angle. All measurements were performed at ambient temperature (20 ± 1 °C). SANS data were reduced using standard procedures provided by NIST,[41] and background scattering from D_2O was subtracted from the data.

4.2.3.5 SANS Form Factor Model and Data Analysis

The SANS data were fit with a form factor model for spherical micelles that considered four terms: the self-correlation of the core, the self-correlation of the corona chains, the cross-term between the core and corona, and the cross-term between different corona chains, [32-34,42]

$$\begin{aligned} P_{micelle}(q) = {} & Q^2\beta_{core}^2 A_{core}^2(q) + Q\beta_{corona}^2 P_{chain}(q) \\ & + 2Q^2\beta_{core}\beta_{corona}A_{core}(q)A_{corona}(q) \\ & + Q(Q-1)\beta_{corona}^2 A_{corona}^2(q) \end{aligned} \quad (6)$$

in which q is the scattering vector, Q is the aggregation number, and β_{core} and β_{corona} are the total excess scattering lengths of the core and corona, respectively. The total excess scattering lengths were defined as $\beta_{core} = \upsilon_{core}(\rho_{core} - \rho_{solvent})$ and $\beta_{corona} = \upsilon_{corona}(\rho_{corona} - \rho_{solvent})$, in which υ_{core} and υ_{corona} are the volumes of the core and corona blocks, and ρ_{core}, ρ_{corona}, and $\rho_{solvent}$ are the scattering length densities of the core, corona, and solvent, respectively. The scattering length densities (ρ) were calculated using the density of PNIPAM,[43] and the molecular volume (V) and scattering length (Σb) for the pincer end-group, in which $\rho = \Sigma b/V$.[44,45] Because of the small contribution of the pincer end-group to the overall scattered intensity, the fits

were not affected by slight changes in the scattering length density of the end-group, (*e.g.* whether or not the aromatic group was included in the calculation).

The scattering amplitude of the core with radius, R_c, was described by the hard sphere form factor

$$A_{core}(q) = 3[\sin(qR_c) - qR_c\cos(qR_c)]/(qR_c)^3 \quad (7)$$

The self-correlation of the corona chains was described by a Debye function, in which the chains are assumed to be Gaussian with a radius of gyration, R_g.

$$P_{chain}(q) = 2\left[\exp\left(-q^2R_g^2\right) - 1 + q^2R_g^2\right]/\left(q^2R_g^2\right)^2 \quad (8)$$

The scattering contribution from the corona chains was calculated as the normalized Fourier transform of the radial density distribution of corona chains, $\rho_{corona}(r)$,

$$A_{corona}(q) = \frac{4\pi\int \rho_{corona}(r)[sin(qr)/qr]r^2dr}{4\pi\int \rho_{corona}(r)r^2dr} \quad (9)$$

in which $\rho_{corona}(r)$ was modeled as a linear combination of 2 *b* splines, as originally developed by Pedersen and coworkers and presented in Equations 2 - 4 above. This model independently fits the width of the corona profile and the relative weighting of the 2 *b* splines, allowing the model to capture differences in corona profiles between samples. Another important advantage of this model is that there is an analytical solution for the Fourier transform of the *b* splines, reducing the computation required

while fitting the data. The Fourier transforms of the corona profile are given in Appendix A.

A Schulz distribution of core radii was included to account for polydispersity in micelle size,

$$G(R_c) = \frac{R_c^Z}{\Gamma(Z+1)}\left(\frac{Z+1}{\langle R_c \rangle}\right)^{Z+1} \exp[-(Z+1)R_c/\langle R_c \rangle] \quad (10)$$

In which $\langle R_c \rangle$ is the mean core radius, and Z is related to the polydispersity, σ, by $\sigma^2 = 1/(Z+1)$. The distribution was truncated at $R_c = 0$. The fit quality was not affected significantly by the polydispersity; therefore, the value was fixed at 0.2.

Then, the coherent scattered intensity was given by,

$$I(q) = \frac{\mathrm{c}}{\langle M_{micelle} \rangle} \int P_{micelle}(q)\, G(R_c) dR_c \quad (11)$$

in which c is the polymer concentration, and $\langle M_{micelle} \rangle$ is the average micelle mass.

Scattering contributions from a structure factor were not included in the SANS data model, as the inclusion of the structure factor did not significantly affect the fits to the data.

The calculated scattered intensity was corrected for instrument resolution, and all data were fit using the procedures provided by NIST.[41] Five parameters were fit during the data analysis: Q, R_c, R_g, the width of the corona profile, and the weighting of the b splines. The SANS data fits, in particular for the aggregation number (Q), were highly dependent on the input concentration; therefore, all filtered samples were dried following the SANS experiments to determine the exact concentration. The error

reported in Table 4.2 was due to the uncertainty in polymer concentration in the solution.

The corona profiles obtained from the SANS data modeling were rescaled using Equation 12,

$$\int 4\pi\hat{\rho}_{corona}(r)r^2dr = Qv_{corona} \quad (12)$$

in which $\hat{\rho}_{corona}(r)$ is the rescaled corona profile and represents the volume fraction of the corona chains, r is the distance from the center of the micelles, Q is the aggregation number, and v_{corona} is the volume of the PNIPAM block.[32,33] The micelle radius from the SANS data analysis was defined as the radius at which the volume fraction of PNIPAM in the corona profile was less than 0.02.[33,46]

4.3 Results

4.3.1 Radial Density Profile Analysis Using Cryo-TEM

The solution assembly of the amphiphilic homopolymer sample **4c** was investigated using cryo-TEM. While polymeric coronas often are not visible in cryo-TEM due to their hydrated nature; the direct visualization of micelle coronas (including PNIPAM) has been reported previously.[30,47-51] As seen in Figure 4.1, cryo-TEM suggested that the amphiphilic homopolymer formed spherical micelles in aqueous solutions. Moreover, assuming mass-thickness contrast dominates (*i.e.* small contribution from the phase contrast),[30,52] the gray scale profile extracted from cryo-TEM micrographs should be related to the electron density profile of the micelles. The profile was fit assuming a radially decreasing density profile that was

modeled as a linear combination of 2 *b* splines. This functional form for the corona profile gave a good fit to the gray scale profile and suggested that the micelle radius was ~ 20 nm, which was consistent with sizes determined using light scattering experiments (Table 4.2).[38]

Table 4.2 Summary of amphiphilic homopolymer micelle characterization data

Sample	R_H (nm) DLS	R (nm)* SANS	$R_{g,corona}$(nm) SANS	Q SANS
4a	12 ± 1	15 ± 1	4.5 ± 0.9	48 ± 2
4b	16 ± 1	17 ± 1	5.1 ± 0.4	43 ± 2
4c	19 ± 1	18 ± 1	6.2 ± 0.5	34 ± 3

*Micelle radius determined from SANS data modeling

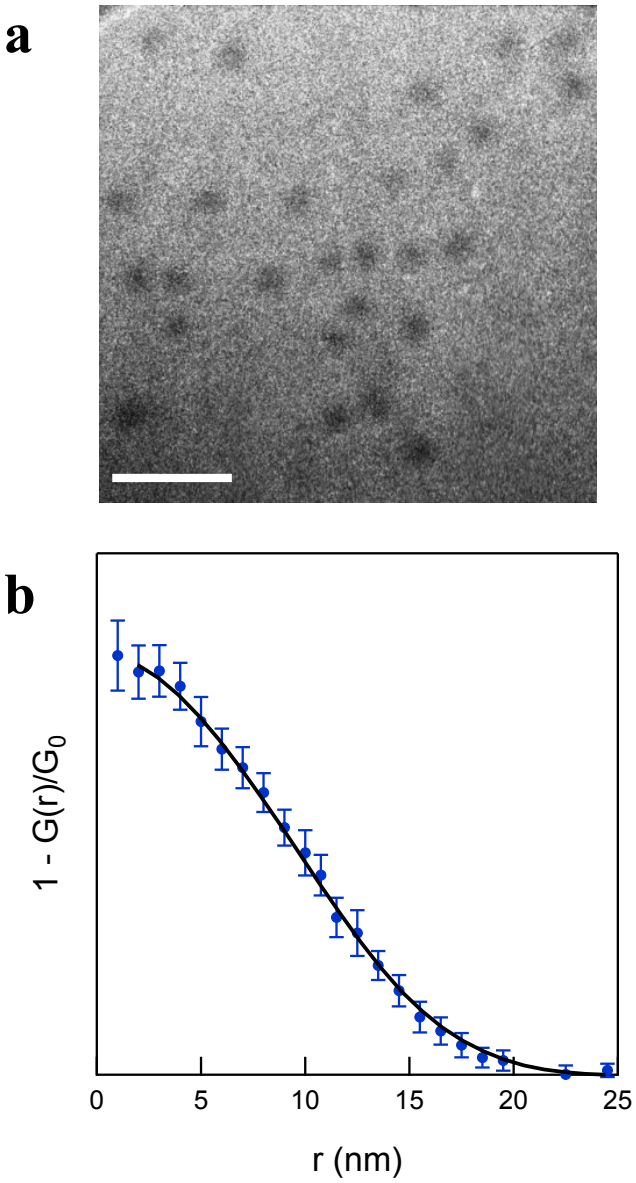

Figure 4.1 **Characterization of micelles formed by sample 4c using cryo-TEM. (a) Cryo-TEM micrograph and (b) corresponding gray scale profile from cryo-TEM micrograph analysis and fit for sample 4c, supporting the PNIPAM chains form a diffuse, hydrated corona. Contrast shown in (a) was enhanced by 5% in ImageJ for clarity; the contrast was not adjusted for the profile analysis. Scale bar is 100 nm. The gray scale profile in (b) was averaged over 50 micelles.**

4.3.2 Micelle Density Profile Analysis Using SANS

To further investigate the structural profile of the micelles, SANS experiments were performed on micelle solutions prepared in D_2O. The SANS data were fit with a form factor model for spherical polymer micelles with a homogenous core and radially decreasing corona density profile, also modeled as a linear combination of 2 *b* splines.[32,33,35,42] Accounting for the corona density profile resulted in good fits to the SANS data, shown in Figure 4.2. A slight upturn in the low *q* data for sample 4a deviated from the model fit, suggesting there may be aggregates in solution. Similarly, Winnik *et al.*, reported an increase in scattered intensity at low *q* upon heating their telechelic-PNIPAM flower micelles, which they fit with a model for micellar aggregates.[11] Here, accounting for the scattering contributions from micellar aggregates did not significantly affect the fit results for the individual micelles and therefore was not included while modeling the SANS data.

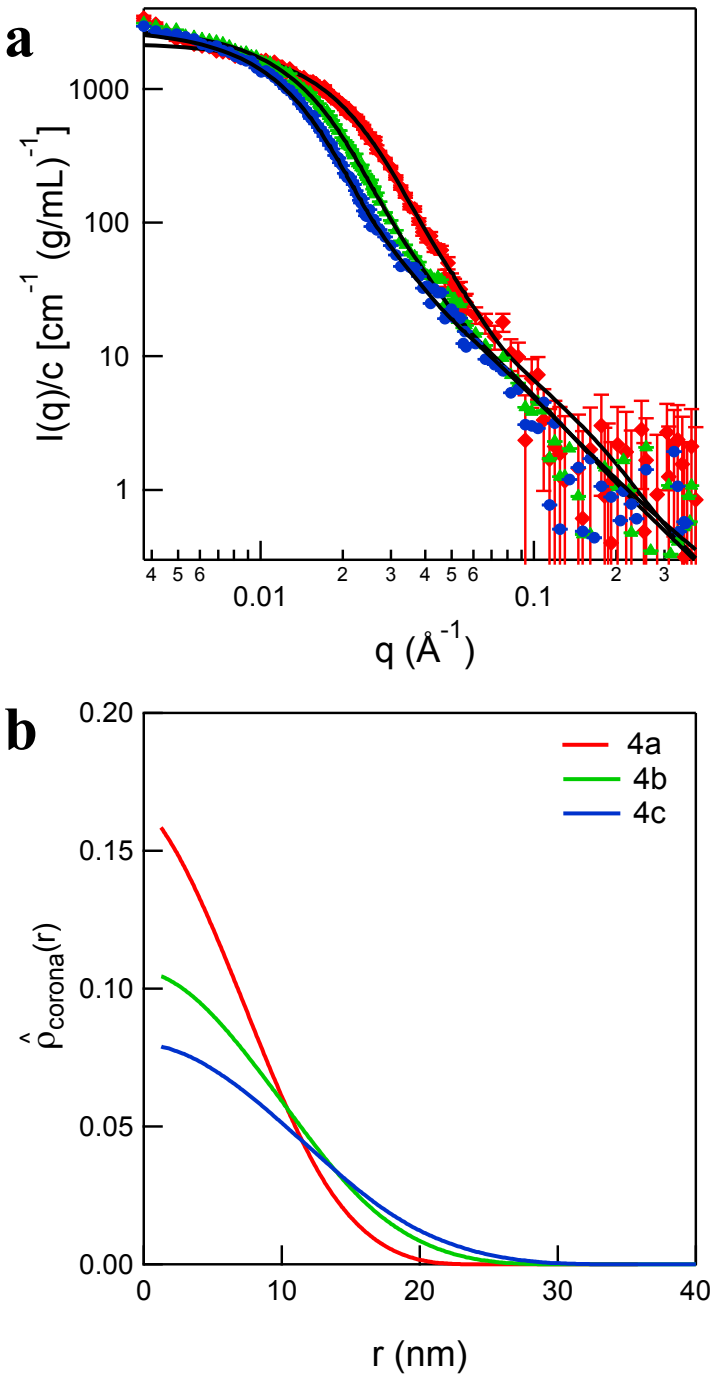

Figure 4.2 **Characterization of the amphiphilic homopolymer micelles using SANS. (a) SANS data (symbols) and fits with a spherical micelle form factor (lines) for 4a, 4b, and 4c in D_2O and (b) micelle corona profiles from the SANS data fits.**

The results of the SANS data modeling are summarized in Table 4.2 and Figure 4.2b. The analysis suggested that the micelle core radius was between 1 nm and 2 nm, which was consistent with the length of a fully extended C_{12} chain.[53,54] However, the fits were not sensitive to values within this range due to the small contribution of the core block to the overall scattered intensity. The micelle cores were surrounded by a diffuse, hydrated corona characteristic of star-like micelles, as seen in the corona profiles in Figure 4.2b. As expected, the $\boldsymbol{R_g}$ of the corona chains and overall micelle size increased with PNIPAM molecular weight (Table 4.2). Additionally, the SANS data suggested that the aggregation number decreased with increasing PNIPAM molecular weight, consistent with scaling theories for block polymer micelles.[55]

4.4 Discussion

The results presented here clearly indicate that the pincer functionalized polymers self-assembled into well-defined micelles. Additionally, the amphiphilic homopolymers studied here followed trends similar to those reported for block polymers. As seen in Table 4.2, the DLS and SANS data indicated that the micelle radius increased with increasing N_{PNIPAM}. The overall size of star-like micelles, particularly those with small cores, depends on the dimensions of the hydrophilic block. Accordingly, the micelle radius, R, should scale with the degree of polymerization of the hydrophilic block, N_{philic}, as $R \sim N_{philic}^{\delta}$.[5,56,57] Fitting the data in Table 4.2 suggests that the N_{PNIPAM} scaling exponent for micelle radius is within the range of literature values for δ, with a value between 0.5 and 1.[56,58] However, additional data points would be needed to definitively assign the scaling dependence, as these fits were based on only 3 samples. Q weakly decreased with increasing

N_{PNIPAM} (Table 4.2), consistent with experimental studies of block polymer micelles in which $Q \sim N_{philic}^{-\beta}$ and β ranged from 0.0 to 0.51.[58] Scaling theories for star-like block polymer micelles also predicted that Q should weakly decrease, in a logarithmic fashion, with increasing N_{philic}.[57,59]

Comparing the corona thickness to the root-mean-square end-to-end distance of PNIPAM in solution[60] suggests that the corona chains are moderately stretched in the micelles studied here (Table 4.3). Stretching of the corona chains has been reported for both amphiphilic homopolymer[54] and block polymer micelles[58] and is attributed to the crowding and associated stretching of the chains near the micelle core. As indicated in Figure 4.2b, sample 4a has the highest polymer volume fraction near the core, corresponding to the most crowded and therefore the most stretched chains. Likewise, the degree of corona chain stretching increases with aggregation number (*i.e.*, 4a > 4b > 4c), which is in agreement with trends reported for block polymer micelles.[58] The extent of corona chain stretching for the amphiphilic homopolymer micelles is comparable to literature results for block polymer micelles with similar aggregation numbers.[58]

Table 4.3 Corona chain stretching in amphiphilic homopolymer micelles calculated using dimensions from SANS data modeling

Sample	N_{PNIPAM}[(a)]	R_0[(b)] (nm)	H[(c)] (nm)	Corona chain stretching H/R_0
4a	120	8.9	12.6	1.4
4b	180	10.9	14.6	1.3
4c	270	13.4	15.8	1.2

[a] N_{PNIPAM} from ^{1}H NMR (Table 4.1)
[b] Calculated root mean square end-to-end distance for PNIPAM in H_2O assuming an average monomer length of 0.25 nm and characteristic ratio, $C_\infty = 10.6$, from Kubota *et al*.[60]
[c] Corona thickness, H, defined as $H = R - R_c$, in which R is the micelle radius from SANS and R_c is the core radius. The calculations above are based on $R_c = 2$ nm.

Modeling the corona profile as a linear combination of 2 *b* splines resulted in good fits to both the cryo-TEM gray scale profile and the SANS data (Figures 4.1 and 4.2). Similarly, previous scattering studies of telechelic-PNIPAM[11] and hydrophobically-modified PEO[44,54] also reported a radially decreasing corona profile. Though the corona profile extracted from cryo-TEM suggests that the corona chains extend to a smaller r than the profiles from SANS, the relative shape of the corona profiles was very similar, as illustrated by the normalized profiles in Figure 4.3. These results showed that corona profiles can be extracted from cryo-TEM micrographs, and highlighted the complementary use of scattering and cryo-TEM in the structural characterization of solution assemblies.

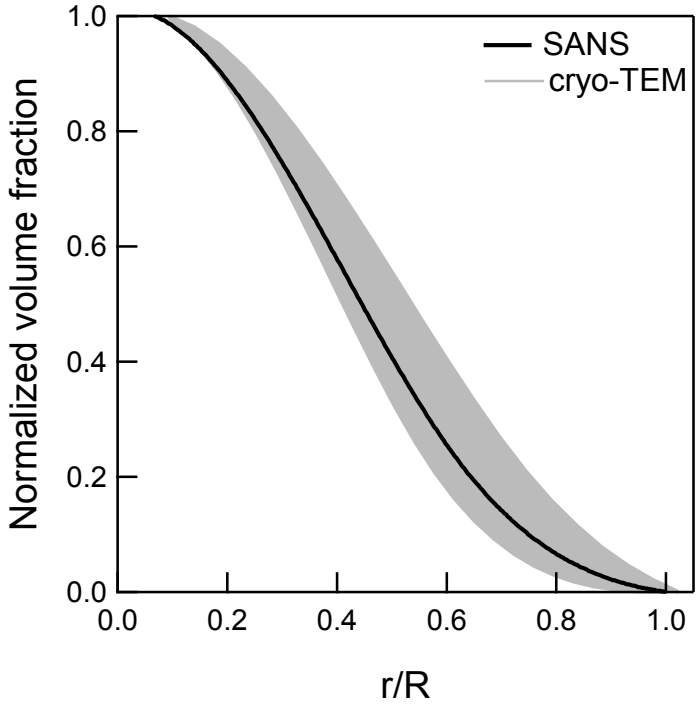

Figure 4.3 **Comparison of normalized corona profiles for sample 4c from cryo-TEM micrograph analysis and SANS data modeling. Shaded area represents the range of dimensionless volume fraction profiles that gave similar fits to the gray scale profile from cryo-TEM. Solid line is the dimensionless profile from the SANS data modeling. R is the radius at which the respective corona profile decreased to 0.**

4.5 Conclusions

The amphiphilic homopolymers studied here self-assembled into well-defined spherical micelles, in which the micelle radius, aggregation number, and corona density profile were dependent on the degree of polymerization of the PNIPAM block. Importantly, detailed information about the micelle density profiles was extracted from the cryo-TEM micrographs and was comparable to the SANS result, demonstrating the immense potential of the complementary use of these two

techniques to characterize nanoscale solution-assemblies. These micelles are promising precursors to solution-assembled nanoreactors and the detailed understanding of the micelle structure will facilitate future investigations into the effects of nanoreactor structure on catalytic performance.

The work presented here highlights the complementary use of cryo-TEM and scattering to elucidate structural details of macromolecular nanoassemblies. The following chapters utilize the powerful combination of cryo-TEM and SANS demonstrated here to understand the effects of cosolvent addition and removal on the structure and dynamics of block polymer micelles. These methods provided unique insights into the nanoscale structures that were unattainable with other techniques and facilitated investigations into the effects of common processing condition on macromolecular assemblies.

REFERENCES

1 Blanazs, A., Armes, S. P. & Ryan, A. J. (2009), *Macromolecular Rapid Communications* **30**, 267-277

2 Kelley, E. G., Albert, J. N. L., Sullivan, M. O. & Epps, T. H. (2013), *Chemical Society Reviews* **42**, 7057-7071

3 Kim, K. T., Meeuwissen, S. A., Nolte, R. J. M. & van Hest, J. C. M. (2010), *Nanoscale* **2**, 844-858

4 M. Lazzari, G. L., S. Lecommandoux. *Block Copolymers in Nanoscience*. Wiley-VCH, 2006.

5 Semenov, A. N., Joanny, J. F. & Khokhlov, A. R. (1995), *Macromolecules* **28**, 1066-1075

6 Changez, M., Kang, N.-G. & Lee, J.-S. (2012), *Small* **8**, 1173-1179

7 Kale, T. S., Klaikherd, A., Popere, B. & Thayumanavan, S. (2009), *Langmuir* **25**, 9660-9670

8 Ringsdorf, H., Venzmer, J. & Winnik, F. M. (1991), *Macromolecules* **24**, 1678-1686

9 Bathfield, M. l. *et al.* (2008), *Macromolecules* **41**, 8346-8353

10 Du, J., Willcock, H., Patterson, J. P., Portman, I. & O'Reilly, R. K. (2011), *Small* **7**, 2070-2080

11 Koga, T., Tanaka, F., Motokawa, R., Koizumi, S. & Winnik, F. M. (2008), *Macromolecules* **41**, 9413-9422

12 Hadjichristidis, N., Pispas, S. & Pitsikalis, M. (1999), *Progress in Polymer Science* **24**, 875-915

13 Boerakker, M. J. *et al.* (2002), *Angewandte Chemie* **41**, 4239-4241

14 Kujawa, P. *et al.* (2006), *Macromolecules* **39**, 341-348

15 Kujawa, P., Tanaka, F. & Winnik, F. M. (2006), *Macromolecules* **39**, 3048-3055

16 Kujawa, P., Watanabe, H., Tanaka, F. & Winnik, F. M. (2005), *European Physical Journal E* **17**, 129-137

17 Serero, Y. *et al.* (1998), *Physical Review Letters* **81**, 5584

18 Heldt, N. *et al.* (2001), *Reactive & Functional Polymers* **48**, 181-191

19 Kitano, H., Akatsuka, Y. & Ise, N. (1991), *Macromolecules* **24**, 42-46

20 Kitano, H., Ishino, Y. & Yabe, K. (2001), *Langmuir* **17**, 2312-2316

21 Li, C., Hu, J., Yin, J. & Liu, S. (2009), *Macromolecules* **42**, 5007-5016

22 Xu, J. T., Tao, L., Boyer, C., Lowe, A. B. & Davis, T. P. (2011), *Macromolecules* **44**, 299-312

23 de Paz Báñez, M. V., Robinson, K. L., Vamvakaki, M., Lascelles, S. F. & Armes, S. P. (2000), *Polymer* **41**, 8501-8511

24 Akiyoshi, K. *et al.* (2000), *Macromolecules* **33**, 3244-3249

25 Renou, F., Nicolai, T., Nicol, E. & Benyahia, L. (2009), *Langmuir* **25**, 515-521

26 Greenland, B. W. *et al.* (2013), *Chemical Communications* **49**, 454-456

27 Cui, H. *et al.* (2007), *Soft Matter* **3**, 945-955

28 Danino, D. (2012), *Current Opinion in Colloid & Interface Science* **17**, 316-329

29 Weissman, H. & Rybtchinski, B. (2012), *Current Opinion in Colloid & Interface Science* **17**, 330-342

30 Crassous, J. J. *et al.* (2009), *Langmuir* **25**, 7862-7871

31 Ku, T.-H. *et al.* (2011), *Journal of the American Chemical Society* **133**, 8392-8395

32 Bang, J., Viswanathan, K., Lodge, T. P., Park, M. J. & Char, K. (2004), *Journal of Chemical Physics* **121**, 11489-11500

33 Kelley, E. G., Smart, T. P., Jackson, A. J., Sullivan, M. O. & Epps, T. H., III. (2011), *Soft Matter* **7**, 7094-7102

34 Pedersen, J. S. & Gerstenberg, M. C. (2003), *Colloids and Surfaces A: Physicochemical and Engineering Aspects* **213**, 175-187

35 Pedersen, J. S., Svaneborg, C., Almdal, K., Hamley, I. W. & Young, R. N. (2003), *Macromolecules* **36**, 416-433

36 Zheng, Y. *et al.* (1999), *The Journal of Physical Chemistry B* **103**, 10331-10334

37 Patterson, J. P. *et al.* (2013), *Polymer Chemistry* **4**, 2033-2039

38 Patterson, J. P. *et al.* (2013), *Macromolecules* **46**, 6319-6325

39 Schneider, C. A., Rasband, W. S. & Eliceiri, K. W. (2012), *Nature Methods* **9**, 671-675

40 Pedersen, J. S., Hamley, I. W., Ryu, C. Y. & Lodge, T. P. (2000), *Macromolecules* **33**, 542-550

41 Kline, S. (2006), *Journal of Applied Crystallography* **39**, 895-900

42 Choi, S. Y., Bates, F. S. & Lodge, T. P. (2009), *Journal of Physical Chemistry B* **113**, 13840-13848

43 Zhang, L., Daniels, E. S., Dimonie, V. L. & Klein, A. (2010), *Journal of Applied Polymer Science* **118**, 2502-2511

44 Beaudoin, E. *et al.* (2002), *Macromolecules* **35**, 7436-7447

45 Caponetti, E. *et al.* (1987), *Journal of Colloid and Interface Science* **116**, 200-210

46 Pedersen, J. S. & Gerstenberg, M. C. (2003), *Colloids Surf., A* **213**, 175-187

47 Betthausen, E., Drechsler, M., Fortsch, M., Schacher, F. H. & Müller, A. H. E. (2011), *Soft Matter* **7**, 8880-8891

48 Synatschke, C. V., Schacher, F. H., Fortsch, M., Drechsler, M. & Müller, A. H. E. (2011), *Soft Matter* **7**, 1714-1725

49 Wolf, A., Walther, A. & Müller, A. H. E. (2011), *Macromolecules* **44**, 9221-9229

50 Zheng, Y. *et al.* (1999), *J. Phys. Chem. B* **103**, 10331-10334

51 Colombani, O. *et al.* (2007), *Macromolecules* **40**, 4351-4362

52 Langmore, J. P. & Smith, M. F. (1992), *Ultramicroscopy* **46**, 349-373

53 Israelachvili, J. N. *Intermolecular & Surface Forces*. 9th edn, Elsevier Science Imprint, 2002.

54 Sommer, C., Pedersen, J. S. & Garamus, V. M. (2005), *Langmuir* **21**, 2137-2149

55 Halperin, A., Tirrell, M. & Lodge, T. P. (1992), *Advances in Polymer Science* **100**, 31-71

56 Halperin, A. (1987), *Macromolecules* **20**, 2943-2946

57 Zhulina, E. B., Adam, M., LaRue, I., Sheiko, S. S. & Rubinstein, M. (2005), *Macromolecules* **38**, 5330-5351

58 Forster, S., Zisenis, M., Wenz, E. & Antonietti, M. (1996), *Journal of Chemical Physics* **104**, 9956-9970

59 Zhulina, E. B. & Borisov, O. V. (2012), *Macromolecules* **45**, 4429-4440

60 Kubota, K., Fujishige, S. & Ando, I. (1990), *Polymer Journal* **22**, 15-20

Chapter 5

STRUCTURAL CHANGES IN BLOCK POLYMER MICELLES INDUCED BY COSOLVENT MIXTURES

This chapter describes the effects of cosolvent addition on the structure of diblock copolymer micelles. The complementary use of cryo-TEM and SANS presented in Chapter 4, along with additional characterization techniques, were used to provide a detailed understanding of the micelle structures in cosolvent mixtures. Text and figures are reprinted and adapted from Kelley, E. G., Smart, T. P., *et al. Soft Matter* **2011**, 7, 7094-7102 by permission of The Royal Society of Chemistry.

5.1 Introduction

Although amphiphile self-assembly produces a diverse array of structures, access to this range of structures requires the synthesis of multiple polymers. Fortunately, non-synthetic methods such as the manipulation of solvent conditions can be used to control the core-corona interfacial free energy for various block polymer systems, and thereby more easily manipulate solution assembly.[1-11] For example, Eisenberg *et al.* demonstrated the reversible transition from spherical micelles to cylindrical micelles to vesicles when the solvent quality for the core block was altered using cosolvent mixtures.[7,12] Additionally, Lund *et al.* studied the effects of water/*N*,*N*-dimethylformamide (H_2O/DMF) cosolvent mixtures on poly(ethylene-*co*-propylene-*b*-ethylene oxide) [PEP-PEO] spherical micelles by small angle neutron scattering (SANS).[2] They reported a decrease in micelle size with increasing DMF content due to the reduction in core-corona interfacial tension and noted that the

decrease in aggregation number was in good agreement with the scaling relationship for star-like micelles by Halperin.[13] While their study demonstrated the effects of interfacial tension on micelle size, they were unable to characterize the effect of interfacial tension on the core-corona interfacial profile due to minimal scattering contributions from the PEP core.

Building on the study of Lund et al.,[2] this chapter investigates the effects of interfacial tension on micelle structures, and in particular, on the core-corona interface. Theoretical and experimental studies of immiscible polymer interfaces in bulk materials have shown that decreasing the interfacial energy between the polymers broadens the interface.[14-16] Extending these studies to the solution assembly of amphiphilic block polymers, the effects of interfacial tension on the core-corona interface in poly(1,2-butadiene-*b*-ethylene oxide) (PB-PEO) micelles are presented here. The interfacial tension was controlled using water/tetrahydrofuran (H_2O/THF) mixtures. THF and H_2O are miscible solvents, in which THF is a good solvent for PB-PEO, while H_2O is selective for the PEO block. Thus, the THF content in the cosolvent mixture could be used to manipulate the core-corona interfacial tension. Upon increasing the THF content and thus reducing the interfacial tension, the core-corona interface evolved from a sharp, well-defined interface in pure H_2O,[17-22] to a diffuse interface at higher THF contents.

The changes in micelle composition profile were quantified primarily through contrast variations in SANS experiments and detailed SANS data modeling. The scattering contributions from the corona were minimized by selectively deuterating the corona of the micelles, allowing for the characterization of the micelle core and core-corona interface. The SANS studies were complemented by small angle X-ray

scattering (SAXS), dynamic light scattering (DLS), cryogenic transmission electron microscopy (cryo-TEM), and proton nuclear magnetic resonance (^{1}H NMR) spectroscopy experiments. Moreover, the experimentally determined micelle sizes were compared to theoretical scaling relationships for the dependence of micelle size on core-corona interfacial tension.

5.2 Experimental

5.2.1 Materials and Polymer Synthesis

Ethylene oxide and *1,3*-butadiene were purchased from Sigma Aldrich. Ethylene oxide-d_4 (EO-d_4, 99.7% D), deuterium oxide (D_2O, 99.9% D), and tetrahydrofuran-d_8 (THF-d_8, 99.6% D) were purchased from Cambridge Isotopes. All other chemicals were purchased from Fisher Scientific. Monomers were purified by distillation from butylmagnesium chloride (EO and EO-d_4) or *n*-butyllithium (*1,3*-butadiene). THF for the polymerizations and solution preparation was degassed with argon and further purified by passage through two neutral alumina columns prior to use. Ultrapure H_2O for micelle solution preparation was obtained from a Milli-Q water purification system. D_2O and THF-d_8 were used without further purification.

PB-PEO and PB-*d*PEO [poly(butadiene-*b*-ethylene oxide-d_4)] were synthesized by anionic polymerization using established protocols described in detail in Chapter 2.[23] The PB-PEO and PB-*d*PEO diblock copolymers in this study were synthesized from the same PB precursor. The PB precursor (M_n=3.2 kg mol^{-1}, Đ = 1.06, 92±1% *1,2*-PB units) was characterized by gel permeation chromatography (GPC), matrix-assisted laser desorption/ionization time-of-flight mass spectrometry (MALDI-TOF MS),[24] and ^{1}H NMR. PB-PEO (M_n=11.2 kg mol^{-1}, Đ=1.03) and PB-

*d*PEO (M_n=11.1 kg mol^{-1}, Đ = 1.05) block polymers were analyzed using GPC and ^{1}H NMR, and the diblock copolymers had hydrophilic weight fractions of 0.72 and 0.71, respectively.

5.2.2 Solution Preparation

Micelle solutions were prepared by adding H_2O to dry polymer powder and stirring the solutions for 3 days. Next, THF was added to achieve the desired solvent composition, and the solutions were stirred for an additional 3 days before analysis. All solutions contained a final concentration of 2.4 mg mL^{-1} polymer in cosolvent solution. Solvents used to prepare the solutions were passed through a 0.2 μm filter to ensure that the samples were dust free.

5.2.3 Micelle Characterization

5.2.3.1 Contact Angle

A thin film of the PB precursor (~100 nm) was prepared by flow coating a polymer solution in THF onto a silicon substrate.[25] Contact angle measurements of H_2O/THF cosolvent mixtures on the PB thin film were carried out on a First Ten Ångstroms (FTÅ) 125 contact angle measuring system. Liquid drops (3 μL) were dispensed and placed on the PB film with a Distriman pipette. Contact angle analysis was performed by using the FTÅ software and the drop shape method to determine the contact angle. Each contact angle was measured <0.5 s after the droplet first came into contact with the PB surface; therefore, measurements were acquired prior to any PB solubilization in the cosolvent mixture. A minimum of five contact angles per sample were measured. The average value of these angles was used in interfacial tension calculations. The interfacial tension (γ) between PB and the H_2O/THF

mixtures was calculated from the measured contact angles according to Young's equation[10]

$$\gamma = \gamma_{PB} - \gamma_{solvent} \cos\theta \quad (1)$$

in which γ_{PB} is the surface tension of PB,[26] $\gamma_{solvent}$ is the surface tension of the H_2O/THF mixture,[27] and θ is the measured contact angle.

5.2.3.2 Dynamic Light Scattering (DLS)

DLS experiments were performed using a Lexel Laser Inc. 488 nm, 100 mW laser, coupled with a Brookhaven Instruments Corporation goniometer. The intensity autocorrelation function was recorded at angles from 20°-140° and analyzed using the CONTIN algorithm.[28] All measurements were performed at 25 °C. Literature values for the viscosity and refractive index of the H_2O/THF cosolvent mixtures used to analyze the DLS data are given in Table 5.1.[29]

Table 5.1 Viscosity and refractive index values for water/THF cosolvent mixtures used to analyze DLS data

% by volume THF	viscosity [cP]	Refractive index
0	0.891	1.3314
2.5	1.186	1.3411
5	1.398	1.3493
10	1.665	1.3624
15	1.702	1.3723
20	1.651	1.3791
30	1.394	1.3879
40	1.129	1.3935
50	0.916	1.3972
60	0.763	1.4001

5.2.3.3 Cryogenic Transmission Electron Microscopy (cryo-TEM)

Samples for cryo-TEM were prepared at 25 °C using a FEI Vitrobot to maintain a constant humidity environment. A droplet of 2-4 μL of micelle solution was added to a holey carbon-coated copper grid, and the grid was blotted to remove excess solution. Subsequently, the grid was plunged into liquid ethane to vitrify the sample. Grids were transferred to a Gatan cryo stage and imaged at 120 keV using a Tecnai G2 12 Twin TEM equipped with a Gatan CCD camera. The temperature of the cryo stage was maintained below -170 °C during imaging. Images were analyzed using Gatan DigitalMicrograph software. The cryo-TEM micrographs presented in this chapter were collected by Dr. Thomas P. Smart.

5.2.3.4 Small Angle X-ray Scattering (SAXS)

SAXS data were obtained on the DND-CAT beamline at the Advanced Photon Source (APS). Data were collected for 60 s using an incident beam wavelength of 0.73 Å and a sample-to-detector distance of 4 m, which gave a scattering vector (q) range of 0.007 $Å^{-1} < q < 0.2$ $Å^{-1}$. The scattering vector modulus (q) is defined as

$q=(4\pi/\lambda)\sin(\theta/2)$, in which θ is the scattering angle. Micelle sizes were calculated from the first maximum in the scattering curve by using the relationship for spherical scatterers $qR=5.763$, where R is the micelle radius.[30]

5.2.3.5 Proton Nuclear Magnetic Resonance (^{1}H NMR) Spectroscopy

Solutions of PB-PEO for ^{1}H NMR spectroscopy experiments in D_2O and THF-d_8 were prepared as described above. ^{1}H NMR spectra were obtained at 400 MHz on a Bruker-DRX400 Spectrometer. 256 scans with a 1 s relaxation delay were collected for each spectrum.

5.2.3.6 Small Angle Neutron Scattering (SANS)

Solutions of PB-PEO and PB-*d*PEO were prepared in D_2O and THF-d_8 according to the procedure described above. SANS experiments were performed on the NG-7 30 m SANS instrument at the National Institute of Standards and Technology, Center for Neutron Research (NIST-CNR). An incident wavelength of 6.0 Å with a wavelength divergence ($\Delta\lambda/\lambda$) of 0.11 was used with sample-to-detector distances of 1.0 m, 4.0 m, and 13.5 m to cover scattering vectors ranging from 0.004 $Å^{-1} < q < 0.4$ $Å^{-1}$. SANS data were reduced to 1D data in IGOR Pro with reduction procedures provided by NIST.[31]

5.2.3.7 SANS Form Factor Model and Data Fitting

SANS data were fit with a form factor model for spherical block polymer micelles described in Chapter 4; however, an additional term was incorporated into the scattering amplitude terms for the core and corona to account for the core-corona interfacial width (Figure 5.1).[32-35]

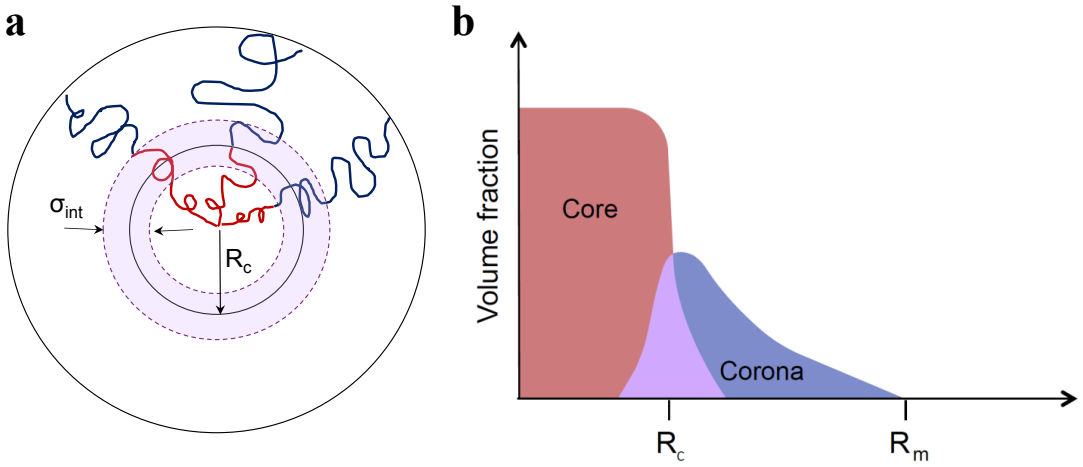

Figure 5.1 Schematic representation of (a) block polymer micelle and (b) micelle density profile used to model SANS data.

Four correlation terms were considered: self-correlation of the core, self-correlation of the corona chains, the cross-term between the core and corona chains, and the cross-term of different corona chains,

$$P_{micelle}(q) = N_{agg}^2\beta_{core}^2A_{core}^2(q) + N_{agg}\beta_{corona}^2P_{chain}(q) + 2N_{agg}^2\beta_{core}\beta_{corona}A_{core}(q)A_{corona}(q) + N_{agg}(N_{agg}-1)\beta_{corona}^2A_{corona}^2(\mathrm{q}) \quad (2)$$

in which q is the scattering vector, Q is the aggregation number, and β_{core} and β_{corona} are the total excess scattering lengths of the core and corona blocks, respectively. The total excess scattering lengths are defined as $\beta_{core} = \upsilon_{core}(\rho_{core} - \rho_{solvent})$ and

$\beta_{corona} = \upsilon_{corona}(\rho_{corona} - \rho_{solvent})$, where υ_{core} and υ_{corona} are the volumes of the core and corona blocks, and ρ_{core}, ρ_{corona}, and $\rho_{solvent}$ are the scattering length densities of the core, corona, and cosolvent mixtures, respectively. The volumes of the core and corona blocks were calculated according to $\upsilon_x = N_x M_{o,x}/d_x N_A$, in which N_x is the degree of polymerization, $M_{o,x}$ is the repeat unit molecular weight, d_x is the density of the polymer and N_A is Avogadro's number. The scattering length density values used in this work are summarized in Table 5.2

Table 5.2 Density and scattering length density values for the materials used in this study

material	density (g/cm^3)	neutron scattering length density ($Å^{-2}$)
D_2O	1.10	6.33×10^{-6}
THF-d_8	0.95	6.35×10^{-6}
PB	0.87	4.11×10^{-7}
PEO	1.13	6.22×10^{-7}
PEO-d_4	1.20	7.10×10^{-6}

The scattering amplitude for a spherical homogeneous core, with radius R_c, is

$$A_{core}(q) = \Phi(qR_c)\exp(-q^2\sigma_{int}^2/2) \quad (3)$$

with $\Phi(x) = 3[\sin x - x\cos x]/x^3$. Here, the exponential term was incorporated to describe a smoothly decaying density profile of width σ_{int} at the core-corona interface.

Self-correlation of the corona chains was approximated by a Debye function,

$$P_{chain}(q) = 2\left[\exp\left(-q^2R_g^2\right) - 1 + q^2R_g^2\right]/\left(q^2R_g^2\right)^2 \quad (4)$$

in which the chains were assumed to be Gaussian coils with radius of gyration, R_g.

A radial density distribution of corona chains, $\rho_{corona}(r)$, was considered, and the scattering amplitude was calculated from the normalized Fourier transform of the radial density distribution of corona chains,

$$A_{corona}(q) = \frac{4\pi \int \rho_{corona}(r)[sin(qr)/qr]r^2 dr}{4\pi \int \rho_{corona}(r) r^2 dr} \exp(-q^2\sigma_{int}^2/2) \qquad (5)$$

The corona density profile, $\rho_{corona}(r)$, was represented using a linear combination of two cubic *b* splines as described in Chapter 4 and Appendix A. This explicit form of $\rho_{corona}(r)$ was originally developed by Pedersen and coworkers[35] and has been successfully implemented to describe scattering from micelles in aqueous[32] and organic solutions.[33-35] Furthermore, this density profile model was able to adapt to changes in the corona profile induced by cosolvent addition because it independently fit the width of the corona profile and the linear combination of 2 *b* splines.

A Schulz distribution of core radii was incorporated to account for polydispersity in micelle size[36]

$$G(R_c) = \frac{R_c^Z}{\Gamma(Z+1)}\left(\frac{Z+1}{\langle R_c \rangle}\right)^{Z+1} \exp[-(Z+1)R_c/\langle R_c \rangle] \qquad (6)$$

in which $\langle R_c \rangle$ is the average core radius, and Z is related to the polydispersity, σ_{Rc}, by ${\sigma_{Rc}}^2 = 1/(Z+1)$. The coherent scattered intensity for the polydisperse micelle model was then given by

$$I(q) = \frac{\mathrm{c}}{\langle M_{micelle} \rangle} \int P_{micelle}(q)\, G(R_c) dR_c + B \tag{7}$$

in which B is the incoherent background. Because intermicellar interactions were negligible at the studied solution concentrations,[37] scattering contributions from a structure factor were not included in the model. The calculated scattering intensity was further corrected for instrument resolution by employing procedures provided by NIST.[31] All data were analyzed in IGOR Pro, and the code for the form factor model is given in Appendix B.

The scattering data for the high THF content samples (≥ 40 vol% THF) were fit with a linear combination of the micelle form factor model described above and the form factor model for the free chains. The scattering of the free chains was described using the Gaussian coil form factor,[38]

$$I(q) = a \times \frac{2\left[(1+Ux)^{-1/U} + x - 1\right]}{(1+U^2)x^2} \tag{8}$$

in which a is the scale factor and x is the dimensionless chain size,

$$x = \frac{{R_g}^2 q^2}{1+2U} \tag{9}$$

and U is related to the dispersity, U = Đ - 1.

The total scattered intensity for the summed models was then given by,

$$I(q) = c \times I_{micelle}(q) + a \times I_{free\ chain}(q) + B \tag{10}$$

in which c is the concentration of chain in the micelle and a is the scale factor for the free chains. The R_g and dispersity of the free chains were determined data for PB-PEO in 80 vol% THF cosolvent mixtures. These parameters for the free chains were then input into the summed model and held constant. The data were fit iteratively such that the scale factors for the micelles and free chains were consistent with the known mass of polymer in solution. *Note that this analysis assumed that the solution was dilute enough such that the free chains and micelles did not interact*.

During the data analysis, each fit parameter was individually perturbed to determine the modeling sensitivity to that specific variable. The reported errors are the range of fit values that resulted in the same goodness of fit.

5.3 Results

5.3.1 PB-Cosolvent Interfacial Tension

To investigate the effects of interfacial tension on PB-PEO micelle assemblies, contact angle measurements on PB thin films were used to determine the interfacial tension between PB and H_2O/THF mixtures. As seen in Figure 5.2, the PB-cosolvent interfacial tension decreased from ~50 mN m^{-1} in pure water to ~5 mN m^{-1} in 70 vol% THF. These results indicated that the THF content in the cosolvent mixtures varied core-corona interfacial tension varied over approximately one order of magnitude and could be used to effectively tune the micelle structure.

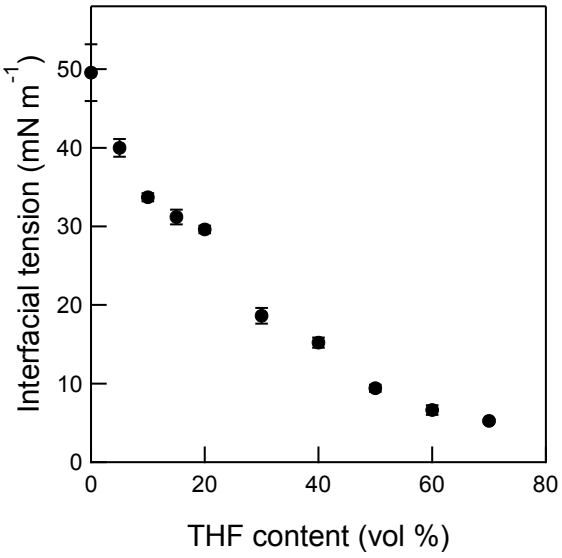

Figure 5.2 PB-cosolvent interfacial tension as a function of THF content. Error bars represent the range of calculated values due to variability in the contact angle measurements.

5.3.2 Effects of Interfacial Tension on Micelle Size

PB-PEO micelle solutions in H_2O/THF mixtures (0 – 60 vol% THF) were analyzed by DLS, SAXS, and cryo-TEM to determine micelle hydrodynamic radius, R_H, (DLS), micelle outer radius, R_m, (SAXS), and micelle core radius, R_c, (cryo-TEM) as a function of THF content (Figure 5.2, Figure 5.3, and Table 5.3). Angle dependent DLS measurements indicated that the micelles remained spherical upon THF addition (Figure 5.3).[39] The characterization data are summarized in Figure 5.4 and show that R_H, R_m, and R_c decreased with THF addition due to the reduction in interfacial tension, consistent with previously reported experimental studies.[2,9,10]

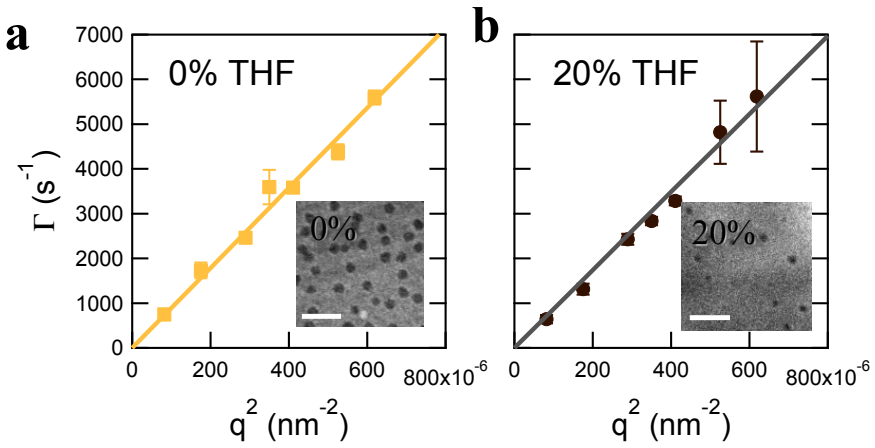

Figure 5.3 **Representative DLS and cryo-TEM data for PB-PEO micelles in water/THF cosolvent mixtures. Plots of the decay constant (Γ) *vs.* q^2 determined from lights scattering for PB-PEO micelles in 0% (a) and 20% THF (b) cosolvent mixtures. Insets are the corresponding cryo-TEM micrographs (scale bar = 100 nm). Note that only the PB cores are visible in the micrographs due to minimal electron density contrast between PEO and water.**

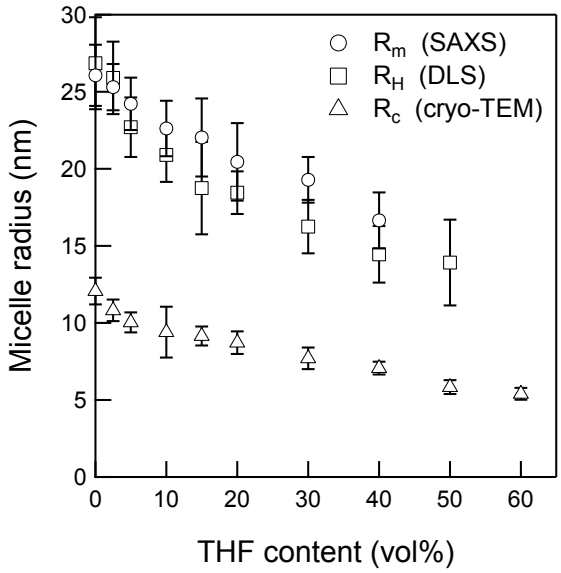

Figure 5.4 **(a) DLS, SAXS, and cryo-TEM data showing the micelle hydrodynamics radius R_H, micelle radius R_m, and micelle core radius R_c, vs THF content in H_2O/THF mixtures. Error bars represent range in measured radii.**

Solvent composition (vol% THF)	Q SANS	Fraction of free chains SANS	R_c (nm) Cryo-TEM	R_c (nm) SANS	σ_{Rc} SANS	σ_{int} (nm) SANS	R_h (nm) DLS	R_m (nm) SAXS	R_m* (nm) SANS	H (nm) SAXS/Cryo-TEM	$PEO\ R_g$ (nm) SANS
0.0	791 ±1	-	12.1 ±0.9	11.2 ±0.1	0.05	0.11 ±0.09	26.9 ±3.0	26.1 ±2.0	27.8 ±0.1	14.0 ±2.2	3.7 ±0.1
2.5	-	-	10.8 ±0.7	11.2 ±0.1	0.08	0.10 ±0.10	25.9 ±2.4	25.3 ±1.5	-	14.5 ±1.7	-
5.0	598 ±1	-	10.0 ±0.7	10.8 ±0.1	0.12	0.10 ±0.10	22.7 ±1.9	24.2 ±1.7	26.7 ±0.1	14.2 ±1.8	4.1 ±0.2
10.0	419 ±1	-	9.4 ±1.7	9.3 ±0.1	0.10	0.15 ±0.15	20.9 ±1.8	22.6 ±1.8	24.4 ±0.1	13.2 ±2.5	4.0 ±0.3
15.0	326 ±1	-	9.2 ±0.6	9.1 ±0.1	0.15	0.15 ±0.05	18.8 ±3.0	22.0 ±2.5	23.2 ±0.1	12.8 ±2.6	4.0 ±0.1
20.0	248 ±1	-	8.7 ±0.7	8.6 ±0.1	0.18	0.15 ±0.05	18.5 ±1.4	20.4 ±2.5	21.9 ±0.1	11.7 ±2.6	4.1 ±0.3
30.0	143 ±1	-	7.7 ±0.7	7.7 ±0.1	0.18	0.15 ±0.15	16.3 ±1.7	19.3 ±1.5	18.6 ±0.1	11.6 ±1.7	3.8 ±0.1
40.0	88 ±5	0.08 ±0.02	7.1 ±0.4	6.7 ±0.1	0.18	0.89 ±0.79	14.5 ±1.8	16.7 ±1.8	16.1 ±0.2	9.6 ±1.8	3.5 ±0.4
50.0	67 ±5	0.10 ±0.02	5.8 ±0.4	6.0 ±0.3	0.18	1 .00 ±0.50	13.9 ±2.8	-	14.8 ±0.4	-	3.6 ±0.1
60.0	60 ±11	0.26 ±0.09	5.4 ±0.4	5.3 ±1.1	0.18	1.28 ±1.08	-	-	13.5 ±1.2	-	2.4 ±0.3
70.0	52 ±19	0.48 ±0.30	-	3.8 ±1.5	0.20	2.18 ±0.54	-	-	12.7 ±1.5	-	1.6 ±0.2
72.0	30 ±5	0.90 ±0.18	-	4.4 ±1.2	0.20	2.31 ±0.51	-	-	11.6 ±0.8	-	1.5 ±0.1

Table 5.3 **Summary of micelle characterization data determined by DLS, SAXS, cryo-TEM, and SANS, in which Q is aggregation number, R_c is core radius, σ_{Rc} is core polydispersity, σ_{int} is interfacial width, R_h is hydrodynamic radius, Rm is micelle radius, H is corona thickness estimated as $H = R_m - R_c$ using R_m (SAXS) and R_c (cryo-TEM), and R_g is radius of gyration of the PEO chains. Note that R_m from SANS was estimated based on corona density profile where the volume fraction of PEO < 0.02.**

Comparing R_c with the corona thickness, H, defined as $H = R_m - R_c$, indicated the micelles were star-like, as $H > R_c$ over the range of THF contents studied (Figure 5.5).[40] According to the theoretical work scaling relationships for star-like micelles, R_c should scale with interfacial tension, γ, as $R_c \sim \gamma^{2/5}$ and H should scale as $H \sim \gamma^{6/25}$.[18] Using the measured values for the PB-cosolvent interfacial tensions, these scaling laws were fit to the experimentally determined core radii and corona thicknesses. As seen in Figure 5.5, the experimental data were in good agreement with these theoretical scaling relationships, suggesting the decrease in micelle size with increasing THF content was due to the reduced interfacial tension.

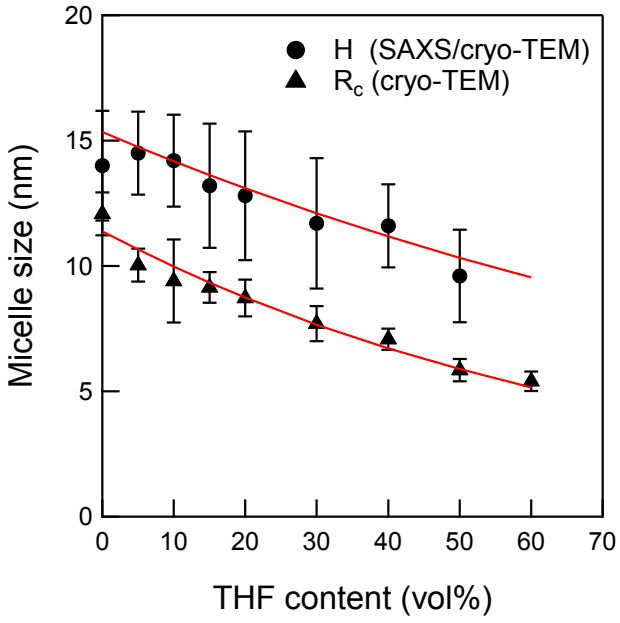

Figure 5.5 **Experimentally determined micelle core radii (R_c) and corona thickness (H) for PB-PEO micelles in H_2O/THF cosolvent mixtures. Error bars for R_c represent the range of measured values. Error bars for H represent the range in calculated values. Solid lines are the theoretical scaling relationships for star like micelles.**

5.3.3 Detailed SANS Data Modeling of Micelles in Cosolvent Mixtures

Contrast variation SANS experiments were performed to further elucidate changes in the micelle structure induced by cosolvent mixtures. The contrast variation between PB-PEO and PB-*d*PEO allowed in-depth examination of the micelle structural profile through simultaneous fitting of the form factor model for block polymer micelles to the complementary deuterated and non-deuterated data sets. Minor discrepancies were noted between the PB-PEO and PB-*d*PEO micelles due to the slight difference in polymer molecular weights. These differences were considered when simultaneously fitting the data such that the differences in fit parameters for core radius, R_c, and aggregation number, Q, were consistent with the small discrepancy in polymer molecular weight. Cosolvent effects on the core size and core-corona interfacial width, σ_{int}, (*i.e.* where the core and corona blocks were mixed) were determined by fitting the PB-*d*PEO data, while changes in the overall micelle size and corona density profile were found by fitting the PB-PEO data.

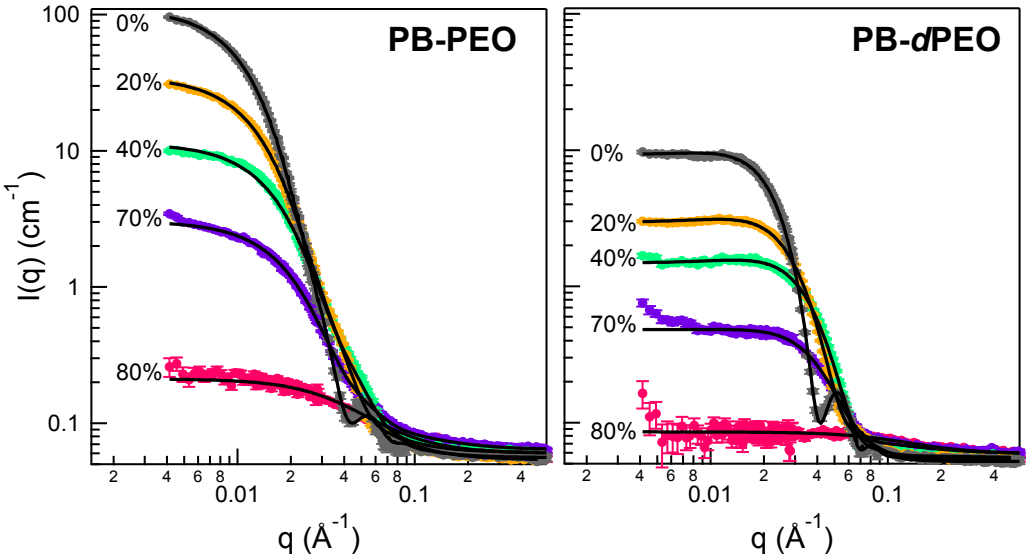

Figure 5.6 **SANS data (symbols) and fits (solid lines) for PB-PEO and PB-*d*PEO micelles in D_2O/THF-d_8 mixtures, where the labels indicate the volume percent of THF-d_8 in the cosolvent mixtures. Error bars represent the standard deviation in the measured intensity.**

Representative SANS data and fits for selected cosolvent compositions are presented in Figure 5.6, and all data are provided in Appendix C. Quality fits for the PB-PEO and PB-*d*PEO SANS data up to 40 vol% THF-d_8 were obtained by using only the micelle form factor model. However, at higher THF-d_8 contents, the presence of free chains in solution affected the scattering at high q.[41] To account for the free chains in solution, the SANS data (40 vol% to 72 vol%) were fit to a linear combination of spherical micelle and Gaussian coil form factors.[38] By enforcing a constant polymer solution concentration, the fraction of polymer free chains was estimated from the relative scaling of the two models. These combined SANS fits suggested that the fraction of free chains increased with THF-d_8 content up to 72 vol% THF-d_8 (Figure 5.7), at which point the micelles disassembled. This result was

consistent with separate turbidity measurements on PB homopolymer solutions (3.2 kg mol^{-1}) indicated that PB was fully soluble in H_2O/THF mixtures containing above ~75 vol% THF (Appendix D).

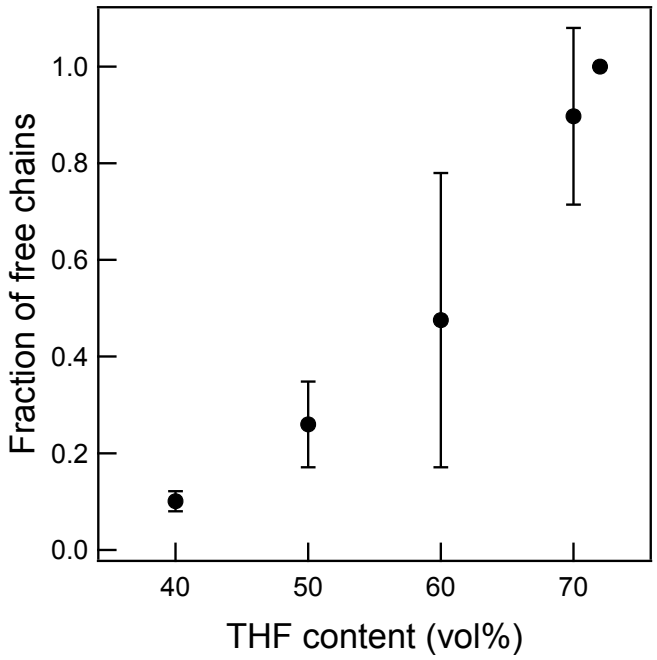

Figure 5.7 Fraction of free chains in the micelle solutions determined from the SANS data modeling. Error bars represent the range of values that gave the same goodness of fit.

The results of the SANS data fits describing the effects of cosolvent composition on micelle structure are summarized in Figures. 5.8 – 5.10 and Table 5.3. A decrease in R_m and R_c with increasing THF-d_8 content was found, consistent with the DLS, SAXS, and cryo-TEM data. Here, R_m was the radius at which the volume fraction of PEO was less than 0.02 in the corona profile.[32] The decrease in R_m and R_c also followed the trend of smaller aggregation numbers (Q) as THF-d_8 was added

(Figure 5.9). While micelle size decreased with THF-d_8 addition, the polydispersity in micelle sizes increased. This increased polydispersity was seen qualitatively in the broadening of the first minimum and maximum in the SANS data and was quantified by the SANS data modeling, which gave reasonable size distributions.

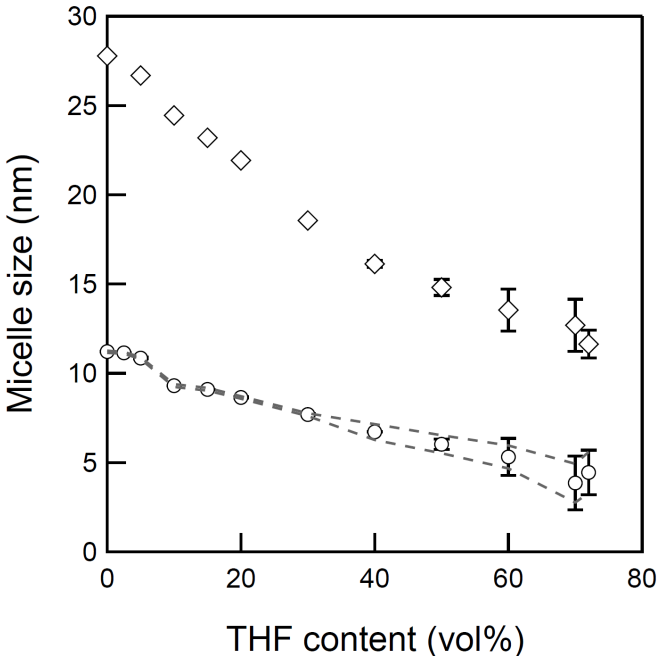

Figure 5.8 **SANS data (symbols) and fits (solid lines) for PB-PEO (a) and PB-*d*PEO (b) micelles in D_2O/THF-d_8 mixtures, where the labels indicate the volume percent of THF-d_8 in the cosolvent mixtures. Error bars represent the standard deviation in the measured intensity.**

The cosolvent effects on the micelle composition profile also were quantified by the SANS data modeling. In pure D_2O, the characteristic sharp interface between the PB core and PEO corona was shown by the negligible σ_{int} value, and this sharp profile persisted up to ~30 vol% THF-d_8 (Figure 5.8 and Table 5.3). However, as

more THF-d_8 was added (>30 vol% THF-d_8), σ_{int} increased. This increase in σ_{int} suggested that PB and PEO were mixing at the core-corona interface, and consequently, that the interface was broadening. Also, the solvent fraction in the core increased with increasing THF-d_8 content, indicating that the micelle cores were swelling with solvent (Figure 5.9) The solvent fraction in the core was calculated using the fit values for Q and R_c, and was not calculated for samples containing >30 vol% THF-d_8 due to the lack of a well-defined core size.

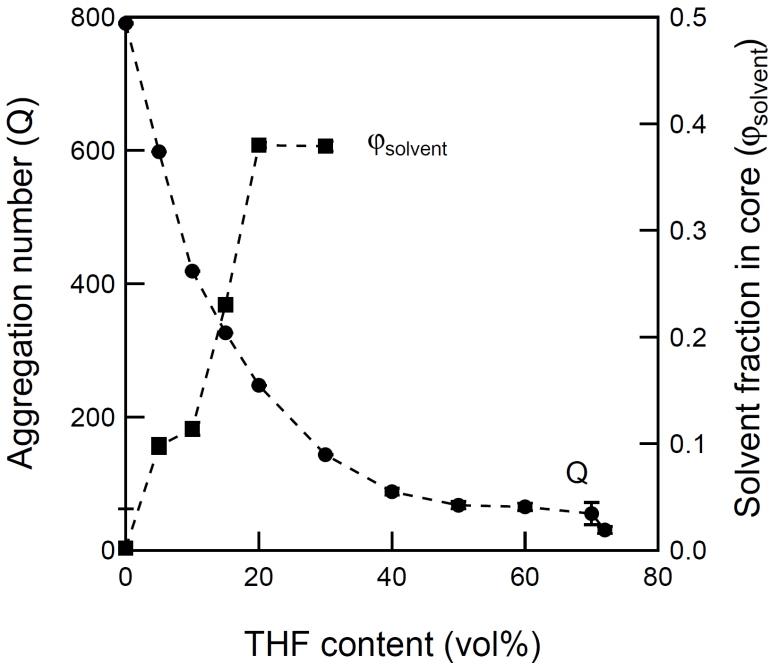

Figure 5.9 **Micelle aggregation number (Q) and solvent fraction in the core ($\varphi_{solvent}$) determined from the SANS data analysis. Error bars in Q represent the range of fit values with similar goodness of fits. Error bars for $\varphi_{solvent}$ represent the range of calculated values due to uncertainty in the fit parameters used in the calculation. Dashes lines are to guide the eye.**

The changing solvent conditions also affected the micelle corona profile. A rescaled corona composition, $\hat{\rho}_{corona}(r)$, was calculated by normalizing the corona density profile obtained from the SANS data fitting, $\rho_{corona}(r,)$ to the total volume of the corona (PEO plus solvent), [40]

$$\int 4\pi\hat{\rho}_{corona}(r)r^2\,dr = \mathrm{Q}v_{corona} \tag{12}$$

Profiles for $\hat{\rho}_{corona}(r)$ *vs.* r are presented in Figure 5.10. The maximum volume fraction of PEO at the core-corona interface, along with the total PEO content in the micelle corona, decreased with reducing interfacial tension. These changes in the micelle corona profiles reflected the improved solvent quality for the core block and the reduction in aggregation number. Also, the corona brush thickness decreased with increasing THF-d_8 content, reflecting the changing curvature of the micelle core surface.

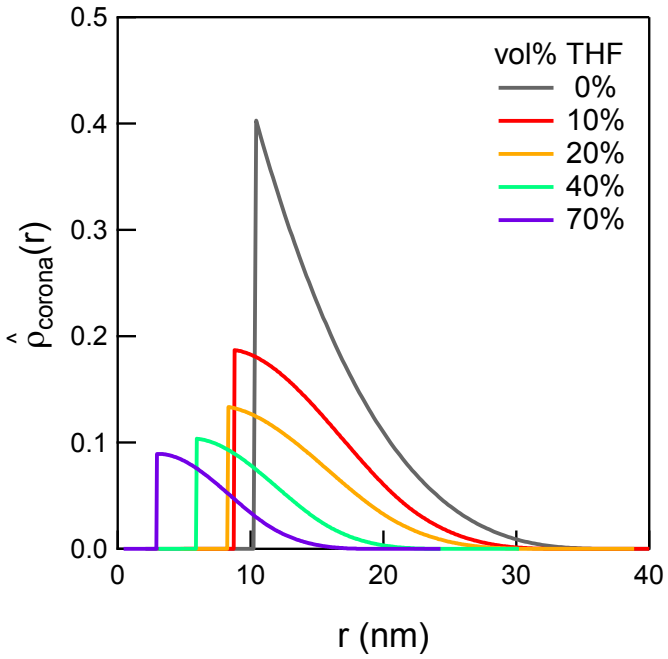

Figure 5.10 Radial composition profile in the PEO corona in PB-PEO micelles in D_2O/THF-d_8 mixtures as determined from SANS data analysis.

To investigate the effects of THF addition on the solvent quality for PEO, SANS experiments were performed on PEO homopolymer (M_n=6.3 kg mol^{-1}) in D_2O/THF-d_8 mixtures ranging from 0 - 70 vol% THF (Figure 5.11). The SANS data were fit with a Debye function to determine changes in the radius of gyration, R_g, as a function of THF-d_8 content.[38] These data confirmed that the changing solvent conditions had little effect on the PEO R_g, similar to the small changes in the micelle corona up to 60 vol% THF-d_8, as determined from SANS modeling (Table 5.3). While a significant decrease in R_g in the micelle corona was noted for >60 vol% THF-d_8, these fit values for R_g were unreliable because the high q scattering in these solutions was dominated by free chains.

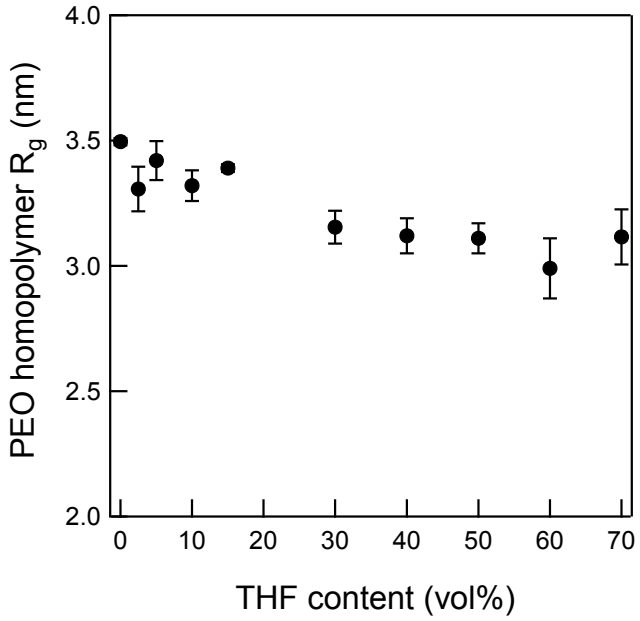

Figure 5.11 Radius of gyration (R_g) of PEO homopolymer (6 kDa) in D_2O/THF-d_8 cosolvent mixtures determined from SANS measurements. SANS data were fit with a Debye function to determine the R_g. Error bars represent the range in fit values for R_g with similar goodness of fits.

The SANS studies presented above were complemented by ^{1}H NMR spectroscopy experiments to probe PB chain mobility at various THF-d_8 contents (Figure 5.12). In pure THF-d_8, the polymer was fully solvated, and peaks corresponding to both PB (between 0.8 - 2.1 ppm and 4.8 - 5.6 ppm) and PEO (3.6 ppm) were detected. In contrast, in pure D_2O, only the peak corresponding to the PEO corona was detected. Because D_2O was a non-solvent for the PB, the PB chains were confined to the micelle core in pure D_2O, and the restricted chain motion led to broad and weak PB peaks. As THF-d_8 was added to the system, the PB mobility increased, as manifested by a sharpening of the corresponding peaks.[42] The fraction of mobile PB was quantified by comparing the integrated PB peak areas in micelle solutions at

various THF-d_8 contents to PB peak areas in pure THF-d_8, where the block polymer was fully solvated. Figure 5.11b shows that the PB mobility increased with THF-d_8 content up to ~50 vol% THF-d_8, at which point the PB had similar mobility to fully solvated chains. This increased PB mobility indicated that the core was swelling with THF-d_8 and that PB chains were likely solvated. Above 50 vol% THF-d_8, the PB peaks continued to sharpen, implying that the polymer chains were becoming more mobile. The continued increase in chain mobility shown by ^{1}H NMR spectroscopy experiments was consistent with a mixture of micelles and free chains in solution, in agreement with the SANS analysis.

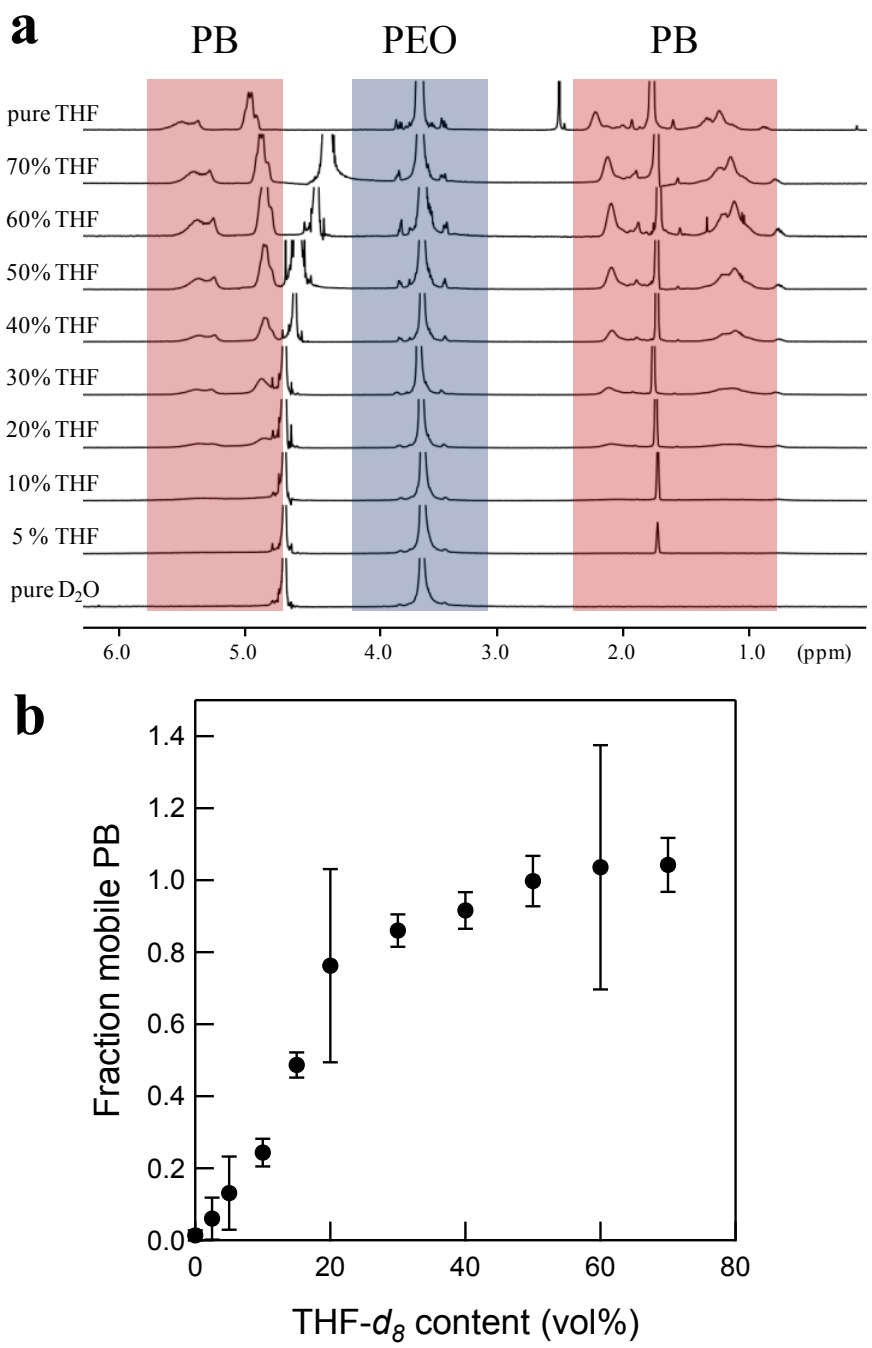

Figure 5.12 (a) ^{1}H NMR spectra of PB-PEO micelles in D_2O/THF-d_8 mixtures, boxed regions highlight the peaks associated with the PB and PEO blocks, and (b) fraction of mobile PB chains in PB-PEO micelles calculated from (a). Error bars in (b) represent standard deviation in values from three experiments.

5.4 Discussion

The work presented here demonstrates control over the structure of PB-PEO micelles by using cosolvent mixtures to manipulate the core-corona interfacial tension. The combination of real and reciprocal space techniques in the analysis of PB-PEO micelles led to new insights into the changes in micelle structure as a function of interfacial tension. The micelle sizes obtained by DLS, SAXS, and cryo-TEM data agreed well with the values obtained from SANS data model fitting. These data sets from multiple analytical techniques showed a decrease in micelle size as the interfacial tension was reduced. The lowered interfacial tension led to an increased core chain interfacial area, which favored the formation of smaller micelles with lower aggregation numbers.

The combination of analytical techniques also allowed detailed characterization of the effects of THF addition on the micelle core size, R_c. While previous studies showed a decrease in overall micelle size with reduced interfacial tension, these studies did not independently measure the micelle core size.[2,10] Instead, they calculated the core size based on the measured aggregation number, and they assumed either that there was no solvent in the core[2] or that the solvent fraction in the core was equal to the volume fraction of organic cosolvent in the micelle solution.[10] The experimental measurements of both the core size and aggregation number show that solvent was indeed present in the core and that the solvent fraction in the core was greater than the volume fraction of THF in the cosolvent mixture (Figure 5.9), in contrast to previous assumptions. The results presented here demonstrate that cosolvent addition not only leads to a decrease in R_c, but an increase in the solvent fraction in the core.

In addition to R_c, the corona thickness, H, decreased as the THF content increased. The experimentally determined H decreased from ~18 nm to ~10 nm over the THF content range used in this study. For the PEO corona chains (N = 183), the theoretical root-mean-square end-to-end distance, R_0, is 9.1 nm.[32] Thus, $H > R_0$ at all THF contents, suggesting that the corona chains were stretched, consistent with the definition of star-like micelles.[13,43] The star-like profile also was evident in the good fits to SANS data using a form factor model that accounted for a radial density distribution of corona chains. Furthermore, comparing the core and corona dimensions showed that $H > R_c$ throughout the range of solvent compositions, characteristic of a star-like structure. Likewise, comparing the experimental results to theoretical scaling relationships for star-like micelles showed a good correlation between experiment and theory for changes in R_c and H with decreasing core-corona interfacial tension (Figure 5.5). The agreement between the experimental results and scaling theory suggested that the decrease in R_c and H was primarily due to the change in interfacial tension induced by solvent addition, and reflected the increase in curvature at the core surface as the micelle size decreased. This result was supported by the small change in the PEO R_g for both the corona chains and the PEO homopolymer with THF addition, which suggested that the changing solvent conditions had very little effect on the PEO chain dimensions.

The SANS experiments also revealed that the decrease in interfacial tension also affected the composition profile at the micelle core-corona interface. Because scattering contributions from the corona were minimized, the SANS model fits for the PB-*d*PEO data were sensitive to the core-corona interfacial width (σ_{int} in the model). In pure D_2O, the micelles had a sharp core-corona interface due to the highly

amphiphilic nature of PB-PEO.[37,44-46] As the THF-d_8 content increased, the core-corona interface became more diffuse due to the reduction in interfacial tension, resulting in broader interfaces at >30 vol% THF-d_8. The effects of interfacial tension on polymer interfaces have been well studied for bulk systems, such as homopolymer blends and block polymers.[14-16,47] The work presented here shows that interfacial tension also controls the core-corona interfacial width in solution assemblies, as illustrated in Figure 5.8, in which a broad core-corona interfacial width was seen in PB-PEO micelles at higher THF-d_8 contents (*i.e.* lower core-corona interfacial tensions). Similarly, recent work by Lund and coworkers studied the effects of H_2O/DMF cosolvent mixtures on the structures of PEP-PEO micelles.[48] DMF addition lead to a morphological transition from spherical to cylindrical micelles. However, careful SANS data analysis indicated that in addition to the morphological transition, DMF addition broadened the core-corona interface.[48]

In addition to the broadening of the core-corona interface, the reduced interfacial tension resulted in a lower PEO volume fraction at the core surface (Figure 5.11). In pure D_2O, there was a high volume fraction of PEO at the core-corona interface, implying that a collapsed layer of PEO surrounded the micelle core to minimize the unfavorable PB-water interactions, consistent with previous studies.[37,49] As the interfacial tension decreased with THF-d_8 addition, the maximum volume fraction of PEO at the core-corona interface decreased, because less shielding of the PB chains was necessary.

Adding THF to the PB-PEO solutions also affected the concentration of free polymer chains in solution. In pure water, the concentration of free chains was negligible due to the extremely low critical micelle concentration (CMC), which is

reported to be on the order of 10^{-3} g L^{-1} for comparable molecular weight PB-PEO block polymers in water.[50,51] However, examination of the scattering at ~ 0.06 Å^{-1} $\leq q \leq 0.1$ Å^{-1} in the SANS data indicated that a significant concentration of free chains was present as the THF-d_8 content increased to >30 vol% (Figure 5.7). While free chains were likely present in solution at lower THF contents, the SANS data were not sensitive to the low concentration of chains. Fitting the SANS data for >30 vol% THF-d_8 with a combined form factor model for micelles and Gaussian chains indicated that the concentration of free chains increased with added THF-d_8 until complete micelle disassembly. The presence of free chains in solution was corroborated by ^{1}H NMR spectroscopy studies that showed increased PB mobility at high THF-d_8 contents. This coexistence of free chains and micelles was likely due to an increase in the CMC, resulting from the reduced interfacial tension caused by THF addition.[52-54] Assuming the maximum concentration of free chains in solution was equal to the CMC, the CMC increased exponentially with decreasing interfacial tension, which was in accordance with micelle formation theory.[52,55] This result also was qualitatively consistent with light scattering experiments that suggested that the CMC was the same order of magnitude as the concentration of free chains determined by SANS.

Another effect of high THF-d_8 contents (>50 vol%) shown in the SANS data was an upturn in intensity at low q values (Figure 5.6). This upturn became more pronounced as the THF-d_8 content was increased and suggested the presence of larger structures in solution. At these high THF contents, there was also a significant concentration of free chains in solution, which could induce depletion interactions and lead to micelle aggregation.[56,57] Similarly, previous studies by Dewalt *et al.* reported

poly(styrene-*b*-ethylene oxide) micelle aggregation in H_2O/THF mixtures at THF contents >50 vol%.[9]

5.5 Conclusions

The work presented here manipulates the structure of PB-PEO micelles in aqueous solutions by adding THF as a cosolvent to reduce the core-corona interfacial tension. The micelle size, including both the core size and corona thickness, can be tuned by adding organic cosolvents to a single block polymer. This cosolvent approach eliminates the need for the synthesis of multiple block polymers to achieve a range of micelle sizes.

The experimental data are in good agreement with theoretical models of star-like micelles for the dependence of core size and corona thickness on interfacial tension. Changes in the internal micelle structure were elucidated by performing contrast variation SANS experiments. The incorporation of both micelle and Gaussian coil form factors in the SANS models facilitated data fitting at high THF contents, where a significant number of free chains in solution were evident. Also, the core-corona interfacial region was characterized by minimizing scattering contributions from the micelle corona (using PB-*d*PEO). These experiments showed that cosolvent addition led to broader core-corona interfaces. While the broadening of polymer interfacial profiles with decreasing interfacial tension has been shown for polymer in bulk, the work presented here first demonstrated that interfacial tension also controls the core-corona interfacial width in solution assemblies. Finally, the SANS data analysis indicated that the micelle cores swelled with THF addition and that the solvent fraction in the core was greater than the volume fraction of THF in the

cosolvent mixtures, which may suggest that previous assumptions regarding the micelle core solvent contents in cosolvent mixtures may not be accurate.

The work presented here highlights the considerable effects of organic cosolvent addition on block polymer micelles. Controlling the core-corona interfacial tension is an effective, non-synthetic means of manipulating solution-assembly to access a variety of unique structures. However, even slight differences in cosolvent composition can have a significant impact on the final morphology, emphasizing the importance of processing conditions (*i.e.* cosolvent composition) on the resulting structure. The following chapters expand on these cosolvent studies and continue to explore the effects of common processing conditions on the structure, dynamics, and long-term stability of block polymer micelles.

REFERENCES

1 Lund, R. *et al.* (2011), *Macromolecules* **44**, 6145-6154

2 Lund, R., Willner, L., Stellbrink, J., Radulescu, A. & Richter, D. (2004), *Macromolecules* **37**, 9984-9993

3 Fernyhough, C., Ryan, A. J. & Battaglia, G. (2009), *Soft Matter* **5**, 1674-1682

4 Fairclough, J. P. A., Norman, A. I., Shaw, B., Nace, V. M. & Heenan, R. K. (2006), *Polymer International* **55**, 793-797

5 Shen, H. & Eisenberg, A. (1999), *Journal of Physical Chemistry B* **103**, 9473-9487

6 Choucair, A. & Eisenberg, A. (2003), *European Physical Journal E* **10**, 37-44

7 Choucair, A., Lavigueur, C. & Eisenberg, A. (2004), *Langmuir* **20**, 3894-3900

8 Liu, C., Hillmyer, M. A. & Lodge, T. P. (2008), *Langmuir* **24**, 12001-12009

9 Dewalt, L. E., Ou-Yang, H. D. & Dimonie, V. L. (1995), *Journal of Applied Polymer Science* **58**, 265-269

10 Seo, Y. S., Kim, M. W., Ou-Yang, D. H. & Peiffer, D. G. (2002), *Polymer* **43**, 5629-5638

11 Kelley, E. G., Smart, T. P., Jackson, A. J., Sullivan, M. O. & Epps, T. H. (2011), *Soft Matter* **7**, 7094-7102

12 Choucair, A. & Eisenberg, A. (2003), *European Physical Journal E* **10**, 37–44

13 Halperin, A. (1987), *Macromolecules* **20**, 2943-2946

14 Helfand, E. & Sapse, A. M. (1975), *The Journal of Chemical Physics* **62**, 1327-1331

15 Helfand, E. & Tagami, Y. (1971), *Journal of Polymer Science Part B: Polymer Letters* **9**, 741-746

16 Helfand, E. & Tagami, Y. (1972), *Journal of Chemical Physics* **56**, 3592-3601

17 Jain, S. & Bates, F. S. (2004), *Macromolecules* **37**, 1511-1523

18 Halperin, A., Tirrell, M. & Lodge, T. P. (1992), *Advances in Polymer Science* **100**, 31-71

19 Won, Y. Y., Davis, H. T. & Bates, F. S. (2003), *Macromolecules* **36**, 953-955

20 Won, Y.-Y., Brannan, A. K., Davis, H. T. & Bates, F. S. (2002), *The Journal of Physical Chemistry B* **106**, 3354-3364

21 Won, Y.-Y., Davis, H. T., Bates, F. S., Agamalian, M. & Wignall, G. D. (2000), *The Journal of Physical Chemistry B* **104**, 7134-7143

22 Zheng, Y. *et al.* (1999), *The Journal of Physical Chemistry B* **103**, 10331-10334

23 Hillmyer, M. A. & Bates, F. S. (1996), *Macromolecules* **29**, 6994-7002

24 Quirk, R. P., Gomochak, D. L., Wesdemiotis, C. & Arnould, M. A. (2003), *Journal of Polymer Science Part A: Polymer Chemistry* **41**, 947-957

25 Stafford, C. M., Roskov, K. E., Epps, T. H., III & Fasolka, M. J. (2006), *Review of Scientific Instruments* **77**, 0239081-0239087

26 Sauer, B. B. & Dipaolo, N. V. (1991), *Journal of Colloid And Interface Science* **144**, 527-537

27 Cheong, W. J. & Carr, P. W. (1987), *Journal of Liquid Chromatography* **10**, 561-581

28 Provencher, S. W. (1982), *Computer Physics Communications* **27**, 229-242

29 Aminabhavi, T. M. & Gopalakrishna, B. (1995), *Journal of Chemical & Engineering Data* **40**, 856-861

30 Roe, R.-J. *Methods of X-ray and Neutron Scattering in Polymer Science*. (Oxford University Press, 2000).

31 Kline, S. R. (2006), *Journal of Applied Crystallography* **39**, 895-900

32 Pedersen, J. S. & Gerstenberg, M. C. (2003), *Colloids and Surfaces A: Physicochemical and Engineering Aspects* **213**, 175-187

33 Bang, J., Viswanathan, K., Lodge, T. P., Park, M. J. & Char, K. (2004), *Journal of Chemical Physics* **121**, 11489-11500

34 Choi, S. Y., Bates, F. S. & Lodge, T. P. (2009), *Journal of Physical Chemistry B* **113**, 13840-13848

35 Pedersen, J. S., Svaneborg, C., Almdal, K., Hamley, I. W. & Young, R. N. (2003), *Macromolecules* **36**, 416-433

36 Bartlett, P. & Ottewill, R. H. (1992), *Journal of Chemical Physics* **96**, 3306-3318

37 Won, Y. Y., Davis, H. T., Bates, F. S., Agamalian, M. & Wignall, G. D. (2000), *Journal of Physical Chemistry B* **104**, 7134-7143

38 Higgins, J. S. & Benoît, H. C. *Polymers and Neutron Scattering*. Vol. 8 (Oxford Science Pubblications, 1996).

39 Xu, R. L., Winnik, M. A., Hallett, F. R., Riess, G. & Croucher, M. D. (1991), *Macromolecules* **24**, 87-93

40 Gref, R. *et al.* (2000), *Colloids and Surfaces B-Biointerfaces* **18**, 301-313

41 Willet, N. *et al.* (2008), *Langmuir* **24**, 3009-3015

42 Kriz, J. *et al.* (1996), *Macromolecules* **29**, 7853-7858

43 Zhulina, E. B., Adam, M., LaRue, I., Sheiko, S. S. & Rubinstein, M. (2005), *Macromolecules* **38**, 5330-5351

44 Jain, S. & Bates, F. S. (2003), *Science* **300**, 460-464

45 Won, Y. Y., Davis, H. T. & Bates, F. S. (2003), *Macromolecules* **36**, 953-955

46 Jain, S. & Bates, F. S. (2004), *Macromolecules* **37**, 1511-1523

47 Semenov, A. N. (1993), *Macromolecules* **26**, 6617-6621

48 Lund, R. *et al.* (2009), *Physical Review Letters* **102**, 188301

49 Smart, T. P., Mykhaylyk, O. O., Ryan, A. J. & Battaglia, G. (2009), *Soft Matter* **5**, 3607-3610

50 Won, Y. Y., Brannan, A. K., Davis, H. T. & Bates, F. S. (2002), *Journal of Physical Chemistry B* **106**, 3354-3364

51 Pispas, S. & Hadjichristidis, N. (2002), *Langmuir* **19**, 48-54

52 Israelachvili, J. N. *Intermolecular & Surface Forces*. 9th edn, (Elsevier Science Imprint, 2002).

53 Yu, Y. S., Zhang, L. F. & Eisenberg, A. (1998), *Macromolecules* **31**, 1144-1154

54 Zhang, L. F. & Eisenberg, A. (1995), *Science* **268**, 1728-1731

55 Leibler, L., Orland, H. & Wheeler, J. C. (1983), *Journal of Chemical Physics* **79**, 3550-3557

56 Abbas, S. & Lodge, T. P. (2007), *Physical Review Letters* **99**, 137802

57 Camargo, M. & Likos, C. N. (2010), *Physical Review Letters* **104**, 078301

Chapter 6

EFFECTS OF COSOLVENT MIXTURES ON BLOCK POLYMER MICELLE DYNAMICS

This chapter investigates the influence of cosolvent addition on the equilibrium chain exchange dynamics of highly amphiphilic block polymer micelles. Specifically, the equilibrium chain exchange kinetics were investigated using sophisticated contrast variation experiments in time-resolved small angle neutron scattering (TR-SANS). The results presented here demonstrate that the decreasing the interfacial tension between the core block and the solvent leads to measurable chain exchange and provide insights into the dynamic processes contributing to the cosolvent-induced micelle structural rearrangements studied in Chapter 5.

6.1 Introduction

Decades of experimental and theoretical work provide a foundation for controlling the static structure of block polymer micelles.[1-3] However, much less is known about the dynamics of these structures, and the factors that govern chain exchange in macromolecular surfactants are largely unexplored.[4,5] Understanding chain exchange mechanisms in block polymer assemblies is essential for controlling self-assembly, creating reproducible structures, and predicting the long-term stability of these materials.

Like the study of static block polymer assemblies, our understanding of the dynamics in these macromolecular surfactants stems from the study of small molecule amphiphiles.[5,6] Small molecule micelles are highly dynamic and the constituent

molecules are continuously redistributed among the assemblies on time scales ranging from μs to ms.[7] Aniansson and Wall first theoretically described and later experimentally demonstrated that these dynamics are dominated by single exchange events, in which an individual surfactant molecules moves from one micelle to another.[8-11]

By comparison, the dynamics in block polymer micelles are far less understood. Halperin and Alexander extended the Anniansson and Wall mechanism for single molecules exchange in surfactant micelles to block polymer assemblies.[12] Their scaling analysis suggested that the energetic barrier to single chain events in block polymer systems is significantly higher than in small molecule systems due to the macromolecular nature of the hydrophobic block. The high energetic barrier leads to significantly longer exchange kinetics, on the order of hours or even days compared to seconds in molecular surfactant assemblies. In agreement with this theoretical prediction, several experimental results have shown that dynamics are arrested in block polymer systems, with no measurable chain exchange taking place on time scales ranging from weeks to even years.[13-18]

Halperin and Alexander further suggested that the relaxation function in block polymer micelles should follow a single exponential decay for single chain events.[12] However, experimental studies indicated that the relaxation function is extremely broad and logarithmic over orders of magnitude in time.[15,19,20] Early studies attributed the broad relaxation times to geometric constraints and hindered expulsion of the core block,[15] but recent work by Lodge and Bates *et al*. demonstrated that the broad relaxation function could be attributed to polydispersity of the core block.[21] Lodge and Bates showed that single chain exchange is hypersensitive to the core block

molecular weight,[22] and thus even a small distribution of core block molecular weights significantly broadens the relaxation function.

Our limited understanding of block polymer dynamics is in part due to the experimental difficulty in accessing the appropriate time and length scales. Because of the long time scales, several approaches have been developed to induce chain exchange on more accessible time scales such as studying mildly hydrophobic polymers, changing temperature, or adding organic cosolvents.[6,15,17,18,20,22-25]

Understanding the chain exchange also requires nanoscale structural resolution. Time-resolved light scattering and cryo-TEM have been used to monitor temporal changes in the overall micelle structure, but do not provide information on the dynamics of the individual chains.[14,17,25-27] Block polymer micelle dynamics have been studied using fluorescence quenching; however, this approach often requires covalently attaching large dye molecules to the polymer chain which can influence the dynamics.[28-30] Pioneering work by Willner and coworkers exploited the contrast variation between hydrogen- and deuterium-labeled polymers in TR-SANS experiments to probe both the length scales and time scales necessary to study single chain exchange in block polymer micelles.[31] Subsequent studies have built on this work to probe the effects of core block molecular weight, cosolvent mixtures, and micelle structure on equilibrium single chain exchange.[6,15,18-24,32-34]

This chapter expands the studies of micelle dynamics and investigates the effects of cosolvent mixtures on chain exchange in poly(1,2-butadiene-*b*-ethylene oxide) (PB-PEO) micelles. Coupled with the data in Chapter 5, the results presented here provide key insights into the mechanisms that lead to cosolvent-induced micelle relaxation. Literature suggests that PB-PEO micelles are kinetically trapped in

aqueous solutions due to the highly unfavorable interaction between PB and water ($\chi_{PB/water} \approx 3.5$).[13,14,35,36] However, adding an organic cosolvent improves the solvent quality for the PB core block and induces structural changes in micelles as discussed in Chapter 5. These structural rearrangements require dynamic processes, suggesting that cosolvent addition also influences the chain exchange in PB-PEO block polymer micelles. No equilibrium chain exchange was measured at high interfacial tensions (low THF contents), suggesting the micelles remain kinetically-trapped. This result is especially interesting in the context of the data in Chapter 5 that demonstrated the addition of even a small amounts of organic cosolvent led to significant changes in the micelle structure. Together, these data indicate that the micelles must relax through an alternate mechanism, such as micelle fission. Conversely, significant chain exchange occurs at lower interfacial tension (high THF contents), implying that the micelles formed at high THF contents are able to achieve their equilibrium structure.

6.2 Experimental

6.2.1 Materials

Chain exchange experiments were performed using the PB-PEO and PB-*d*PEO polymers described in Table 2.1 and studied in Chapter 5.

6.2.2 Solution Preparation

Individual PB-PEO and PB-dPEO micelle solutions were prepared by dissolving each dry polymer powder in a separate D_2O/H_2O mixture and then stirring for 3 days. Then, deuterated tetrahydrofuran (THF-d_8) was added to reach the desired cosolvent composition. The isotopic composition of the solvent (summarized in

Table 6.1) was chosen to contrast match a perfectly mixed PEO/dPEO corona. The composition of the solvent was calculated according to,

$$\rho_{solvent} = \phi_{H_2O}\rho_{H_2O} + \left(1 - \phi_{H_2O} - \phi_{THF-\mathrm{d_8}}\right)\rho_{D_2O} + \phi_{THF-\mathrm{d_8}}\rho_{THF-\mathrm{d_8}} \quad (1)$$

in which ϕ_{H_2O} is the calculated volume fraction of H_2O, $\phi_{THF-\mathrm{d_8}}$ is the desired volume fraction of THF-d_8, and ρ_{H_2O}, ρ_{D_2O}, and $\rho_{THF-\mathrm{d_8}}$ are the scattering length densities of H_2O, D_2O and THF-d_8, respectively (Table 5.2). The scattering length density of the solvent, $\rho_{solvent}$ was set equal to the scattering length density of a completely mixed 50/50 PEO/*d*PEO corona,

$$\rho_{PEO/dPEO} = 0.5\rho_{PEO} + 0.5\rho_{dPEO} \quad (2)$$

in which ρ_{PEO} and ρ_{dPEO} are the scattering length densities of PEO and *d*PEO, respectively (Table 5.2), and $\rho_{PEO/dPEO} = 3.52 \times 10^{-6}$ Å^{-2}.

Both the PB-PEO and PB-*d*PEO solutions had a final polymer concentration of 2.4 mg mL^{-1}. At t = 0, equal volumes of the PB-PEO and PB-*d*PEO solutions were mixed and analyzed with SANS as described below.

Table 6.1 Solvent mixture compositions for TR-SANS experiments

Sample	% by volume		
	H_2O	**D_2O**	**THF-d_8**
0 vol% THF	36	64	-
10 vol% THF	36	54	10
30 vol% THF	36	34	30

Pre-mixed PB-PEO/PB-*d*PEO (50% PB-PEO by weight) micelle solutions were prepared using a similar approach. First, the PB-PEO and PB-*d*PEO polymers were blended in benzene, stirred overnight, and then freeze-dried to ensure complete solvent removal. Then, the polymer blend was dissolved in a D_2O/H_2O mixture and stirred for 3 days. THF-d_8 was added to reach the desired solvent composition and the solution was stirred for an additional 3 days prior to the SANS experiments. The final solution concentration of polymer was 2.4 mg mL^{-1}.

6.2.3 Time-Resolved Small Angle Neutron Scattering (TR-SANS)

SANS experiments were performed on the CG-2 General Purpose SANS instrument at the High Flux Isotope Reactor (HFIR) at Oak Ridge National Laboratory (ORNL). A sample-to-detector distance of 14 m was used with an incident neutron wavelength (λ) of 4.75 Å to cover a scattering vector (q) range from 0.006 $Å^{-1} < q <$ 0.09 $Å^{-1}$. Scattering data were recorded for 5 min and were reduced using the procedures provided by ORNL. The data were corrected for background scattering, empty cell scattering, sample transmission, sample thickness, and detector sensitivity and were normalized to an absolute scale using a pre-calibrated secondary standard.

6.2.4 TR-SANS Data Analysis

In dilute solutions, the scattered intensity $I(q,t)$ is given by $I(q,t) = \varphi(\Delta\rho)^2 P(q)$ in which φ is the volume fraction of the micelles, $\Delta\rho$ is the scattering contrast, and $P(q)$ is the micelle form factor. Assuming the sample concentration [φ] and the form factor [$P(q)$] do not change over time, any changes in scattered intensity are due to changes in the scattering contrast,

$$\Delta\rho = \rho_{micelle}(t) - \rho_{solvent} \tag{3}$$

in which $\rho_{micelle}$ is the scattering length density of the micelle and $\rho_{solvent}$ is the scattering length density of the solvent. The scattering length density of the solvent is fixed, and therefore $I(q,t) \propto \rho_{micelle}(t)$. Because $\rho_{micelle}(t)$ is proportional to the volume fraction of PEO (or *d*PEO) chains in the micelle, the instantaneous state of chain exchange can be directly related to the scattered intensity and represented by the time correlation function,

$$R(t) = \left(\frac{I(t) - I(\infty)}{I(0) - I(\infty)}\right)^{1/2} \tag{4}$$

in which $I(t)$ and $I(\infty)$ are the scattered intensities at t = 0 and t = ∞ (corresponding to a perfectly mixed corona micelle), respectively.

The equilibrium chain exchange kinetics were analyzed using the method developed by Choi *et al*.[22] Single chain exchange from one micelle to another requires 3 steps: (1) extraction of the core block, (2) diffusion of the chain through the solvent, and (3) reinsertion into another micelle (Figure 6.1).

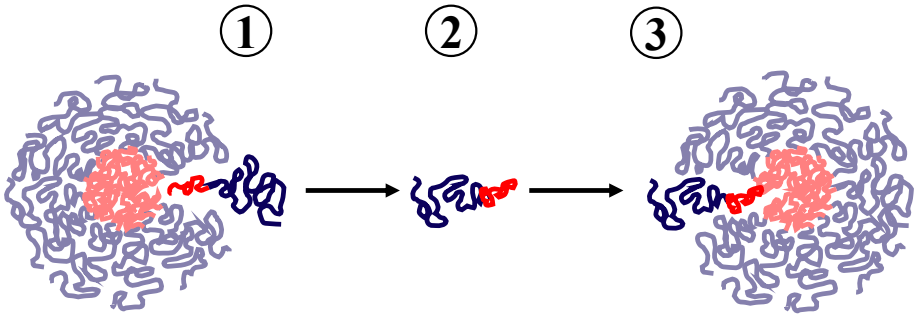

Figure 6.1 Schematic representation of single chain exchange mechanism, showing (1) extraction of the core block, (2) diffusion of the chain through the solvent, and (3) reinsertion of the chain into another micelle. Extraction of the core block (step 1) is assumed to the rate-limiting step.

Assuming that the extraction of the core block is the rate limiting step,[12,15,22,37] the flux of chain exchange should be related to the expulsion rate, $K(t) = \exp(-t/\tau(N)\times E_a)$, in which τ(N) is the characteristic exchange time and E_a is the energy barrier to chain exchange. Assuming the micelle cores are in the melt state, the core block dynamics are described by the Rouse relation time, $\tau_{Rouse} = (N^2 b^2 \zeta)/(6\pi^2 kT)$, in which N is the degree of polymerization, b is the statistical segment length, ζ is the monomeric friction factor, k is the Boltzmann constant, and T is the temperature.[22] It is important to note that this scaling only applies to unentangled polymers.

The core block comes into contact with the solvent during chain exchange; therefore, removing a chain from a micelle also carries a thermodynamic penalty. This contact results in enthalpically unfavorable interactions between the core block and the solvent, resulting in an overall energy penalty of exp(-αχN), in which α is an unknown constant of order 1 and χ is the Flory-Huggins interaction parameter between

the core block and solvent. Thus, the time correlation function for chain exchange can be expressed as

$$K(t,N) = exp\left[-t\frac{6\pi^2 kT}{N^2 b^2 \zeta} exp\ (-\alpha\chi N)\right] \quad (5)$$

As recently described Choi *et al.*, $K(t)$ has a double exponential dependence on chain length.[22] Accordingly, the rate of chain exchange is hypersensitive to the distribution of N. Dispersity in N is inherent in polymeric systems and even a small distribution of N will significantly broaden the time correlation function.

Dispersity in polymeric systems is typically described by a Schulz-Zimm distribution,[38,39]

$$P(N_i) = \frac{z^{z+1}}{\Gamma(z+1)}\frac{N_i^{z-1}}{N_n^z}\exp\left(\frac{-zN_i}{N_n}\right) \quad (6)$$

in which $z = 1/[N_w/N_n) - 1]$, and N_w and N_n are the weight-average and number-average degrees of polymerization, respectively.

The final relation function is given by

$$R(t) = \int_1^\infty P(N)K(t,N)dN \quad (7)$$

In this analysis, there are only two fitting parameters: $\alpha\chi$ and the dispersity, N_w/N_n.

6.3 Results

6.3.1 TR-SANS Studies of Micelles in Cosolvent Mixtures

The single chain dynamics of PB-PEO micelles were investigated by exploiting contrast variation experiments as depicted in Figure 6.2. In these experiments, equal volumes of PB-PEO and PB-*d*PEO micelle solutions were mixed at t = 0, giving rise to the maximum scattered intensity due to contrast between the coronas and the solvent. After mixing the micelle solutions, two possible outcomes were considered. In the first scenario, chain exchange would occur, leading to randomization of the PB-PEO and PB-*d*PEO chains in the micelles. This mixing of the chains would reduce the corona/solvent contrast and decrease the scattered intensity, as the isotopic composition of the solvent was selected to contrast-match a randomly mixed PEO/*d*PEO corona. The minimum scattered intensity in a randomly mixed PB-PEO/PB-*d*PEO micelle is represented by the pre-mixed samples, in which the polymers were blended before dispersing the polymers in water. In the second scenario, single chain exchange would not occur and the scattered intensity would remain nearly constant with time.

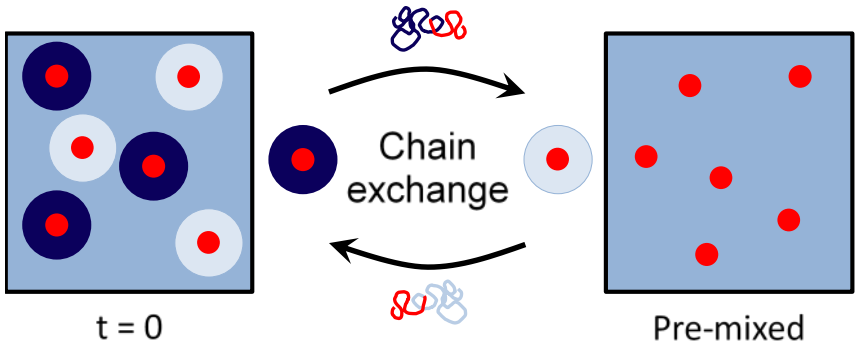

Figure 6.2 **Schematic representation of chain exchange experiments. At t= 0, PB-PEO and PB-*d*PEO micelles are mixed. Single chain exchange leads to randomization of the PEO/*d*PEO chains in the micelle corona, which contrast matches the solvent.**

As seen in Figure 6.3, the scattered intensity did not decrease over an ~19 day period, supporting the second scenario and a lack of appreciable chain exchange in micelles prepared in pure water. Similarly, no chain exchange was measured for micelles prepared in 10 vol% THF-d_8, even at elevated temperatures (Figure 6.3).

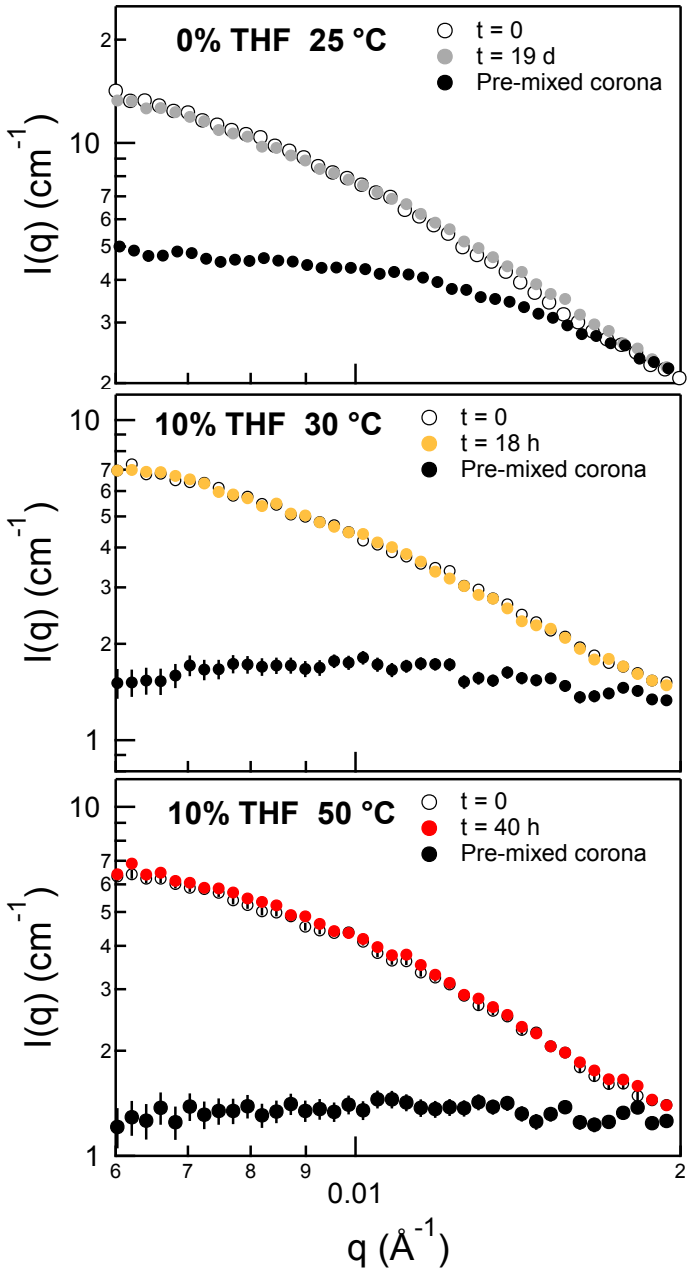

Figure 6.3 **TR-SANS curves for mixtures of PB-PEO and PB-*d*PEO micelles in 30 vol% THF-d_8 cosolvent mixtures in D_2O/H_2O at 30 °C (top), 10 vol% THF-d_8 at 30 °C (middle), and 10 vol% THF-d_8 at 50 °C (bottom).**

Conversely, equilibrium chain exchange events readily occurred in micelles prepared in 30% THF-d_8 at elevated temperatures, as seen by the significant decrease in scattered intensity (Figure 6.4). Also, the rate of chain exchange increased with increasing temperature. At 30 °C, no measurable chain exchange took place after 19 h. However, increasing the temperature to 55 °C resulted in a measurable decrease in scattering intensity after 13.6 h, indicative of mixing of the PB-PEO/PB-*d*PEO chains. Further increasing the temperature to 60 °C lead to an almost statistical distribution of chains within 8 h, as seen in similarity of the t = 8 h and pre-mixed corona curves. Comparing the results at 55 °C and 60 °C indicated that even a 5 °C difference in temperature significantly influenced the exchange kinetics in these systems. *Note that no degradation of the block polymer was found after annealing at 60 °C for 24 h.*

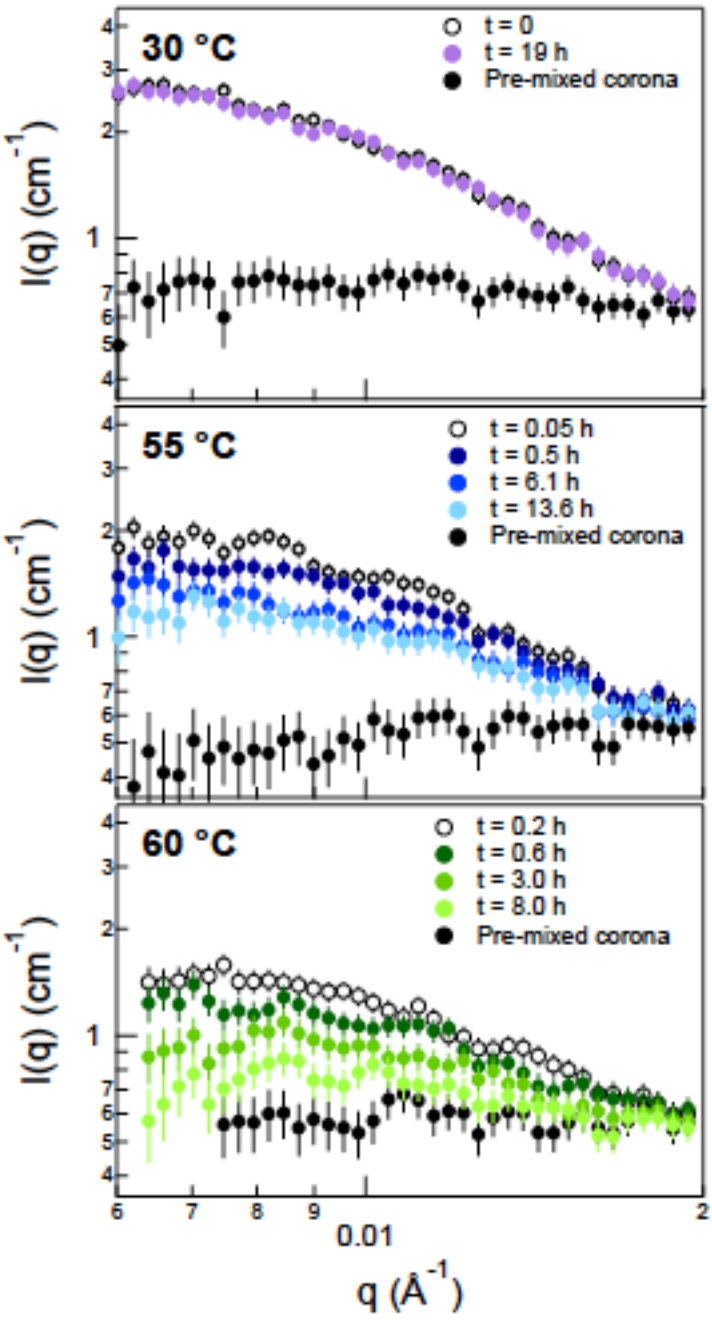

Figure 6.4 **TR-SANS curves for mixtures of PB-PEO and PB-*d*PEO micelles in 30 vol% THF-d_8 cosolvent mixtures at 30 °C (top), 55 °C (middle), and 60 °C (bottom).**

6.3.2 Chain Exchange Kinetics in Low Interfacial Tension Systems

The scattered intensity is directly related to the fraction of PEO (or *d*PEO) chains in the corona according to Equation 4, and therefore the scattered intensity is also reflective of the extent of chain exchange. Rather than using the scattered intensity at a specific q-value to calculate R(t), the scattered intensities were integrated over a q-range of 0.01 $Å^{-1} < q < 0.02$ $Å^{-1}$. This analysis helped to minimize the uncertainty in the calculated R(t) values due to the uncertainty in the measured I(t) values. The relaxation function for the 30 vol% THF-d_8 at different temperatures is presented in Figure 6.5a. The relaxation functions were logarithmic with time, consistent with previous reports in literature.[20,22,34]

To access a broader range of relaxation times, the time-temperature superposition (TTS) principle was applied to the data sets in Figure 6.5a. This principle is used routinely in rheological studies of polymer melt dynamics to account for changes in the molecular relaxation times at a temperature (T) relative to a reference temperature (T_{ref}).[22,40,41] While TTS is not strictly applicable to block polymer systems if the temperature-dependencies of the polymer blocks differ,[41] single chain exchange is dictated primarily by the temperature-dependent relaxation of the hydrophobic block. Accordingly, the TTS principle has been applied successfully to the exchange kinetics in several block polymer micelle systems.[21,22,33,34,42] In this work, the individual temperature data sets were shifted along the time-axis until they overlapped with the T_{ref} = 55 °C data set. The empirical shift factors (a_T) also are plotted as $\log[a_T(T)]$ in the inset to Figure 6.5b.

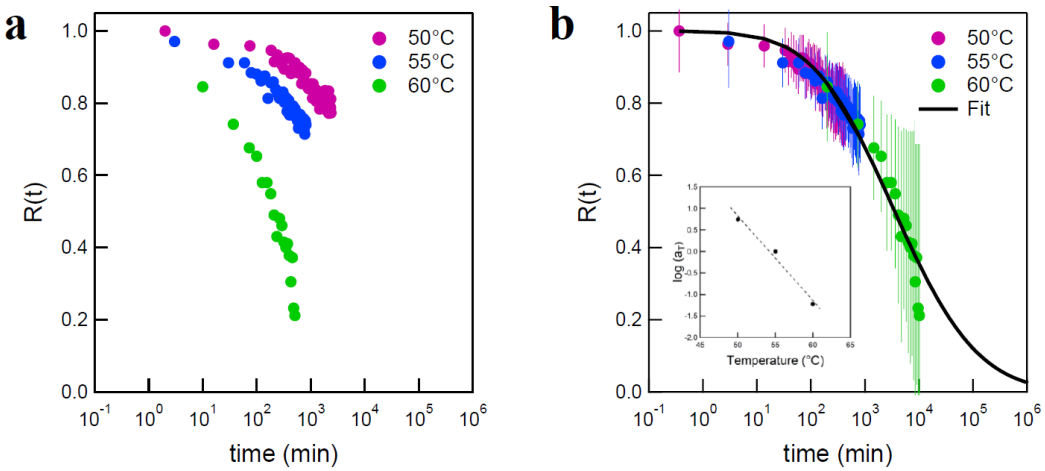

Figure 6.5 **(a) Relaxation function for the 30 vol% THF-d_8 micelle solution as a function of temperature. (b) Time-temperature superposition of TR-SANS data and fit for T_{ref} = 55 °C. Empirical shift factors for time-temperature superposition are given in inset of (b).**

The relaxation function for the 30 vol% THF-d_8 solution was fit according to Equation 7 by varying only the dispersity index (N_w/N_n) and the core block-solvent interaction ($\alpha\chi$). The monomeric friction factor (ζ) and the statistical segment length (b) for 1,2 polybutadiene were taken from literature.[43,44] Both the input and fit results are summarized in Table 6.2. Importantly, the fit quality was highly sensitive to the fit parameters but only slightly affected by the other input parameters. For example, a two-fold increase in the monomeric friction factor or statistical segment length did not affect the fit value for dispersity and resulted in less than a 10% change in the fit value of $\alpha\chi$. Conversely, the fit value of the dispersity significantly affected the shape of the relaxation function; simply changing the value of N_w/N_n from 1.0 (monodisperse) to 1.03 broadened the relaxation function and provided a much better fit to the data. This

fit value of the dispersity was in reasonable agreement with values obtained from SEC and MALDI-TOF MS for the PB-OH precursor (Table 2.1). Also, a 10% change in the $\alpha\chi$ value shifted the relaxation function over orders of magnitude in time.

Table 6.2 Input and fit parameters for fitting TR-SANS data for 30 vol% THF PB-PEO micelle solution at 55 °C

N_n (input)	ζ [kg s^{-1}] (input)	b [nm] (input)	N_w/N_n (fit)	$\alpha\chi$ (fit)
59	7.59 X 10^{-5}	0.67	1.03	0.23

6.4 Discussion

The complete lack of chain exchange in pure water seen here is consistent with several previous reports on block polymer micelles that show that these systems are kinetically trapped over time scales of days, months, and even years.[13-18] Interestingly, while adding a small amount of THF (10 vol%) led to significant changes in the micelle size as discussed in Chapter 5, it did not induce measurable chain exchange. The TR-SANS studies suggested that the micelles were still kinetically-trapped structures at high interfacial tensions (low THF contents). These results also provided insight into how the micelles rearranged upon cosolvent addition. The lack of single chain exchange suggested that the micelles rearranged through fusion/fission events at high interfacial tensions. Recent work by Meli *et al*. studied the formation of PB-PEO micelles in ionic liquids and found that the micelles decreased in size upon thermal annealing.[45,46] Similar to the work presented here, there was no measurable single chain exchange, leading Meli and coworkers to conclude that the micelles relaxed through fission events.[45]

Unlike the low THF content micelles, the micelle samples in 30 vol% THF showed measurable chain exchange at high temperatures over a period of several hours. Early TR-SANS experiments by Lund and coworkers elegantly demonstrated that manipulating cosolvent composition is an effective means of tuning block polymer single chain exchange dynamics to experimentally accessible time scales. Comparing the results for PB-PEO in water/THF mixtures to their results for poly(ethylene-*alt*-propylene-*b*-ethylene oxide) (PEP-PEO) in water/dimethylformamide (DMF) mixtures suggests that measurable chain exchange events occur at similar core-solvent interfacial tensions (γ). In their studies, almost complete chain exchange occurred within 24 h at $\gamma = 19.7$ mN m^{-1}. This finding is in good agreement with the results in Figure 6.4 demonstrating that complete chain exchange occurred within approximately 8 h at $\gamma = 18.6$ mN m^{-1} (30 vol% THF).

Choi *et al.* recently developed a theoretical explanation for the broad relaxation functions measured during chain exchange experiments, and demonstrated that these processes were hypersensitive to the core block molecular weight and molecular weight distribution.[22] Importantly, their work suggested that the relaxation kinetics also have a double exponential dependence on the hydrophobic polymer-solvent interaction parameter (χ), implying that the exchange kinetics are equally sensitive to the solvent quality. This predication is consistent with the results presented here, which show vastly different dynamics depending on the cosolvent composition. The theoretical relaxation function quantifies the core-solvent interaction in terms of χ rather than interfacial tension. However, the core-solvent interfacial tension is directly related to the interaction parameter according to $\gamma^2 \propto \chi$.[15,47] Based on the results in Chapter 5, adding 30 vol% THF to water reduces the core-solvent interfacial tension

from 49.6 mN m^{-1} to 18.6 mN m^{-1}, which corresponds to an approximately 90% decrease in χ. Assuming that $\chi_{PB\text{-}water} \approx 3.5$, $\chi_{PB\text{-}cosolvent}$ should be on the order of 0.4 in a 30 vol% THF cosolvent mixture. This value is the same order of magnitude of $\alpha\chi = .23$ at T = 55 °C from the TR-SANS data analysis, in which α is a constant on the order of unity. Literature values for α range from $0.27 < \alpha < 1.3$,[21,22,48] supporting that the fit value for χ is in very good agreement with the expected value.

Given the good agreement between the expected and fit values for χ, the relaxation functions for all of the high THF content samples were estimated using the same analysis described above. The measured interfacial tension and calculated values of χ are presented in Table 6.3. The relaxation functions at T = 25 °C were calculated according to Equation 7 and are plotted in Figure 6.6.

As seen in Figure 6.6, the dynamics at high THF content cosolvent mixtures (> 40 vol% THF) occur over 10 orders of magnitude in time. In samples containing $\geq$ 50 vol% THF the chain exchange dynamics occur within minutes, supporting that these structures are at equilibrium. These fast chain exchange time scales also suggest that single chain events contributed to the structural rearrangements upon cosolvent addition that were studied in Chapter 5. Moreover, these results demonstrate that even slight differences in $\alpha\chi$ significantly affect the relaxation function, highlighting the influence of solvent quality on not only the structure, but also the dynamics of block polymer micelles.

Table 6.3 Estimated χ values for the different H_2O/THF mixtures at 25 °C

THF content (vol%)	Interfacial tension (dyne/cm)	χ
40	15.2	0.33
50	9.4	0.13
60	6.6	0.062
70	5.3	0.040

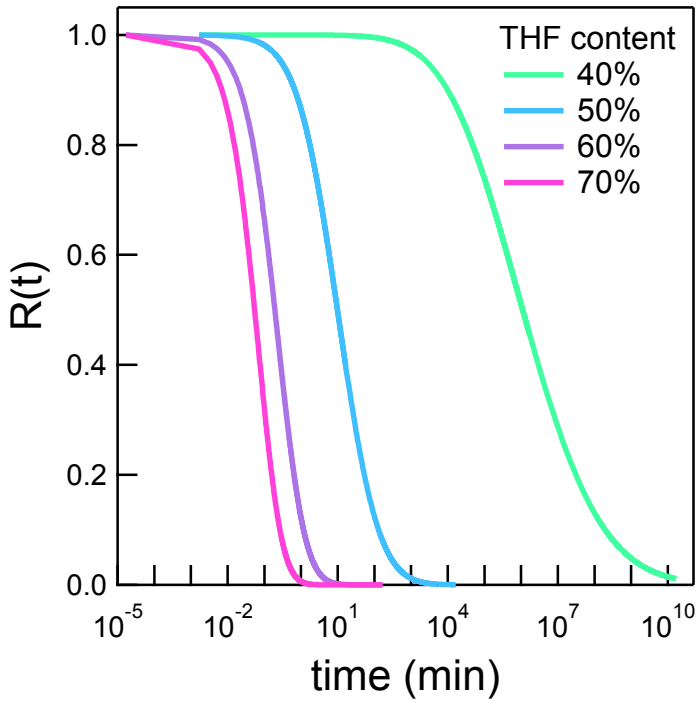

Figure 6.6 Estimated relaxation functions for PB-PEO micelles in H_2O/THF cosolvent mixtures at 25 °C.

6.5 Conclusions

This chapter investigates the effects of cosolvent mixtures on the chain exchange dynamics of PB-PEO diblock copolymer micelles. Contrast variation in TR-SANS experiments revealed that the micelles were kinetically trapped at low THF contents (high core block-cosolvent interfacial tension), with no measurable exchange taking place over long time scales. However, chain exchange events occurred over measurable time scales at elevated temperatures in micelles prepared in 30 vol% THF cosolvent mixtures. The core-solvent interaction parameter determined by fitting the relaxation function was consistent with the decrease in interfacial tension measured in Chapter 5. This analysis suggests that the micelles prepared in the high THF contents cosolvent mixtures ($\geq$ 50 vol% THF) are likely the equilibrium structures and that single chain events contribute to the structural rearrangements studied in Chapter 5. Thus, these results provide insights into the dynamic processes that lead to structural rearrangements and highlight the influence of cosolvent mixtures on both the structure and dynamics of block polymer micelles.

REFERENCES

1 Hayward, R. C. & Pochan, D. J. (2010), *Macromolecules* **43**, 3577-3584

2 Blanazs, A., Armes, S. P. & Ryan, A. J. (2009), *Macromolecular Rapid Communications* **30**, 267-277

3 Smart, T. *et al.* (2008), *Nano Today* **3**, 38-46

4 Nicolai, T., Colombani, O. & Chassenieux, C. (2010), *Soft Matter* **6**, 3111-3118

5 Denkova, A. G., Mendes, E. & Coppens, M. O. (2010), *Soft Matter* **6**, 2351-2357

6 Lund, R. *et al.* (2011), *Macromolecules* **44**, 6145-6154

7 Wennerstrom, H. & Lindman, B. (1979), *Physics Reports-Review Section of Physics Letters* **52**, 1-86

8 Aniansson, E. A. G. & Wall, S. N. (1974), *Journal of Physical Chemistry* **78**, 1024-1030

9 Aniansson, E. A. G. & Wall, S. N. (1975), *Journal of Physical Chemistry* **79**, 857-858

10 Aniansson, E. A. G. *et al.* (1976), *Journal of Physical Chemistry* **80**, 905-922

11 Wall, S. N. & Aniansson, G. E. A. (1980), *Journal of Physical Chemistry* **84**, 727-736

12 Halperin, A. & Alexander, S. (1989), *Macromolecules* **22**, 2403-2412

13 Won, Y. Y., Davis, H. T. & Bates, F. S. (2003), *Macromolecules* **36**, 953-955

14 Jain, S. & Bates, F. S. (2004), *Macromolecules* **37**, 1511-1523

15 Lund, R., Willner, L., Richter, D. & Dormidontova, E. E. (2006), *Macromolecules* **39**, 4566-4575

16 Jacquin, M. *et al.* (2007), *Journal of Colloid and Interface Science* **316**, 897-911

17 Zhang, L., Shen, H. & Eisenberg, A. (1997), *Macromolecules* **30**, 1001-1011

18 Lund, R., Willner, L. & Richter, D. (2013), *Advances in Polymer Science* **259**, 51-158

19 Lund, R. *et al.* (2007), *Journal of Applied Crystallography* **40**, S327-S331

20 Lund, R., Willner, L., Stellbrink, J., Lindner, P. & Richter, D. (2006), *Physical Review Letters* **96**, 068302

21 Choi, S. H., Bates, F. S. & Lodge, T. P. (2011), *Macromolecules* **44**, 3594-3604

22 Choi, S. H., Lodge, T. P. & Bates, F. S. (2010), *Physical Review Letters* **104**, 047802

23 Lund, R., Willner, L., Stellbrink, J., Radulescu, A. & Richter, D. (2004), *Macromolecules* **37**, 9984-9993

24 Zinn, T., Willner, L., Lund, R., Pipich, V. & Richter, D. (2012), *Soft Matter* **8**, 623-626

25 Kositza, M. J., Bohne, C., Alexandridis, P., Hatton, T. A. & Holzwarth, J. F. (1999), *Macromolecules* **32**, 5539-5551

26 Zhu, Z. *et al.* (2007), *Macromolecules* **40**, 6393-6400

27 Zhang, J., Xu, J. & Liu, S. (2008), *The Journal of Physical Chemistry B* **112**, 11284-11291

28 Creutz, S., van Stam, J., Antoun, S., De Schryver, F. C. & Jérôme, R. (1997), *Macromolecules* **30**, 4078-4083

29 Creutz, S., van Stam, J., De Schryver, F. C. & Jérôme, R. (1998), *Macromolecules* **31**, 681-689

30 Prochazka, K. *et al.* (1992), *Macromolecules* **25**, 454-460

31 Willner, L., Poppe, A., Allgaier, J., Monkenbusch, M. & Richter, D. (2001), *Europhysics Letters* **55**, 667-673

32 Lund, R. *Small Angle Neutron Scattering as a Tool to Study Kinetics of Block Copolymer Micelles*. Vol. 161 Springer-Verlag Berlin, 2010.

33 Lu, J., Bates, F. S. & Lodge, T. P. (2013), *ACS Macro Letters* **2**, 451-455

34 Lu, J., Choi, S., Bates, F. S. & Lodge, T. P. (2012), *ACS Macro Letters* **1**, 982-985

35 Jain, S. & Bates, F. S. (2003), *Science* **300**, 460-464

36 Won, Y.-Y., Davis, H. T., Bates, F. S., Agamalian, M. & Wignall, G. D. (2000), *The Journal of Physical Chemistry B* **104**, 7134-7143

37 Dormidontova, E. E. (1999), *Macromolecules* **32**, 7630-7644

38 Schulz, G. V. (1939), *Zeitschrift Fur Physikalische Chemie-Abteilung B-Chemie Der Elementarprozesse Aufbau Der Materie* **43**, 25-46

39 Zimm, B. H. (1948), *Journal of Chemical Physics* **16**, 1099-1116

40 Rubinstein, M. & Colby, R. H. *Polymer Physics*. Oxford, 2008.

41 Hiemenz, P. C. & Lodge, T. P. *Polymer Chemistry*. 2nd edn, CRC Press, 2007.

42 Schaeffel, D. *et al.* (2014), *ACS Macro Letters*, 428-432

43 Liu, W., Yang, Y. & He, T. (1988), *Polymer* **29**, 1789-1792

44 Ren, Y., Lodge, T. P. & Hillmyer, M. A. (2002), *Macromolecules* **35**, 3889-3894

45 Meli, L. & Lodge, T. P. (2009), *Macromolecules* **42**, 580-583

46 Meli, L., Santiago, J. M. & Lodge, T. P. (2010), *Macromolecules* **43**, 2018-2027

47 Broseta, D., Fredrickson, G. H., Helfand, E. & Leibler, L. (1990), *Macromolecules* **23**, 132-139

48 Cavicchi, K. A. & Lodge, T. P. (2003), *Macromolecules* **36**, 7158-7164

Chapter 7

CONSQUENCES OF COSOLVENT REMOVAL ON THE STABILITY OF BLOCK POLYMER MICELLES

This chapter explores the effects of organic cosolvent removal on the stability of block polymer assemblies. Chapters 5 and 6 demonstrated that cosolvent addition significantly affects the structure and dynamics of block polymer micelles, respectively, and this chapter demonstrates that cosolvent removal can have unexpected implications for the long terms stability of these assemblies. This chapter shows that unequivocal step-change shifts in micelle populations occur over several weeks following transfer into a highly selective solvent. The unexpected micelle growth evolves through a bimodal distribution separated by multiple fusion events and critically depends on solution agitation. Notably, these results underscore fundamental similarities between assembly processes in amphiphilic polymer, small molecule, and protein systems. Parts of this work were reproduced or adapted with permissions from Kelley, E. G.; Murphy, R. P. *et al.* Nature Communications **2014** DOI: 10.1038/ncomms4599.

7.1 Introduction

Self-assembly schemes provide a simple and tuneable approach for creating a myriad of well-defined nanostructures from designer macromolecules in bulk, thin film, and solution environments. Decades of fundamental research provide a foundation for understanding and controlling self-assembled morphologies, making macromolecules pivotal in the development of many emerging nanotechnologies. In

particular, polymeric nanostructures in solution have attracted significant attention in the drug delivery, cosmetics, dispersant technology, sensor, and nanoreactor arenas.[1-3] Many of the envisioned applications endeavour to exploit solution assemblies as nanocontainers for the encapsulation of small molecule cargoes such as drugs/therapeutics or other reagents, requiring a detailed understanding of the dynamic processes and long-term stability of solution-assembled nanostructures.

Amphiphilic macromolecules, such as block polymers, are promising for the abovementioned applications as molecular design offers enormous chemical versatility and exquisite control over the size and shape of solution assemblies. Like their small molecule surfactant analogues, amphiphilic macromolecules form various nanostructures in aqueous solutions including spherical micelles, cylindrical micelles, and vesicle bilayers.[4-6] Of particular interest are the unique material properties conferred by the macromolecular nature of the hydrophobic block, such as extremely low critical aggregation concentrations (CACS) and exceptionally slow inter-aggregate chain exchange in highly selective solvents such as water.[6-9] These characteristics overcome key limitations of small molecule aggregates by improving the retention of encapsulated cargo for drug delivery[6,8] and nanoreactor applications.[10] The slow dynamic processes inherent to macromolecular amphiphiles also lead to kinetically-trapped structures, requiring careful optimization of preparation conditions to produce well-defined, uniform, and reproducible solution assemblies.[8]

Many common preparation methods employ cosolvent mixtures to create well-defined and classical solution nanostructures that mirror the morphologies expected from equilibrium thermodynamics (e.g. spherical micelles, cylindrical micelles, and vesicles).[8,11,12] In these cases, the block polymer is dissolved in a

common solvent for both polymer blocks, and then a selective solvent is added. This selective solvent normally increases the energy barrier to dynamic processes and potentially allows one to kinetically trap specific morphologies.[8] Several groups have exploited cosolvent processing routes to produce non-equilibrium and exotic nanostructures such as patchy spheres,[13] striped cylinders,[13,14] and toroids.[15] By manipulating the solvent selectivity for the block polymer constituents, these examples demonstrate the power of cosolvent processing to create complex, hierarchical structures from simple building blocks.[8,13]

Cosolvent processing principles also are employed regularly in the loading of self-assembled morphologies with various hydrophobic cargoes such as dyes and therapeutic agents for diagnostics and drug delivery applications.[16-18] Cosolvent methods are essential to solubilize both the hydrophobic cargo and amphiphilic block polymer to facilitate efficient encapsulation within self-assembled nanocarriers. As nanocarriers are routinely used in aqueous solution, these preparation methods also hinge on the assumption that the assemblies are kinetically-trapped following transfer from an organic/aqueous solution into water. Nanocarrier functionality is directly determined by size and shape, and hence the validity of this assumption is of the utmost importance. However, the resulting metastable nanostructures may rearrange given a sufficiently large driving force.[8]

Although the effects of cosolvent introduction on the generation of block polymer assemblies are well-researched,[19-22] the consequences of cosolvent removal on self-assembled structures typically are overlooked. While some macromolecular assemblies are known to be kinetically-trapped over time scales of days[22-24] or even months,[25] a cohesive understanding of polymeric micelle dynamics is still lacking.

This information gap exists because the dynamic processes are influenced by numerous coupled factors that can depend upon how far removed the assemblies are from their equilibrium configuration (*e.g.* aggregation number, size, and shape).[7,9,26,27]

This chapter demonstrates that significant dynamic processes can occur in block polymer micelles following cosolvent removal, even in highly selective solvents, provided that the system is perturbed sufficiently far from equilibrium. In the absence of agitation, the micelles were stable, consistent with scaling theories that predict insurmountable energy barriers to dynamic processes.[19,28] However, gentle agitation, which is not considered in these scaling theories, led to a marked increase in the micelle size. The micelle sizes evolved through a bimodal distribution, in which well-defined step-changes in size led to a monodisperse final nanostructure population with an aggregation number approximately eight times larger than that of the starting population. These results provide the first detailed experimental evidence for a distinct bimodal size distribution during a fusion-controlled micelle growth process and emphasize the influence of common preparation conditions (*e.g.* cosolvent addition, dialysis, agitation) on the long-term stability on block polymer assemblies.

7.2 Experimental

7.2.1 Materials

The PB-PEO and PB-*d*PEO polymers studied in this chapter are described in Table 2.1.

7.2.2 Micelle Solution Preparation

Micelle solutions were prepared by adding 18 MΩ water to dry polymer powder and stirring the solutions for 3 days. Then, THF (optima, 99.9%, Fisher Scientific) was added to achieve the desired cosolvent composition, and the solutions were stirred for an additional 3 days. The micelle solutions were dialzed (Spectra/Por Regenerated Cellulose Dialysis Tubing, MWCO 12 to 14 kg mol^{-1}) against water for 24 h with 3 water changes to completely remove the cosolvent. ^{1}H NMR experiments confirmed there was no THF in the sample after the first solvent change. Day 0 refers to the end of the dialysis. Solutions were magnetically stirred (200 rpm) at room temperature between experiments.

The polymer concentration post-dialysis was determined at the end of the studies by either measuring the UV-Vis absorbance of the polymer solution samples or by drying a known volume of the solution specimen and weighing the remaining polymer. For the UV-Vis experiments, the measured absorbance values for the solution samples were compared to a calibration curve for micelle solutions with known concentrations. *Note that the measured UV-Vis absorbance depended on the micelle size. Therefore, the absorbance of the dialyzed samples was measured at least 20 days after dialysis when the micelle sizes plateaued.* As expected due to swelling of the dialysis tubing, the sample concentrations after dialysis were approximately half of the initial concentration. The polymer concentration post-dialysis are summarized in Table 7.1.

Table 7.1 Micelle solution concentrations before and after dialysis.

Sample	Concentration before dialysis[a] (mg mL^{-1})	Concentration after dialysis[b] (mg mL^{-1})
PB-PEO	10.0 ± 0.1	5.5 ± 0.1
PB-PEO	5.0 ± 0.1	2.6 ± 0.1
PB-PEO	2.4 ± 0.1	1.4 ± 0.1
88 wt% PB-*d*PEO/12 wt% PB-PEO	10.1 ± 0.1	5.6 ± 0.3
88 wt% PB-*d*PEO/12 wt% PB-PEO	5.0 ± 0.1	2.7 ± 0.3
88 wt% PB-*d*PEO/12 wt% PB-PEO	2.4 ± 0.1	2.1 ± 0.3

[a] Calculated based on the polymer and solvent masses used in solution preparation. Uncertainty in concentration was due to error in measured masses.
[b] Determined using UV-Vis absorbance. Uncertainty in concentration represents the 95% confidence interval.

7.2.3 Dynamic Light Scattering (DLS)

DLS experiments were performed using a Brookhaven Instruments Light Scattering System (BI-200SM, Brookhaven Instruments Corporation) equipped with a Lexel Laser operating at 488 nm. Measurements were made at a scattering angle of 90°, and all experiments were performed at 25 ^{o}C. The autocorrelation functions were fit with the quadratic cumulant expansion. Literature values for the viscosity and refractive index of water/THF mixtures used to analyze the DLS data before cosolvent removal are listed in Table 5.1.[29]

7.2.4 Small Angle X-ray Scattering (SAXS)

SAXS experiments were performed on the 12-ID-C beamline at the Advanced Photon Source (APS) at Argonne National Lab. Data were collected using an incident X-ray wavelength (λ) of 0.73 Å and a sample to detector distance of 5.3 m to give a scattering wave vector range from 0.004 Å^{-1} < q < 0.15 Å^{-1}. The scattering wave vector is defined as $q = (4\pi/\lambda) \sin(\theta/2)$; θ is the scattering angle.

7.2.5 Cryogenic Transmission Electron Microscopy (cryo-TEM)

Samples for cryo-TEM were prepared using an FEI Vitrobot at 22 ^{o}C and 100% relative humidity. Prior to sample loading, carbon-coated copper TEM grids (Quantifoil R 2/1 or Quantifoil S 7/2) were plasma etched for 60 s. A 3 μL drop of micelle solution was pipetted onto the grid inside the sample chamber. Using an automated system, the grid was blotted with filter paper twice to remove the excess solution. Blot offset (none), blot time (3 s), wait time (1 s), and drain time (1 s) were consistent for each sample. After blotting, grids were submerged in liquid ethane to vitrify the sample. Grids were stored in liquid nitrogen before imaging.

Imaging was performed on a Tecnai G2 12 Twin TEM operating at 120 kV. Images were recorded using a Gatan CCD camera at a nominal underfocus to enhance phase contrast. The temperature of the sample probe was maintained between -176 ^{o}C and -180 ^{o}C during imaging.

Core radii were determined from the cryo-TEM micrographs using ImageJ software.[30] First, the image noise was suppressed using a despeckle algorithm, and a bandpass filter was applied. Subsequently, a contrast threshold was used to remove the background, leaving the outlined area of PB cores. The core radii were calculated from the core areas, assuming that the PB cores were spherical and that their 2D projections were circular. Multiple images (6 to 12) were analyzed from different grid locations, with a total sample size between 450 and 3000 micelles per histogram. Bin sizes for the histograms were 1 nm.

7.2.6 Small Angle Neutron Scattering (SANS)

7.2.6.1 Chain Exchange Sample Preparation

Pre-mixed PB-PEO/PB-*d*PEO (50% PB-PEO by weight) micelle solutions were prepared using the following approach. First, the PB-PEO and PB-*d*PEO polymers were blended in benzene, stirred overnight, and then freeze-dried to ensure complete solvent removal. Then, the polymer blend was dissolved in a D_2O/H_2O mixture (64% D_2O by volume) at a concentration of 2 mg mL^{-1} polymer in solvent and stirred for 3 days. The isotopic composition of 64 vol% D_2O was chosen to contrast-match a perfectly mixed PEO/*d*PEO corona, see Chapter 6 for additional details on solvent composition calculations.

Individual PB-PEO and PB-*d*PEO micelle solutions for post-mixed experiments were prepared by dissolving each dry polymer powder in a separate D_2O/H_2O mixture (64% D_2O by volume) and then stirring for 3 days. Both solutions had a final concentration of 2 mg mL^{-1} polymer in solvent. For the t = 0 sample, equal volumes of the PB-PEO and PB-*d*PEO solutions were mixed and analyzed with SANS. For the t = 10 d sample, equal volume of the PB-PEO and PB-*d*PEO solutions were mixed, magnetically stirred (200 rpm) at room temperature for 10 days, and then analyzed with SANS**.**

7.2.6.2 Size Distribution Sample Preparation

To determine the micelle core size distributions using SANS, solutions were prepared using blended PB-PEO/PB-*d*PEO (88 wt% PB-*d*PEO) polymers to contrast-match the micelle corona to the D_2O solvent,

$$\phi_{dPEO}\rho_{dPEO} + (1 - \phi_{dPEO})\rho_{PEO} = \rho_{D_2O} \quad (1)$$

in which ϕ_{dPEO} is the fraction of PB-*d*PEO, and ρ_{dPEO}, ρ_{PEO}, and ρ_{D_2O} are the scattering length densities of *d*PEO, PEO, and D_2O, respectively (Table 5.2).

The PB-PEO and PB-*d*PEO were blended in benzene, stirred overnight, and freeze-dried. Micelle solutions of the blended polymers were prepared in water/THF cosolvent mixtures as described above and dialyzed against deuterium oxide (D_2O, 99.9% D, Cambridge Isotopes). After dialysis, the solutions were magnetically stirred (200 rpm) at room temperature.

7.2.6.3 SANS Experiments

SANS experiments were performed on the NG-7 30 m SANS instrument at the National Institute of Standards and Technology (NIST), Center for Neutron Research (NCNR). An incident wavelength of 6.0 Å was used with sample to detector distances of 1 m, 4 m, and 13.5 m to cover a q-range from 0.004 $Å^{-1} < q < 0.4$ $Å^{-1}$. All measurements were performed at ambient temperature. The data were reduced and analyzed in IGOR Pro using the standard procedures provided by NIST.[31]

7.3 Results

7.3.1 Effects of Cosolvent Removal on Micelle Size

The consequences of cosolvent removal on the dynamics of block polymer micelles were studied using a poly(1,2-butadiene-*b*-ethylene oxide) [PB-PEO] diblock polymer. PB-PEO was selected for these studies because the low molecular weight and low glass transition temperature of the hydrophobic PB block permitted investigations into the micelle dynamics independent of entanglement or glassy effects in the micelle core. [23,25]

Micelles were prepared in water/THF cosolvent mixtures using the method outlined in Chapter 5 of this dissertation. First, the polymer was dissolved in water, resulting in well-defined spherical micelles with PB cores surrounded by PEO coronas. *Note that similar micelle sizes were obtained by adding water to dry polymer powder or a thin polymer film, supporting that the micelles in pure water were close to their equilibrium size.* After stirring for 72 h, THF was added to reach the desired cosolvent composition (between 0 and 50 vol% THF). DLS data showing the temporal changes in micelle solution behavior following cosolvent removal are provided in Figure 7.1. As discussed in Chapter 5, the initial micelle radii were inversely related to THF content in the cosolvent mixture, seen here as the decrease in hydrodynamic radius *vs.* THF fraction ($<R_H>$ values at Day -1 in Figure 7.1b).[20,21]

Following cosolvent removal by dialysis, all of the micelle sizes were unchanged in non-agitated solutions, regardless of the initial THF content in the cosolvent mixture (Figure 7.1a). This result was consistent with scaling theories that predict large energy barriers to dynamic processes in macromolecular assemblies.[26,28] However, gentle agitation (magnetic stirring at 200 rpm, estimated volume average shear rate ~ 20 s^{-1})[32] led to an unexpected temporal evolution in micelle size that depended on the composition of the cosolvent mixture (Figure 7.1b).

The $<R_H>$ of micelles prepared in cosolvent mixtures that contained ≤ 10 vol% THF remained constant over 90 days following THF removal, although these nanostructures were smaller than the micelles prepared in pure water (Figure 7.1b). This lack of size evolution suggested that the micelles were near equilibrium or unable to overcome the energetic barrier for rearrangement. The stability of micelles prepared from the pure water and low THF content solutions was consistent with

reports indicating that PB-PEO micelles should be kinetically-trapped in aqueous solutions due to the highly unfavorable PB-water interaction ($\chi_{PB/water} \approx 3.5$).[23,25]

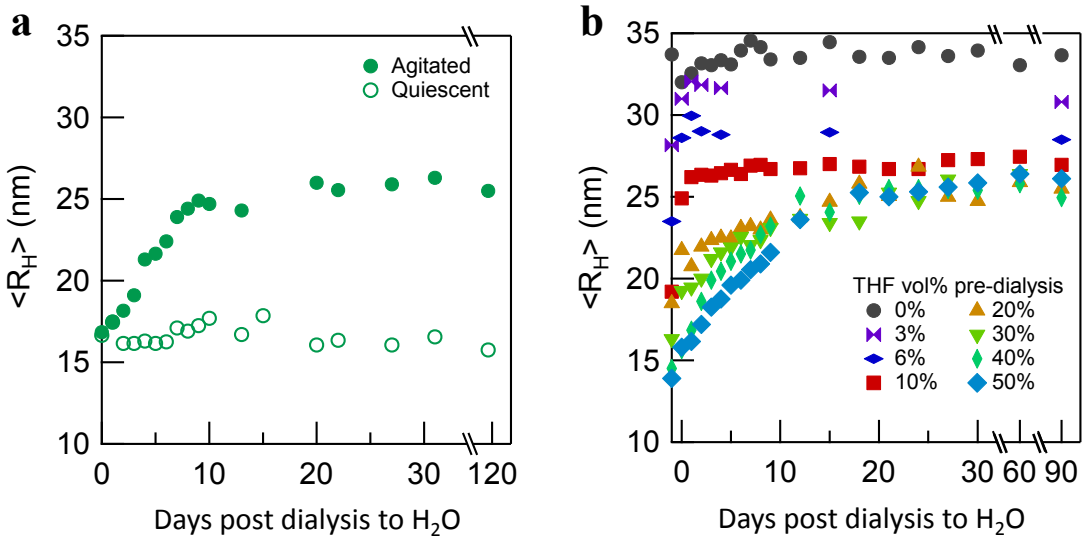

Figure 7.1 (a) DLS data showing the effects of stirring on the change in $<R_H>$ following dialysis to H_2O (Day 0 to Day 120). The THF content and polymer concentration prior to dialysis were 43 vol% and 10 mg mL^{-1}, respectively. The agitated sample was stirred at 200 rpm. (b) DLS data showing the change in $<R_H>$ before (Day -1) and after (Day 0 to 90) THF cosolvent removal as a function of THF content in stirred samples. The polymer concentration was 2 mg mL^{-1} before dialysis to water. In all cases, the solutions were stirred at 200 rpm. The variability in $<R_H>$ was 1 to 3 nm.

In contrast, micelles prepared in cosolvent mixtures that contained > 10 vol% THF exhibited significant size increases in the ~20 days following THF removal, despite the unfavorable PB-water interaction. The DLS data indicated that the micelles prepared from high THF content mixtures approached a similar final size of

$\langle R_H \rangle \approx 25$ nm following transfer into pure water, independent of their initial size in the cosolvent mixture.

SAXS analyses reinforced the trends seen in the DLS results and provided insight into changes in the dispersity of micelle sizes following cosolvent removal. The shift in primary peak location to higher *q* values with increasing THF content (Figure 7.2a) confirmed the inverse relationship between micelle size and THF content upon cosolvent addition. The disappearance of the main peak on Day 3 (Figure 7.2b) for the specimens made from 30 - 50 vol% THF solutions suggested an appreciable increase in the size dispersity in the days immediately following cosolvent removal. The reappearance of the peak at lower *q* values on Day 30 (Figure 7.2c) indicated that micelles had coalesced into a final population of larger and nearly monodisperse assemblies. The initial increase and subsequent decrease in dispersity suggested the presence of multiple micelle populations during the growth process. Moreover, the final micelle sizes were similar for the specimens made from 10 - 50 vol% THF solutions, supporting the plateau in growth noted in the DLS results.

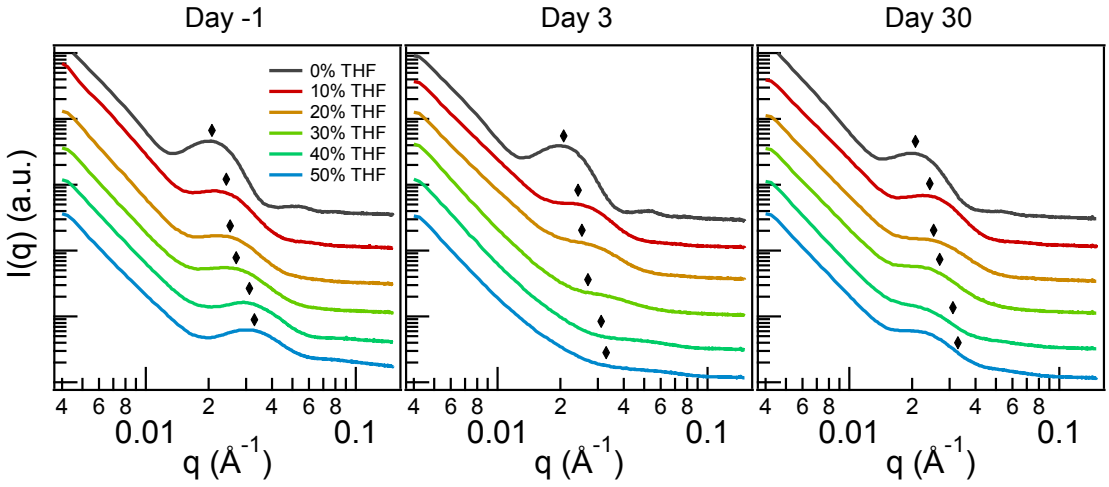

Figure 7.2 SAXS data for micelles prepared in various water/THF mixtures (0 - 50 vol% THF) before (Day -1) and after (Day 3 and Day 30) dialysis to pure water. The concentration before dialysis was 2 mg mL^{-1} and all samples were stirred after dialysis. Black diamonds mark the peak location before dialysis to water. SAXS curves were shifted vertically for clarity.

The differences in growth behavior of the micelles prepared from low *vs*. high THF cosolvent mixtures were reasonable on the basis of the free energy contributions that govern amphiphilic block polymer self-assembly.[20] The larger micelles formed in the low THF content mixtures likely were close to their equilibrium size and unable to overcome the energetic barrier to dynamic processes. In contrast, the smaller micelles formed in high THF content mixtures had a larger interfacial area per chain than the micelles formed in pure water, leading to highly unfavorable PB-water interactions following dialysis. A size increase of the smaller micelles would reduce the interfacial area per chain and lower the free energy of the system. Although free energy analyses suggested that the growth of the smaller micelles in water would be energetically favorable, the size increase in Figures 7.1 and 7.2 was not expected when considering

micelle growth mechanisms and their associated energetic barriers in highly amphiphilic systems.[19,23,25,26,28,33] These results possibly indicated new insights into block polymer micelle stability and prompted further investigation.

7.3.2 Investigation into Micelle Growth Mechanism

The growth of PB-PEO micelles following solvent transfer into pure water was examined using SANS and cryo-TEM. Specifically, single chain exchange in water was investigated using SANS by exploiting contrast variation and monitoring the temporal changes in the scattered intensity as described in detail in Chapter 6.[22,34-37] Initially, separate PB-PEO and PB-*d*PEO [poly(1,2-butadiene-*b*-ethylene oxide-d_4)] micelle solutions were prepared in an H_2O/D_2O mixture. These separate solutions were mixed at time t = 0, giving rise to a maximum in scattered intensity due to contrast between the coronas and solvent [I(q) values at t = 0 in Figure 7.3]. After mixing the separate PB-PEO and PB-*d*PEO micelle solutions, the resulting solution was gently stirred (200 rpm) for 10 days before analysis.

As seen in Figure 7.3, the scattered intensity did not decrease over an ~10 day period [I(q) values at t = 10 d], supporting a lack of appreciable chain exchange by micelle fusion/fission and/or single chain events. This result was consistent with the extremely high energy barrier to dynamic events in pure water and suggested that gentle stirring alone does not induce chain exchange. The theories for single chain exchange in block polymer micelles predict that the rate of chain exchange should only depend on the properties of the hydrophobic block and not on the size/aggregation number of the micelles. [19,34,38] Thus, these results suggested that the single chain events were highly unfavorable in pure water, even in a stirred system and were not contributed the micelle growth noted in Figures 7.1 and 7.2.

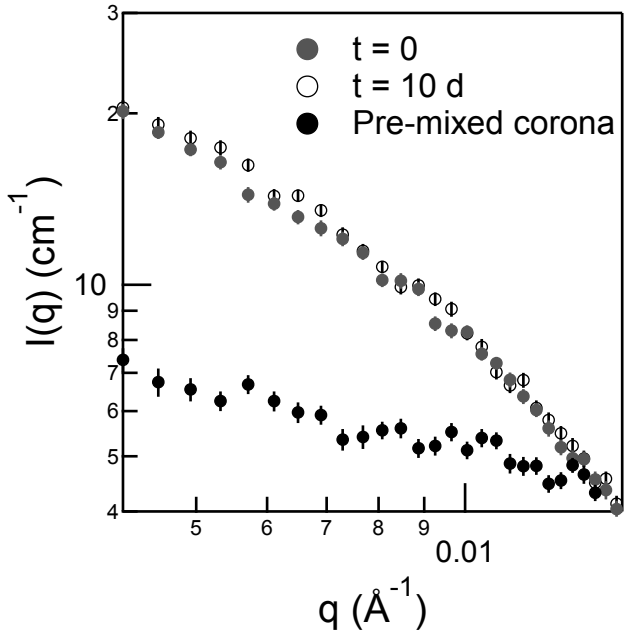

Figure 7.3 SANS curves for mixtures of PB-PEO and PB-*d*PEO micelles (open and gray circles) and pre-mixed PB-PEO/PB-*d*PEO micelles (black circles) in D_2O/H_2O at 25 °C. The t= 10 d sample was gently stirred at 200 rpm.

As chain exchange was not prevalent in the PB-PEO system, fusion processes were examined as the other mechanism that could promote micelle reorganization. Importantly, the energy barrier to fusion should depend on the micelle aggregation number.[26,39,40] Cryo-TEM was used to visualize the micelle size growth throughout the 90 day process. The resulting micrographs are shown in Figure 7.4, in which the darker domains correspond to the dense PB cores while the fainter halos correspond to the PEO coronas.[41,42] The core radii at Day 0 were described by a single and nearly monodisperse distribution. Surprisingly, a second distinct distribution of core radii centered at 10-11 nm appeared after approximately 1 week in samples prepared from 30 vol% and 50 vol% THF. This second distribution corresponded to an approximate

eight-fold increase in core volume or aggregation number from the initial distribution (aggregation numbers of approximately 100 and 800 for the smaller and larger core sizes, respectively). By Day 90, these solutions contained a greater fraction of micelles with larger core radii (~ 10 nm), suggesting that the population weighting had shifted from the smaller to the larger distribution over time. In contrast, micelles prepared in 0 % by volume and 10 % by volume THF solutions did not change in size over 90 d following dialysis. The presence of two distinct micelle populations in the micelle solutions prepared from high THF content cosolvent mixtures supported that the micelles were growing through a fusion-controlled process.

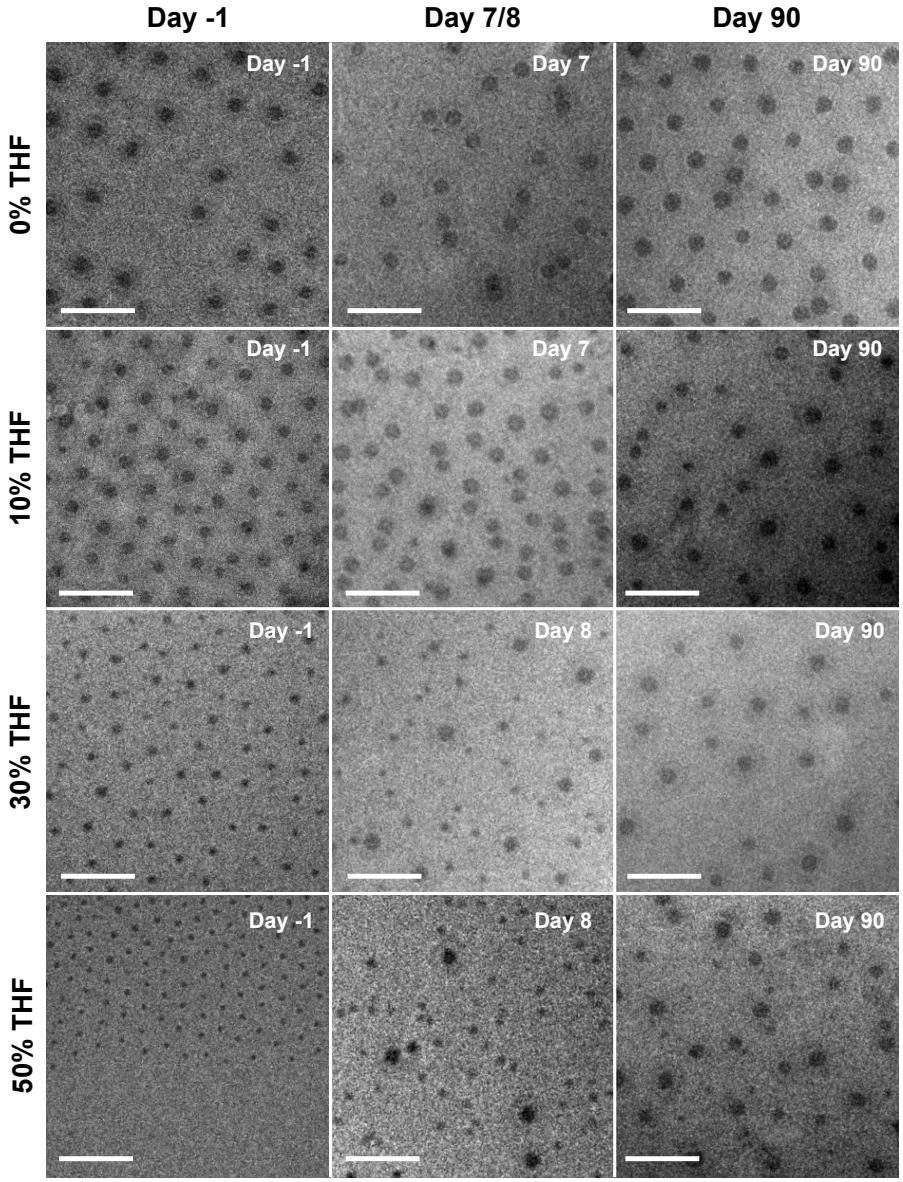

Figure 7.4 **Cryo-TEM studies of PB-PEO micelle size evolution following cosolvent removal. Micelle solutions were prepared at a polymer concentration of 2 mg mL^{-1} with 0-50 vol% THF in water. Day -1 analyses were performed in the cosolvent mixtures prior to dialysis against pure water. Subsequently, on Day 0, solutions were dialyzed against pure water to remove the THF. Day 7, Day 8, and Day 90 correspond to the number of days following dialysis. Note that images at different magnifications were scaled for ease of comparison. Scale bars represent 100 nm.**

7.3.3 Size Evolution Concentration Dependence

Fusion events are predicted to follow second-order kinetics, and therefore should show an increase in rate as the micelle concentration increases.[27,40] The size evolution was examined as a function of micelle concentration using cryo-TEM (Figure 7.5) and SANS (Figure 7.6). The cryo-TEM images showed that on Day 10/11, the 2 mg mL^{-1} and 5 mg mL^{-1} solutions still contained an appreciable bimodal population of micelles, while the 10 mg mL^{-1} solution had transitioned to primarily larger micelles with core sizes centered at ~ 10 nm (Figure 7.5). These micrographs suggested that the relative weighting of the larger population increased with micelle concentration, further supporting the hypothesis that the micelles grew through fusion events.

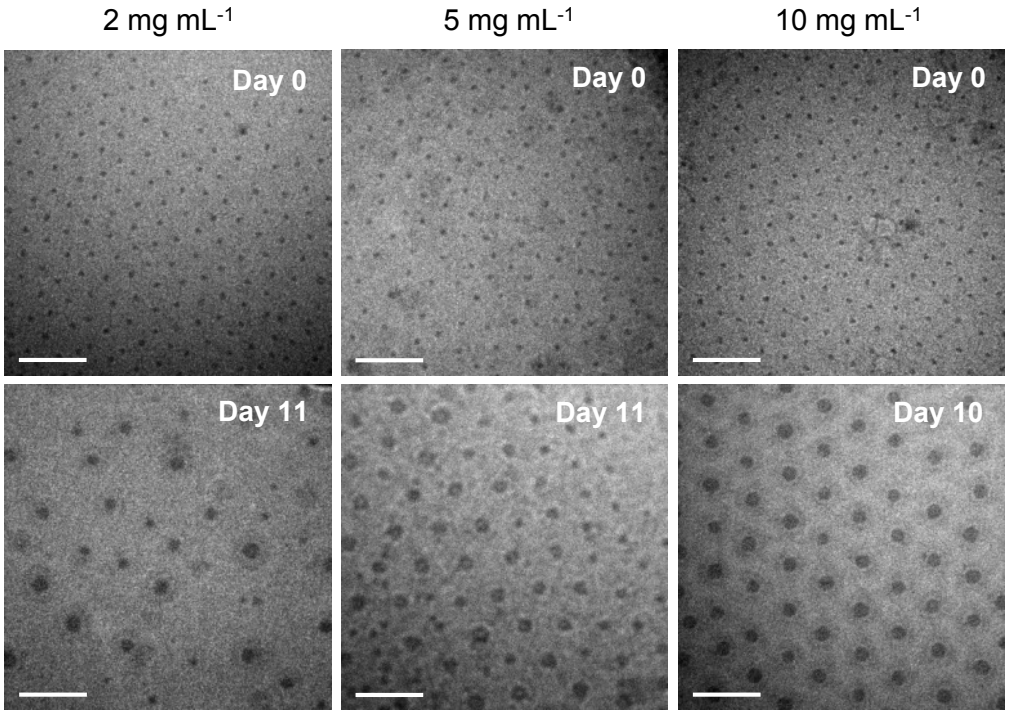

Figure 7.5 Cryo-TEM micrographs showing changes in PB-PEO micelle core radii between Day 0 and Day 20 for several polymer concentrations. The initial polymer concentrations were 2 mg mL^{-1}, 5 mg mL^{-1}, and 10 mg mL^{-1}. After dialysis, the concentrations followed the same trend but were approximately half the initial concentration (Section 7.2.2). In each case, the THF content was 43 vol% prior to dialysis into water. Scale bars are 100 nm.

Although microscopy provides unique structural insights (*e.g.* an unexpected bimodal distribution) that are difficult to identify solely through scattering analysis,[43,44] typical TEM sample sizes are small (~10^3 micelles) compared to the much larger sample size (~10^{15} micelles) that is examined with scattering techniques. Thus, SANS experiments were performed to ensure that the measured micelle size distributions were not influenced by cryo-TEM sample preparation. For these experiments, the micelle coronas were contrast-matched to the solvent (D_2O) by

blending PB-PEO and PB-*d*PEO polymers, thereby allowing only the PB core size distribution to be probed. The SANS data showed a marked difference in micelle populations for the 2 mg mL^{-1} sample *vs.* the higher concentration samples (Figure 7.6). The distinct maxima and minima in the 5 mg mL^{-1} and 10 mg mL^{-1} data indicated that a significant population of larger micelles were present in the higher concentration samples. Also, the maxima and minima were located at approximately the same q values for the 5 mg mL^{-1} and 10 mg mL^{-1} samples, supporting that the larger micelles were the same size in both samples.

The trends in the SANS data were substantiated by modeling the data using a bimodal distribution of Schulz spheres, which gave significantly better fits than the model for monomodal spheres (Appendix E). The resulting fits to the SANS data and corresponding number frequency distributions of core radii are presented for the different polymer concentrations in Figure 7.6. The bimodal SANS core radii distribution centered at ~5 nm and ~10 nm was in good agreement with the cryo-TEM results. Additionally, the SANS results indicated that the relative weighting of the larger to smaller core population increased with increasing polymer concentration, again supporting the fusion mechanism for micelle growth.

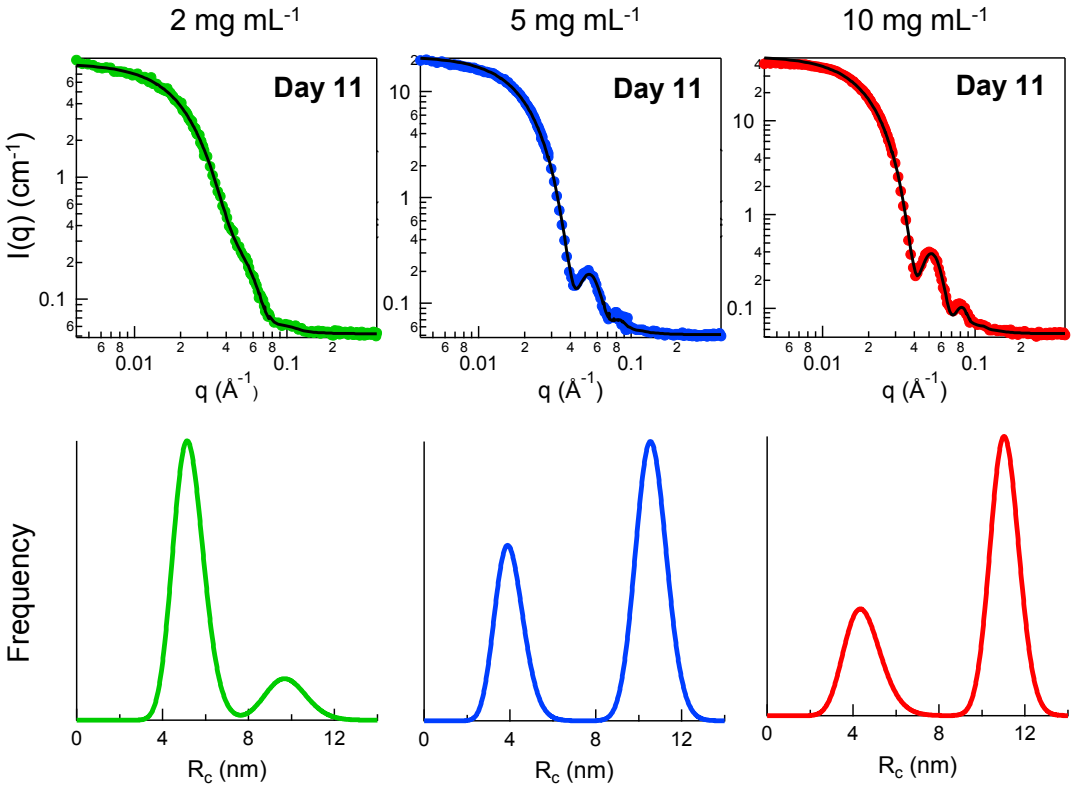

Figure 7.6 **(top) SANS data (points) and fits (solid lines) for micelle solutions at different concentrations. (bottom) Corresponding number frequency distribution of core radii from fits to SANS data. The initial polymer concentrations were 2 mg mL^{-1}, 5 mg mL^{-1}, and 10 mg mL^{-1}. After dialysis, the concentrations followed the same trend but were approximately half the initial concentration (Section 7.2.2). Samples for the SANS experiments were prepared in 43 vol% THF and dialyzed against D_2O, and SANS experiments were performed at Day 11 post dialysis to D_2O. The sensitivity of the number frequencies from the SANS data modeling was approximately ± 5% for the 2 mg mL^{-1} data and ± 15% for the 5 mg mL^{-1} and 10 mg mL^{-1} data.**

7.3.4 Size Evolution through a Bimodal Pathway

Both the cryo-TEM and SANS experiments suggested that the micelles were growing through a bimodal size distribution. However, this result was entirely unexpected in the context of existing theories for block polymer micelle dynamics. According to these scaling theories for micelles, the energy barrier to micelle fusion is expected to scale with aggregation number and should increase with increasing aggregation number.[26,39,45] Based on these scaling arguments, the fusion of intermediate sized micelles should be slower than the fusion of smaller micelles, and theoretical[26] and computational work[40] posited that distinct multimodal size distributions would exist for micelles undergoing fusion growth. This behavior differs from that of micelles growing through single chain events (*i.e.* unimer insertion and expulsion), which are characterized by a single shifting size distribution.[40,46,47]

To gain a better understanding of the micelle size distribution evolution, the growth was monitored over 21 days for a 43 vol% THF sample. As seen in Figure 7.7, the core radii at Day 0 were described by a single and nearly monodisperse distribution centered at 5 nm to 6 nm. The second distribution of core radii centered at 10 nm to 11 nm appeared after only 1 d of stirring. This distinct bimodal distribution persisted through Day 10, with the population weighting shifting from the smaller to the larger distribution over time. By Day 16 to 21, the core size distributions exhibited a single and nearly monodisperse population of larger micelles, consistent with the time scales determined from DLS. Surprisingly, there were no obvious intermediate micelle populations at any point during the growth process, and the sizes evolved through a purely bimodal distribution.

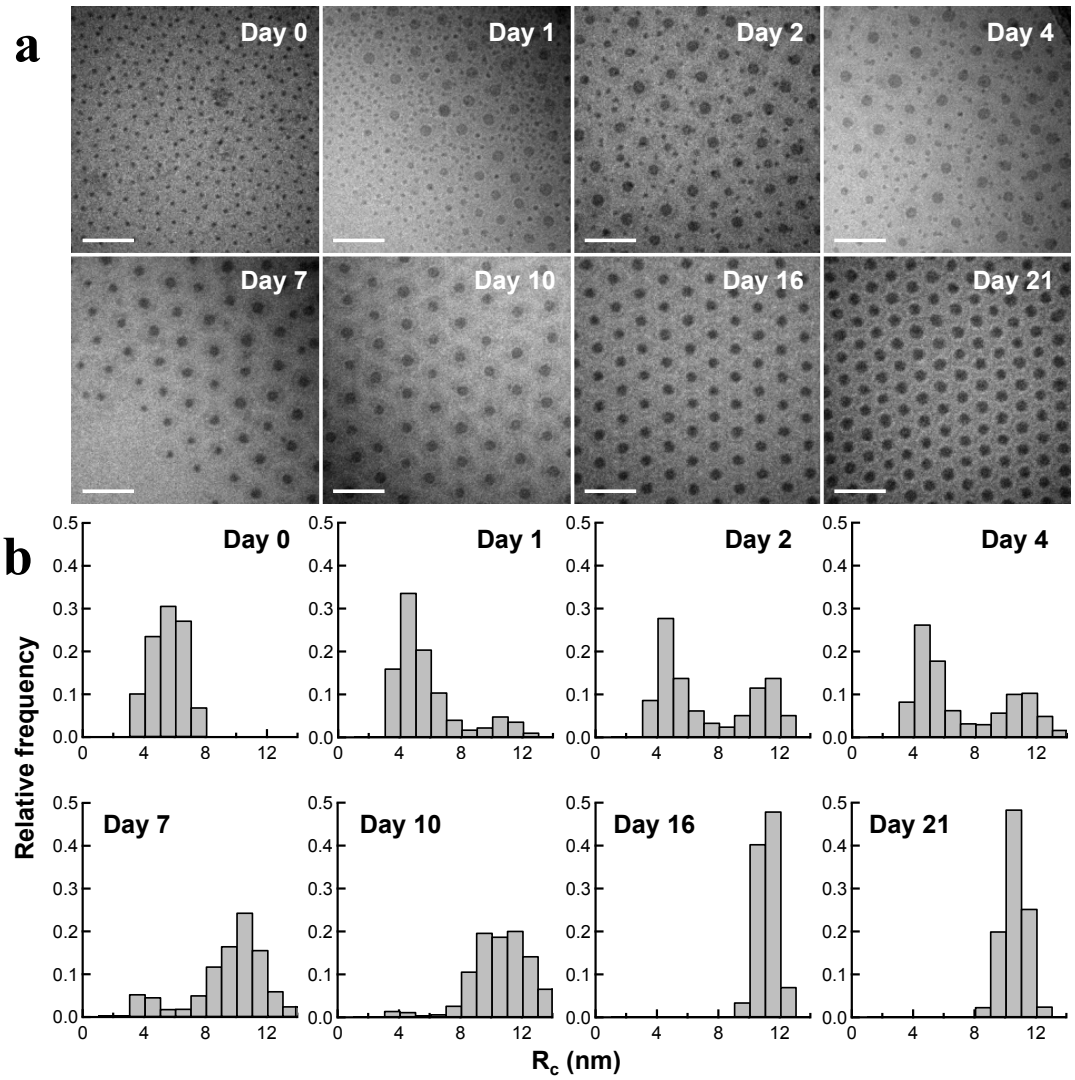

Figure 7.7 (a) Cryo-TEM images showing changes in PB-PEO core radii 21 days post-dialysis. The polymer concentration was initially 10 mg mL^{-1} and the THF content was 43 vol% before dialysis. Scale bars represent 100 nm. (b) Corresponding histograms of micelle sizes obtained from analysis of cryo-TEM images. Sample size for each histogram ranged from 450 and 3000 micelles.

7.4 Discussion

The bimodal micelle growth behavior in the PB-PEO micelle solutions has critical implications for block polymer micelle stability in highly selective solvents. Specifically, when micellar assemblies are perturbed far enough from their equilibrium size (and aggregation number), the micelles can evolve through a fusion-controlled process, and moreover, through a distinct bimodal distribution that is separated by multiple fusion events.

The energy barrier to micelle fusion is related to the corona chain stretching and is expected to scale with aggregation number.[26,39,45] Halperin and Alexander suggested that the energy required to deform the corona during micelle fusion is of order ~ 1 kT per chain, giving a total energy barrier to micelle fusion of order $\sim 10^2$ kT to $\sim 10^3$ kT.[19] This large of an energy barrier cannot be overcome by the thermal energy of the system. Moreover, if fusion events could occur, the energy barrier should grow with increasing aggregation number and fusion of intermediate sized micelles should be slower than fusion of the smaller micelles. This scaling would lead to distinct intermediate micelle populations if the micelles were growing by step-wise two body collisions. The results presented here do not reflect either of these predictions and instead suggest that the micelles are evolving through an alternate growth mechanism.

Bimodal distributions often are indicative of a nucleation and growth mechanism (*i.e.* cooperative self-assembly). Cooperative self-assembly processes have been reported in numerous systems including proteins,[48] peptide-based molecules,[49] small molecules,[48,50] and nanoparticles[51] and are characterized by a bimodal distribution of small oligomers and larger aggregates. In the PB-PEO micelle system studied here, the small micelles may fuse to form metastable intermediates,

which then rapidly fuse with additional smaller micelles to produce a bimodal size distribution. This proposed growth mechanism is potentially similar to the cooperative micellization processes in small molecule amphiphiles, in which the final micelle size is imposed by repulsive interactions between the head groups.[52] Similarly, corona chain repulsion may limit the micelle growth seen here, leading to the final size plateau independent of the initial size. Notably, this final size was smaller than micelles formed by directly dispersing the polymer in water, underscoring the path-dependent and kinetically-controlled self-assembly in macromolecular systems

Interestingly, the micelle size evolution critically depended on solution agitation, suggesting that the growth may be a shear-induced and/or interfacial phenomenon. Several reports have shown that shear can significantly affect the formation of macromolecular assemblies,[53-55] and studies of pre-formed micelles have shown that dilute star-like micelles can deform[61] and align under shear.[62] The literature precedence of the susceptibility of macromolecular assemblies to shear could indicate that the small micelles aggregate (floc) under flow and subsequently coalesce, resulting in a bimodal distribution. Similar shear-induced flocculation and coalescence has been reported in emulsions and shown to lead to bimodal distributions.[63] However, a rough estimation of the kinetic energy of the micelles during mixing suggests that the maximum energy of a micelle collision (~ 10^2 kT) may not be sufficient to overcome the predicted energy barrier to micelle fusion (~ 10^2 to 10^3 kT) and that the micelle growth likely is not the result of shear-induced collisions. Alternatively, several reports indicate that proteins can aggregate during agitation by adsorbing to and subsequently unfolding at the air/water interface.[56-58]

Amphiphilic block polymers also are known to assemble at air/water interfaces,[59,60] which seems to suggest that the bimodal growth pathway is due to an interface-induced micelle nucleation and growth process.

7.5 Conclusions

The results reported in this chapter highlight the considerable influence of cosolvent preparation methods on the long-term stability of macromolecular assemblies and demonstrate the strong interplay between thermodynamic *vs.* kinetic constraints in these systems. Chapters 5 and 6 demonstrate that adding an organic cosolvent significantly influences the micelle size and dynamics, and this work shows that removing this cosolvent can have unexpected consequences on the long-term stability of these assemblies. These results suggest that micelle fusion/fission events occur in amphiphilic block polymer micelles when the system is perturbed far from equilibrium, even in highly selective solvents.

Notably, the unexpected micelle growth was likely a coupled interfacial and shear phenomenon, leading to a bimodal size distribution separated by multiple fusion events with no dominant intermediate populations. While the effects of perturbation and agitation often are overlooked in polymeric assemblies, these results accentuate similarities between the processing effects in polymeric systems and those that are influential in small molecule and protein assemblies. The intimate relationship between processing conditions and subsequent dynamics has critical implications on the stability of macromolecular-based nanocarriers. Furthermore, these findings emphasize the need for more quantitative investigations into the underlying mechanisms affecting micelle stability and their energetic barriers to enable a thorough understanding of the complex dynamic processes in amphiphilic block

polymer solution assemblies. The following chapter will explore the effects of routine laboratory agitation methods on the stability of block polymer assemblies towards the goal of better understanding these often-overlooked effects.

REFERENCES

1 Alexandridis, P. & Lindman, B. *Amphiphilic block copolymers: self assembly and applications*. Elsevier, 2000.

2 Kelley, E. G., Albert, J. N. L., Sullivan, M. O. & Epps, T. H. (2013), *Chemical Society Reviews* **42**, 7057-7071

3 Yang, J. (2002), *Current Opinion in Colloid & Interface Science* **7**, 276-281

4 Blanazs, A., Armes, S. P. & Ryan, A. J. (2009), *Macromolecular Rapid Communications* **30**, 267-277

5 Mai, Y. Y. & Eisenberg, A. (2012), *Chemical Society Reviews* **41**, 5969-5985

6 Smart, T. *et al.* (2008), *Nano Today* **3**, 38-46

7 Denkova, A. G., Mendes, E. & Coppens, M. O. (2010), *Soft Matter* **6**, 2351-2357

8 Hayward, R. C. & Pochan, D. J. (2010), *Macromolecules* **43**, 3577-3584

9 Nicolai, T., Colombani, O. & Chassenieux, C. (2010), *Soft Matter* **6**, 3111-3118

10 Lu, A. & O'Reilly, R. K. (2013), *Current Opinion in Biotechnology* **24**, 639-645

11 Yu, Y. S., Zhang, L. F. & Eisenberg, A. (1997), *Langmuir* **13**, 2578-2581

12 Zhang, L. & Eisenberg, A. (1995), *Science* **268**, 1728-1731

13 Groschel, A. H. *et al.* (2012), *Nature Communications* **3**, 1707

14 Cui, H. G., Chen, Z. Y., Zhong, S., Wooley, K. L. & Pochan, D. J. (2007), *Science* **317**, 647-650

15 Pochan, D. J. *et al.* (2004), *Science* **306**, 94-97

16 Aliabadi, H. M. *et al.* (2007), *International Journal of Pharmaceutics* **329**, 158-165

17 Owen, S. C., Chan, D. P. Y. & Shoichet, M. S. (2012), *Nano Today* **7**, 53-65

18 Tyrrell, Z. L., Shen, Y. Q. & Radosz, M. (2010), *Progress in Polymer Science* **35**, 1128-1143

19 Halperin, A. & Alexander, S. (1989), *Macromolecules* **22**, 2403-2412

20 Halperin, A., Tirrell, M. & Lodge, T. P. (1992), *Advances in Polymer Science* **100**, 31-71

21 Kelley, E. G., Smart, T. P., Jackson, A. J., Sullivan, M. O. & Epps, T. H. (2011), *Soft Matter* **7**, 7094-7102

22 Lund, R., Willner, L., Richter, D. & Dormidontova, E. E. (2006), *Macromolecules* **39**, 4566-4575

23 Won, Y. Y., Davis, H. T. & Bates, F. S. (2003), *Macromolecules* **36**, 953-955

24 Zhang, L., Shen, H. & Eisenberg, A. (1997), *Macromolecules* **30**, 1001-1011

25 Jain, S. & Bates, F. S. (2004), *Macromolecules* **37**, 1511-1523

26 Dormidontova, E. E. (1999), *Macromolecules* **32**, 7630-7644

27 Meli, L., Santiago, J. M. & Lodge, T. P. (2010), *Macromolecules* **43**, 2018-2027

28 Nyrkova, I. A. & Semenov, A. N. (2005), *Macromolecular Theory and Simulations* **14**, 569-585

29 Aminabhavi, T. M. & Gopalakrishna, B. (1995), *Journal of Chemical & Engineering Data* **40**, 856-861

30 Schneider, C. A., Rasband, W. S. & Eliceiri, K. W. (2012), *Nature Methods* **9**, 671-675

31 Kline, S. (2006), *Journal of Applied Crystallography* **39**, 895-900

32 Bai, G., Bee, J. S., Biddlecombe, J. G., Chen, Q. & Leach, W. T. (2012), *International Journal of Pharmaceutics* **423**, 264-280

33 Esselink, F. J., Semenov, A. N., ten Brinke, G., Hadziioannou, G. & Oostergetel, G. T. (1995), *Macromolecules* **28**, 3479-3481

34 Choi, S. H., Lodge, T. P. & Bates, F. S. (2010), *Physical Review Letters* **104**, 047802

35 Lu, J., Bates, F. S. & Lodge, T. P. (2013), *ACS Macro Letters* **2**, 451-455

36 Lu, J., Choi, S., Bates, F. S. & Lodge, T. P. (2012), *ACS Macro Letters* **1**, 982-985

37 Lund, R. *et al.* (2011), *Macromolecules* **44**, 6145-6154

38 Zinn, T., Willner, L., Lund, R., Pipich, V. & Richter, D. (2012), *Soft Matter* **8**, 623-626

39 Esselink, F. J., Dormidontova, E. E. & Hadziioannou, G. (1998), *Macromolecules* **31**, 4873-4878

40 Li, Z. L. & Dormidontova, E. E. (2010), *Macromolecules* **43**, 3521-3531

41 Zheng, Y. *et al.* (1999), *Journal of Physical Chemistry B* **103**, 10331-10334

42 Won, Y.-Y., Brannan, A. K., Davis, H. T. & Bates, F. S. (2002), *Journal of Physical Chemistry B* **106**, 3354-3364

43 Weissman, H. & Rybtchinski, B. (2012), *Current Opinion in Colloid & Interface Science* **17**, 330-342

44 Danino, D. (2012), *Current Opinion in Colloid & Interface Science* **17**, 316-329

45 Esselink, F. J., Dormidontova, E. & Hadziioannou, G. (1998), *Macromolecules* **31**, 2925-2932

46 Nose, T. & Iyama, K. (2000), *Computational and Theoretical Polymer Science* **10**, 249-257

47 Honda, C., Hasegawa, Y., Hirunuma, R. & Nose, T. (1994), *Macromolecules* **27**, 7660-7668

48 De Greef, T. F. A. *et al.* (2009), *Chemical Reviews* **109**, 5687-5754

49 Carnall, J. M. A. *et al.* (2010), *Science* **327**, 1502-1506

50 Stepanenko, V., Li, X.-Q., Gershberg, J. & Würthner, F. (2013), *Chemistry – A European Journal* **19**, 4176-4183

51 Wang, J. *et al.* (2013), *Journal of the American Chemical Society* **135**, 11417-11420

52 Tanford, C. *The Hydrophobic Effect: Formation of Micelles and Biological Membranes*. 2nd edn, Wiley-Interscience, 1979.

53 Wang, C.-W., Sinton, D. & Moffitt, M. G. (2011), *Journal of the American Chemical Society* **133**, 18853-18864

54 Sorrells, J. L., Tsai, Y.-H. & Wooley, K. L. (2010), *Journal of Polymer Science Part A: Polymer Chemistry* **48**, 4465-4472

55 Yu, H. & Jiang, W. (2009), *Macromolecules* **42**, 3399-3404

56 Nielsen, L. *et al.* (2001), *Biochemistry* **40**, 6036-6046

57 Thomas, C. R. & Geer, D. (2011), *Biotechnology Letters* **33**, 443-456

58 Patapoff, T. W. & Esue, O. (2009), *Pharmaceutical Development and Technology* **14**, 659-664

59 Li, S. *et al.* (1993), *Langmuir* **9**, 2243-2246

60 Ahmed, F., Hategan, A., Discher, D. E. & Discher, B. M. (2003), *Langmuir* **19**, 6505-6511

61 Ripoll, M., Winkler, R. G. & Gompper, G. (2006), *Physical Review Letters* **96**, 188302

62 Stellbrink, J., Lonetti, B., Rother, G., Willner, L. & Richter, D. (2008), *Journal of Physics-Condensed Matter* **20**

63 Schokker, E. P. & Dalgleish, D. G. (1998), *Colloids and Surfaces A: Physicochemical and Engineering Aspects* **145**, 61-69

Chapter 8

INFLUENCE OF MIXING ON CHAIN EXCHANGE IN HIGHLY AMPHIPHILIC BLOCK POLYMER MICELLES

Motivated by the agitation-induced size evolution studied in Chapter 7, this chapter explores the effects of common mixing types on chain exchange in highly amphiphilic block polymer micelles. Specifically, this work exploits contrast variation in small angle neutron scattering (SANS) to determine the shear and interfacial effects on chain exchange and shows that mixing can induce chain exchange, even in highly selective solvents. This work was done in collaboration with Ryan P. Murphy.

8.1 Introduction

Seminal studies of amphiphilic block polymer assemblies demonstrated a unique aspect of these assemblies not seen in small molecule surfactants: completely arrested chain exchange. Early dynamic studies described block polymer solution assemblies as 'non-ergodic', implying that the assemblies are locally isolated and do not reach a global equilibrium.[1,2] The final morphology is dictated by processing conditions, and the same block polymer can form multiple kinetically-trapped morphologies depending on the solution preparation method. Clearly, understanding the effects of common preparation methods on the resulting assemblies is essential for future development of these materials.

Elegant work from several research groups has capitalized on kinetically controlled block polymer assembly to create hierarchical structures through carefully

developed processing routes. For example, Gröschel *et al.* controlled the solvent selectivity for the core blocks to create multicompartment 'football'-, 'clover'-, and 'hamburger'-type micelles.[3] Similarly, work by Pochan and Wooley demonstrated that subtly manipulating the corona block interactions leads to exotic solution structures such as disks,[4] toroids,[5] and helices.[6]

Other works focused on the effects of routinely used micelle preparation conditions on the self-assembled structures. Recent work by Lodge and coworkers investigated the effects of three common micelle preparation methods on the resulting assemblies, and showed that the final micelle size depended on the assembly pathway.[7,8] Their work showed that using a cosolvent preparation route kinetically trapped small, monodisperse assemblies, whereas directly dissolving the polymer resulted in large, polydisperse assemblies that relaxed to smaller sizes upon thermal annealing.[7,8] More complicated processing routes also have been developed towards the goal of creating well-defined solution assemblies, such as self-assembly schemes based on emulsion-based methods,[9-12] flash nanoprecipitation,[13-15] and microfluidic mixing.[16-18] In one example, Weitz and coworkers successfully designed a microfluidic device to create well-defined, monodisperse polymeric vesicles.[16]

Despite the literature precedent highlighting the importance of processing conditions on block polymer assemblies, the influence of mixing on these assemblies is often overlooked. Many experimental works report that the solution was stirred during micelle preparation, yet only a few works have systematically explored the agitation effects on the resulting assemblies.[17,19-23] For example, studies by Jiang *et al.* showed that discrete spherical micelles were formed at slow stir speeds while cylindrical micelles and large aggregates were formed at fast stir speeds in

PS-P2VP-PEO [poly(styrene-*b*-2 vinylpyridine-*b*-ethylene oxide)] triblock terpolymer micelles. Similarly, Moffitt and coworkers demonstrated sphere-to-cylinder, sphere-to-vesicle, and cylinder-to-sphere transitions in PS-PAA [poly(styrene-*b*-acrylic acid)] micelles under high shear conditions imposed by a specially designed microfluidic mixing device.[17,23] These reports demonstrate that the final solution morphology can be highly influenced by the solution stir/shear rate and underscore the need for systematic investigations into the effects of mixing on block polymer assemblies.

In addition to preparation conditions, micelle formulations developed for applications such as drug delivery may be subjected to agitation during processing, packaging, shipping, and storage. Similar concerns have motivated significant research efforts to understand the profound effects of agitation on emulsions commonly found in pharmaceutical and personal care products[24,25] and protein stability during biopharmaceutical development.[26-29] At a basic level, emulsions, proteins, and block polymer micelles all share a structural similarity in that they contain a hydrophobic core surrounded by a protective hydrophilic layer. This structural similarity further suggests that agitation may significantly affect the stability of block polymer micelles.

There are several consequences of solution agitation that could influence soft material assembly: added shear forces on the solution, increased collision frequency, enhanced mass transport to and from the air/water interface, and air/water interface regeneration.[24,25,27] Agitation-induced shear and/or interfacial effects in block polymer assemblies are largely unexplored; however, there are a few reports in literature that suggest these effects may play an important role in macromolecule self-assembly and stability. Rheological studies of preformed star-like micelles

suggest that these structures can deform[30] and align under shear.[31] Similarly, interfacial effects also are expected to play a large role in block polymer assemblies, as these materials are known to assemble at air/water interfaces.[32,33]

This chapter explores agitation-induced effects on chain exchange in poly(1,2-butadiene-*b*-ethylene oxide) (PB-PEO) micelles in water. These studies were motivated by the results in Chapter 7, which showed the distinct effects of stirring on the stability of non-equilibrium micelles. The work presented here investigates the effects common mixing types used in solution preparation on chain exchange in block polymer micelles. The results clearly demonstrate significant chain exchange occurs after only minutes of vortex mixing in aqueous PB-PEO micelles, which are kinetically trapped in quiescent solutions for weeks.[1,2,34] Comparing different mixing types indicates that the agitation-induced chain exchange is a coupled shear and interfacial effect. Moreover, the exchange kinetics are linear with mix time, suggesting the reaction is zero-order and surface-limited. The results presented herein illustrate the drastic impact of mixing on chain exchange and further demonstrate the intricate relationship between block polymer assembly and processing conditions.

8.2 Experimental Section

8.2.1 Materials

The PB-PEO and PB-*d*PEO polymer studied in this chapter are summarized in Table 2.1.

8.2.2 Micelle Solution Preparation and Mixing

8.2.2.1 Solution Preparation

Two types of micelle solutions were prepared for these experiments. Pre-mixed micelles were prepared by blending the polymers before micelle formation such that the final assemblies contained a completely randomized PEO/*d*PEO corona. Post-mixed micelles were prepared from separate PB-PEO and PB-*d*PEO micelle solutions, such that the final solution contained assemblies with either a PEO or a *d*PEO corona.

Pre-mixed PB-PEO/PB-*d*PEO (50% PB-PEO by weight) micelle solutions were prepared using the following approach. First, the PB-PEO and PB-*d*PEO polymers were blended in benzene, stirred overnight, and then freeze-dried to ensure complete solvent removal. Then, the polymer blend was dissolved in a D_2O/H_2O mixture (64% D_2O by volume) at the desired concentration and stirred for 3 days. The isotopic composition of 64 vol% D_2O was chosen to contrast-match the perfectly mixed PEO/*d*PEO corona. See Chapter 6 for additional details on the solvent composition calculation.

Individual PB-PEO and PB-*d*PEO micelle solutions for post-mixed experiments were prepared at the desired concentrations by dissolving each dry polymer powder in a separate D_2O/H_2O mixture (64% D_2O by volume) and then stirring for 3 days. The post-mixed samples corresponded to a 50/50 (vol%/vol%) mixture of PB-PEO/PB-*d*PEO micelles. At t = 0 sample, equal volumes of the PB-PEO and PB-*d*PEO solutions were mixed and the resulting solution was agitated as described below.

8.2.2.2 Micelle Solution Mixing

Couette Cell Mixing Samples were sheared using an Anton Paar MCR 501 rheometer during the flow SANS experiments.[35] The sample was sheared using a 30 mm titanium cup and 29 mm titanium bob, giving a 0.5 mm gap and a total scattering pathlength of 1 mm. Approximately 2 mL of sample was needed to fill the Couette cell. All experiments were performed at 25 °C and a D_2O solvent trap was used to prevent sample evaporation.

Sparging A 5 mg mL^{-1} micelle solution was sparged with N_2 for 60 min. The N_2 flow rate was maintained at 10 mL min^{-1} using flow controllers. *Note that the a small amount of solvent (~1 vol%) evaporated while sparging the solution; therefore, additional solvent was added before analysis to replace the lost solvent.*

Vortex Mixing Samples were vortex mixed using a Fisher Scientific Analog Vortex Mixer. All samples were mixed at the maximum speed of approximately 3200 rpm (speed setting 10). Unless otherwise stated, the total mix volume for all solutions was 1 mL (0.5 mL of PB-PEO solution and 0.5 mL PB-*d*PEO solution). All samples were vortexed in 1 dram vials. Samples were mixed for two-minute intervals and allowed to equilibrate for approximately one minute between the mixing intervals. The mixing and equilibration cycles were repeated until the desired total mix time was reached. After each mixing interval, the solution temperature was measured using a digital thermometer. Solution temperatures did not exceed 30 °C during the mixing. *Note that stabilized bubbles/foams were observed in several (but not all) of the samples after vortex mixing. However, there was not an obvious trend or relationship between the samples that contained bubbles.*

8.2.3 Small Angle Neutron Scattering (SANS)

8.2.3.1 Flow SANS

Flow SANS experiments were performed on the NG-7 30 m SANS instrument at the National Institute of Standards and Technology Center for Neutron Research. (NCNR). The Couette cell was placed in the neutron beam, allowing for direct analysis of the sample under flow (see Section 8.2.2.2 for Couette cell details).[35] An incident neutron wavelength of $\lambda = 5.5$ Å was used with detector distances of 1 m, 4 m, and 10 m to cover a q-range from 0.004 $Å^{-1} < q < 0.4$ $Å^{-1}$. The scattering vector q is defined as $q = (4\pi/\lambda) \sin(\theta/2)$, in which θ is the scattering angle. The scattering from the post-mixed sample was measured while the sample was quiescent. Subsequently, the sample was sheared at 5000 s^{-1} and the scattering data was measured at the longest detector distance (10 m). The data were collected in 10 min intervals and reduced using the standard procedures provided by NIST.[36]

8.2.3.2 Static SANS

SANS experiments were performed on the NG-7 30 m SANS instrument at the NCNR. An incident wavelength of 6.0 Å was used with sample-to-detector distances of 1 m, 4 m, and 13.5 m to cover a q-range from 0.004 $Å^{-1} < q < 0.4$ $Å^{-1}$. For the chain exchange experiments, the data were collected at the longest detector distance (13.5 m) for 5 min. *Note that these scattering experiments were performed using the 2 mm path length demountable cells to obtain better data statistics in the short acquisition time.* All measurements were performed at ambient temperature. The data were reduced in IGOR Pro using the standard procedures provided by NIST.[36]

SANS data were analyzed using the factor model for block polymer micelles described in Chapters 4 and 5. The post-mixed sample was fit assuming a mixture of

PB-PEO and PB-*d*PEO micelles. The volume fractions of PB-PEO and PB-*d*PEO micelles were fixed based on the known mixing ratio. Also, the scattering length density of the core block, corona blocks, and D_2O/H_2O solvent mixtures were input into the model. The core radii, polydispersity, and parameters for the micelle corona were fit during the analysis and constrained such that model gave reasonable fit results for both the PB-PEO and PB-*d*PEO micelles. For the post-mixed and vortexed samples, the scattering length density of the corona was set equal to that of the solvent. Therefore, the fit was not affected by the parameters related to the micelle corona. The scattering length density of the core block was input into the model and the micelle core radii and polydispersity values were fit.

8.3 Results

8.3.1 Effects of Mixing on Chain Exchange

The effects of mixing on chain exchange in highly amphiphilic block polymer micelles were explored by exploiting contrast variation in SANS experiments as described in Chapter 6. The results in Chapter 6 showed that no measurable chain exchange occurred in quiescent PB-PEO micelle solutions over times scales of weeks. Similarly, Chapter 7 demonstrated that gentle mixing *via* magnetic stirring did not lead to single chain exchange in aqueous solutions. However, the results in Chapter 7 also suggested that gentle stirring led to micelle growth in non-equilibrium assemblies. Motivated by the stirring-induced growth, this chapter systematically investigates the effects of common mixing methods used in micelle solution preparation on chain exchange and attempts to decouple interfacial and/or shear effects.

Figure 8.1 summarizes the SANS results for chain exchange in three differently mixed systems: Couette flow, sparging, and vortex mixing. As seen in Figure 8.1a, the scattered intensity from a sample sheared in a Couette cell at 5000 s^{-1} for 90 min matched the scattered intensity of the post-mixed micelles, indicating that no chain exchange events occurred. Similarly, no measurable chain exchange occurred after 60 min of sparging with N_2 gas (Figure 8.1b). However, the pronounced decrease in scattered intensity upon vortex mixing suggested that significant chain exchange events occurred after only 5 min of agitation with high shear and interfacial area (Figure 8.1c). Increasing the mix time further reduced the scattered intensity such that a completely randomized micelle solution was achieved after only 20 min of mixing.

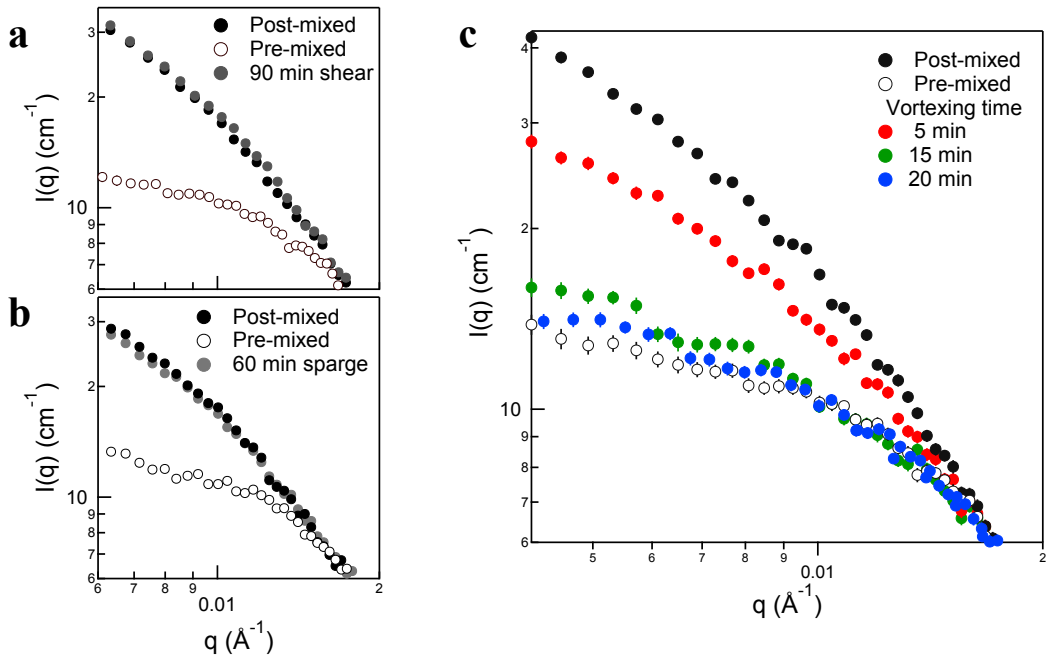

Figure 8.1 Effects of common mixing types on chain exchange in block polymer micelles. PB-PEO micelles were (a) sheared in a Couette cell at $\dot{\gamma}$ = 5000 s^{-1} for 90 min (b) sparged with N_2 for 60 min or (c) vortexed at approximately 3000 rpm for up to 20 min. All solutions contained 5 mg mL^{-1} polymer in D_2O/H_2O mixtures. Scattering data were collected at 25 °C.

The measured SANS intensity is a function of both the micelle form factor (*e.g.* micelle size and structure) and the contrast in the system. Accordingly, the decrease in scattered intensity noted in Figure 8.1c could be affected by mixing-induced changes in the micelle structure in addition to chain exchange. Therefore, the SANS data were collected over a broader *q*-range to investigate the effects of vortex mixing on the micelle structure. Figure 8.2 shows the scattering data for a pre-mixed and post-mixed micelle solution as well as for a solution that was vortex mixed for 20 min. The similar *q*-values of the minima and maxima in all three

samples supports that all of the micelles have similar core radii and core radii distributions. This finding was corroborated by fitting the data with a form factor model for block polymer micelles. The scattering length density of the corona was set equal to that of the solvent for the pre-mixed and vortexed samples, and the contrast between the PEO and *d*PEO micelle coronas and the solvent was included when modeling the post-mixed sample. The modeling results are summarized in Table 8.1, which further supports that the vortex mixing did not affect the micelle size or size distribution. Therefore, the decrease in scattered intensity at low q was due only to chain exchange and the associated decrease in scattering contrast.

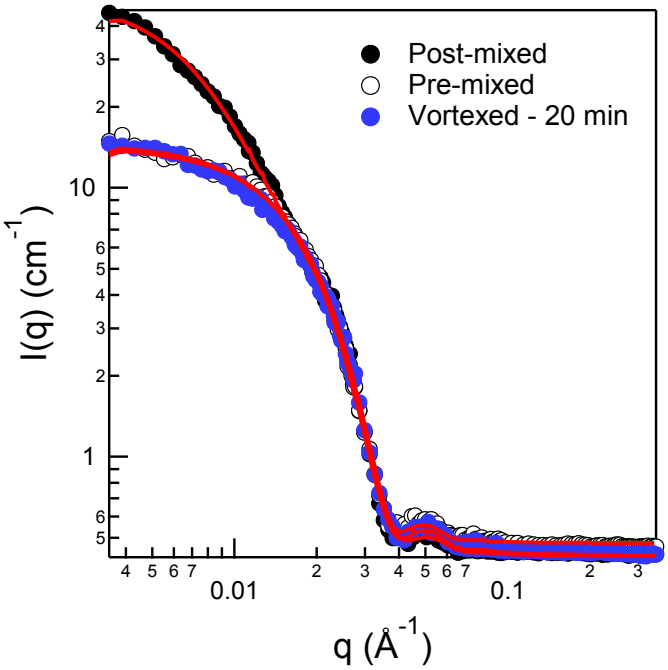

Figure 8.2 Effects of mixing on micelle structure. SANS data (points) and form factor fits (red lines) for the post-mixed, pre-mixed, and vortexed micelle samples. The data sets were analyzed with a form factor model for block polymer micelles.

Table 8.1 Summary of SANS data modeling results for the post-mixed, pre-mixed, and vortexed samples in Figure 8.2

Sample	Aggregation number	Core radius (nm)	Polydispersity
Post-mixed	896 ± 17 (PB-PEO)	11.2 ± 0.5	0.06
	851 ±160 (PB-*d*PEO)	11.4 ± 0.6	0.06
Pre-mixed	909 ± 5	11.6 ± 0.5	0.06
Vortexed	890 ± 5	11.5 ±0.5	0.1

Having confirmed that the decrease in scattered intensity was due to chain exchange, additional SANS studies were performed to better understand the underlying mechanism. Computational fluid dynamic (CFD) simulations reported in literature showed that the volume average shear ($\dot{\gamma}$) rate during the vortex mixing sample was approximately $\dot{\gamma} \sim 1000$ s^{-1}.[27] Therefore, the shear rates used during the Couette flow and vortex mixing experiments were on the same order of magnitude. However, vortex mixing generates significantly more air/water contact than Couette flow, suggesting that the combination of shear mixing and air/water contact enabled the chain exchange. The importance of the air/water interface was investigated by varying the liquid volume in the sample vial and thereby changing the volume of the headspace. As seen in Figure 8.3, when there was plenty of headspace (vial less than half full), 15 min of vortex mixing produced a completely randomized sample. Increasing the sample volume and almost filling the vial (4 mL of solution) reduced the headspace and 15 min of vortex mixing led to significantly less chain exchange. These results further supported that the air/water interface is essential to the mixing-induced chain exchange and indicated that the exchange was interface-limited.

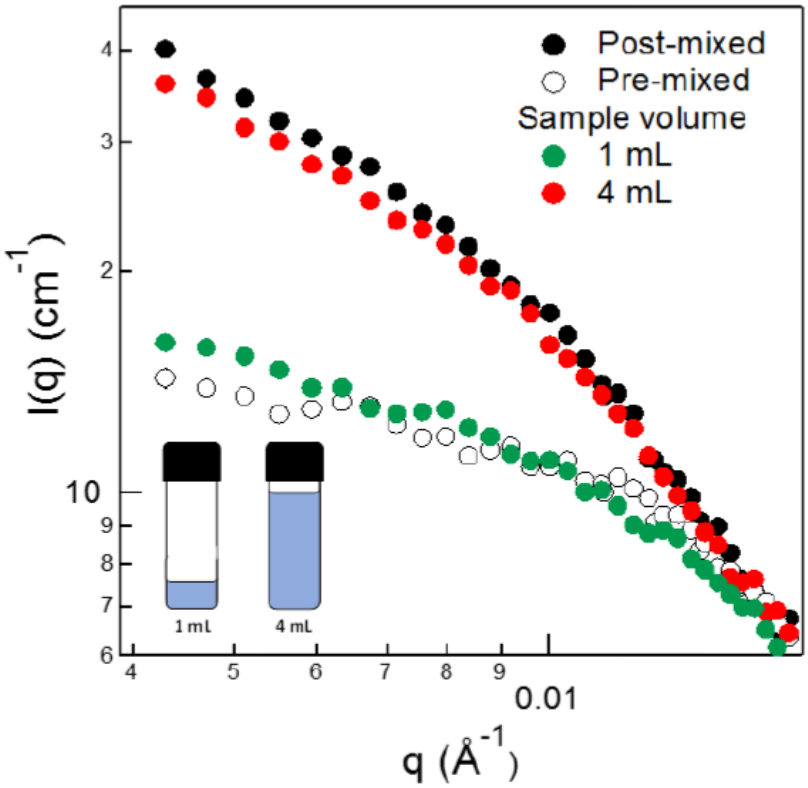

Figure 8.3 Effects of vial headspace (amount of air) on mixing induced chain exchange. Each solution was vortex-mixed in a 1 dram vial; however, the volume of sample within the vial was varied. Increasing the sample volume (decreasing the headspace) significantly reduced the rate of chain exchange. Both solutions contained 5 mg mL^{-1} polymer in D_2O/H_2O mixtures and were vortex mixed for 15 min. Scattering data were collected at 25 °C.

8.3.2 Mixing-Induced Chain Exchange Kinetics

To further probe the kinetics of the mixing-induced chain exchange, the experiments were repeated at multiple different micelle concentrations. Increasing the vortex time resulted in more chain exchange in all micelle solutions (Figure 8.4); however, comparing the exchange behavior in different samples demonstrated that the rate of chain exchange decreased with increasing concentration. For example, the

2.4 mg mL^{-1} sample was completely randomized after 10 min of mixing, while the 10 mg mL^{-1} sample required 60 min of mixing.

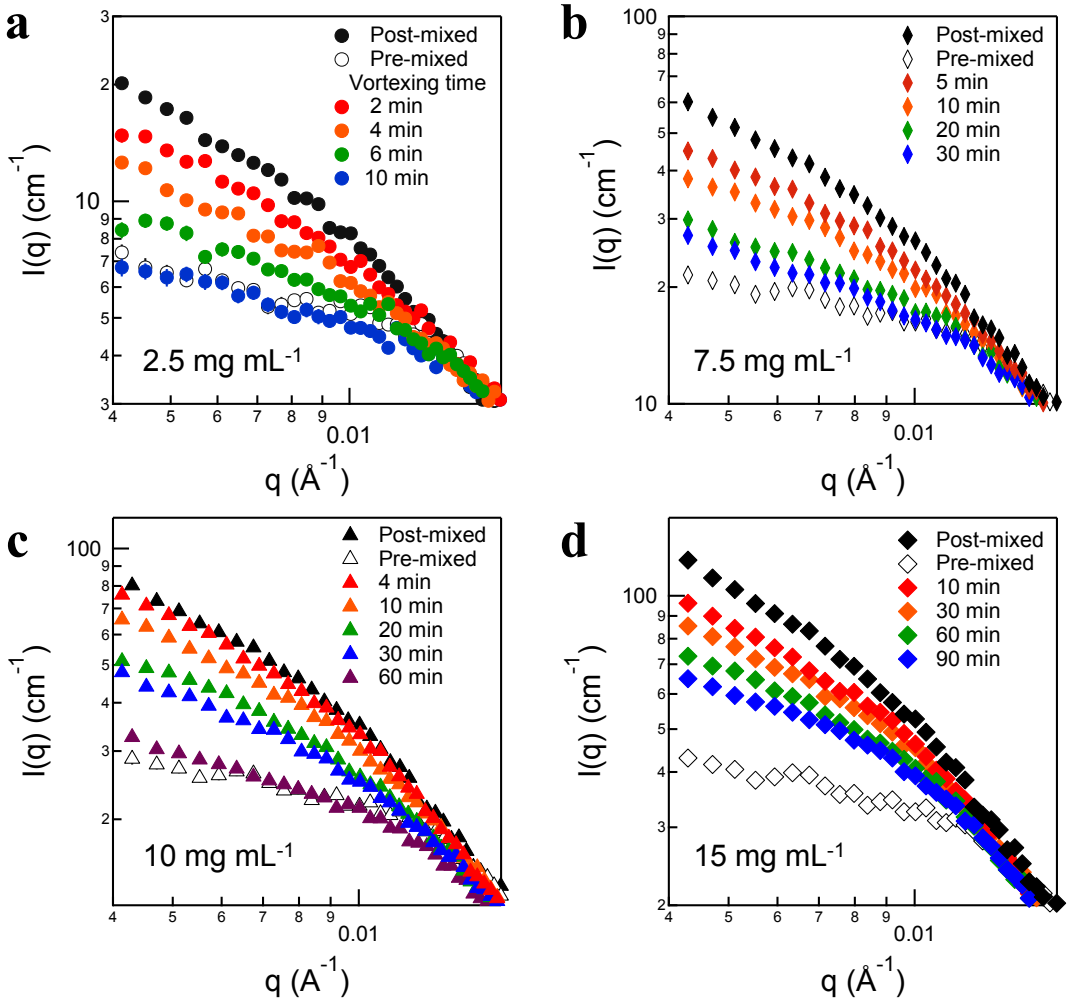

Figure 8.4 Effects of micelle concentration on vortex-induced chain exchange in block polymer micelles. SANS data for (a) 2.5 mg mL^{-1} (b) 7.5 mg mL^{-1} (c) 10 mg mL^{-1} and (d) 15 mg mL^{-1} samples vortex-mixed for varying times.

The chain exchange kinetics were quantified further using the analysis described in literature and discussed in more detail in Chapter 6.[37-39] The measured scattered intensity can be related to the extent of chain exchange according to

$$R(t) = \left(\frac{I(t) - I(\infty)}{I(0) - I(\infty)}\right)^{1/2} \quad (1)$$

in which R(t) = 1 corresponds to no chain exchange and R(t) = 0 corresponds to complete chain exchange or a randomized micelle solution. As seen in Figure 8.5, R(t) was linear with mix time in the 2.4 mg mL^{-1} to 10 mg mL^{-1} solutions, indicative of a zero-order kinetics. In contrast, R(t) changed more slowly and was nonlinear with mix time in the 15 mg mL^{-1} solution, suggesting the exchange was not surface-limited and other factors were influencing the kinetics.

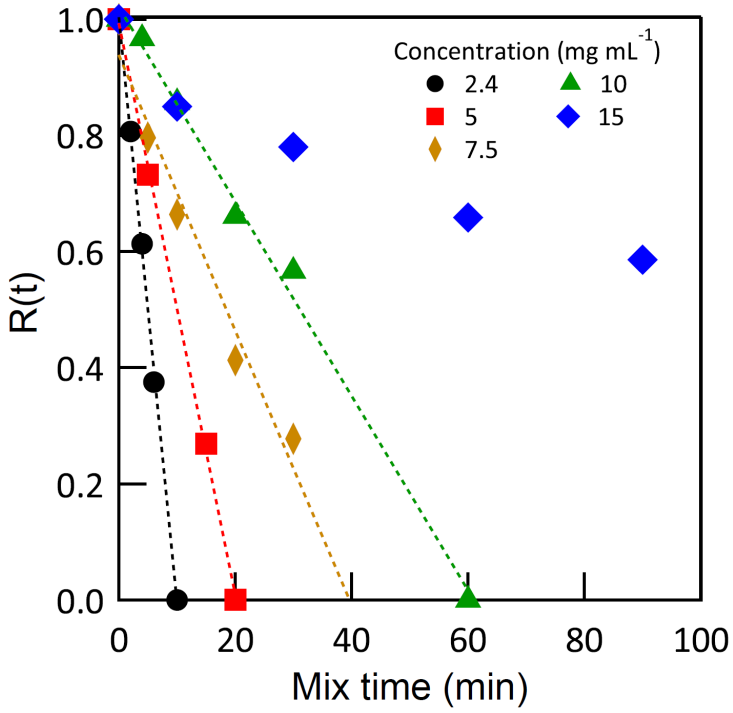

Figure 8.5 Chain exchange kinetics plotted as R(t) *vs.* vortex mix time for PB-PEO micelles at varying concentrations.

To take into account the total number of chains in solution, the data were replotted as the concentration of chain exchanged, c[1-R(t)], in which c is the polymer concentration in solution. As seen in Figure 8.6, the 2.4 mg mL^{-1} and 5 mg mL^{-1} data collapse onto one curve, suggesting that the same rate constant governs the chain exchange in these systems. Figure 8.6 further shows that the exchange rate decreases with increasing concentration, as the slopes (and therefore the rate constant) of the 7.5 mg mL^{-1} and 10 mg mL^{-1} data progressively decrease.

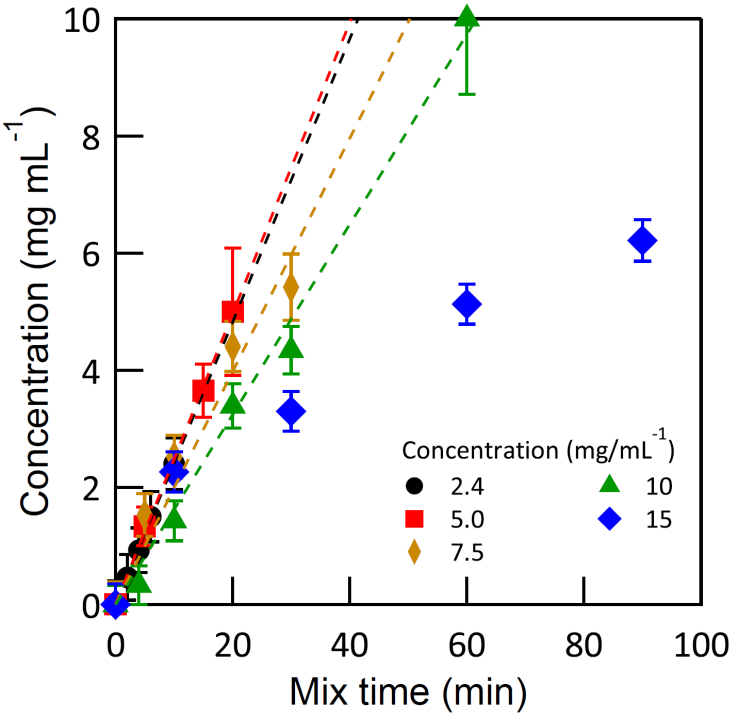

Figure 8.6 Vortex-induced chain exchange kinetics in block polymer micelles. Kinetics of chain exchange for different concentration micelles plotted as the concentration of exchanged chains. The kinetics for the low concentration micelle solutions are linear with mix time; however, the rate constant appears to decrease with increasing concentration. The kinetics for the highest concentration sample (15 mg mL^{-1}) are the slowest and deviate from linearity.

8.4 Discussion

The results presented herein suggest that mixing can have a profound impact on chain exchange, even in highly amphiphilic block polymer micelles. Previous work, including the results presented in Chapter 6, have shown that quiescent PB-PEO micelles are effectively frozen in pure water over week-long time scales.[2,34] Yet here, a completely randomized PB-PEO micelle solution in *pure* water is achieved in as little as 10 min of vortex mixing. Vortex mixing routinely is used in micelle solution

preparation, and the results presented here suggest that this processing step may significantly influence the resulting assembly.

Comparing different mixing types suggests that both high shear and high air/water contact are required to induce chain exchange. No chain exchange was seen in the sample mixed by sparging, which has high interfacial area and low shear. Similarly, high shear in the absence of air/water contact also did not lead to chain exchange based on the results from experiments conducted in a Couette cell. While the volume average shear rates in both the Couette and vortex mixed samples were estimated to be on the same order of magnitude, vortex mixing resulted in a completely randomized micelle solution. These results indicate that both the high shear and high air/water contact characteristic of vortex mixing led to chain exchange, suggesting that the underlying mechanism is a coupled shear and interfacial effect.

Amphiphilic block polymers are known to be interfacially active and readily absorb at air/water interfaces.[40-46] At the air/water interface, block polymers self-assemble into two-dimensional nanostructures in which the hydrophobic block is exposed to the air and anchors the polymer to the interface (Figure 8.7).[40-43] For example, studies by Isa and coworkers demonstrated that poly(styrene-*b*-ethylene oxide) (PS-PEO) diblock copolymers adsorbed so strongly to the air/water interface that desorption was never detected.[43] Their studies suggest that the energy barrier to PS-PEO desorption from the air/water interface was likely greater than ~ 10^3 kT. A desorption energy barrier this high can only by overcome by perturbing the interface and creating high surface pressures (> 15 mN m^{-1}).[43]

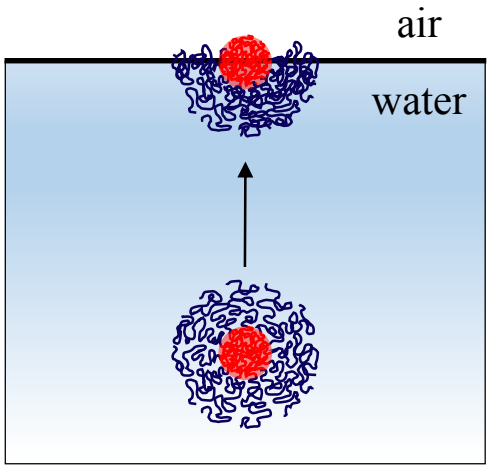

Figure 8.7 Schematic representation of block polymer micelle adsorption to the air/water interface. The hydrophobic block is exposed to air and is surrounded (laterally and underneath) by the hydrophilic block in water.

In the context of the vortex-induced chain exchange studied here, the high energy barrier to micelle desorption suggests that the air/water interface needs to deform and be regenerated for chain exchange to occur. CFD simulations by Bai *et al.* illustrated that vortex mixing regenerates more air/water interface and recirculates more bulk fluid to the interface than any other mixing method.[27] In the present study, the micelles may adsorb to the air/water interface which then rapidly collapses, forcing the micelle chains to mix. This hypothesis suggests that the chain exchange is limited by the available free air/water interface, which is consistent with the linear kinetics seen for the 2.4 mg mL^{-1} to the 10 mg mL^{-1} samples. Interestingly, several studies of agitation-induced protein kinetics also showed a linear relationship between the extent of aggregation and mix time, suggesting that the air/water interface renewal critically determines the protein stability.[47-49]

The proposed interface-limited mechanism also implies that the exchange rate is directly related to the air/water interface turnover rate. Estimating the exchange kinetics based on the CFD simulation results for the interface regeneration rate suggests the time scales are on the order of 10 – 100 min.[27] The estimated time scales are in good agreement with the experimentally measured rates, supporting that interface regeneration rate is important in determining the exchange kinetics. The exact relationship between the exchange kinetics and interface lifetime could be determined by changing the interface turnover by either slowing the vortex mixing[27] or using a more controlled mixing geometry that provides a quantitative measure of the interface regeneration rate.[48,49]

The rate constant in zero-order (interface-limited) kinetics typically is independent of concentration; however, the agitation-induced exchange rate was found to decrease with increasing concentration. Also, the 15 mg mL^{-1} sample appeared to deviate from the linear kinetics, further suggesting that other factors were affecting the chain exchange. While the solution viscosity increases with polymer concentration,[50] which in turn could influence the interface regeneration rate, [50,51] the overall change in viscosity in the dilute solutions studied here is expected to be small. Alternatively, the bulk concentration has been shown to affect nanoparticle adsorption to the interface.[51] Simulation and experimental studies demonstrated that strong adsorption of polymer-stabilized nanoparticles to the air/water interface resulted in a high surface density of particles and temporarily slowed additional adsorption events.[51] These results may indicate that the micelle adsorption to the air/water interface slows with increasing concentration, leading to the decrease in exchange kinetics. However,

additional studies are necessary to determine if the increase in polymer concentration influences the adsorption kinetics.[51,52]

It is interesting to note that the 15 mg mL^{-1} sample was approaching the concentration at which micelles begin to interact with one another,[53] which may indicate that interparticle interactions were affecting the agitation-induced chain exchange. Similarly, experimental work by Bates and Lodge showed that chain exchange in quiescent poly(styrene-*b*-ethylene-*alt*-propylene) micelle solutions was an order of magnitude slower in concentrated solutions (15 vol% polymer in solvent) compared to dilute solutions (< 1 vol% polymer in solvent).[37] Subsequent theoretical work by Halperin later suggested the slowed rate of exchange was due to overlap of the coronal chains, which lead to an osmotic penalty for inserting an expelled chain into a micelle.[54] However, more detailed investigations into the underlying mechanism are needed to fully understand the concentration effects seen here.

While agitation-induced shear and interfacial effects are largely unexplored in block polymer assemblies, the results presented here parallel studies of protein stability during agitation. Agitation-induced instability has major implication for protein therapeutics and has motivated significant research efforts in understanding shear and/or interfacial effects on protein solutions.[26] Importantly, studies of proteins have demonstrated that coupled shear and interfacial effects are especially deleterious to protein stability, and several proteins are known to adsorb to and subsequently unfold at air/water interfaces under agitation.[28,55,56] These studies on block polymer micelles underscore fundamental similarities between processing effects in block polymer micelles and protein systems. In fact, one method of minimizing protein aggregation is to add a nonionic surfactant to the solution, as the surfactant will

saturate the air/water interface and thereby minimize protein adsorption.[57,58] The decades of research into shear and interfacial effects in the biopharmaceutical field provide a valuable framework for understanding similar effects on the stability of block polymer micelles.

8.5 Conclusions

The results presented here demonstrate the extreme influence of mixing on chain exchange, even in highly selective solvent systems. Importantly these results suggest that the agitation-induced chain exchange is a coupled shear and interfacial effect. Most notably, the work presented here suggests that introducing an air/water interface leads to new pathways for dynamic processes not seen in the bulk solution. These results also highlight fundamental similarities between block polymer micelle and protein stability. While additional studies are needed to fully understand the shear and interfacial effects in block polymer assemblies, studies of protein stability provide a solid framework for exploring the complex effects. These studies of agitation-induced chain exchange have critical implications for block polymer micelle dynamics and further emphasize the importance of selecting and controlling processing conditions when preparing macromolecular assemblies.

REFERENCES

1 Jain, S. & Bates, F. S. (2003), *Science* **300**, 460-464

2 Jain, S. & Bates, F. S. (2004), *Macromolecules* **37**, 1511-1523

3 Groschel, A. H. *et al.* (2012), *Nature Communications* **3**, 1707

4 Zhu, J. H. *et al.* (2013), *Nature Communications* **4**, 3297

5 Pochan, D. J. *et al.* (2004), *Science* **306**, 94-97

6 Zhong, S., Cui, H., Chen, Z., Wooley, K. L. & Pochan, D. J. (2008), *Soft Matter* **4**, 90-93

7 Meli, L. & Lodge, T. P. (2009), *Macromolecules* **42**, 580-583

8 Meli, L., Santiago, J. M. & Lodge, T. P. (2010), *Macromolecules* **43**, 2018-2027

9 Geng, Y. & Discher, D. E. (2005), *Journal of the American Chemical Society* **127**, 12780-12781

10 Yildiz, M. E., Prud'homme, R. K., Robb, I. & Adamson, D. H. (2007), *Polymers for Advanced Technologies* **18**, 427-432

11 Zhu, J. & Hayward, R. C. (2008), *Angewandte Chemie-International Edition* **47**, 2113-2116

12 Zhu, J. T. & Hayward, R. C. (2008), *Journal of the American Chemical Society* **130**, 7496-7502

13 Gindy, M. E., Panagiotopoulos, A. Z. & Prud'homme, R. K. (2008), *Langmuir* **24**, 83-90

14 Johnson, B. K. & Prud'homme, R. K. (2003), *Physical Review Letters* **91**, 118302

15 Johnson, B. K. & Prud'homme, R. K. (2003), *Australian Journal of Chemistry* **56**, 1021-1024

16 Shum, H. C., Kim, J.-W. & Weitz, D. A. (2008), *Journal of the American Chemical Society* **130**, 9543-9549

17 Wang, C.-W., Sinton, D. & Moffitt, M. G. (2011), *Journal of the American Chemical Society* **133**, 18853-18864

18 Karnik, R. *et al.* (2008), *Nano Letters* **8**, 2906-2912

19 Wang, Z. & Jiang, W. (2010), *Chemical Physics Letters* **487**, 84-87

20 Yu, H. & Jiang, W. (2009), *Macromolecules* **42**, 3399-3404

21 Cui, J., Xu, J., Zhu, Y. & Jiang, W. (2013), *Langmuir* **29**, 15704-15710

22 Sorrells, J. L., Tsai, Y.-H. & Wooley, K. L. (2010), *Journal of Polymer Science Part A: Polymer Chemistry* **48**, 4465-4472

23 Wang, C.-W., Sinton, D. & Moffitt, M. G. (2013), *ACS Nano* **7**, 1424-1436

24 Leal-Calderon, F., Schmitt, V. & Bibette, J. *Emulsion science: basic principles*. Springer, 2007.

25 Schuster, D. *Encylopedia of Emulsion Technology: Basic theory, measurement, applications*. Vol. 3 CRC Press, 1987.

26 Thomas, C. R. & Geer, D. (2011), *Biotechnology Letters* **33**, 443-456

27 Bai, G., Bee, J. S., Biddlecombe, J. G., Chen, Q. & Leach, W. T. (2012), *International Journal of Pharmaceutics* **423**, 264-280

28 Kiese, S., Papppenberger, A., Friess, W. & Mahler, H.-C. (2008), *Journal of Pharmaceutical Sciences* **97**, 4347-4366

29 Nielsen, L. *et al.* (2001), *Biochemistry* **40**, 6036-6046

30 Ripoll, M., Winkler, R. G. & Gompper, G. (2006), *Physical Review Letters* **96**, 188302

31 Stellbrink, J., Lonetti, B., Rother, G., Willner, L. & Richter, D. (2008), *Journal of Physics-Condensed Matter* **20**

32 Li, S. *et al.* (1993), *Langmuir* **9**, 2243-2246

33 Ahmed, F., Hategan, A., Discher, D. E. & Discher, B. M. (2003), *Langmuir* **19**, 6505-6511

34 Won, Y. Y., Davis, H. T. & Bates, F. S. (2003), *Macromolecules* **36**, 953-955

35 Eberle, A. P. R. & Porcar, L. (2012), *Current Opinion in Colloid & Interface Science* **17**, 33-43

36 Kline, S. (2006), *Journal of Applied Crystallography* **39**, 895-900

37 Choi, S. H., Bates, F. S. & Lodge, T. P. (2011), *Macromolecules* **44**, 3594-3604

38 Choi, S. H., Lodge, T. P. & Bates, F. S. (2010), *Physical Review Letters* **104**, 047802

39 Lu, J., Choi, S., Bates, F. S. & Lodge, T. P. (2012), *ACS Macro Letters* **1**, 982-985

40 Perepichka, I. I., Badia, A. & Bazuin, C. G. (2010), *ACS Nano* **4**, 6825-6835

41 Cox, J. K., Yu, K., Constantine, B., Eisenberg, A. & Lennox, R. B. (1999), *Langmuir* **15**, 7714-7718

42 Price, E. W., Harirchian-Saei, S. & Moffitt, M. G. (2010), *Langmuir* **27**, 1364-1372

43 Zell, Z. A., Isa, L., Ilg, P., Leal, L. G. & Squires, T. M. (2013), *Langmuir* **30**, 110-119

44 Shull, K. R., Winey, K. I., Thomas, E. L. & Kramer, E. J. (1991), *Macromolecules* **24**, 2748-2751

45 Richards, R. W., Rochford, B. R. & Webster, J. R. P. (1997), *Polymer* **38**, 1169-1177

46 An, S. W. *et al.* (1998), *The Journal of Physical Chemistry B* **102**, 387-393

47 Wiesbauer, J., Prassl, R. & Nidetzky, B. (2013), *Langmuir* **29**, 15240-15250

48 Bee, J. S. *et al.* (2012), *Soft Matter* **8**, 10329-10335

49 Rudiuk, S., Cohen-Tannoudji, L., Huille, S. & Tribet, C. (2012), *Soft Matter* **8**, 2651-2661

50 Mewis, J. & Wagner, N. J. *Colloidal suspension rheology*. Cambridge University Press, 2013.

51 Schwenke, K., Isa, L. & Del Gado, E. (2014), *Langmuir* **30**, 3069-3074

52 Isa, L. *et al.* (2011), *Soft Matter* **7**, 7663-7675

53 Won, Y.-Y., Davis, H. T., Bates, F. S., Agamalian, M. & Wignall, G. D. (2000), *The Journal of Physical Chemistry B* **104**, 7134-7143

54 Halperin, A. (2011), *Macromolecules* **44**, 5072-5074

55 Sluzky, V., Tamada, J. A., Klibanov, A. M. & Langer, R. (1991), *Proceedings of the National Academy of Sciences* **88**, 9377-9381

56 Nielsen, L. *et al.* (2001), *Biochemistry* **40**, 6036-6046

57 Chou, D. K., Krishnamurthy, R., Randolph, T. W., Carpenter, J. F. & Manning, M. C. (2005), *Journal of Pharmaceutical Sciences* **94**, 1368-1381

58 Kerwin, B. A. (2008), *Journal of Pharmaceutical Sciences* **97**, 2924-2935

Chapter 9

DESIGN AND SYNTHESIS OF AMPHIPHILIC POLYMER-PEPTIDE CONJUGATES

This chapter presents the rational design and modular synthesis of enzyme-responsive polymer-peptide conjugates. The synthetic strategy takes advantage of quantitative polymer end-functionalization chemistries and solid phase chemistries to create well-defined conjugates. Importantly, the synthetic strategy presented here enables control over both the peptide sequence and location within the polymer chain, which has important implications for developing effective targeted drug delivery vehicles.

9.1 Introduction

Up to this point, this dissertation has focused on understanding and controlling amphiphilic block polymer solution assembly towards the goal of creating well-defined, reproducible assemblies for drug delivery applications. While nanostructure size and shape is known to play a crucial role in these applications, the nanostructure surface functionality is equally important.[1-6] In particular, significant research efforts have focused on incorporating targeting ligands onto polymeric assemblies to enhance their performance as delivery vehicles.[2,3] Accordingly, the goal of this chapter was to develop a tunable, modular synthetic approach for incorporating peptide targeting groups into amphiphilic block polymers.

A major motivation behind developing polymeric nanocarriers is the pressing clinical need for improved drug targeting to increase the concentration of therapeutics

in diseased cells while not affecting the surrounding tissues.[7-9] This efficient delivery is especially important for administering chemotherapeutics to treat cancer that are highly toxic and have numerous adverse side-effects. [2,3,7-10] Significant research efforts have worked towards the development of more effective treatments for this devastating disease by exploiting two types to tumor targeting mechanisms: passive and active target. Nanostructures selectively accumulate in solid tumors due to the leaky vasculature and limited lymphatic drainage, which permits passive targeting by tuning the delivery vehicle size [known as the enhanced permeability and retention (EPR) effect].[11,12] Nonionic or zwitterionic polymeric micelles are ideal candidates for passive targeting, as the dense hydrated coronas resist opsonization *in vivo*, prolonging circulation times and further enhancing tumor accumulation.[1] This ability to evade recognition by the immune system has led to the development of a myriad of polymeric "stealth" nanoassemblies for drug delivery applications.[2,5,13,14] Another advantage of polymeric assemblies is their synthetic versatility, which facilitates facile attachment of small molecules, peptides, and proteins to the nanostructures.[15] These ligands can interact with specific enzymes or receptors to enhance cellular uptake, which is referred to as active targeting. However, the attachment of targeting ligands also can evoke an immune response *in vivo*, leading to rapid clearance of the delivery vehicle from the body.[16]

The desire to simultaneously take advantage of passive and active targeting places seemingly contradictory demands on drug delivery vehicle design. Ligands must be shielded to improve circulation times yet accessible to interact with cell surface receptors (Figure 9.1). Elegant work by Langer and Farokhzad *et al.* demonstrated that a delicate balance between ligand display and stealth properties led

to maximal drug carrier uptake by prostate cancer cells *in vitro* and *in vivo*.[17] Strategies to control ligand display most often rely on varying the amount of targeting ligand attached to the surface of preformed assemblies or on blending pre-functionalized and unfunctionalized polymers before assembling the materials into delivery vehicles.[17-20] While these approaches enhance drug delivery vehicle performance, they only indirectly allow for control over the ligand display within the drug delivery vehicle. Herein, a synthetic approach for *directly* controlling the location of targeting ligands within the polymeric materials is developed towards the goal of balancing the needs for both stealth/prolonged circulation as well as active targeting.

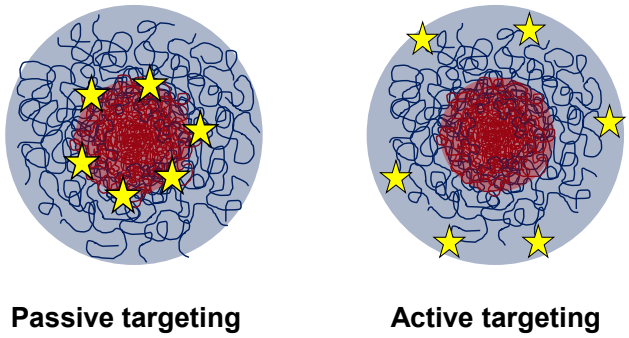

Figure 9.1 Schematic representation of the contradictory need for shielded ligand (stars) during circulation to take advantage of passive targeting yet accessible ligands to bind to cells and take advantage of active targeting.

Specifically, this work aims to develop a robust synthetic approach to create amphiphilic polymer-peptide conjugates containing peptide linkage designed to target cancer cells and allow the material to evolve with the delivery pathway as depicted in

Figure 9.2. The peptide linkage contains a matrix metalloproteinase (MMP) cleavage site and an $\alpha_v\beta_3$ integrin binding sequence. MMPs are a class of secreted proteases that play an important role in tumor invasion and metastasis, making them an attractive target for cancer-targeted therapeutics.[8] For example, Gianneschi *et al.* developed a series of block polymer micelles containing MMP-labile peptide sequences that showed enhanced accumulation and retention in tumors as compared to non-labile controls.[21,22] Similarly, $\alpha_v\beta_3$ integrins are overexpressed in tumors,[8] and attaching the short three amino acid sequence Arginine-Glycine-Aspartic Acid (RGD) to delivery vehicles has significantly enhanced the uptake of polymeric micelles,[19,23] vesicles,[24] liposomes,[25,26] and nanoparticles[27,28] in tumor cells.

The synthesis of the polymer-peptide conjugates is demonstrated using a model system with poly(ethylene oxide) (PEO) as a hydrophilic block and poly(ethyl ethylene) (PEE) as a hydrophobic block. PEO was selected because it is nonimmunogenic and well-known to resist opsonization *in vivo* and enhance circulation times.[29,30] PEE was chosen over polybutadiene (PB) as the hydrophobic block for these studies to avoid potential side reactions between the PB double bonds and azides while developing the conjugation chemistries.[31] Like PB, PEE is highly hydrophobic and these assemblies are expected to have a low critical micelle concentration.[32] Also, PEE-based solution assemblies can be formed by directly dispersing the materials in water due to the low glass transition temperature ($T_g \sim$ 20 °C) of PEE.[33]

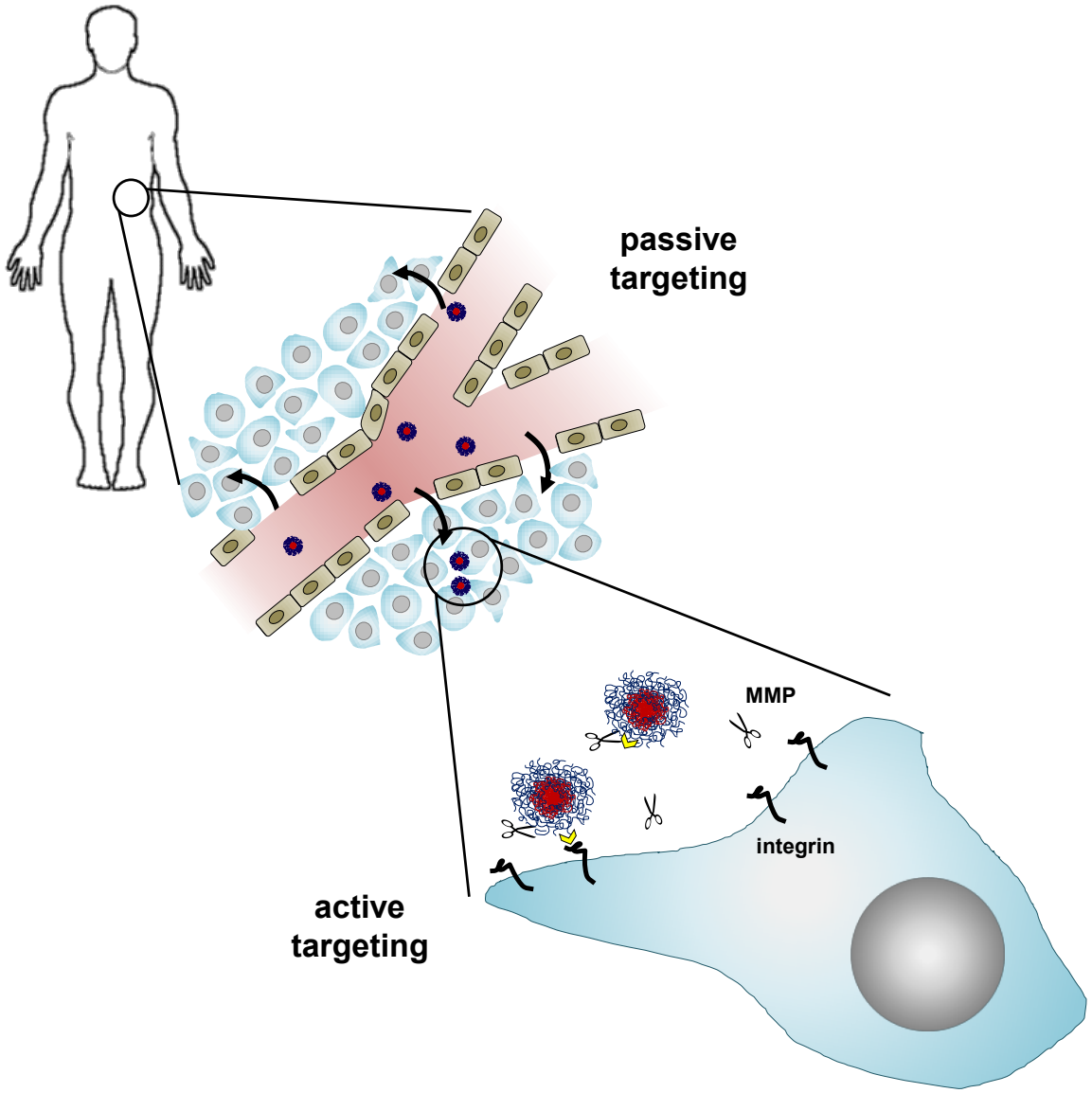

Figure 9.2 **Schematic representation of enzyme-responsive polymer-peptide conjugate design. The micelles accumulate in the tumor by passive targeting. Within the tumor, the peptide linkage is cleaved by the MMP proteases, exposing the targeting ligand and facilitating cellular uptake by receptor-mediated endocytosis.**

9.2 Experimental

9.2.1 Materials

Ethylene oxide (EO) and 1,3 butadiene were purchased from Sigma Aldrich and were purified by distillation from butylmagnesium chloride (EO) or *n*-butyllithium (butadiene). Tetrahydrofuran (THF) for the polymerization and click reactions was degassed with argon and purified by passage through two neutral alumina columns. Toluene for hydrogenation reactions was degassed with argon and then purified by passage through a neutral alumina and Q5 column. Dimethylsulfoxide (DMSO) and dimethylformamide (DMF) used in the functionalization and click reactions were dried over calcium hydride overnight, filtered, distilled under reduced pressure, and then stored over molecular sieves under argon. Anhydrous 1-methyl-2-pyrrolidone (NMP, 99.5%, Acros Organics) for the click reactions was purchased from Fisher Scientific and used as received. *p*-toluenesulfonyl hydrazide (TSH, 97%, Sigma Aldrich) for the chemical hydrogenation reactions was recrystallized from ethanol, dried under vacuum, and stored at 4 °C until use. Tripropylamine (TPA, > 98%, Sigma Aldrich), used to prevent side reactions during the hydrogenation, was stirred over calcium hydride for 30 min and then distilled under reduced pressure before use. Copper bromide [Cu(I)Br] was washed with glacial acetic acid and then ethanol, dried under vacuum, and stored in an air-free glovebox. Amino acids for the peptide synthesis were purchased from Novabiochem (EMD Millipore, USA) and were used as received. The Fmoc-Lys(Dabcyl)-OH and Fmoc-propargylglycine were purchased from AnaSpec (Fremont, CA) and used as received. Heterobifunctional Fmoc-NH-PEO-COOH (2 kg mol^{-1}, > 95% functionalized) and Fmoc-NH-PEO_{12}-COOH (840 g mol^{-1}, > 95%

functionalized) were purchased from Creative PEGWorks (Winston Salem, NC) and Iris Biotech (Marktredwitz, Germany), respectively. Both polymers were used as received. Type I bacterial collagenase was obtained from Worthington (Lakewood, NJ). All other chemicals were purchased from Fisher Scientific and used as received.

9.2.2 Hydrophobic Block Synthesis and Functionalization.

9.2.2.1 Poly(ethyl ethylene) Synthesis *via* Chemical Hydrogenation

Hydroxyl-terminated poly(ethyl ethylene) (PEE-OH) was synthesized by chemical hydrogenations of hydroxyl-terminated poly(1,2 butadiene) (PB-OH) using a diimide produced *in situ* by thermal decomposition of *p*-toluenesulfonyl hydrazide (TSH). Diimide hydrogenations have been shown to be a highly effective, low pressure alternative to catalytic hydrogenations, achieving > 80% conversion of the double bonds in as little as 4 h.[34-38] Importantly, this hydrogenation chemistry does not affect the hydroxyl end-group,[35,36,38] which is essential for subsequent functionalization reactions.

The hydrogenation reaction conditions were optimized to ensure complete saturation of the double bonds while preventing unwanted side reactions. While theoretically only one TSH molecule per double bond should be needed for complete hydrogenation, previous work has demonstrated that not all of the generated diimide reacts with polymer double bonds. Once the diimide is formed, there are two competing reactions: hydrogenation of the double bond and disproportionation of the diimide to hydrazine.[34,37] Therefore all reactions were performed using an excess of TSH. However, the addition of too much TSH can lead to undesirable side reactions. The byproduct from *in situ* TSH degradation, *p*-toluenesulfinic acid, also can attack

the double bonds, leading to molecular weight degradation and attachment of sulfur-containing species to the polymer backbone.[37] To mitigate these side reactions, the hydrogenations were performed at dilute concentrations and a high boiling point tertiary amine, tripropylamine (TPA), was added to the reaction. Addition of TPA has been shown to prevent addition of sulfur containing byproducts to the backbone of butadiene and isoprene-containing polymers. [37]

In a typical reaction, 1 g of PB-OH was dissolved in approximately 100 mL of dry toluene (*ca.* 1 wt% polymer in solvent to minimize side reactions). The polymer solution was added to a custom-built reaction flask equipped with a condenser and two septum ports. Subsequently, TSH and TPA (2 equivalents per PB double bond) were added to the reaction mixture. *Note that the TSH is only slightly soluble in toluene at room temperature but dissolves upon heating*. The reaction mixture was sparged with N_2 for 30 min and then heated to 100 °C to fully dissolve the TSH. The reaction mixture turned light yellow upon dissolution of the TSH. Subsequently, the reaction mixture was heated to 120 °C for 4 h and then 135 °C for 3 h. At the end of the reaction the solution was cooled to room temperature, the solid precipitates were removed by vacuum filtration, and the toluene was removed by rotary evaporation. The polymer was dissolved in heptanes and washed with methanol containing 1% w/v $CaCl_2$ to suppress emulsion formation. The organic phase was washed a total of 10 times to remove the *p*-tolyl mercaptan byproduct, and then the polymer was dried under vacuum for ~ 12 h or until all of the solvent was removed as confirmed by proton nuclear magnetic resonance (^{1}H NMR) spectroscopy.

9.2.2.2 Synthesis of Azide-Functionalized PEE

The hydroxyl end-group of PEE-OH was converted to an azide via a two-step reaction. First, PEE-OH was mesylated to give PEE-mesyl. PEE-OH and 5 equivalents of triethylamine (TEA) were dissolved in dichloromethane (DCM) at a concentration of approximately 10 mM polymer in solvent. The solution was sparged with argon for 15 min and cooled to 0 °C on an ice bath. Then, 2.5 equivalents of methanesulfonyl chloride (mesyl chloride) was dissolved in *ca.* 0.5 mL of DCM, and the mesyl chloride solution was added dropwise to the polymer solution on ice. The polymer solution was allowed to warm to room temperature and stirred overnight. At the end of the reaction, the polymer was diluted with DCM and rapidly washed with water, dilute HCl in water, saturated sodium bicarbonate in water, and water. The DCM was removed by rotary evaporation, and the polymer was redissolved in benzene and freeze-dried.

Subsequently, the mesylated PEE was reacted with sodium azide to yield the azide end-functionalized PEE-N_3. PEE-mesyl was dissolved in ~ 2.5 mL of dry THF. Then, 10 equivalents of sodium azide was dissolved in 1.6 mL of dry DMF and was added to the reaction vial. The final solvent composition was approximately 40/60 vol% THF/DMF. The vial was sealed under argon and the solution was stirred at 40 °C for 48 h. At the end of the reaction, the polymer was precipitated into methanol, and the solution was centrifuged at 4 °C for 1 h to pellet the polymer. The precipitation was repeated twice to remove the excess sodium azide, and then the polymer was redissolved in benzene and freeze-dried.

9.2.3 Hydrophilic Block Synthesis

9.2.3.1 Solid Phase Peptide Synthesis (SPPS)

Peptides were synthesized using standard fluroenylmethyl carbamate (Fmoc) chemistry. All syntheses were performed using an automated solid phase peptide synthesizer (Tribute, Protein Technologies, Inc.) with inline Fmoc-deprotection monitoring. The peptides were synthesized at 0.1 mmol scale using Chemmatrix Rink-Amide low loading resin (0.27 mmol/g resin). Amino acid additions were performed using 6 molar equivalents of amino acid and standard N,N,N',N'-tetramethyl-O-(1*H*-benzyotriazol-1-yl)uranium hexafluorophosphate (HBTU) and N-methylmorpholine coupling chemistry. Each addition step used 3 mL of solvent and the reaction was allowed to proceed for 2 h.

Upon completion of the synthesis, peptides were cleaved off the resin using a 95/2.5/2.5 vol% trifluoroacetic acid (TFA)/triisopropylsilane (TIS)/water cleavage cocktail. The cleavage was performed for 3 h and the solution was concentrated under nitrogen gas before precipitating the peptide into cold diethyl ether. The peptide was recovered by centrifugation at 4000 rpm for 5 min at 4 °C, and the resulting pellet was redissolved in water and lyophilized.

9.2.3.2 Dye Labeled Peptide for Förster Resonance Energy Transfer (FRET) Experiments

Peptide Synthesis and Lys(Dabcyl) Addition

The enzyme-sensitive peptide was labeled with carboxyfluorescein (FAM, fluorescence donor) and 4-((4-(dimethylamino)phenyl)azo)benzoic acid (Dabcyl, fluorescence quencher) on either side of the MMP-cleavage sequence [final labeled sequence: N-GRGDSPGGK(FAM)GPQG↓IWGQK(Dabcyl)GGG-C]. The peptide

was synthesized using standard Fmoc-based solid phase peptide synthesis on a 0.1 mmol scale as described above. The Dabcyl was incorporated using a pre-labeled amino acid. For this addition step, 4 equivalents of Fmoc-Lys(Dabcyl)-COOH was dissolved in 2 mL of DMF, and this solution was added to the resin. The coupling reaction was run for 3 h, and then the resin was thoroughly washed until the washes were colorless. Subsequently, a capping solution [20 vol% acetic anhydride in DMF and 1.5 molar equivalents of diisopropylethylamine (DIPEA)] was added to the resin to react any unreacted amines [*i.e.* peptides that would not contain the Lys(Dabcyl)]. The capping reaction was allowed to proceed for 30 min, and then the resin was thoroughly washed with DCM and DMF. The glutamine (Q) addition immediately following the Lys(Dabcyl) was double coupled, and the remaining amino acid additions were performed using the standard conditions. *Note that the other lysine added (13th amino acid) was Dde-protected [Fmoc-Lys(Dde)-COOH] to facilitate carboxyfluorescein addition.*

Carboxyfluorescein Addition

The N-terminal Fmoc-group was left on the peptide after the last amino acid addition, and then Dde protecting group was selectively removed. The Dde deprotection solution contained 1.25 g hydroxylamine hydrochloride and 0.92 g imidazole in 5 mL NMP (*Note: the deprotection solution may need to be heated slightly to fully dissolve all of the reagents*). The deprotection solution was added to the resin, and the reaction was mixed for 3 h. After removal of the deprotection solution, the resin was thoroughly washed with DMF. The carboxyfluorescein was added using standard HBTU/N-methylmorpholine coupling conditions. 4 equivalents

of carboxyfluorescein and HBTU were dissolved in 2 mL of DMF containing 0.4 M methylmorpholine. The dye solution was added to the resin and the reaction was sparged for 3 h. The dye solution was removed, and the resin was washed with DMF until the rinses were colorless. The carboxyfluorescein addition was repeated twice, and then the hydroxyl groups on the dye were protected with triphenylmethyl chloride (trityl chloride) to prevent any side reactions during removal of the N-terminal Fmoc group. To protect the hydroxyl groups, 6 molar equivalents of trityl chloride and DIPEA were dissolved in 3 mL of DMF. The trityl chloride solution was added to the resin and mixed for 8 h. Then the solution was removed and the resin was thoroughly washed. The trityl protection step was repeated twice. Finally, the N-terminal Fmoc group was removed using the standard piperidine deprotection conditions.

Upon completion of the synthesis, the labeled peptide was cleaved from the resin using a 95/2.5/2.5 vol% TFA/TIS/water cleavage cocktail. The cleavage was performed for 3 h and the solution was concentrated under nitrogen gas before the peptide was precipitated into cold diethyl ether. The peptide was recovered by centrifugation at 4000 rpm for 5 min at 4 °C and the resulting pellet was redissolved in water and lyophilized. The molecular weight was confirmed by matrix assisted laser desportion/ionization time of flight mass spectrometry (MALDI-TOF MS). Reverse phase high performance liquid chromatography (RP-HPLC) experiments indicated that the crude peptide was pure and that > 85 % of the peptide product was dual labeled with both Dabcyl and carboxyfluorescein. The labeled peptide was used for FRET experiments without any additional purification.

9.2.3.3 On-resin Polymer Conjugation

Heterobifunctional Fmoc-NH-PEO-COOH (2 kg mol^{-1}, Creative PEGWorks) was coupled to the N-terminus of the synthesized peptides on resin using (benzotriazol-1-yloxyl)tripyrrolidinophosphonium hexafluorophosphate (PyBOP)/DIPEA coupling chemistry. Conjugation reactions were performed on a ~0.04 mmol scale. The resin was swelled with DCM for 30 min, and a solution containing 2 equivalents PEO, 2 equivalents PyBOP, and 4 equivalents of DIPEA in DCM was added to the resin. Additional DCM and NMP were added to fully cover the resin such that the final solvent composition was approximately 70/30 vol% DCM/NMP. The reaction was sparged with argon for 96 h, and additional solvent was added every 12 h to keep the resin covered. The PEO solution was removed from the resin, and the resin was washed with DCM (5 times), DMF (5 times), and DCM (5 times) to remove the unreacted PEO.

'End' PEO-Peptide Conjugates

For conjugates that contained the peptide at the end of the hydrophilic block, the amine on the PEO was coupled with hexynoic acid. [Final sequence (N to C terminus): alkyne-PEO-GRGDSPGGEGPQG↓IWGQKG]. First, any unreacted N-terminal amines on the peptide were capped using acetic anhydride. This step prevented unreacted peptides from being functionalized with an alkyne group to simplify future purification steps. A solution containing 20 vol% acetic anhydride in DMF was added to the resin and sparged for 5 min. Then 1.5 molar equivalents of DIPEA were added to the reaction and the reaction was sparged for an additional 25 min. Upon completion of the reaction, the resin was washed thoroughly and the capping step was repeated. After the capping step, the Fmoc group was removed from

the PEO using standard conditions (20 vol% piperdine in DMF for 30 min). Finally, hexynoic acid was coupled to the free amine on the PEO. A solution containing 8 molar equivalents each of hexynoic acid, PyBOP, and DIPEA in NMP was added to the resin. Additional solvent was added to fully cover the resin, and the final solvent composition was approximately 60/40 vol% DCM/NMP. The reaction was sparged overnight, and the resin was washed thoroughly with DCM and NMP. Upon completion of the reaction, the PEO-peptide conjugate was cleaved from the resin using a 95/2.5/2.5 vol% TFA/TIS/water cleavage cocktail. The cleavage solution was concentrated under nitrogen and the PEO-peptide was precipitated into cold diethyl ether. The conjugate was recovered by centrifugation, dissolved in water, and lyophilized.

'Interface' PEO-Peptide Conjugates

For conjugates that contained the peptide at the interface between the hydrophilic and hydrophilic block, the free amine on the PEO was acetylated. [Final sequence (N to C terminus): PEO -GEGPQG↓IWGQKGGRGDSPGG(alkyne)]. First, the N-terminal Fmoc-group was removed using the standard methods. A solution containing 20 vol% piperdine in DMF was added to the resin and mixed for 30 min. Then, the resin was thoroughly washed, and the deprotection step was repeated. Subsequently, a capping solution containing 20 vol% acetic anhydride in DMF was added to the resin, and the solution was sparged for 5 min. Then, 1.5 molar equivalents of DIPEA were added to the solution, and the reaction was sparged for an additional 25 min. The resin was thoroughly washed, and the capping step was

repeated a total of two times. The final PEO-peptide conjugate was cleaved from the resin and recovered as described above.

9.2.3.4 Peptide Synthesis using Pre-functionalized Resin

PEO-peptide conjugates also were synthesized by growing the peptide from a pre-functionalized resin. First the resin was functionalized with a heterobifunctional Fmoc-NH-PEO_{12}-COOH (840 g mol^{-1}, Iris Biotech). The conjugates were synthesized on a 0.1 mmol scale. Fmoc rink amide resin was swelled with DMF and the Fmoc group was removed with standard deprotection conditions. Then, 1.5 equivalents of Fmoc-NH-PEO-COOH, 1.5 equivalents of HBTU, and 3 equivalents of DIPEA were dissolved in a 1:1 mixture of DCM:DMF. The PEO solution was added to the resin and additional DCM and DMF were added to fully cover the resin, with a total solvent volume of ~3.5 mL. The coupling reaction was allowed to proceed for 24 h. The PEO solution was removed, the resin was thoroughly washed with DCM, and then dried. The increase in resin mass following the coupling reaction suggested the conjugation efficiency was ~60%, giving a resin loading of ~0.4 mmol/g. The unreacted amines on the resin then were capped to ensure that the peptide only grew from the polymer chain. A capping solution containing 20 vol% acetic anhydride in DMF and 15 equivalents of DIPEA was added to the resin and mixed for 45 min. The capping solution was removed from the resin, and the resin was washed before repeating the capping step.

Subsequently, the peptide was grown from the functional PEO using SPPS as described in Section 9.3.2.1. The resin was swelled, and the Fmoc group was removed from the PEO using standard conditions. Amino acid additions were performed using

0.6 mmol of amino acid and HBTU in 2 mL of a 0.4 M methylmorpholine in DMF solution. Each addition step was mixed for 1.5 h.

The final PEO-peptide conjugate was cleaved from the resin using a 95/2.5/2.5 vol% TFA/TIS/water cleavage cocktail. The cleavage was performed for 2 h and the solution was concentrated under nitrogen gas before precipitating the peptide into cold diethyl ether. The peptide was recovered by centrifugation, redissolved in water, and lyophilized.

9.2.4 Polymer-Peptide Conjugation using Copper-Catalyzed Azide-Alkyne Cycloaddition Reactions

The hydrophobic PEE-N_3 and hydrophilic PEO-peptide-alkyne blocks were coupled using copper-catalyzed azide-alkyne cycloaddition (click) reactions to yield the final amphiphilic conjugate. Cycloaddition reactions were performed in either dry THF/NMP or dry THF/DMSO solvent mixtures to solubilize both the hydrophobic and hydrophilic materials.

Click Reactions in THF/NMP Solvent Mixtures

In a typical reaction, 15 mg of peptide or PEO-peptide was dissolved in approximately 2.5 mL of NMP and heated to 40 °C to dissolve. Simultaneously, 1.5 molar equivalents of PEE-N_3 was dissolved in approximately 1 mL of dry THF. The PEO-peptide and PEE solutions were mixed and degassed by 5 freeze-pump-thaw cycles. Subsequently, the ampule containing the materials was transferred into the glovebox and 10 molar equivalents of copper bromide and 20 molar equivalents of 2,2'-bipyridine (bipy) ligand were added to the reaction mixture. The reaction

mixtures turned dark red upon complexation of the copper with bipy. The ampule was removed from the glovebox and heated to 40 °C. The reaction was allowed to proceed for 24 h and then the reaction was terminated by opening the ampule to air. The THF/NMP solvent mixture was removed by vacuum distillation at 80 °C.

Click Reactions in THF/DMSO Solvent Mixtures

In a typical reaction, 10 mg of PEE-N_3 was dissolved in approximately 1 mL of dry THF and 1.2 molar equivalents of peptide or PEO-peptide was dissolved in 0.7 mL of dry DMSO. The solutions were mixed, transferred to an ampule, and degassed by 5 freeze-pump-thaw cycles. In the glovebox, 5 molar equivalents of both copper bromide and N,N,N',N",N"-pentamethyldiethylenetriamne (PMDETA) ligand were dissolved in approximately 0.2 mL of THF and added to the reaction mixture. The reaction was diluted to a final volume of ~3 mL and the final solvent composition was approximately 50/50 vol% THF/DMSO. The reaction mixture was cloudy at room temperature, but clear at 40 °C. The reaction was stirred at 40 °C for 48 h and then terminated by opening the ampule to air. The DMSO and THF were removed by vacuum distillation at 80 °C.

9.2.5 Material Characterization

9.2.5.1 Size Exclusion Chromatography (SEC)

SEC data were obtained on a Viscotek VE 2001 equipped with Styragel HR1 and HR4 columns in series. The reported intensity is the differential refractive index. All experiments were performed using THF as the mobile phase, and the dispersities were calculated based on polystyrene standards.

9.2.5.2 Proton Nuclear Magnetic Resonance (^{1}H NMR) Spectroscopy

^{1}H NMR experiments were performed on a Bruker AV-400 instrument. All NMR samples were prepared in deuterated chloroform at an approximate concentration of 10 mg mL^{-1}. Reported chemical shifts are relative to tetramethylsilane (TMS).

9.2.5.3 High Performance Reverse Phase Liquid Chromatography (RP-HPLC)

The purity of the crude peptide and polymer-peptide conjugates was determined using a Shimazdu, Inc UFLC 20 RP-HPLC. Samples were analyzed using an analytical C18 column (Viva C18, Restek). The samples were dissolved in ddH_2O at a concentration of approximately 1 mg mL^{-1} and 50 μL of sample solution was injected for analysis. The mobile phase was a linear AB gradient, in which solvent A was water containing 0.1 vol% TFA and sample B was acetonitrile containing 0.1 vol% TFA. The standard gradient used was 5% to 55% by volume B over 40 min. The UV-Vis absorbance of the eluent was monitored at 210 nm (peptide backbone) and 280 nm (tryptophan residues).

The polymer-peptide conjugates were purified by preparative RP-HPLC using a C18 preparative column (Restek). The samples were dissolved at a concentration of approximately 10 mg mL^{-1} and 250 μL of the sample solution was injected for each run. The polymer-peptide conjugates were eluted off the column using a gradient from 15 vol% to 65 vol% Solvent B over 30 min.

9.2.5.4 Matrix Assisted Laser Desorption Ionization Time of Flight Mass Spectrometry (MALDI-TOF MS)

MALDI-TOF MS samples were prepared using α-cyano-4-hydroxycinnamic acid matrix (~10 mg mL^{-1}) in a 50/50 vol% acetonitrile/water mixture. The matrix

was spotted on the stainless steel target and allowed to dry. Subsequently, the samples was dissolved in water (~1 mg mL^{-1}) and spotted on the target, followed by another layer of matrix. Mass spectra for the peptide and polymer-peptide conjugates were collected in either reflector or linear mode.

9.2.5.5 FRET Experiments

Samples were prepared in a pH 7.4 buffer containing 20 mM Tris base, 10 mM $CaCl_2$ and 150 mM NaCl. For the control experiments, 20 mM ethylenediamnetetracidic acid (EDTA) was added to the buffer to inhibit the enzyme by chelating the calcium ions, as the calcium ions are required for the enzyme stability and activity. The FRET peptide was dissolved in buffer with and without EDTA, and 50 μL of collagenase solution (1 unit/μL) was added. The final sample was diluted to 500 μL using buffer, and the final concentration was 2 mM peptide. The solutions were incubated at 37 °C overnight. Subsequently, the samples were diluted with 500 μL methanol to prevent xanthene ring stacking the during fluorescence measurements. Samples were excited at a wavelength 492 nm and the fluorescence emission was measured from 450 to 700 nm.

9.2.5.6 Thin Layer Chromatography (TLC)

TLC experiments were performed using silica plates (EMD Biosciences). Samples were developed using a 1:3 (parts by volume) mixture of hexanes and ethyl acetate. The TLC plates were stained with a vanillin stain (6 g vanillin, 1.5 mL concentrated sulfuric acid, 95 mL of 96% ethanol). The plates were dipped into the stain solution and then heated with a heat gun until the colored spots appeared.

9.2.5.7 Attenuated Total Reflection Fourier Transform Infrared Spectroscopy (ATR-FTIR)

ATR-FTIR spectra were collected using a Nicolet 8700 FTIR spectrometer equipped with a diamond crystal. Polymer samples were prepared in THF and polymer-peptide conjugate samples were prepared in THF/water mixtures. The sample solutions were drop-cast onto the crystal and allowed to dry. Subsequently, the samples were heated to 40 °C for 10 min to remove any residual solvent before performing the measurements. The instrument resolution was set at 4 cm^{-1}, and 16 scans were collected.

9.3 Results

The polymer-peptide conjugates were synthesized using a modular synthetic scheme that combined polymer end-group functionalization, solid phase peptide synthesis, and coupling reactions. This synthetic approach presented here was developed and optimized to enable efficient synthesis of well-defined conjugates as described below. Additional chemistries are described in Appendices F and G.

9.3.1 Hydrophobic Block Synthesis and Functionalization

The hydrophobic PEE block was synthesized using chemical hydrogenation and then functionalized for click chemistry. The reaction scheme is depicted in Figure 9.3 and discussed in more detail below.

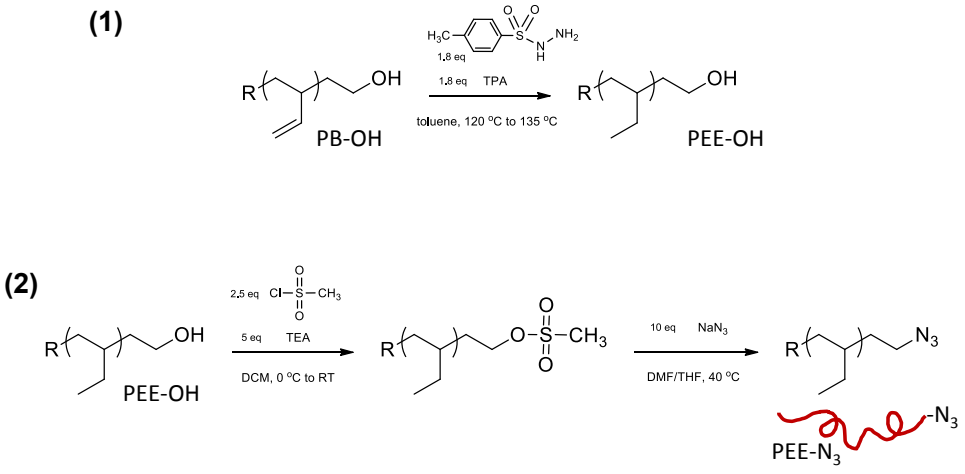

Figure 9.3 Synthesis scheme for the hydrophobic PEE-N_3 block via (1) chemical hydrogenation using a diimide and (2) end-group functionalization.

Complete chemical hydrogenation of the PB-OH precursor without undesirable side reactions was accomplished using 1.8 molar equivalents each of TSH and TPA

per butadiene repeat unit in a 1 wt% polymer solution. SEC data showed that the molecular weight distribution was not affected by the hydrogenation, indicating that the polymer did not crosslink or degrade during the reaction (Figure 9.4). The slight shift to longer elution times after hydrogenation reflected the differences in PB and PEE chain flexibility.[39] PEE (C_∞ = 5.3) is a more flexible chain than PB (C_∞ = 7.0), which means that the unperturbed chain dimensions are smaller for PEE than PB at the same molecular weight and leads to a shift to longer elution times in SEC.[39] Similarly, the absolute molecular weights calculated using a universal calibration curve and the Mark-Houwink parameters for the PB and PEE were the same within experimental error (~10 %).[39,40]

Figure 9.5 presents the ^{1}H NMR spectra for the PB-OH precursor and corresponding PEE-OH polymer. As seen by ^{1}H NMR, the complete disappearance of the peaks at 4.8 and 5.2 ppm (-CH=C***H₂*** and –C***H***=C***H-***, PB) and appearance of a sharp peak at 0.9 ppm (-C***H₃***, PEE) confirmed that all of the double bonds were hydrogenated. Importantly, there were no chemical shifts corresponding to the attachment of sulfur-containing groups to the polymer backbone.[37] Also, the degree of polymerization for the PB-OH and PEE-OH calculated based on the hydroxyl end-group (~ 3.6 ppm) were in good agreement, supporting that the end-group functionality was retained.

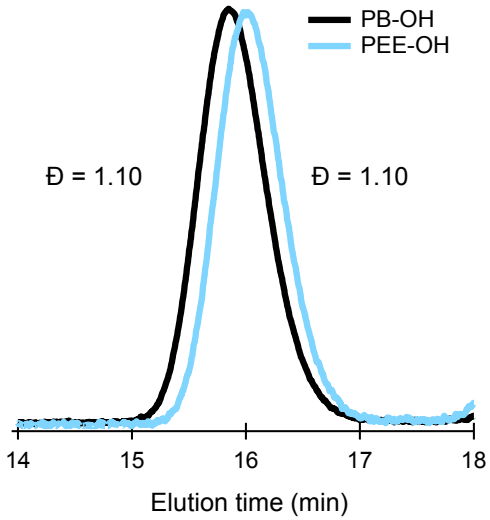

Figure 9.4 **SEC traces for PB-OH precursor and PEE-OH polymer. THF was used as an eluent, and the recorded intensity was the differential refractive index. Dispersities were calculated based on polystyrene standards.**

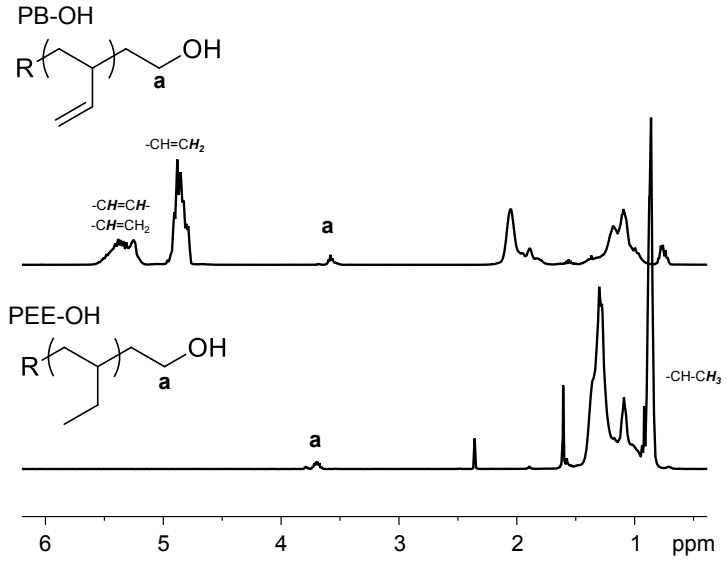

Figure 9.5 **^{1}H NMR spectra confirming the complete hydrogenation of PB-OH to yield PEE-OH.**

The hydroxyl end-group was converted to an azide *via* a two-step reaction [Figure 9.3 (2)]. The PEE-OH was first reacted with mesyl chloride and subsequently with sodium azide, resulting in complete conversion of the hydroxyl group to the azide as determined by ^{1}H NMR (Figure 9.6).

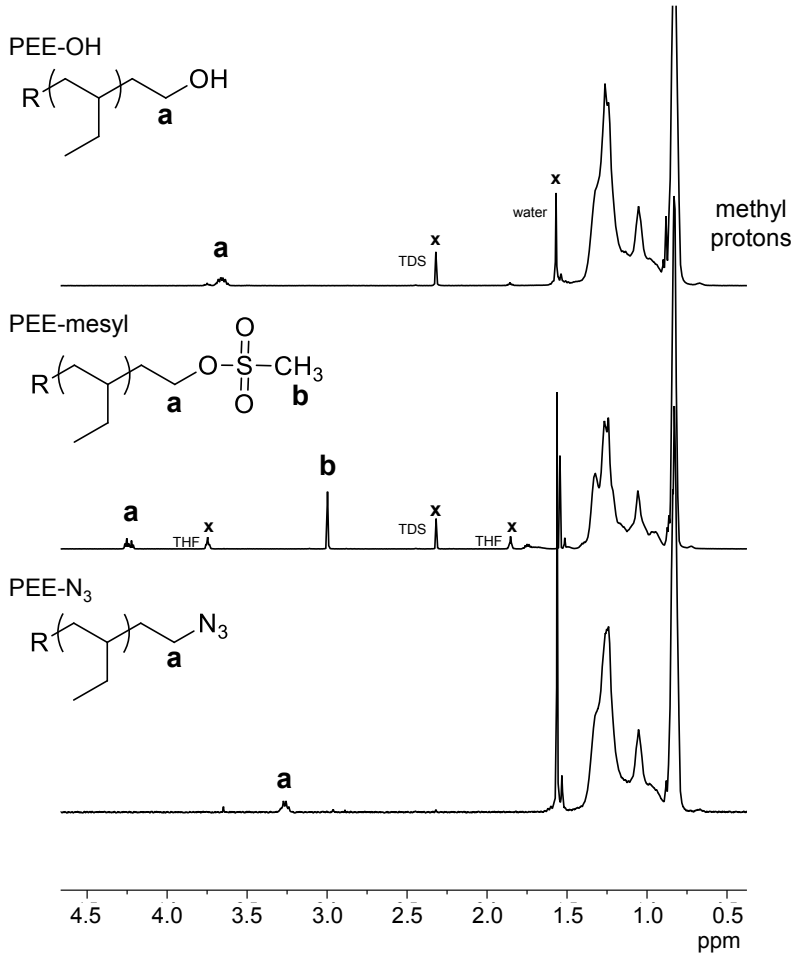

Figure 9.6 **^{1}H NMR spectra of end-functionalized PEE. The PEE-OH and PEE-mesyl samples contained residual *p*-tolyl mercaptan (TDS, < 5 wt%) from the chemical hydrogenation reaction. The presence of the TDS did not affect the end-functionalization reactions, and TDS was removed by the methanol precipitations during the PEE-N_3 purification.**

9.3.2 Hydrophilic Block Design and Synthesis

The hydrophilic PEO-peptide was synthesized using solid phase chemistries as depicted in Figure 9.7 and discussed in more detail below.

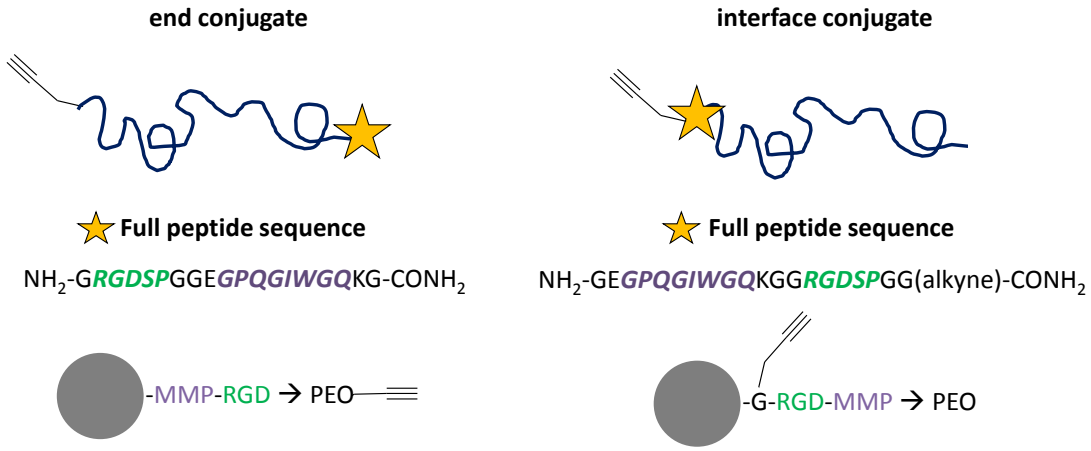

Figure 9.7 Schematic representation of hydrophilic PEO-peptide block synthesis.

The bioresponsive peptide linkage designed in this work incorporated an enzyme-sensitive motif combined with a cell targeting sequence, such that enzymatic cleavage of the linkage would reveal the targeting sequence and facilitate cellular internalization as depicted in Figure 9.2. The peptide linkage included a matrix metalloproteinase (MMP) cleavage site: GPQG↓IWGQ in which the arrow denotes the cleavage site.[41] This specific sequence is known to have high activity to MMP-1 and MMP-8 and has been incorporated into cell-responsive hydrogels[42,43] and surface-mediated drug delivery systems.[44] The MMP-labile sequence is quite hydrophobic (P, I, and W residues); therefore, hydrophilic residues (E and K) were incorporated on either side of the MMP-labile sequence to increase the hydrophilicity

and also incorporate the functional groups necessary for subsequent FRET experiments. The peptide also included an RGDSP integrin binding sequence, which is derived from natural fibronectin.[45-47] While the minimal sequence necessary for cell recognition is RGD, incorporating the S and P amino acids increases the binding specificity.[48,49] This short cell-targeting sequence has been incorporated into numerous biomaterials ranging from drug delivery vehicles to cell-responsive hydrogels.[50]

The enzyme sensitivity of the peptide was confirmed using FRET experiments. For these experiments, the peptide was labeled with a fluorescence donor (carboxyfluorescein, FAM) and a fluorescence quencher (Dabcyl) flanking the MMP cleavage site. The fluorescence was quenched while the peptide was intact and the dyes were in close proximity; however, peptide cleavage increased the distance between the dyes, leading to an increase in fluorescence (Figure 9.8a). As seen in Figure 9.8b, the fluorescence intensity increased upon addition of active collagenase, confirming that the peptide was cleaved by the enzyme.

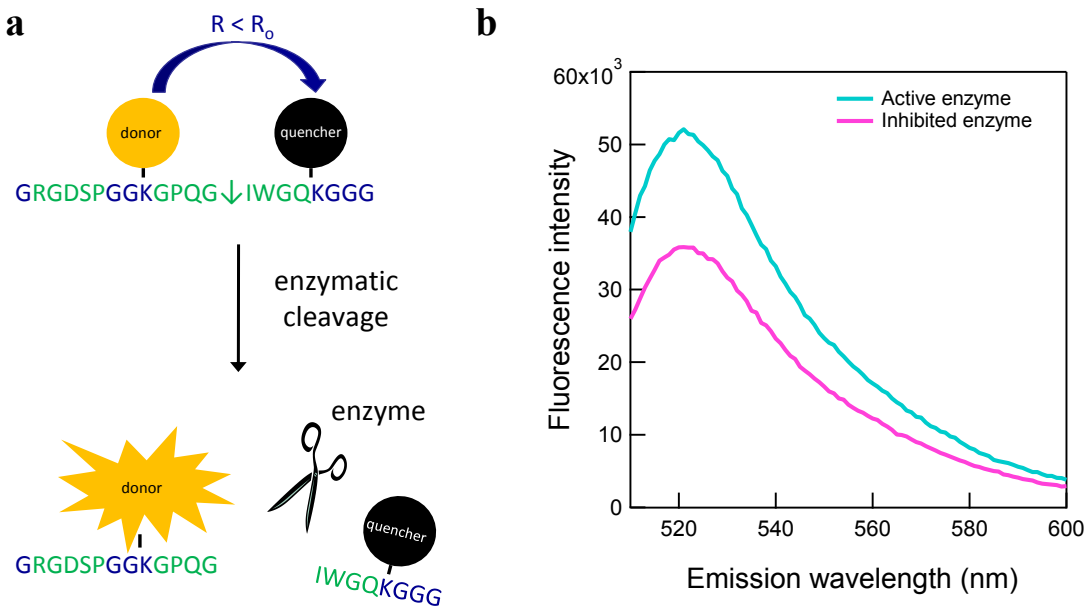

Figure 9.8 Probing peptide sensitivity to enzymatic cleavage using FRET. (a) Schematic representation of FRET experiments and (b) fluorescence data showing increased fluorescence in peptide samples incubated with active enzyme (collagenase + Ca^{+} ions) compared to inhibited enzyme (collagenase), supporting that the peptide linkage is enzyme sensitive.

Having confirmed that the peptide was enzyme-responsive, the location of the linkage within the amphiphilic conjugate was varied by synthesizing two variations of the peptide sequence as depicted in Figure 9.7. Importantly, the peptide sequences were designed to be overall hydrophilic and net neutral at physiological pH. Also, two glycine residues were incorporated between the functional portions of the peptide sequence, and an N-terminal glycine was included in the sequence to facilitate the on-resin polymer-peptide conjugation reaction.[51] *Note that from an implementation standpoint, it is difficult to add more than two sequential glycine residues during SPPS without using double coupling steps. The addition of multiple small amino acids*

likely increases the flexibility of the N-terminus, making it more difficult to couple subsequent amino acids.

The hydrophilic block synthetic strategy relies on coupling the PEO to the peptide on resin. Accordingly, the peptide synthesis conditions were optimized because any deletion sequences could not be removed from the final product. As seen in Figure 9.9a, the single sharp peak in the RP-HPLC trace for the crude product showed the high purity of the peptide. MALDI-TOF MS confirmed the molecular weight of the desired peptide and also supported that there were no major impurities in the crude product (Figure 9.9b). The higher molecular weight peaks in the mass spectrum corresponded to different cations (Na^+ and K^+) associated with the peptide or side chain protecting groups that were not completely removed during the cleavage step. Overall, these data supported that the desired peptide linkages were synthesized to a very high purity.

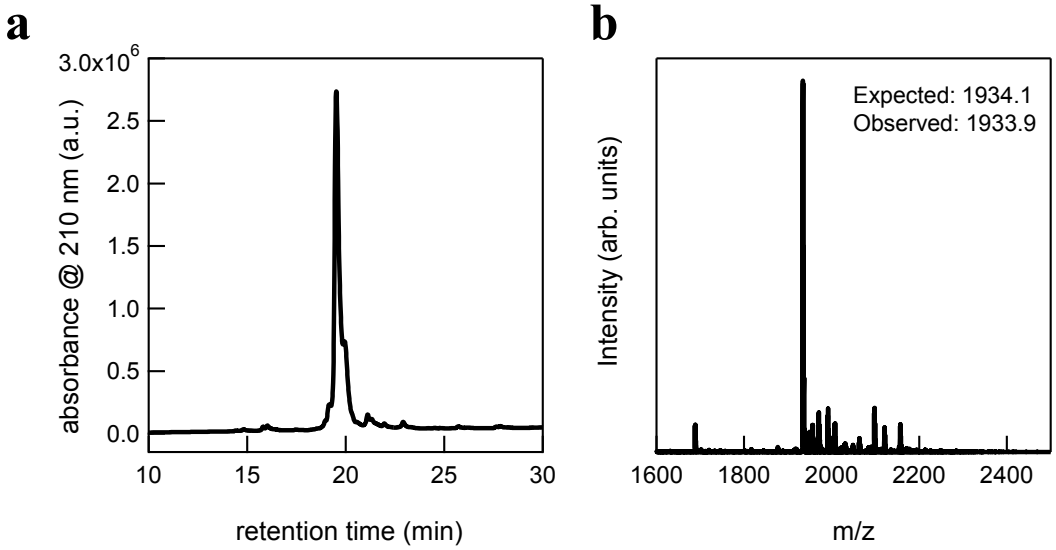

Figure 9.9. Characterization of crude 'interface' peptide. (a) RP-HPLC trace indicating the peptide was synthesized to high purity and (b) MALDI-TOF MS data showing the majority product was the desired sequence. Sequence: N-GEPQGI↓WGQKGGRGDSPGG(alkyne)-C.

The hydrophilic block synthesis was completed by coupling a heterobifunctional PEO to the enzyme-sensitive peptide on resin. This coupling approach greatly simplified purification of the hydrophilic block, as any unreacted PEO could be removed by simply washing the resin. The trade-off to coupling the PEO to the peptide on resin was low yields due to the steric limitations of the solid phase reaction. Several measures were taken to increase the PEO coupling efficiency. All conjugate syntheses were performed on ChemMatrix PEG-based resin, which swells significantly more than traditional polystyrene-based resins, and the resin loading was reduced to $\leq$ 0.3 mmol/g resin. Also, the PEO coupling reactions were performed in DCM-rich solvent mixtures because DCM swelled the resin more than NMP or DMF.

Shown in Figure 9.10 are the RP-HPLC and MALDI-TOF MS data confirming the successful synthesis of both the 'end' and 'interface' hydrophilic blocks. The HPLC traces showed two peaks at ~20 min and ~40 min corresponding to unreacted peptide and PEO-peptide, respectively. Comparing the relative areas under the curves suggested the conjugation efficiencies were approximately 35% and 75% for the 'interface' and 'end' conjugates, respectively. Considering the molecular weight of the peptide and PEO, these coupling efficiencies were comparable to, and in many cases higher than, those from reactions reported in literature.[51-53]

The same reaction conditions were used for both PEO-peptide syntheses, suggesting the discrepancy in reaction efficiency (35% *vs.* 75%) was due to differences in the peptide sequence. Lu and Felix demonstrated that the accessibility of the peptide's N-terminus greatly affected the coupling efficiency.[51] Both peptides had an unhindered amino acid at the N-terminus (glycine, G); however, the accessibility of the N-terminus in the 'interface' peptide likely was affected by the adjacent proline (P) residue. This result highlights the considerable influence of peptide sequence on the efficiency of polymer-peptide coupling reactions.

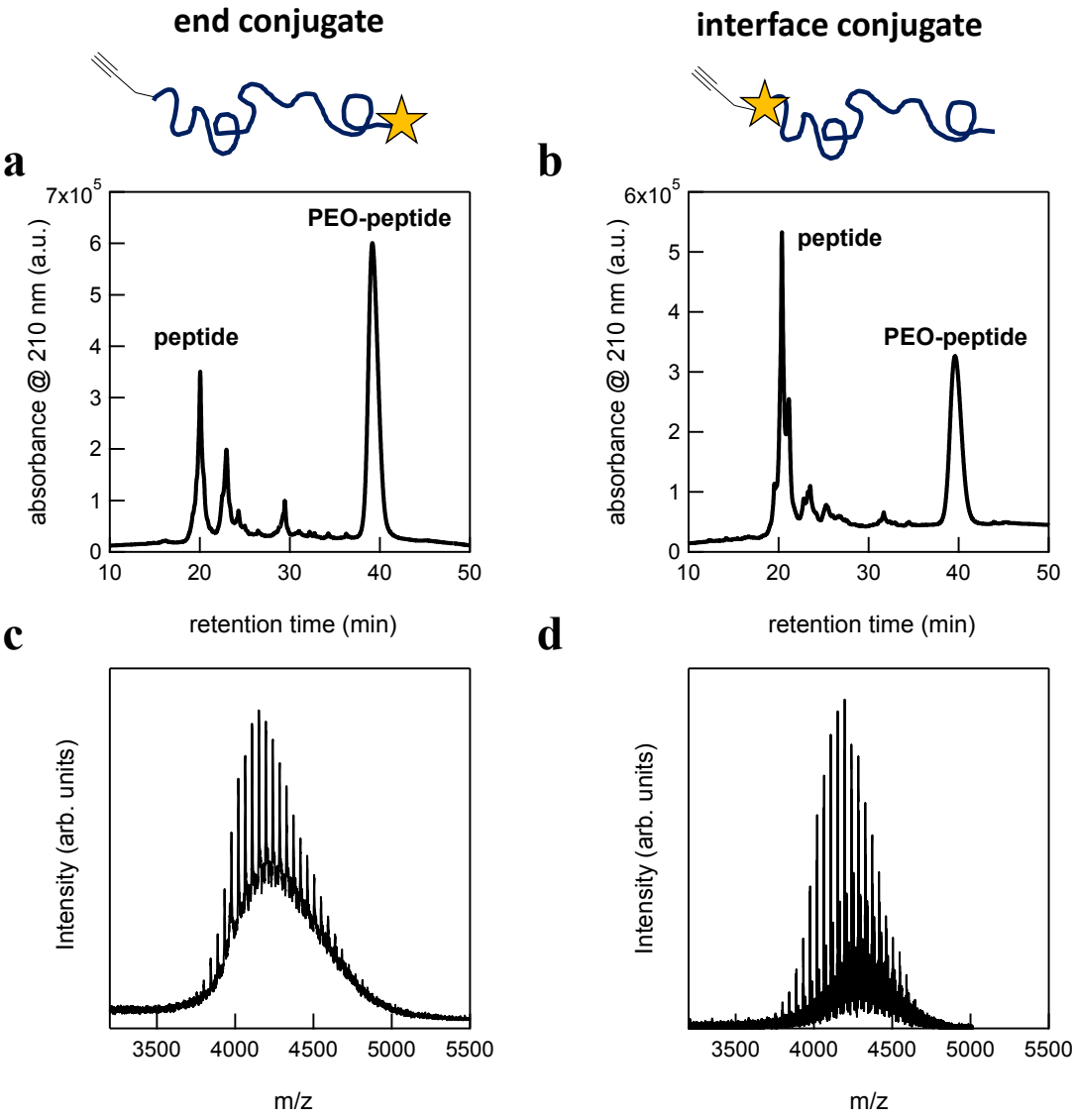

Figure 9.10 Characterization of PEO-peptide conjugates synthesized on resin. Crude RP-HPLC traces (a and b) and MALDI-TOF mass spectrum (c and d) for the end and interface conjugates, respectively. The expected and observed molecular weight for the PEO-peptide conjugates were ~4200 g mol^{-1}.

The PEO-peptide conjugates also were synthesized by first functionalizing the resin with a heterobifunctional PEO and then growing the peptide from the polymer chains as depicted in Figure 9.11a. The synthesis was demonstrated using the peptide sequence designed above, giving a final conjugate sequence of N-GRGDSPGGEGPQG↓IWGQKG-PEO_{12}-C. Presented in Figure 9.11 are the characterization data demonstrating successful PEO-peptide synthesis. The RP-HPLC trace showed two clean peaks at 29 min and 32 min, corresponding to the PEO-peptide and unreacted PEO, respectively (Figure 9.11b). There was no peak at lower retention times, confirming that peptide only grew off of the PEO chains. Also, comparing the areas under the curve suggests ~ 70% of the PEO was functionalized with peptide. As seen in Figure 9.11c, MALDI-TOF MS confirmed successful PEO-peptide synthesis. Together these results demonstrate that high purity PEO-peptide conjugates also can be synthesized by growing the peptide from a PEO-functionalized resin.

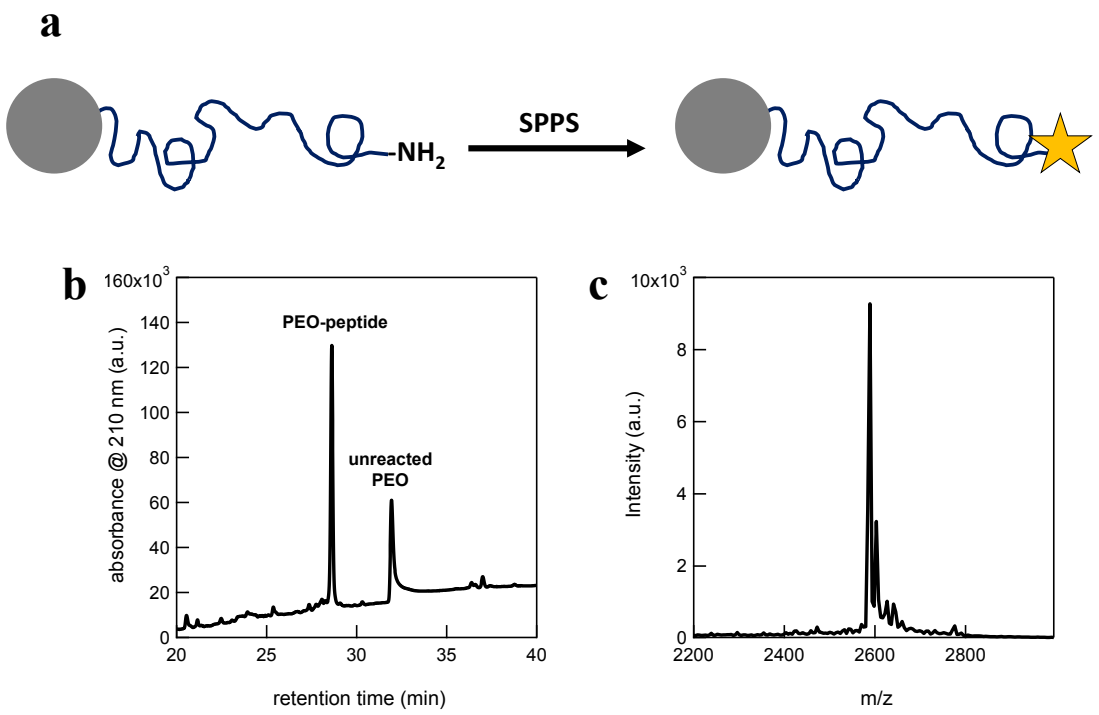

Figure 9.11 Characterization of PEO-peptide conjugate synthesized by first functionalizing the resin with a heterobifunctional PEO and then growing the peptide from the polymer chain. (a) Schematic representation of the synthetic scheme. (b) RP-HPLC data of the crude reaction product containing a peak at 27 min and 32 min corresponding to the PEO-peptide and unreacted PEO, respectively. (c) MALDI-TOF MS confirming PEO-peptide synthesis. Expected molecular weight: 2474 g mol^{-1}, observed molecular weight: 2602 g mol^{-1}. The discrepancy between the expected and observed molecular weights likely was due to incomplete deprotection of the peptide.

9.3.3 Amphiphilic Polymer-Peptide Conjugate Synthesis

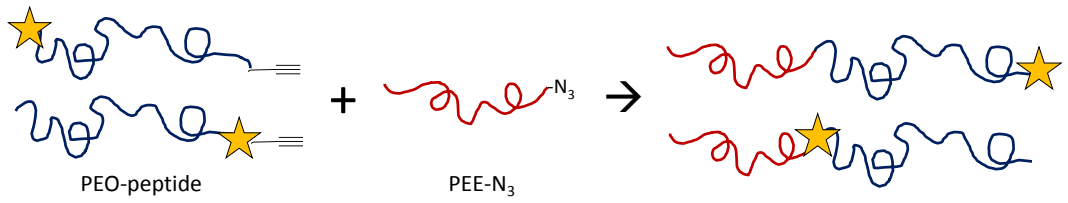

Figure 9.12 Schematic representation of amphiphilic polymer-peptide conjugate synthesis.

The full amphiphilic conjugates were synthesized by coupling PEE-N_3 with the PEO-peptide-alkyne using copper-catalyzed azide-alkyne cycloaddition (click) chemistry (Figure 9.12). Importantly, this click reaction is highly selective and compatible with the amino acid side chains, allowing the reaction to be performed with the unprotected peptides.[54] Copper-catalyzed click chemistry also is highly efficient, making it a popular coupling strategy in literature.[55-58] While this reaction has previously been used successfully to synthesize a variety of polymeric materials, including polymer-peptide conjugates,[24,59-61] a major challenge in the synthesis reported here was finding an appropriate solvent system for the reaction. Table 9.1 summarizes solubility studies on the different reaction components in common click solvents. As seen in Table 9.1, all three components were not soluble in a single solvent, necessitating the use of solvent mixtures. A number of test reactions between PEE-N_3 and alkyne-functionalized peptides and PEO-peptide conjugates were performed to find a suitable solvent system for the coupling reactions. Ultimately, two solvent systems were found to work well for PEE-PEO-peptide synthesis: THF/NMP

and THF/DMSO mixtures. The THF was selected to solubilize the PEE block, and NMP or DMSO was chosen to solubilize the PEO-peptide.

Table 9.1 Summary of unprotected peptide, PEO, and PEE solubility in common solvents used for copper-catalyzed azide-alkyne cycloaddition reactions*

Solvent/ Macromolecule	Water	THF	NMP	DMF	DMSO	DCM
Peptide (unprotected)						
PEO						
PEE						

*Green: soluble; yellow: slightly soluble (required heating to ~ 40 °C to fully dissolve); and red: not soluble.

The challenges in finding a suitable solvent system for the PEE-PEO-peptide conjugates also extended to characterizing the materials. The reaction products were not readily soluble in THF and strongly interacted with the SEC columns; therefore, the successful reaction could not be confirmed with SEC. Instead, the differences in material solubility were exploited, and the coupling reactions were monitored with thin layer chromatography (TLC). TLC on the reactants showed a spot at $R_f \sim 0.3$ for the PEE-N_3 and at $R_f = 0$ (on the spotting line) for the peptide and PEO-peptide, while TLC on the coupling products showed a single spot at $R_f = 0$. The disappearance of the spot at $R_f \sim 0.3$ suggested complete coupling between the PEE-N_3 and PEO-peptide in both THF/DMSO and THF/NMP mixtures.

The successful coupling reactions were confirmed with ATR-FTIR analyses. As seen in Figure 9.13, there was a distinct azide peak at 2100 cm^{-1} in the FTIR spectrum for the PEE-N_3 reactant. Complete disappearance of this peak in the PEE-peptide conjugate spectrum further supported complete coupling between the blocks.

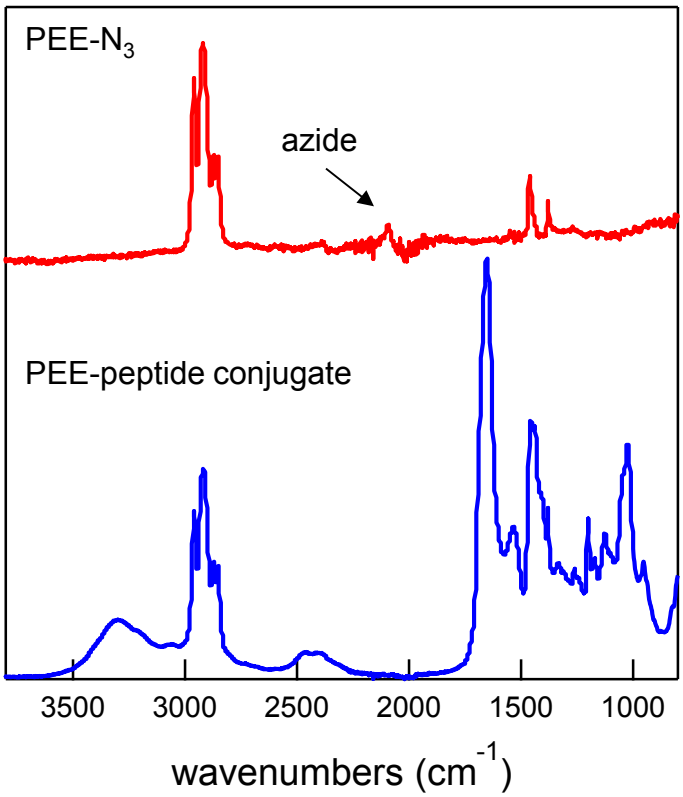

Figure 9.13 Monitoring PEE-N_3 + peptide-alkyne coupling with ATR-FTIR. The peak at 2100 cm^{-1} in the PEE-N_3 spectrum corresponded to the azide stretches. This peak was not seen in the PEE-peptide conjugate spectrum, suggesting complete coupling between the blocks.

9.4 Discussion

This chapter presents a modular, highly tunable synthetic strategy for creating well-defined amphiphilic polymer-peptide conjugates. A unique advantage of the synthetic strategy outlined here is the exquisite control over both the peptide sequence and peptide location within the polymer backbone. Polypeptide-based block polymers reported in literature often are synthesized using N-carboxyanhydride (NCA) ring-opening polymerization.[62-66] While NCA ring-opening polymerization enables synthesis of high molecular weight polypeptides, it is limited to one or two amino acids and does not allow for control over the sequence. Alternatively, sequence specific peptides have been incorporated into initiators[67-69] or monomers[70-72] for use in controlled polymerization reactions; however, these approaches offer little flexibility regarding the peptide location within the polymer chain or incorporate the peptide as a side-chain functionality. While these other synthetic approaches have been used to create well-defined polypeptide-based block polymers, they do not offer the level of control over both the peptide sequence and location within the polymer backbone as demonstrated here.

Control over both the peptide sequence and location within the polymeric materials has important implications for the design of effective drug delivery materials. Incorporating a specific sequence of amino acids enables targeting of highly specific enzymes or receptors, whereas manipulating the display (*e.g.* position within the polymer chain; density) of targeting ligands potentially tunes their interactions with the biological environment. Recent studies of liposomal delivery systems decorated with targeting ligands demonstrated that tuning both the targeting peptide sequence and display led to significantly enhanced cellular uptake in several cancer cell lines.[73,74] These results emphasize the need not only to develop targeted

delivery vehicles, but also to systematically explore the effects of both the ligand chemistry and accessibility on the vehicle performance. The synthetic versatility demonstrated here provides a handle for tuning the peptide sequence and conjugate chain architecture, thereby facilitating necessary investigations into the effects of conjugate architecture on the self-assembly behavior and performance in biomedical applications.

Another important advantage of the approach developed here is the modular nature of the synthetic scheme. For example, the specific hydrophilic to hydrophobic block ratio was selected to favor spherical micelle formation; however, other morphologies easily could by targeted by simply changing the molecular weight of the hydrophobic block and using the same PEO-peptide conjugates. Similarly, the chemistries are easily extended to other peptide and polymeric systems, enabling the synthesis of a large library of materials from a few basic building blocks.

9.5 Conclusions

This chapter presents a modular, highly tunable synthetic strategy for creating well-defined polymer-peptide conjugates. The strategy combines quantitative polymer end-group functionalization with solid phase peptide synthesis and coupling approaches. The specific chemistries were demonstrated through the synthesis of amphiphilic PEE-PEO-peptide conjugates; however, the general approach is easily extended to other polymer- and peptide-based materials. Importantly, the synthesis demonstrated here not only allows for incorporation of sequence specific peptides into polymer materials, but also tunes the location of the peptide linkage within the polymer backbone. This level of control over conjugate architecture is not possible in common polymer-peptide conjugation strategies, yet is essential for understanding the intimate structure-property relationship inherent to polymeric materials in biological environments.

A growing number of works demonstrate the importance of both nanostructure (*e.g.* shape, size, density profile) and surface functionality on the performance of polymeric assemblies for biomedical applications. Overall this dissertation provides an improved understanding of factors that influence solution assembly behavior and develops a method for incorporating and tuning the display of targeting ligands within these assemblies. Together, these efforts provide the foundation for the rational design of targeted drug delivery vehicles, enabling control over both the structure and functionality of polymeric assemblies.

REFERENCES

1 Canton, I. & Battaglia, G. (2012), *Chemical Society Reviews* **41**, 2718-2739

2 Shi, J., Votruba, A. R., Farokhzad, O. C. & Langer, R. (2010), *Nano Letters* **10**, 3223-3230

3 Farokhzad, O. C. & Langer, R. (2009), *ACS Nano* **3**, 16-20

4 Heidel, J. & Davis, M. (2011), *Pharmaceutical Research* **28**, 187-199

5 Duncan, R. & Gaspar, R. (2011), *Molecular Pharmaceutics* **8**, 2101-2141

6 Wang, J., Byrne, J. D., Napier, M. E. & DeSimone, J. M. (2011), *Small* **7**, 1919-1931

7 Brannon-Peppas, L. & Blanchette, J. O. (2004), *Advanced Drug Delivery Reviews* **56**, 1649-1659

8 Byrne, J. D., Betancourt, T. & Brannon-Peppas, L. (2008), *Advanced Drug Delivery Reviews* **60**, 1615-1626

9 Strebhardt, K. & Ullrich, A. (2008), *Nature Reviews Cancer* **8**, 473-480

10 Sheridan, C. (2012), *Nature Biotechnology* **30**, 471-473

11 Fang, J., Nakamura, H. & Maeda, H. (2011), *Advanced Drug Delivery Reviews* **63**, 136-151

12 Maeda, H., Wu, J., Sawa, T., Matsumura, Y. & Hori, K. (2000), *Journal of Controlled Release* **65**, 271-284

13 Duncan, R. (2003), *Nature Reviews Drug Discovery* **2**, 347-360

14 Kelley, E. G., Albert, J. N. L., Sullivan, M. O. & Epps, T. H. (2013), *Chemical Society Reviews* **42**, 7057-7071

15 Gu, F. X. *et al.* (2007), *Nano Today* **2**, 14-21

16 Huang, X. *et al.* (2010), *ACS Nano* **4**, 5887-5896

17 Gu, F. *et al.* (2008), *Proceedings of the National Academy of Sciences* **105**, 2586-2591

18 Pangburn, T. O., Bates, F. S. & Kokkoli, E. (2012), *Soft Matter* **8**, 4449-4461

19 Nasongkla, N. *et al.* (2004), *Angewandte Chemie International Edition* **43**, 6323-6327

20 Sutton, D., Nasongkla, N., Blanco, E. & Gao, J. (2007), *Pharmaceutical Research* **24**, 1029-1046

21 Chien, M.-P. *et al.* (2013), *Journal of the American Chemical Society* **135**, 18710-18713

22 Chien, M.-P. *et al.* (2013), *Advanced Materials* **25**, 3599-3604

23 Hu, Z. *et al.* (2008), *Journal of Biomedical Materials Research Part A* **85A**, 797-807

24 Pangburn, T. O., Bates, F. S. & Kokkoli, E. (2012), *Soft Matter* **8**, 4449-4461

25 Xiong, X.-B. *et al.* (2005), *Journal of Controlled Release* **107**, 262-275

26 Cressman, S., Dobson, I., Lee, J. B., Tam, Y. Y. C. & Cullis, P. R. (2009), *Bioconjugate Chemistry* **20**, 1404-1411

27 Arosio, D., Manzoni, L., Araldi, E. M. V. & Scolastico, C. (2011), *Bioconjugate Chemistry* **22**, 664-672

28 Montet, X., Funovics, M., Montet-Abou, K., Weissleder, R. & Josephson, L. (2006), *Journal of Medicinal Chemistry* **49**, 6087-6093

29 Veronese, F. M. & Pasut, G. (2005), *Drug Discovery Today* **10**, 1451-1458

30 Knop, K., Hoogenboom, R., Fischer, D. & Schubert, U. S. (2010), *Angewandte Chemie International Edition* **49**, 6288-6308

31 Ladmiral, V., Legge, T. M., Zhao, Y. L. & Perrier, S. (2008), *Macromolecules* **41**, 6728-6732

32 Hajduk, D. A., Kossuth, M. B., Hillmyer, M. A. & Bates, F. S. (1998), *The Journal of Physical Chemistry B* **102**, 4269-4276

33 Won, Y.-Y., Brannan, A. K., Davis, H. T. & Bates, F. S. (2002), *The Journal of Physical Chemistry B* **106**, 3354-3364

34 Tureau, M. S. & Epps, T. H. (2012), *Macromolecules* **45**, 8347-8355

35 Podesva, J. & Holler, P. (1999), *Journal of Applied Polymer Science* **74**, 3203-3213

36 Podesva, J., Spevacek, J. & Dybal, J. (1999), *Journal of Applied Polymer Science* **74**, 3214-3224

37 Hahn, S. F. (1992), *Journal of Polymer Science Part A: Polymer Chemistry* **30**, 397-408

38 Xu, J. T., Jin, W. & Fan, Z. Q. (2005), *Journal of Applied Polymer Science* **98**, 208-215

39 Xu, Z., Hadjichristidis, N., Carella, J. M. & Fetters, L. J. (1983), *Macromolecules* **16**, 925-929

40 Young, R. J. & Lovell, P. A. *Introduction to Polymers*. 2nd edn, CRC Press, 1991.

41 Nagase, H. & Fields, G. B. (1996), *Biopolymers* **40**, 399-416

42 Alge, D. L., Azagarsamy, M. A., Donohue, D. F. & Anseth, K. S. (2013), *Biomacromolecules* **14**, 949-953

43 Lutolf, M. P. *et al.* (2003), *Proceedings of the National Academy of Sciences* **100**, 5413-5418

44 Blocker, K. M., Kiick, K. L. & Sullivan, M. O. (2011), *Langmuir* **27**, 2739-2746

45 Pierschbacher, M. D. & Ruoslahti, E. (1984), *Nature* **309**, 30-33

46 Ruoslahti, E. & Pierschbacher, M. D. (1986), *Cell* **44**, 517-518

47 Ruoslahti, E. & Pierschbacher, M. D. (1987), *Science* **238**, 491-497

48 Pierschbacher, M. D. & Ruoslahti, E. (1984), *Proceedings of the National Academy of Sciences of the United States of America-Biological Sciences* **81**, 5985-5988

49 Pierschbacher, M. D. & Ruoslahti, E. (1987), *Journal of Biological Chemistry* **262**, 17294-17298

50 Hersel, U., Dahmen, C. & Kessler, H. (2003), *Biomaterials* **24**, 4385-4415

51 Lu, Y. A. & Felix, A. M. (1994), *Reactive Polymers* **22**, 221-229

52 Dube, N., Presley, A. D., Shu, J. Y. & Xu, T. (2011), *Macromolecular Rapid Communications* **32**, 344-353

53 Rösler, A., Klok, H.-A., Hamley, I. W., Castelletto, V. & Mykhaylyk, O. O. (2003), *Biomacromolecules* **4**, 859-863

54 Lutz, J. F., Borner, H. G. & Weichenhan, K. (2007), *Australian Journal of Chemistry* **60**, 410-413

55 Iha, R. K. *et al.* (2009), *Chemical Reviews (Washington, DC, United States)* **109**, 5620-5686

56 Günay, K. A., Theato, P. & Klok, H.-A. (2012), *Journal of Polymer Science, Part A: Polymer Chemistry* **51**, 1-28

57 Binder, W. H. & Sachsenhofer, R. (2007), *Macromolecular Rapid Communications* **28**, 15-54

58 Mansfeld, U., Pietsch, C., Hoogenboom, R., Becer, C. R. & Schubert, U. S. (2010), *Polymer Chemistry* **1**, 1560-1598

59 Agut, W., Taton, D. & Lecommandoux, S. (2007), *Macromolecules* **40**, 5653-5661

60 Dehn, S., Chapman, R., Jolliffe, K. A. & Perrier, S. (2011), *Polymer Reviews* **51**, 214-234

61 Lutz, J. F., Borner, H. G. & Weichenhan, K. (2006), *Macromolecules* **39**, 6376-6383

62 Cheng, J. & Deming, T. (2012), *Topics in Current Chemistry* **310**, 1-26

63 Sanson, C. *et al.* (2010), *Langmuir* **26**, 2751-2760

64 Habraken, G. J. M., Peeters, M., Thornton, P. D., Koning, C. E. & Heise, A. (2011), *Biomacromolecules* **12**, 3761-3769

65 Naik, S. S., Ray, J. G. & Savin, D. A. (2011), *Langmuir* **27**, 7231-7240

66 Ray, J. G. *et al.* (2012), *Macromolecular Rapid Communications* **33**, 819-826

67 Yang, J., Luo, K., Pan, H., Kopečková, P. & Kopeček, J. (2011), *Reactive and Functional Polymers* **71**, 294-302

68 de Graaf, A. J. *et al.* (2012), *Macromolecules* **45**, 842-851

69 Becker, M. L., Liu, J. & Wooley, K. L. (2003), *Chemical Communications*, 180-181

70 Chu, D. S. H., Johnson, R. N. & Pun, S. H. (2012), *Journal of Controlled Release* **157**, 445-454

71 Kammeyer, J. K., Blum, A. P., Adamiak, L., Hahn, M. E. & Gianneschi, N. C. (2013), *Polymer Chemistry* **4**, 3929-3933

72 Hahn, M. E., Randolph, L. M., Adamiak, L., Thompson, M. P. & Gianneschi, N. C. (2013), *Chemical Communications* **49**, 2873-2875

73 Stefanick, J. F., Ashley, J. D. & Bilgicer, B. (2013), *ACS Nano* **7**, 8115-8127

74 Stefanick, J. F., Ashley, J. D., Kiziltepe, T. & Bilgicer, B. (2013), *ACS Nano* **7**, 2935-2947

Chapter 10

THESIS SUMMARY AND RECOMMENDATIONS FOR FUTURE WORK

10.1 Thesis Summary

Akin to small molecule lipids and surfactants, amphiphilic block polymers self-assemble into a variety of well-defined structures in aqueous solutions such as micelles and vesicles. However, their macromolecular architecture leads to several advantages compared to their small molecule analogues, including increased chemical versatility, exquisite control over the size and structure of solution assemblies, extremely low critical aggregation concentrations, and exceptionally slow chain exchange. The slow dynamic processes inherent to polymeric assemblies is an attractive advantage for applications in emerging nanotechnologies, but also leads to kinetically-trapped structures and path-dependent self-assembly. Consequently, careful optimization of preparation conditions are necessary to create well-defined, uniform, and reproducible macromolecular solution assemblies. Altogether, this dissertation work demonstrates the design, synthesis, and self-assembly of macromolecular amphiphiles with the ultimate goal of creating well-defined nanocontainers for catalysis and drug delivery applications.

The work presented in this dissertation explores the effects of common processing conditions on the structure and dynamics of block polymer assemblies and develops a modular synthetic approach for controlling the display of targeting ligands within these assemblies. Overall, the efforts presented here enable better control over

both the structure and surface functionality of block polymer micelles, providing a foundation for the rational design of novel materials.

10.1.1 Developing Complementary Methods for Characterizing Solution Assembled Structures

In many of the envisioned applications of macromolecular solution assemblies, the nanostructure's performance ultimately is dictated by its size and shape in solution, and the successful development of these materials requires detailed *in situ* characterization of their structure. For this purpose, Chapter 4 focused on developing complementary methods for obtaining detailed structural information on polymeric assemblies.[1] In particular, the solution assembly of a series hydrophilic polymers end-functionalized with a pincer ligand for catalysis applications was explored using small angle neutron scattering (SANS) and cryogenic transmission electron microscopy (cryo-TEM). Chapter 4 described the implementation of a detailed form factor model to capture the radially decreasing corona density profile characteristic of polymeric micelles. This form factor model, along with others in literature, often is used to describe the detailed density distribution of polymeric assemblies.[2] However, as demonstrated in Chapter 4 and other publications,[3-5] cryo-TEM also is sensitive to the local density distribution of the polymeric assemblies. Radial density profiles extracted from the cryo-TEM micrographs were in good agreement with profiles determined from SANS data modeling, suggesting that detailed information about the micelle density profiles can be extracted directly from cryo-TEM micrographs. Moreover, the profiles obtained from cryo-TEM can provide valuable *a priori* information about the self-assembled structure for SANS data modeling.

The powerful combination of cryo-TEM and SANS provided the framework for investigating self-assembly phenomena throughout this dissertation. As discussed below, these techniques provide valuable insights into the effects of common processing conditions on the structure and dynamics of block polymer assemblies that were unattainable with other characterization methods.

10.1.2 Understanding Effects of Common Processing Conditions on Block Polymer Assemblies

Cosolvent mixtures routinely are utilized in the self-assembly of amphiphilic block polymers to produce well-defined nanostructures,[6-11] to trap exotic non-equilibrium structures,[12-18] and to load hydrophobic cargoes into nanocontainers.[19-21] Despite the prevalence of cosolvent processing routes, very few works have investigated the effects of organic cosolvent addition and removal on the structure and dynamics of block polymer assemblies.

To better understand this essential processing step, the effects of organic cosolvent addition on the structure and chain exchange dynamics of poly(butadiene-*b*-ethylene oxide) PB-PEO micelles were investigated. In aqueous solutions, PB-PEO self assembles into well-defined spherical micelles with PB cores surrounded by PEO coronas. Increasing the tetrahydrofuran (THF) content in water mixtures improved the solvent quality for the PB block and reduced the core-corona interfacial tension. A combination of complementary characterization methods showed that the micelle size decreased increasing THF content, in good agreement with scaling theories for star-like block polymer micelles.[22]

Further insights into the micelle structure were gained through contrast variation experiments with SANS. Detailed SANS data modeling revealed that THF

addition also led to a broadening of the core-corona interface.[23] The effects of interfacial tension on the interfacial profile are well studied for bulk systems, such as homopolymer blends and block polymers,[24-27] and the results presented herein demonstrate that interfacial tension also controls the core-corona interfacial width in solution assemblies.

The cosolvent-induced structural rearrangements implied that THF addition also led to dynamic processes in these highly amphiphilic block polymer assemblies. The micelle dynamics in cosolvent mixtures were investigated using contrast variation experiments in time-resolved SANS (TR-SANS) using the elegant methods originally developed by Willner and coworkers.[28] Interestingly, while the addition of small volumes of THF lead to distinct changes in micelle structure, the TR-SANS results showed no measurable chain exchange in these systems. This complete lack of chain exchange was consist with literature reports that suggested PB-PEO micelles are kinetically-trapped in highly selective solvents and implied that the micelles at low THF contents relaxed through fission events.[29-31] Conversely, higher THF content cosolvent mixtures enabled chain exchange events, which suggested that micelle systems under these conditions were potentially able to obtain their equilibrium structures.

Subsequent to cosolvent addition, most micelle preparation methods dialyze the solution to remove the organic solvent. These preparation methods assume that the micelles are kinetically stable following transfer from a cosolvent mixture into a purely aqueous solution. However, the work in Chapter 7 showed that this assumption is not always valid and explored unforeseen consequences of cosolvent removal on the long-term stability of block polymer micelles.[32] The complementary use of cryo-TEM

and scattering techniques revealed that unequivocal changes in micelle size occurred over several weeks following cosolvent removal. Surprisingly, the micelle sizes evolved through a distinct bimodal distribution separated by multiple fusion events. The bimodal growth was unexpected based on the high energy barriers to dynamic processes in highly selective solvents[33-37] and prompted further investigation into the growth mechanism. These studies revealed that the micelle growth critically depended on stirring the solution and implied that the growth was a shear and/or interfacial effect.

Motivated by the agitation-induced micelle growth seen following cosolvent removal, Chapter 8 explored the effects of common mixing types on chain exchange in PB-PEO micelles. These studies revealed that mixing can induce chain exchange in *aqueous solutions,* resulting in a completely randomized micelle solution after as little as 10 min of vortex mixing. Comparing different agitation methods suggested that the chain exchange was a coupled shear and interfacial effect. Most notably, the results presented here demonstrated that introducing a fluid air/water interface led to dynamic processes not seen in bulk solution.

While agitation effects are largely unexplored in block polymer assemblies, the seminal results presented in this dissertation underscore fundamental similarities between these synthetic macromolecules and proteins. Processing effects on protein stability are well studied, and research in the biopharmaceutical industry provides a framework for studying similar effects in polymeric assemblies.[38-43] The agitation-induced growth and chain exchange studied here have critical implications for block polymer micelle dynamics and further highlight the extreme influence of processing conditions on the resulting assemblies.

10.1.3 Designing Amphiphilic Polymer-Peptide Conjugates

Many targeted delivery methods have failed to achieve clinical approval, due in part to challenges in materials development.[44,45] A key unsolved issue is the need to decouple carrier 'stealth'/immune system evasion from active targeting, as attaching targeting ligands alters the physicochemical properties of nanostructures and has been shown to compromise circulation times. Accordingly, this dissertation sought to develop methods for controlling the display of targeting ligands within block polymer assemblies. Chapter 9 presented a modular synthetic scheme that enabled exquisite control over the peptide sequence and location with the backbone of an amphiphilic block polymer. The synthetic strategy combined quantitative polymer end-group chemistries with solid phase peptide synthesis and coupling techniques. The chemistries were demonstrated by incorporating a matrix metalloproteinase (MMP) enzyme sensitive peptide linkage into the backbone of a poly(ethyl ethylene *b*-ethylene oxide) (PEE-PEO) block polymer; however, this approach is easily extended to other peptide linkages and polymer chemistries. The level of control over the polymer-peptide conjugate architecture presented here is not possible using current synthetic strategies in literature, yet is essential for understanding the intricate effects of ligand display on delivery vehicle performance.

10.2 Recommendations for Future Work

Literature precedent highlights the promising potential of block polymer assemblies for drug delivery and catalysis applications. However, fundamental questions regarding block polymer solution assembly pathways and dynamics remain unanswered, yet are key to understanding material processing effects, creating reproducible assemblies, and predicting long-term performance. Also, there is a continued need to understand the relationships between a material's physicochemical properties and its performance in biomedical applications. Described in the following sections are recommendations for future work to explore block polymer micelle dynamics, develop materials libraries, and probe structure-property relationships in polymer-based nanoassemblies. Together these recommendations will guide the rational design of effective polymeric nanocarriers.

10.2.1 Exploring Block Polymer Micelle Dynamics

While the molecular factors controlling block polymer amphiphile self-assembly and structure are similar to those in small molecule amphiphiles, the macromolecular nature of the hydrophobic block leads to significantly different dynamics. Questions regarding equilibrium chain exchange and relaxation mechanisms in these macromolecular assemblies remain unanswered. Moreover, as demonstrated in this dissertation, agitation and other key features in solution assembly processing can induce kinetically-controlled processes that significantly affect the structure, dynamics, and long-term stability of these assemblies. Understanding the self-assembly behavior in amphiphilic block polymers will facilitate further development of these materials for a variety of applications.

10.2.1.1 Polymer Properties and Solution Additive Effects

Since the pioneering experiments by Willner and coworkers,[28] TR-SANS has provided valuable insights into the equilibrium chain exchange dynamics of block polymer micelles.[47,48] Through the use of this technique, the effects on chain exchange of core block molecular weight and dispersity,[49-51] micelle concentration,[52,53] cosolvent mixtures,[54] and morphology[55] are better understood. However, the effects of certain block polymer properties (*e.g.* entanglement and crystallinity) on chain exchange remain unexplored. Moreover, the effects of other additives such as homopolymers or drugs have only begun to be investigated. Developing these missing relationships is not only of interest from a fundamental standpoint, but is also essential to developing these materials for nanotechnology applications.

The key function of a nanocontainer is to efficiently encapsulate hydrophobic cargoes, thereby improving the pharmacokinetic profile of a drug or increasing the local concentration of catalysts and reagents. It is well documented in literature that increasing the hydrophobic block molecular weight increases the micelle core size,[22,47,56] which enables encapsulation of greater volumes of hydrophobic payload within a single nanocarrier.[57,58] Another consequence of increasing the polymer molecular weight is increasing the number of entanglements within the core block. Presumably, core block entanglement would increase the kinetic stability of the assemblies and slow chain exchange, however, the exact effects of entanglement have not been studied.

The block polymer micelles studied in Chapter 6 and elsewhere in literature are amorphous, unentangled systems. In fact, the theory developed by Bates and Lodge *et al.* for chain exchange assumes the micelle core block is unentangled and follows Rouse dynamics.[49] Studying the chain exchange over a range of core block

molecular weights could provide important insights into these effects. Also, the polymer systems studied in this dissertation provide a unique opportunity to study the effects of entanglement on chain exchange. Both poly(1,2-butadiene) (PB) and poly(ethyl ethylene) (PEE) are highly hydrophobic polymers with low glass transition temperatures (T_g); T_g = -12 °C for 1,2 PB and T_g = -20 °C for PEE. However, the polymers have very different entanglement molecular weights (M_e), M_e = 2.0 kg mol^{-1} and 9.5 kg mol^{-1} for 1,2 PB and PEE, respectively.[59,60] PB and PEE polymers with the same degree of polymerization readily are synthesized using anionic polymerization and chemical hydrogenation (Chapters 2 and 9), facilitating investigations into the effects of entanglement on chain exchange in block polymer micelles.

Developments in controlled radical polymerization methods and polymer coupling chemistries over the last decade have greatly facilitated the synthesis of functional block polymers containing organocatalysts, stimuli-responsive groups, and targeting ligands.[61,62] However, many times the final block polymer contains residual homopolymer from either incomplete end-functionalization or coupling reactions. This residual homopolymer could significantly affect the resulting solution assembly behavior; accordingly, these effects must be explored to further develop new materials for nanocontainer applications.

Exploring the effects of residual homopolymer will further elucidate its influence on both the micellization and dynamics in block polymer systems. For example, scaling theories by Halperin suggested that adding hydrophilic homopolymer increases the corona screening in block polymer micelles which should decrease the rate of chain exchange; however, this effect has not been explored experimentally.[53] Moreover, work by Lodge and coworkers showed that depletion interactions induced

by adding corona block homopolymer increased the micelle aggregation number and effective hard sphere radius,[63] and recent studies by Mahanthappa *et al.* showed that addition of a hydrophilic homopolymer induced a fusion-controlled sphere-to-cylinder transition in aqueous block polymer assemblies.[64] Together, these works suggest that adding homopolymer can significantly affect the structure and dynamics of block polymer assemblies, and understanding these effects is especially important in cases in which the polymerization method does not yield well defined block polymers.

Literature suggests that encapsulating hydrophobic molecules within polymer assemblies also influences both their structure[20,65-69] and stability;[70] however, very reports have systematically investigated the extent of these effects. For example, recent work by Schulz and coworkers described a drug-induced cylinder-to-sphere transition in poly(2-oxazoline)-based block polymer assemblies.[65] The polymer formed cylindrical micelles in the absence of drug while the addition of small amounts of hydrophobic drug (<20 wt% drug in polymer) led to the formation of spherical micelles. Moreover, this drug-induced morphology change occurred over periods of months.[65] There are significant synergies in understanding the influence of hydrophobic cargoes on polymeric assemblies for applications as drug delivery vehicles and aqueous nanoreactors, and further investigating these effects will facilitate the streamlined optimization of these technologies.

10.2.1.2 Kinetically-Controlled Agitation Effects

In addition to factors that control the thermodynamic driving force for chain exchange, notable results in this dissertation demonstrate that kinetic factors can have a profound effect on the chain exchange and long-term stability in macromolecular assemblies. Important results presented herein suggest that introducing shear forces

and an air/water interface leads to equilibration mechanisms not seen in bulk solution. However, further experiments are needed to fully realize the extent of agitation-induced phenomena in block polymer assemblies. Outlined below are recommendations for future studies aimed at (1) understanding effects of agitation effects during micellization, (2) further decoupling shear and/or interfacial effects during micelle processing, (3) expanding the studies of agitation-induced phenomena to additional polymer systems, and (4) extending the kinetically-controlled processing effects to the development of novel materials.

All data indicate that PB-PEO micelles are kinetically-trapped in aqueous solutions,[29,30,71] yet the structures formed upon directly dispersing the polymer in water are *highly* reproducible. This well-defined self-assembly seems to contradict the completely frozen micelle dynamics previously reported for similar assemblies in the literature and imply that agitation effects play an important role in micelle formation from bulk polymer. For example, studies by Jiang *et al.* showed that poly(styrene-*b*-2 vinylpyridine-*b*-ethylene oxide) triblock terpolymers formed discrete spherical micelles at low stir speeds while cylindrical micelles and large aggregates were formed at high stir speeds. Systematic investigations into the effects of solution agitation on micellization (*i.e.* mix type, stir speed, presence of a hydrophobic interface) will decouple shear and interfacial effects and elucidate the assembly pathway, providing a greater handle for controlling the final structure formed by amphiphilic macromolecules.

Understanding the influence of shear forces and hydrophobic interfaces is not only important for controlling micelle formation, but also subsequent processing steps. Micelle formulations may be subjected to agitation during packaging, shipping, and

storage. During these processes the system will be exposed to different hydrophobic interfaces (*e.g.* air/water interface, vial surfaces, septum caps) at varying shear forces, and elucidating these effects will enable greater control over the nanostructure. For example, quantitative investigations into the effects of chemical nature of the interface (*e.g.* air *vs.* other hydrophobic liquids) and the fluidity of the interface (*e.g.* deformable liquid *vs.* solids) will elucidate the important processing variables. Moreover, exploring factors such as the micelle concentration *vs.* volume of the air/water interface (*i.e.* headspace) concentrations as well as the solution viscosity will decouple the complex parameter space and provide necessary insights into kinetically-controlled mechanisms. Finally, all of the agitation experiments performed in this dissertation used routine laboratory mixing methods, but these method have poorly-defined turbulent flow. Performing similar experiments with more controlled mixing that allows for control over stir speed, power input, air/water contact, *etc*. will help determine the important mixing parameters.[43]

The results presented herein suggest that introducing a fluid air/water interface provides access to dynamic pathways with a lower energy barrier, enabling processes not seen in bulk solutions. However, all experiments were performed on a low T_g, unentangled, amorphous polymer, and future experiments expanding these studies to higher molecular weight and/or crystalline materials relevant to the desired applications will broaden the impact of these studies. Also, the lower-energy assembly pathway may facilitate the formation of uniform and reproducible assemblies from block polymer systems that typically require cosolvent processing routes (*e.g.* polystyrene-based assemblies).[7,9-11,72,73]

Finally, kinetically-controlled assembly pathways provide access to novel structures for emerging nanotechnology applications. Several groups have utilized this control to create complex, hierarchical assemblies not accessible through thermodynamically-controlled assembly pathways.[12,14,15,18,72] Similarly, agitation-controlled chain exchange could be extended to the formulation of targeted nanocarriers for drug delivery applications. Current preparation strategies blend pre-functionalized and unfunctionalized polymers before assembling the materials into delivery vehicles.[74-77] An alternate approach could exploit vortex-mixing to blend ligand-functionalized and bare assemblies as a means of controlling both ligand density and display within targeted nanocarriers. Alternatively, vortex mixing could be used to mix the cargoes of loaded micelles to facilitate co-delivery of multiple therapeutics,[78] simultaneously deliver therapeutics and diagnostic imaging agents (theranostics) to targeted tissues,[45,79] or to mix reagents for catalytic reactions. Overall, developing a better understanding of agitation effects of block polymer micelles will not only provide greater control over the final nanostructure, but provide facile access to novel assemblies not easily attained through traditional processing routes.

10.2.2 Developing Libraries of Amphiphilic Polymer-Peptide Conjugates

A growing number of works demonstrates the importance of surface functionality in determining a drug delivery vehicle's performance.[44,45,61,74,80-82] In particular, the major relationships between a nanostructure's physicochemical properties and the material's cytotoxicity, cellular internalization, and intracellular trafficking can be refined significantly using the synthetic approaches described in this dissertation. Outlined below are synthetic strategies to build materials libraries and explore the effects of ligand display, polymer chemistry, and self-assembled nanostructure on drug delivery vehicle performance.

10.2.2.1 Controlling Peptide Location

Literature suggests that precise control over the display of targeting ligands is essential to creating well-defined, effective drug delivery vehicles.[74,83,84] Previous work by Bates and coworkers demonstrated that attaching peptides to the end of a polymer chain can significantly alter the self-assembly of amphiphilic block polymers due to peptide-peptide interactions.[85] Moreover, *in vivo* studies of targeted drug delivery vehicles suggested that surface ligands can evoke an immune response and induce rapid clearance of the vehicles.[86] The lack of well-defined self-assembly combined with poor *in vivo* performance in these reports suggests that end-functionalization of the polymer chains (*i.e.* peptides displayed at the micelle surface) is not an ideal strategy for creating effective targeted drug delivery vehicles. The other extreme is to completely shield the targeting ligand by incorporating the peptide at the interface between the hydrophobic and hydrophilic blocks. However, Wang and coworkers demonstrated that incorporating ligands at the core-corona interface in polymer micelles resulted in low bioavailability, and only ~10 % of the

ligands were accessible to bind to the target.[87] Therefore, tuning the display of the targeting ligand within the hydrophilic block, as depicted in Figure 10.1, will achieve an optimal balance between the necessary stealth and bioavailability characteristics for effective targeted drug delivery vehicles.

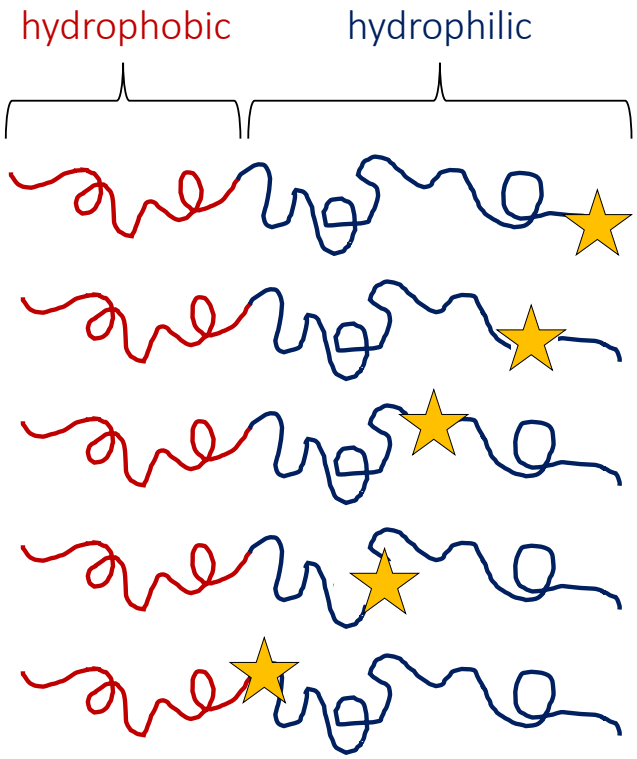

Figure 10.1 Schematic representation of amphiphilic polymer-peptide conjugate library with location of the functional peptide linkage (stars) varied throughout the hydrophilic backbone.

Chapter 9 presented a novel approach for synthetically controlling the location of functional peptide linkages within an amphiphilic polymer. The utility of the approach was demonstrated by creating two conjugates, with: (1) the peptide linkage

placed at the end of the hydrophilic block and (2) the peptide linkage placed at the interface of the hydrophobic and hydrophilic blocks. However, the modular nature of the synthetic scheme can be exploited further to provide even greater control over the display of targeting ligands as depicted in Figure 10.2. The PEO-peptide conjugation strategies presented in this dissertation can be combined to synthesize conjugates with the peptide embedded within the hydrophilic block by first pre-functionalizing the resin with a heterobifunctional PEO, then growing the peptide from the functional polymer, and finally conjugating a second PEO to the N-terminus of the peptide. Moreover, tuning the molecular weights of the two PEO polymers will allow for precise control over the peptide location within the hydrophilic backbone. This level of control over ligand display will enable systematic investigations into the delicate balance between stealth and bioavailability necessary for effective targeted drug delivery.

Figure 10.2 Schematic representation of polymer-peptide conjugate synthesis with the peptide linkage embedded within the hydrophilic backbone. First, the resin is functionalized with a heterobifunctional hydrophilic polymer, then the peptide linkage is synthesized using solid phase peptide synthesis (SPPS), and finally a second hydrophilic polymer is coupled to the N-terminus of the peptide.

10.2.2.2 Exploring Other Block Chemistries

A growing number of works highlight the importance of selecting the appropriate block polymer chemistries in the design of these materials for biomedical applications. Interactions between the hydrophobic block and the drug influence both

the drug encapsulation efficiency as well as the drug release profile,[65,67] while interactions between the hydrophilic block and the biological environments dictate that nanocarriers *in vivo* fate.[88,89] Moreover, advances in polymer chemistry have greatly facilitated the synthesis of stimuli-responsive materials, allowing the assembly to evolve with the delivery pathway to overcome the numerous barrier to targeted drug delivery.[61,90]

While the hydrophobic block is shielded by the corona and does not directly interact with the biological environment, the hydrophobic block chemistry can significantly influence the *in vivo* performance of the drug delivery vehicle.[57] For example, Prud'homme and coworkers systematically explored the effects of the hydrophobic block chemistry on the *in vivo* and *in vitro* performance of polymeric nanostructures and showed that the amorphous/crystalline nature of the hydrophobic block affected the *in vivo* circulation times.[91] Their work demonstrated nanocarriers containing amorphous hydrophobic blocks [such as polystyrene, poly($_{D,L}$-lactide), or poly(lactide-co-glycolide)] did not activate the complement system, while those containing crystalline polycaprolactone (PCL) hydrophobic blocks significantly activated the complement system depending on the PCL molecular weight.[91] They hypothesized that the core block crystallization disrupted the hydrophilic surface coverage, evoking an immune response and leading to rapid clearance of the delivery vehicle. Moreover, work by Heise *et al.* suggested that the T_g of the hydrophobic block affected enzymatic cleavage of the corona block in their polymeric micelles[92] and interactions between the payload and the polymeric delivery vehicle influenced the drug release profile.[65,93] Further exploring the effects of hydrophobic block chemistry on drug encapsulation efficiencies, drug release profiles, and nanocarrier

performance in biological environments is essential for designing effective delivery vehicles.

There are numerous examples of hydrophobic block chemistries used throughout literature; however, there is far less variety in the hydrophilic block selection.[57] The most used hydrophilic polymer in biomedical applications is PEO [which is structurally equivalent to poly(ethylene glycol) (PEG)].[45,57,80,89,94,95] PEO is well known for its ability to resist protein binding and prolong circulation times *in vivo*. These advantageous properties of PEO have led to its clinical use in liposome-based chemotherapeutics and protein-polymer conjugates to treat several diseases.[45,89,94] While there are many advantages and multiple clinical success stories with PEO-based therapeutics, there also several reports of hypersensitivity reactions after oral and intravenous administration of these therapeutics.[95,96] Consequently, there is a growing interest in developing alternative hydrophilic polymers from biomedical applications.[95-98] For example, recent work by the Reineke and Hillmyer groups developed glycopolymer-based micelles that were both biocompatible and stable in full serum conditions for hours.[96] Also, there are several examples of zwitterionic polymers that show great promise as ultralow-fouling materials for biomedical applications.[98-101] Inspired by the zwitterionic lipids found in cell membranes, phosphatidylcholines-based polymers have been shown to outperform PEO in anti-biofouling surfaces.[97,98] Zwitterionic polymers bind water even more strongly than PEO due to electrostatically-induced interactions with water, leading to greatly reduced protein binding. This promising advantage has inspired the development of zwitterionic polymers as low fouling materials for solid surfaces such as medical implants and biosensors[97-101] as well as drug delivery vehicles.[100] The

growing interest in developing PEO alternative has led to the development of promising hydrophilic polymer chemistries that warrant further investigation for biomedical applications.

The modular synthetic scheme developed in this dissertation is easily extended to other polymer systems, enabling the synthesis of polymer libraries from a few basic building blocks as depicted in Figure 10.3. This approach will help decouple the influence of the hydrophobic block, hydrophilic block, and ligand display on factors such as serum stability, cytotoxicity, and cellular internalization pathway. Understanding the influence of these nanocarrier properties on their performance in biomedical applications ultimately will enable the rational design of more effective treatment methods.

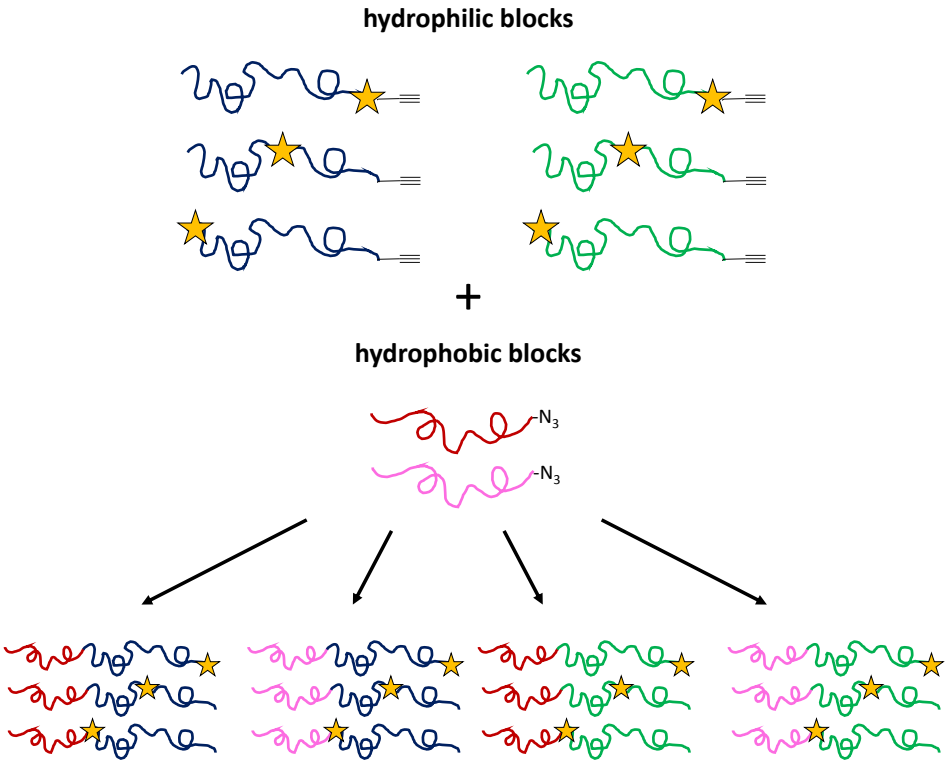

10.3 Schematic representation of materials library synthesized using the modular chemistries described in this dissertation.

Finally, all of the polymers used in this dissertation were synthesized by anionic polymerization because it allows for synthesis of well-defined polymers with controlled molecular weights, low dispersity indices, and quantitative end-group functionalization. However, this polymerization method is not compatible with functional monomers, limiting the block chemistries that can be explored. Advances in controlled radical polymerization techniques such as reversible addition-fragmentation chain-transfer (RAFT) polymerization and atom transfer radical polymerization (ATRP) greatly expand the library of monomers that can be synthesized into well-defined polymers. Functionalities for click chemistry also can be directly incorporated into RAFT chain transfer agents (CTA)s[102] and ATRP

initiators,[103] enabling direct synthesis of functional monomers without the need for additional reaction steps. Moreover, these chemistries also facilitate the synthesis of stimuli-responsive materials that provide a means of triggering drug release at targeted sites.[61,90] Advances in polymer chemistry and responsive materials coupled with the synthetic strategy in Chapter 9 will greatly expand the libraries of functional amphiphilic polymer-peptide conjugates that can be explored for use as drug delivery vehicles.

10.2.2.3 Targeting Different Morphologies

Block polymer composition directly dictates the self-assembled morphology, which in turn can influence the drug loading capacity, circulation times, and internalization efficiency. The synthetic strategy described in this dissertation enables the exploration of morphology effects by simply tuning the hydrophobic block molecular weight (Figure 10.4). While the majority of this dissertation has focused on spherical micelles, both cylindrical micelles and vesicles (also known as polymersomes) are known to have advantageous properties for drug delivery applications. Like spherical micelles, cylindrical micelles can effectively encapsulate hydrophobic cargoes and can be internalized in cells.[104-108] However, work by Discher *et al.* showed that flexible and highly elongated cylindrical micelles circulated *in vivo* for 10 times longer than spherical micelles.[104] Similarly, polymersomes have a unique advantage compared to spherical micelles in that polymersomes can be used to simultaneously encapsulate both hydrophobic and hydrophilic cargoes.[61,109-111] The ability to encapsulate multiple cargoes within a single carrier could enable simultaneous delivery of multiple drugs and/or imaging agents to a targeted site.

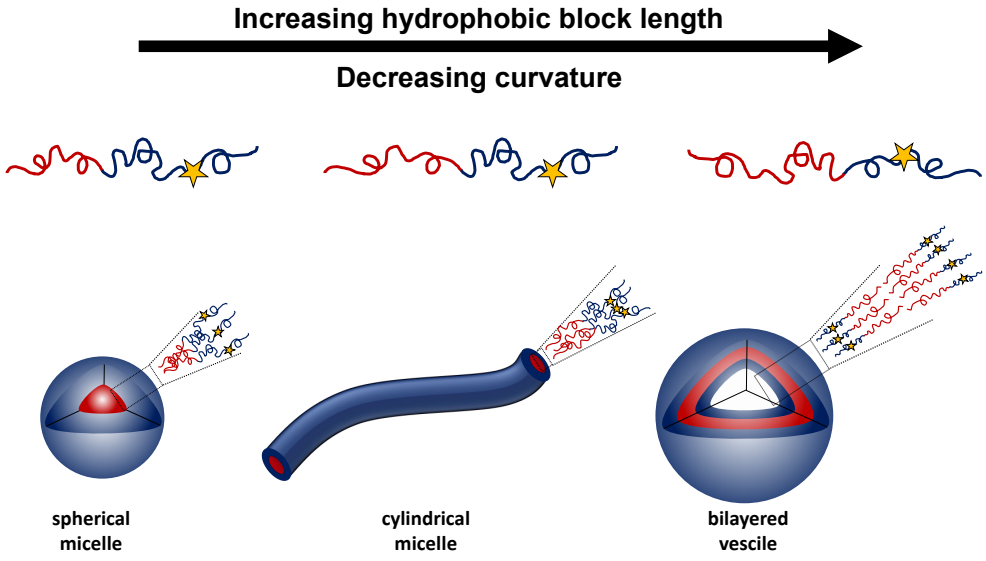

Figure 10.4 Schematic representation of controlling self-assembled morphology by varying the hydrophobic to hydrophilic block ratio in amphiphilic polymer-peptide conjugates.

10.2.3 Probing Structure-Property Relationships in Targeted Drug Delivery Vehicles

The solution assembly literature repeatedly demonstrates the importance of precise nanostructure characteristics on their performance in biomedical applications, and there is a continued need to strengthen direct links between detailed synthesis and equally detailed *in situ* nanostructure characterization. Section 10.2.2 describes methods for synthesizing large material libraries; however, to fully understand the efficacy of these complex self-assembling materials, the specific sizes, shapes, and surface properties must be investigated. The complementary methodologies for solution assembly characterization described in this dissertation and discussed below will provide necessary insights into the complex relationship between a solution assembly's structure/physicochemical properties and its effectiveness as a drug delivery vehicle.

10.2.3.1 Understanding Nanostructure Morphology in Biologically Relevant Environments

A key remaining challenge in drug delivery is the need to understand the structure of the delivery material under physiologically relevant conditions. Cartoon representations (including the figures in this chapter) do not capture the complexity of polymeric assemblies and present an idealized representation of the structure. Moreover, the structures can be affected significantly by the physiological environment, which includes high salt concentrations, high protein concentrations, and flow.

There is enormous potential to gain a more comprehensive understanding of structure-property relationships in nanomedicines by taking advantage of SANS. There are only a few reports in literature that have utilized this powerful technique to understand polymer-drug conjugate structures,[112] pH-dependent structural changes,[113] and the effects of cationic polymer structure on the efficiency of nucleic acid binding.[114] For example, SANS studies of model polymers and mucin (a viscous protein coating on endothelial cells that is an effective barrier to drug delivery) revealed that charged polymers strongly interacted with mucin, leading to a significant reduction in the rate of diffusion.[115] These results have important implications for designing polymeric delivery vehicles that target mucin-rich environments. Similarly, SANS studies of polymeric assemblies in high salt conditions[116,117] or in the presence of serum proteins[118,119] can provide necessary insights into the effects of physiological conditions on their structure, further enabling the rational design of drug delivery vehicles.

10.2.3.2 Determining the Ligand Location within Targeted Drug Delivery Vehicles

This dissertation develops methods for synthetically controlling the location of targeting ligands within the backbone of an amphiphilic block polymer. However, to fully capitalize on these materials, the location of the peptide within the polymer backbone must be directly correlated with the peptide location within the self-assembled structure. This correlation can be achieved by exploiting methods used in protein crystallography and taking advantage of anomalous X-ray scattering. Anomalous scatterers and/or heavy atoms, often are incorporated into protein crystals to help solve protein structures.[120-123] Similarly, incorporating selenium-labeled amino acids into the peptide linkage within the polymer-peptide conjugates and taking advantage of anomalous small angle X-ray scattering (ASAXS) will allow for precise determination of the peptide linkage location within the self-assembled structure (Figure 10.5).

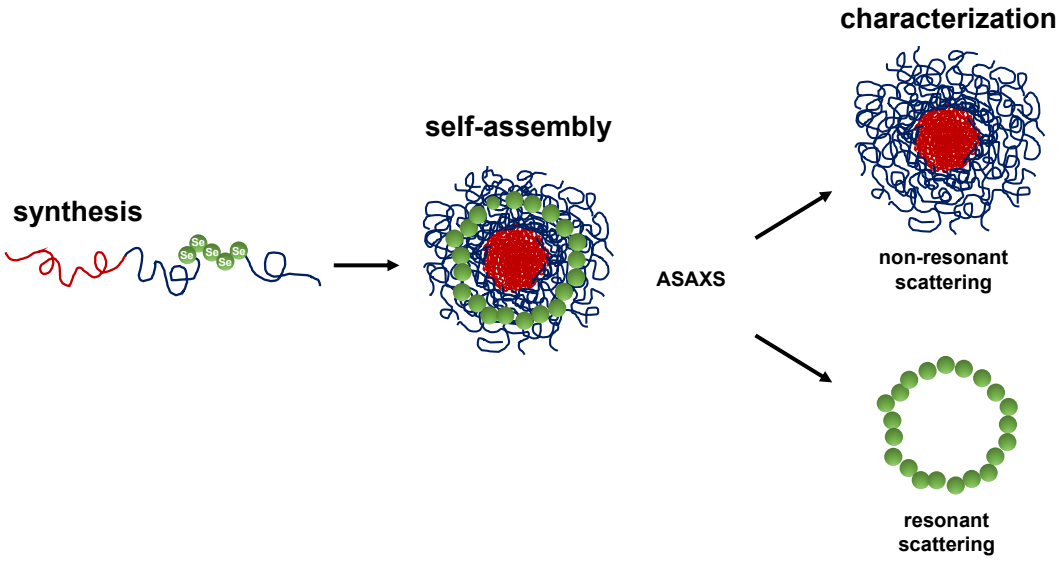

Figure 10.5 Schematic representation of synthesis, self-assembly, and characterization of amphiphilic polymer-peptide conjugates using anomalous small angle X-ray scattering (ASAXS). For ASAXS experiments, selenium-labeled amino acids are incorporated into the targeting ligand, and then ASAXS experiments are performed at multiple X-ray energies above and below the Se K-edge. The scattered intensity can then be decomposed into the non-resonant and resonant scattering from the entire micelle structure and anomalous scatterer (Se), respectively, facilitating precise determination of the ligand location with the self-assembled structure.

***Theoretical Background*[124]**

Anomalous scattering takes advantage of the energy-dependent X-ray scattering factor *f* of an element in the vicinity of the adsorption edge,

$$f(E) = f_0 + f'(E) + if''(E) \quad (1)$$

in which f_0 is the atomic number and *f'* and *f"* are the real and imaginary parts of *f* that are tabulated for most elements. Presented in Figure 10.6 are the *f'* and *f"* for

selenium.[125] Importantly, the K-edge of selenium (12.658 keV) is accessible by synchrotron X-ray sources (typical energy range, E = 7 keV to 20 keV).

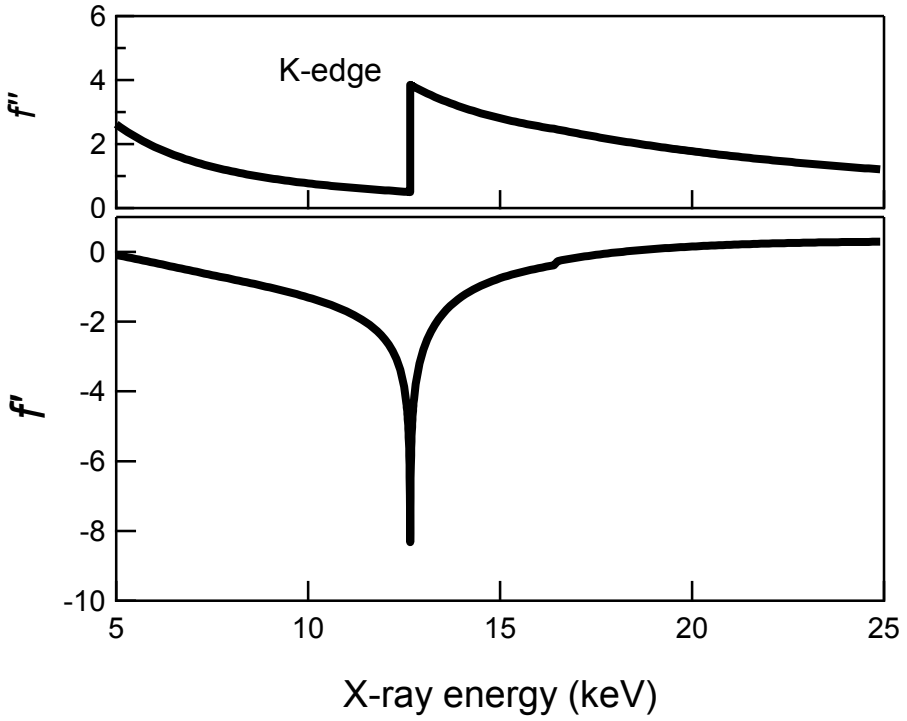

Figure 10.6 Energy dependent real (f') and imaginary (f'') parts of X-ray scattering factor for selenium. The K-edge (12.658 keV) is accessible at synchrotron radiation sources for ASAXS experiments.

For dilute, non-interacting systems, the scattered intensity is then given by,

$$I(q,E) = F_0^2(q) + 2f'(E)F_0(q)\upsilon(q) + [f'^2(E) + f''^2(E)]\nu^2 \qquad (2)$$

in which F_0 is the energy independent, non-resonant scattering (*i.e.* the usual scattering contrast well below the adsorption edge) and $\upsilon(r)$ is the energy dependent, resonant scattering term related to the spatial distribution of anomalous scattering units within the structure.

ASAXS on Soft Materials

Use of ASAXS primarily has been limited to hard materials due to the low concentration of anomalous scatterers in soft materials. Furthermore, the susceptibility of soft materials to beam damage requires carefully optimized experimental setups.[124] Despite these challenges, ASAXS has been used to explore the counterion distribution in surfactant micelles[124] and polyelectrolyte brushes,[126] to understand the structure of bromine-containing polymers,[127] and to probe the location of hydrophobic small molecules in liposomes[128] and polymer micelles.[129] Moreover, recent instrument developments at the European Synchtron Radiation Facility (ESRF) have optimized the high brilliance SAXS beamline ID2 for ASAXS experiments on soft materials.[124]

To probe the targeting ligand location within the polymeric assemblies, commercially available Fmoc-protected selenomethionine (Anaspec, Inc.) can be incorporated within the peptide linkage during standard solid phase peptide synthesis. Recording the ASAXS measurements at multiple energies both above and below the K-edge of selenium (12.658 keV) will facilitate decomposition of the scattered intensity into the resonant and non-resonant components.[124] The energy independent, non-resonant scattering then can be modeled with a form factor model for block polymer micelles, while the energy-dependent resonant scattering can be modeled with a form factor model for a hollow shell (Figure 10.5). Comparing these modeling results will allow for precise determination of the ligand location within the self-assembled nanostructure, which remains unattainable with other characterization methods.

10.2.4 Summary of Future Directions

The experiments outlined above will provide insights into block polymer self-assembly necessary to create well-defined, reproducible nanocarriers for novel applications. Specifically, further exploring the effects of solution agitation on the structure, dynamics, and long-term stability of polymer micelles will decouple the shear and/or interfacial phenomena and greatly facilitate the development of block polymer assemblies for applications as both aqueous nanoreactors and drug delivery vehicles. Moreover, the modular synthetic scheme developed in this dissertation enables control over the sequence and display of targeting ligands (10.2.2.1), the hydrophobic and hydrophilic block chemistries (10.2.2.2), and the conjugate architecture and compositions (10.2.2.3), and also provides a means of incorporating labeled amino acids to directly correlate the polymer-peptide conjugate architecture with ligand display within the nanostructure (10.2.3.2). Together, these approaches will build crucial structure-property relationships for biological applications of polymeric assemblies and guide the rational design of effective drug delivery vehicles. The synergistic understanding of processing conditions and block polymer properties on the resulting self-assembled nanostructures presented within this dissertation are an important next step in advancing these materials for emerging nanotechnologies.

REFERENCES

1 Patterson, J. P. *et al.* (2013), *Macromolecules* **46**, 6319-6325

2 Pedersen, J. S. & Svaneborg, C. (2002), *Current Opinion in Colloid & Interface Science* **7**, 158-166

3 Crassous, J. J., Ballauff, M., Drechsler, M., Schmidt, J. & Talmon, Y. (2006), *Langmuir* **22**, 2403-2406

4 Crassous, J. J. *et al.* (2009), *Langmuir* **25**, 7862-7871

5 Zheng, Y. *et al.* (1999), *The Journal of Physical Chemistry B* **103**, 10331-10334

6 Choucair, A., Lavigueur, C. & Eisenberg, A. (2004), *Langmuir* **20**, 3894-3900

7 Shen, H. & Eisenberg, A. (1999), *Journal of Physical Chemistry B* **103**, 9473-9487

8 Yu, Y. S., Zhang, L. F. & Eisenberg, A. (1998), *Macromolecules* **31**, 1144-1154

9 Zhang, L. & Eisenberg, A. (1995), *Science* **268**, 1728-1731

10 Zhang, L., Shen, H. & Eisenberg, A. (1997), *Macromolecules* **30**, 1001-1011

11 Zhang, L. F. & Eisenberg, A. (1995), *Science* **268**, 1728-1731

12 Cui, H. G., Chen, Z. Y., Zhong, S., Wooley, K. L. & Pochan, D. J. (2007), *Science* **317**, 647-650

13 Pochan, D. J. *et al.* (2004), *Science* **306**, 94-97

14 Zhong, S., Cui, H., Chen, Z., Wooley, K. L. & Pochan, D. J. (2008), *Soft Matter* **4**, 90-93

15 Zhu, J. H. *et al.* (2013), *Nature Communications* **4**, 3297

16 Zhu, J. & Hayward, R. C. (2008), *Angewandte Chemie-International Edition* **47**, 2113-2116

17 Zhu, J. T. & Hayward, R. C. (2008), *Journal of the American Chemical Society* **130**, 7496-7502

18 Groschel, A. H. *et al.* (2012), *Nature Communications* **3**, 1707

19 Aliabadi, H. M. *et al.* (2007), *International Journal of Pharmaceutics* **329**, 158-165

20 Owen, S. C., Chan, D. P. Y. & Shoichet, M. S. (2012), *Nano Today* **7**, 53-65

21 Tyrrell, Z. L., Shen, Y. Q. & Radosz, M. (2010), *Progress in Polymer Science* **35**, 1128-1143

22 Halperin, A., Tirrell, M. & Lodge, T. P. (1992), *Advances in Polymer Science* **100**, 31-71

23 Kelley, E. G., Smart, T. P., Jackson, A. J., Sullivan, M. O. & Epps, T. H. (2011), *Soft Matter* **7**, 7094-7102

24 Broseta, D., Fredrickson, G. H., Helfand, E. & Leibler, L. (1990), *Macromolecules* **23**, 132-139

25 Helfand, E. & Sapse, A. M. (1975), *The Journal of Chemical Physics* **62**, 1327-1331

26 Helfand, E. & Tagami, Y. (1971), *Journal of Polymer Science Part B: Polymer Physics* **9**, 741-746

27 Helfand, E. & Tagami, Y. (1972), *Journal of Chemical Physics* **56**, 3592-3601

28 Willner, L., Poppe, A., Allgaier, J., Monkenbusch, M. & Richter, D. (2001), *Europhysics Letters* **55**, 667-673

29 Jain, S. & Bates, F. S. (2004), *Macromolecules* **37**, 1511-1523

30 Won, Y. Y., Davis, H. T. & Bates, F. S. (2003), *Macromolecules* **36**, 953-955

31 Meli, L., Santiago, J. M. & Lodge, T. P. (2010), *Macromolecules* **43**, 2018-2027

32 Kelley, E. G. *et al.* (2014), *Nature Communications* **5**, 4599

33 Dormidontova, E. E. (1999), *Macromolecules* **32**, 7630-7644

34 Esselink, F. J., Dormidontova, E. & Hadziioannou, G. (1998), *Macromolecules* **31**, 2925-2932

35 Esselink, F. J., Dormidontova, E. E. & Hadziioannou, G. (1998), *Macromolecules* **31**, 4873-4878

36 Nyrkova, I. A. & Semenov, A. N. (2005), *Macromolecular Theory and Simulations* **14**, 569-585

37 Nyrkova, I. A. & Semenov, A. N. (2005), *Faraday Discussions* **128**, 113-127

38 Bai, G., Bee, J. S., Biddlecombe, J. G., Chen, Q. & Leach, W. T. (2012), *International Journal of Pharmaceutics* **423**, 264-280

39 Chou, D. K., Krishnamurthy, R., Randolph, T. W., Carpenter, J. F. & Manning, M. C. (2005), *Journal of Pharmaceutical Sciences* **94**, 1368-1381

40 Kerwin, B. A. (2008), *Journal of Pharmaceutical Sciences* **97**, 2924-2935

41 Kiese, S., Papppenberger, A., Friess, W. & Mahler, H.-C. (2008), *Journal of Pharmaceutical Sciences* **97**, 4347-4366

42 Sluzky, V., Tamada, J. A., Klibanov, A. M. & Langer, R. (1991), *Proceedings of the National Academy of Sciences* **88**, 9377-9381

43 Thomas, C. R. & Geer, D. (2011), *Biotechnology Letters* **33**, 443-456

44 Farokhzad, O. C. & Langer, R. (2009), *ACS Nano* **3**, 16-20

45 Duncan, R. & Gaspar, R. (2011), *Molecular Pharmaceutics* **8**, 2101-2141

46 Matsumura, Y. (2008), *Japanese Journal of Clinical Oncology* **38**, 793-802

47 Lund, R., Willner, L. & Richter, D. (2013), *Advances in Polymer Science* **259**, 51-158

48 Lund, R. *Small Angle Neutron Scattering as a Tool to Study Kinetics of Block Copolymer Micelles*. Vol. 161 Springer-Verlag Berlin, 2010.

49 Choi, S. H., Lodge, T. P. & Bates, F. S. (2010), *Physical Review Letters* **104**, 047802

50 Zinn, T., Willner, L., Lund, R., Pipich, V. & Richter, D. (2012), *Soft Matter* **8**, 623-626

51 Lu, J., Bates, F. S. & Lodge, T. P. (2013), *ACS Macro Letters* **2**, 451-455

52 Choi, S. H., Bates, F. S. & Lodge, T. P. (2011), *Macromolecules* **44**, 3594-3604

53 Halperin, A. (2011), *Macromolecules* **44**, 5072-5074

54 Lund, R., Willner, L., Richter, D. & Dormidontova, E. E. (2006), *Macromolecules* **39**, 4566-4575

55 Lund, R. *et al.* (2011), *Macromolecules* **44**, 6145-6154

56 Mai, Y. Y. & Eisenberg, A. (2012), *Chemical Society Reviews* **41**, 5969-5985

57 Allen, C., Maysinger, D. & Eisenberg, A. (1999), *Colloids and Surfaces B: Biointerfaces* **16**, 3-27

58 Shuai, X., Ai, H., Nasongkla, N., Kim, S. & Gao, J. (2004), *Journal of Controlled Release* **98**, 415-426

59 Fetters, L. J., Lohse, D. J., Richter, D., Witten, T. A. & Zirkel, A. (1994), *Macromolecules* **27**, 4639-4647

60 Won, Y.-Y., Brannan, A. K., Davis, H. T. & Bates, F. S. (2002), *The Journal of Physical Chemistry B* **106**, 3354-3364

61 Kelley, E. G., Albert, J. N. L., Sullivan, M. O. & Epps, T. H. (2013), *Chemical Society Reviews* **42**, 7057-7071

62 Iha, R. K. *et al.* (2009), *Chemical Reviews* **109**, 5620-5686

63 Abbas, S. & Lodge, T. P. (2007), *Physical Review Letters* **99**, 137802

64 Repollet-Pedrosa, M. H. & Mahanthappa, M. K. (2013), *Soft Matter*

65 Schulz, A. *et al.* (2014), *ACS Nano* **8**, 2686-2696

66 Mikhail, A. S. & Allen, C. (2010), *Biomacromolecules* **11**, 1273-1280

67 Khimani, M., Ganguly, R., Aswal, V. K., Nath, S. & Bahadur, P. (2012), *Journal of Physical Chemistry B* **116**, 14943-14950

68 Sharma, P. K., Reilly, M. J., Jones, D. N., Robinson, P. M. & Bhatia, S. R. (2008), *Colloids and Surfaces B-Biointerfaces* **61**, 53-60

69 Valero, M. & Dreiss, C. A. (2010), *Langmuir* **26**, 10561-10571

70 Yokoyama, M. *et al.* (1998), *Journal of Controlled Release* **50**, 79-92

71 Jain, S. & Bates, F. S. (2003), *Science* **300**, 460-464

72 Hayward, R. C. & Pochan, D. J. (2010), *Macromolecules* **43**, 3577-3584

73 Khougaz, K., Zhong, X. F. & Eisenberg, A. (1996), *Macromolecules* **29**, 3937-3949

74 Gu, F. *et al.* (2008), *Proceedings of the National Academy of Sciences* **105**, 2586-2591

75 Pangburn, T. O., Bates, F. S. & Kokkoli, E. (2012), *Soft Matter* **8**, 4449-4461

76 Nasongkla, N. *et al.* (2004), *Angewandte Chemie International Edition* **43**, 6323-6327

77 Sutton, D., Nasongkla, N., Blanco, E. & Gao, J. (2007), *Pharmaceutical Research* **24**, 1029-1046

78 Shi, J., Votruba, A. R., Farokhzad, O. C. & Langer, R. (2010), *Nano Letters* **10**, 3223-3230

79 Kelkar, S. S. & Reineke, T. M. (2011), *Bioconjugate Chemistry* **22**, 1879-1903

80 Canton, I. & Battaglia, G. (2012), *Chemical Society Reviews* **41**, 2718-2739

81 Grandinetti, G. & Reineke, T. M. (2012), *Molecular Pharmaceutics* **9**, 2256-2267

82 Heidel, J. D. & Davis, M. E. (2011), *Pharmaceutical Research* **28**, 187-199

83 Stefanick, J. F., Ashley, J. D. & Bilgicer, B. (2013), *ACS Nano* **7**, 8115-8127

84 Stefanick, J. F., Ashley, J. D., Kiziltepe, T. & Bilgicer, B. (2013), *ACS Nano* **7**, 2935-2947

85 Zupancich, J. A., Bates, F. S. & Hillmyer, M. A. (2009), *Biomacromolecules* **10**, 1554-1563

86 Huang, X. *et al.* (2010), *ACS Nano* **4**, 5887-5896

87 Wang, X., Liu, L., Luo, Y. & Zhao, H. (2008), *Langmuir* **25**, 744-750

88 Otsuka, H., Nagasaki, Y. & Kataoka, K. (2003), *Advanced Drug Delivery Reviews* **55**, 403-419

89 Veronese, F. M. & Pasut, G. (2005), *Drug Discovery Today* **10**, 1451-1458

90 Randolph, L. M., Chien, M.-P. & Gianneschi, N. C. (2012), *Chemical Science* **3**, 1363-1380

91 D'Addio, S. M. *et al.* (2012), *Journal of Controlled Release* **162**, 208-217

92 Habraken, G. J. M., Peeters, M., Thornton, P. D., Koning, C. E. & Heise, A. (2011), *Biomacromolecules* **12**, 3761-3769

93 Ansell, S. M. *et al.* (2008), *Journal of Medicinal Chemistry* **51**, 3288-3296

94 Duncan, R. (2003), *Nature Reviews Drug Discovery* **2**, 347-360

95 Knop, K., Hoogenboom, R., Fischer, D. & Schubert, U. S. (2010), *Angewandte Chemie International Edition* **49**, 6288-6308

96 Yin, L., Dalsin, M. C., Sizovs, A., Reineke, T. M. & Hillmyer, M. A. (2012), *Macromolecules* **45**, 4322-4332

97 Krishnan, S., Weinman, C. J. & Ober, C. K. (2008), *Journal of Materials Chemistry* **18**, 3405-3413

98 Jiang, S. & Cao, Z. (2010), *Advanced Materials* **22**, 920-932

99 Chen, X., Lawrence, J., Parelkar, S. & Emrick, T. (2012), *Macromolecules* **46**, 119-127

100 Liu, S. & Armes, S. P. (2002), *Angewandte Chemie International Edition* **41**, 1413-1416

101 Lowe, A. B. & McCormick, C. L. (2002), *Chemical Reviews* **102**, 4177-4190

102 Hansell, C. F. *et al.* (2011), *Journal of the American Chemical Society* **133**, 13828-13831

103 Kuan, W.-F., Roy, R., Rong, L., Hsiao, B. S. & Epps, T. H. (2012), *ACS Macro Letters* **1**, 519-523

104 Geng, Y. *et al.* (2007), *Nature Nanotechnology* **2**, 249-255

105 Younghoon, K., Paul, D., David, A. C. & Dennis, E. D. (2005), *Nanotechnology* **16**, S484

106 Cai, S., Vijayan, K., Cheng, D., Lima, E. & Discher, D. (2007), *Pharmaceutical Research* **24**, 2099-2109

107 Shuvaev, V. V. *et al.* (2011), *ACS Nano* **5**, 6991-6999

108 Christian, D. A. *et al.* (2009), *Molecular Pharmaceutics* **6**, 1343-1352

109 Discher, D. E. & Eisenberg, A. (2002), *Science* **297**, 967-973

110 Ghoroghchian, P. P. *et al.* (2006), *Soft Matter* **2**, 973-980

111 Mueller, W. *et al.* (2008), *Macromolecules* **42**, 357-361

112 Paul, A., Vicent, M. J. & Duncan, R. (2007), *Biomacromolecules* **8**, 1573-1579

113 Griffiths, P. C. *et al.* (2004), *Biomacromolecules* **5**, 1422-1427

114 Griffiths, P. C. *et al.* (2008), *Biomacromolecules* **9**, 1170-1178

115 Griffiths, P. C. *et al.* (2009), *Biomacromolecules* **11**, 120-125

116 Kataoka, K., Harada, A. & Nagasaki, Y. (2001), *Advanced Drug Delivery Reviews* **47**, 113-131

117 Lee, A. S., Gast, A. P., Bütün, V. & Armes, S. P. (1999), *Macromolecules* **32**, 4302-4310

118 Barrán-Berdón, A. L. *et al.* (2013), *Langmuir* **29**, 6485-6494

119 Tenzer, S. *et al.* (2013), *Nature Nanotechnology* **8**, 772-U1000

120 Garman, E. & Murray, J. W. (2003), *Acta Crystallographica Section D-Biological Crystallography* **59**, 1903-1913

121 Morth, J. P., Sorensen, T. L.-M. & Nissen, P. (2006), *Acta Crystallographica Section D* **62**, 877-882

122 Pickering, I. J., George, G. N., Van Fleet-Stalder, V., Chasteen, T. G. & Prince, R. C. (1999), *JBIC Journal of Biological Inorganic Chemistry* **4**, 791-794

123 Sharff, A. J., Koronakis, E., Luisi, B. & Koronakis, V. (2000), *Acta Crystallographica Section D* **56**, 785-788

124 Sztucki, M., Di Cola, E. & Narayanan, T. (2010), *Journal of Applied Crystallography* **43**, 1479-1487

125 http://skuld.bmsc.washington.edu/scatter/AS_periodic.html.

126 Dingenouts, N. *et al.* (2004), *Macromolecules* **37**, 8152-8159

127 Akiba, I. *et al.* (2012), *Macromolecules* **45**, 6150-6157

128 Varga, Z., Bóta, A. & Goerigk, G. (2006), *The Journal of Physical Chemistry B* **110**, 11029-11032

129 Sanada, Y. *et al.* (2013), *Journal of the American Chemical Society* **135**, 2574-2582

Appendix A

RADIAL CORONA PROFILE FOR SANS DATA MODEL

As discussed in Chapters 4 and 5, the corona profile $\rho_{corona}(r)$ was described as linear combination of 2 *b* splines, $\rho_1(r)$ and $\rho_2(r)$,

$$\rho_{corona}(r) = \frac{\rho_1(r) + a\rho_2(r)}{1 + a} \tag{A1}$$

In which a is a fitting parameter and $\rho_1(r)$ and $\rho_2(r)$ are given by

$$\rho_1(r) = \frac{4(r - R_c - s)^3 - (r - R_c - 2s)^3}{4s^3} \qquad for\ R_c \le r < R_c + s$$

$$\rho_1(r) = \frac{-(r - R_c - 2s)^3}{4s^3} \qquad for\ R_c + s \le r < R_c + 2s$$

$$\rho_1(r) = 0 \qquad elsewhere \tag{A2}$$

and

$$\rho_2(r) = \frac{-(r - R_c - s)^3}{4s^3} \qquad for\ R_c \le r < R_c + s$$

$$\rho_2(r) = 0 \qquad elsewhere \tag{A3}$$

The Fourier transforms of the individual components are then given by,

$$S_1(q) = C_{norm,1}\left[\frac{24\cos[q(R_c+2s)]}{q^6} + \frac{6(R_c+2s\sin[q(R_c+2s)])}{q^5} - \frac{96\cos[q(R_c+s)]}{q^6} - \frac{24(R_c+s)\sin[q(R_c+s)]}{q^5} + \frac{4(q^4R_cs^3+3q^2R_cs+18)\cos(qR_c)}{q^6} - \frac{2[2q^2s^3-9(R_c-2s)\sin(qR_c)]}{q^5}\right] \quad \text{(A4)}$$

In which

$$C_{norm,1}^{-1} = \frac{s^4(15R_c^2+14R_cs+5s^2)}{5} \quad \text{(A5)}$$

and

$$S_2(q) = C_{norm,2}\left[\frac{96\cos[q(R_c+2s)]}{q^6} + \frac{24(R_c+2s)\sin[q(R_c-2s)]}{q^5} + \frac{4(q^4R_cs^3-6q^2s(R_c-s)-24)\cos(qR_c)}{q^6} + \frac{4[q^2s^2(3R_c-s)-6(R_c-3s)]\sin(qR_c)}{q^5}\right] \quad \text{(A6)}$$

In which

$$C_{norm,2}^{-1} = \frac{s^4(15R_c^2+6R_cs+s^2)}{15} \quad \text{(A7)}$$

The corona scattering amplitude $A_{corona}(q)$ is then given by

$$A_{corona}(q) = \frac{S_1(q)+aS_2(q)}{1+a} \quad \text{(A8)}$$

Appendix B

CODE FOR MICELLE FORM FACTOR MODEL

The form factor model for spherical block polymer micelles described in Chapters 4 and 5 was programmed in IGOR Pro to interface with the fitting procedures provided by NIST. The code for the form factor model is provided below.

```
#pragma rtGlobals=1             // Use modern global access method.
#pragma IgorVersion=6.0

////////////////////////////////////////////////////
//
// This is a form factor for block polymer micelles
// assumes hard sphere for core
// corona density profile is a linear combination of 2 b splines
// fuzzy interface between core and corona
//
////////////////////////////////////////////////////

//this macro sets up all the necessary parameters and waves that are
//needed to calculate the model function.
//
Macro PlotPoly_bshell(num,qmin,qmax)
        Variable num=200, qmin=0.001, qmax=0.7
        Prompt num "Enter number of data points for model: "
        Prompt qmin "Enter minimum q-value (A^-1) for model: "
        Prompt qmax "Enter maximum q-value (A^-1) for model: "
//
        Make/O/D/n=(num) xwave_Poly_bshell, ywave_Poly_bshell
        xwave_Poly_bshell =  alog(log(qmin) + x*((log(qmax)-
        log(qmin))/num))
```

```
//define default values for input paramter
	Make/O/D coef_Poly_bshell = {0.007, 100, 100, 0.1, 10 , 30 , 90,  0.2,
	4.11e-7, 6.38e-7, 6.33e-6, 0.05, 1000,12}
	make/o/t parameters_Poly_bshell = {"scale", "aggregation
	number","core radius (A)","core polydispersity","interfacial width
	(A)","Rg corona (A)", "s (A) ", "a",  "SLD core (A-2)","SLD shell (A-
	2)","SLD solvent (A-2)","bkgd (cm-1)","vcorona(A)","vcore(A)"}
	Edit parameters_Poly_bshell, coef_Poly_bshell

	Variable/G root:g_Poly_bshell=0
	root:g_Poly_bshell := Poly_bshell(coef_Poly_bshell,
	ywave_Poly_bshell, xwave_Poly_bshell)
	Display ywave_Poly_bshell vs xwave_Poly_bshell
	ModifyGraph marker=29, msize=2, mode=4
	ModifyGraph log=1,grid=1,mirror=2
	Label bottom "q (A\\S-1\\M) "
	Label left "I(q) (cm\\S-1\\M)"
	AutoPositionWindow/M=1/R=$(WinName(0,1)) $WinName(0,2)

	AddModelToStrings("Poly_bshell","coef_Poly_bshell","parameters_Po
	ly_bshell","Poly_bshell")
//
End`

//
//this macro sets up all the necessary parameters and waves that are
//needed to calculate the smeared model function.
//
//no input parameters are necessary, it MUST use the experimental q-values
// from the experimental data read in from an AVE/QSIG data file
////////////////////////////////////////////////////
// - sets up a dependency to a wrapper, not the actual SmearedModelFunction
Macro PlotSmearedPoly_bshell(str)

	String str
	Prompt str,"Pick the data folder containing the resolution you
	want",popup,getAList(4)

	// if any of the resolution waves are missing => abort
	if(ResolutionWavesMissingDF(str))		//updated to NOT use
	global strings (in GaussUtils)
		Abort
	endif
```

```
	SetDataFolder $("root:"+str)

	// Setup parameter table for model function
	Make/O/D smear_coef_Poly_bshell =  {0.007, 100, 100, 0.1, 10 , 30 , 90
	,  0.2, 4.11e-7, 6.38e-7, 6.33e-6, 0.05, 1000,12}

	make/o/t smear_parameters_Poly_bshell = {"scale", "aggregation
	number","core radius (A)","core polydispersity","interfacial width
	(A)","Rg corona (A)", "s (A) ", "a",  "SLD core (A-2)","SLD shell (A-
	2)","SLD solvent (A-2)","bkgd (cm-1)","vcorona(A)","vcore(A)"}
	Edit smear_parameters_Poly_bshell,smear_coef_Poly_bshell
		//display parameters in a table

	 // output smeared intensity wave, dimensions are identical to
	 experimental QSIG values
	// make extra copy of experimental q-values for easy plotting
	Duplicate/O $(str+"_q") smeared_Poly_bshell,smeared_qvals
	SetScale d,0,0,"1/cm",smeared_Poly_bshell

	Variable/G gs_bshell=0
	 gs_bshell :=
	 fSmearedPoly_bshell(smear_coef_Poly_bshell,smeared_Poly_bshell,s
	 meared_qvals)		//this wrapper fills the STRUCT

	Display smeared_Poly_bshell vs smeared_qvals
	ModifyGraph log=1,marker=29,msize=2,mode=4
	Label bottom "q (Å\\S-1\\M)"
	Label left "I(q) (cm\\S-1\\M)"
	AutoPositionWindow/M=1/R=$(WinName(0,1)) $WinName(0,2)

	SetDataFolder root:
	AddModelToStrings("SmearedPoly_bshell","smear_coef_Poly_bshell",
	"smear_parameters_Poly_bshell","Poly_bshell")
End


// nothing to change here
//
//AAO version, uses XOP if available
// simply calls the original single point calculation with
// a wave assignment (this will behave nicely if given point ranges)
Function Poly_bshell(cw,yw,xw) : FitFunc
```

```
	Wave cw,yw,xw

#if exists("bshellX")
	yw = Poly_bshellX(cw,xw)
#else
	yw = fPoly_bshell(cw,xw)
#endif
	return(0)
End


// calculates intensity for a
// for a single q-value

//~~~~~~~~~~~~~~~~~~~~~~~~~
// unsmeared model calculation
//~~~~~~~~~~~~~~~~~~~~~~~~~

Function fPoly_bshell(w,x) : FitFunc
	Wave w
	Variable x

	// variables are:
	//[0] scale
	//[1] aggregation number
	//[2] core radius (A)
	//[3] core polydispersity (sigma)
	//[4] Interfacial width (A)
	//[5] Rg of corona chain
	//[6] s determines width of corona profile
	//[7] a fitting parameter for weighting of b splines
	//[8] SLD core (A-2)
	//[9] SLD corona (A-2)
	//[10] SLD solvent (A-2)
	//[11] background (cm-1)
	//[12] volume of corona block (A3)
	//[13] volume of core block (A3)

	Variable scale,NN, rc,sigma, iw, rg, ss, aa, sldcor, sldshell, sldsol, bgd,
	vcorona, vcore
	scale = w[0]
	NN = w[1]
	rc = w[2]
```

```
sigma = w[3]
iw = w[4]
rg = w[5]
ss = w[6]
aa = w[7]
sldcor = w[8]
sldshell = w[9]
sldsol = w[10]
bgd = w[11]
vcorona = w[12]
vcore = w[13]

// define width of Schultz distrbution in terms of polydispersity
variable zz
zz = (1/sigma)^2-1

Variable qq
//rename the input q-value, purely for readability
qq = x

//~~~~~~~~~~~~~~~~~~~~~~~~~~~~~~~~~~~~~~~~~~~~~~~~~~~~~~~~~~~~
//incorporation of polydispersity
//integrate from factor over a schultz distribution in core radii
//~~~~~~~~~~~~~~~~~~~~~~~~~~~~~~~~~~~~~~~~~~~~~~~~~~~~~~~~~~~~

Variable a, b, la, lb
Variable ii, zi, nord, yy, summ, intensity
String weightStr, zStr

// setup Gaussian quadrature integration

nord = 20                    //select number of Gaussian points

weightStr = "gauss"+num2str(nord)+"wt"
zStr = "gauss"+num2str(nord)+"z"

if (WaveExists($weightStr) == 0) // wave reference is not valid,
        Make/D/N=(nord) $weightStr,$zStr
        Wave gauWt = $weightStr
        Wave gauZ = $zStr               // wave references to pass
        if(nord==20)
                Make20GaussPoints(gauWt,gauZ)
        else
```

```
                Make76GaussPoints(gauWt,gauZ)
        endif
else
        if(exists(weightStr) > 1)
           Abort "wave name is already in use"                    //executed
          only if name is in use elsewhere
        endif
        Wave gauWt = $weightStr
        Wave gauZ = $zStr               // create the wave references
endif

// establish limits of integration
// limits are technically 0 --> infinity, but choose non-zero regions of
distribution

// multiples of standard deviation from mean
Variable range = 4

// lower integration limit in terms of core radii
a = rc*(1-range*sigma)

        if (a<0)
                a = 0
        endif

        if (sigma >0.3)
                range = 3.4 + (sigma-0.3)*18
        //otherwise numerical error when sigma >0.3, making a <0
        endif

b = rc*(1 + range*sigma)       //upper limit of integration

la = a
lb = b

// evaluate integral at Gauss points
summ = 0.0              //initialize integral

for(ii=0;ii<nord;ii+=1)

// calculate Gauss points on integration interval (r-value for evaluation)
        zi = ( gauZ[ii]*(lb-la) + lb + la )/2.0
```

```
            // call integrand function
        yy = gauWt[ii] * formfactor_bshell(qq, zi, rc, NN, sigma, iw, rg, ss, aa,
        sldcor, sldshell, sldsol,zz, vcorona,vcore)

//add to the running total of the quadrature
        summ += yy

        endfor

        // calculate value of integral to return
        intensity = (lb-la)/2.0*summ

        //normalize by micelle mass
        //micelle mass = aggregation number* volume of 1 polymer chain *
        specific density of polymer chain

        //must input polymer density here
        variable mm, rho
        rho = 1 //change this line to be polymer density
        mm = NN*(vcore+vcorona)*rho

        //Units of mm here have ended up as  A^3 g cm^-3
        //Unit of intensity are A^2 before mass normalization
        intensity /= mm
        //Units of intensity are now A-1 g^-1 cm^3

        //convert to g^-1 cm^2
        intensity  *=  1.0e8

        //scale - concentration in g cm^-3
        intensity *= scale
        //intensity is now in cm^-1

        //add bkg
        intensity += bgd

        return(intensity)
        End


//~~~~~~~~~~~~~~~~~~~~~~~~~~~~~~~~~~~~~~~~~~~~~~~~~~~~~~~~~~~~~~~~~~~~~~~~~~~~
//calculates form factor for spherical micelles
//~~~~~~~~~~~~~~~~~~~~~~~~~~~~~~~~~~~~~~~~~~~~~~~~~~~~~~~~~~~~~~~~~~~~~~~~~~~~
```

```
Function formfactor_bshell(qq, ri, rc, NN, sigma, iw, rg, ss, aa, sldcor, sldshell,
sldsol,zz, vcorona,vcore)

        Variable qq, ri, rc, NN, sigma, iw, rg, ss, aa, sldcor, sldshell, sldsol,zz,
        vcorona,vcore            // variables passed in

        //note ri = current radii in integration

        //scattering from core
        Variable siq, coq, qr, acore

        qr = qq*ri
        siq = sin(qr)
        coq = qr*cos(qr)
        acore = 3*(siq-coq)/(qr^3)*exp(-0.5*qq*qq*iw*iw)

        //corona chain self-correlation term
        //equation 3
        variable Pc, xpc

        xpc = qq*qq*rg*rg
        Pc = 2*(exp(-xpc) - 1 + xpc)/(xpc^2)

        //scattering from corona
        //assumes radially decreasing denisty profile in corona
        //density profile modeled as linear combination of 2 cubic b splines
        //see Appendix A for equations

        variable sc1, sc11, sc12, sc13,sc14, sc15, sc16, c1norm

        //equation A4 in Bang et al.
        sc11 = 24*cos(qq*(ri + 2*ss))/qq^6
        sc12 = 6*(ri + 2*ss)*sin(qq*(ri + 2*ss))/qq^5
        sc13 = 96*cos(qq*(ri + ss))/qq^6
        sc14 = 24*(ri + ss)*sin(qq*(ri + ss))/qq^5
        sc15 = 4*(qq^4*ri*ss^3 + 3*qq^2*ri*ss + 18)*cos(qq*ri)/qq^6
        sc16 = 2*(2*qq^2*ss^3 - 9*(ri - 2*ss))*sin(qq*ri)/qq^5

        c1norm = ss^4*(15*ri^2 + 14*ri*ss + 5*ss^2)
        c1norm = 5/c1norm

        sc1 = c1norm*(sc11 + sc12 - sc13 - sc14 + sc15 - sc16)
```

```
variable sc2, sc21, sc22, sc23, sc24, c2norm

//equation A6 in Bang et al.
sc21 = 96*cos(qq*(ri + ss))/qq^6
sc22 = 24*(ri + ss)*sin(qq*(ri + ss))/qq^5
sc23 = 4*(qq^4*ri*ss^3 - 6*qq^2*ss*(ri - ss)  - 24)*cos(qq*ri)/qq^6
sc24 = 4*(qq^2*ss^2*(3*ri - ss) - 6*(ri - 3*ss))*sin(qq*ri)/qq^5

c2norm = ss^4*(15*ri^2 + 6*ri*ss + ss^2)
c2norm = 15/c2norm

sc2 = c2norm*(sc21 + sc22 + sc23 + sc24)

variable acorona

//equation A8
acorona = (sc1 + aa*sc2)*exp(-qq*qq*iw*iw/2)/(1 + aa)


//calculated volumes of core and corona chains
//needed for scattering contrast

//calculating scattering contrasts
variable bcore, bcorona
bcore = vcore*(sldcor - sldsol)
bcorona = vcorona*(sldshell - sldsol)


//form factor

variable PP

//core cross term
PP = NN*NN*bcore*bcore*acore*acore

//shell cross term
PP += NN*(NN - 1)*bcorona*bcorona*acorona*acorona

//core-shell cross term
PP += 2*NN*NN*bcore*bcorona*acore*acorona

//shell chain cross terms
PP += NN*bcorona*bcorona*Pc
```

```
	//calculate Schultz distribution at ri
	variable dr
	dr = Schultz_Point(ri, rc, zz)

	return (PP*dr)

	End

//~~~~~~~~~~~~~~~~~~~~~~~~~~~~~~~~~~~~~~~~~~~~~~~~~~~~~~~~~~~~~~~~~~~~~~~~~~~~
// calculates Schultz distribution at r
//~~~~~~~~~~~~~~~~~~~~~~~~~~~~~~~~~~~~~~~~~~~~~~~~~~~~~~~~~~~~~~~~~~~~~~~~~~~~

Function Schultz_Point(x, avg, zz)

Variable x,avg,zz
Variable dr

dr = zz*ln(x) - gammln(zz+1) + (zz+1)*ln((zz+1)/avg) - (x/avg*(zz+1))

return(exp(dr))

End


////////////////////////////////////////////////////////////////
// smeared model calculation
//
// you don't need to do anything with this function, as long as
// your bshell works correctly, you get the resolution-smeared
// version for free.
//
// this is all there is to the smeared model calculation!
Function SmearedPoly_bshell(s) : FitFunc
	Struct ResSmearAAOStruct &s

//	the name of your unsmeared model (AAO) is the first argument
	Smear_Model_20(Poly_bshell,s.coefW,s.xW,s.yW,s.resW)

	return(0)
End
```

```
////////////////////////////////////////////////////////////////
//wrapper to calculate the smeared model as an AAO-Struct
// fills the struct and calls the ususal function with the STRUCT parameter
// used only for the dependency, not for fitting

Function fSmearedPoly_bshell(coefW,yW,xW)
	Wave coefW,yW,xW

	String str = getWavesDataFolder(yW,0)
	String DF="root:"+str+":"

	WAVE resW = $(DF+str+"_res")

	STRUCT ResSmearAAOStruct fs
	WAVE fs.coefW = coefW
	WAVE fs.yW = yW
	WAVE fs.xW = xW
	WAVE fs.resW = resW

	Variable err
	err = SmearedPoly_bshell(fs)

	return (0)
End
```

Appendix C

SANS DATA AND FITS FOR BLOCK POLYMER MICELLES IN COSOLVENT MIXTURES

Presented in this appendix are the SANS data and corresponding fits for all of the PB-PEO and PB-*d*PEO micelles in water/THF cosolvent mixtures studied in Chapter 5. Data for cosolvent compositions $\leq$ 30 vol% THF were modeled with the form factor for block polymer micelles described in Chapters 4 and 5, 40 vol% to 72 vol% THF were modeled with a linear combination of form factors for block polymer micelles and free chains (modeled as polydisperse Gaussian coils), and $\geq$ 75 vol% THF were modeled as Gaussian chains. The modeling is described in detail in Chapter 5, and the fitting parameters are presented in Table 5.1. Additional fitting parameters for the corona density profile are summarized in Table C1.

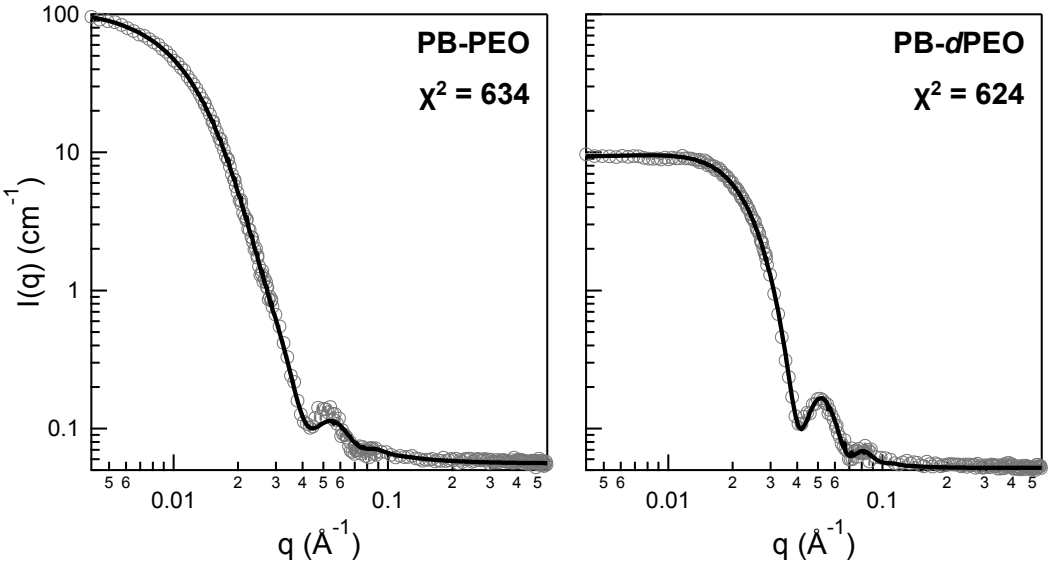

Figure C1 SANS data (points) and fits (lines) for PB-PEO and PB-*d*PEO micelles in a 0 vol% THF cosolvent mixture (pure water).

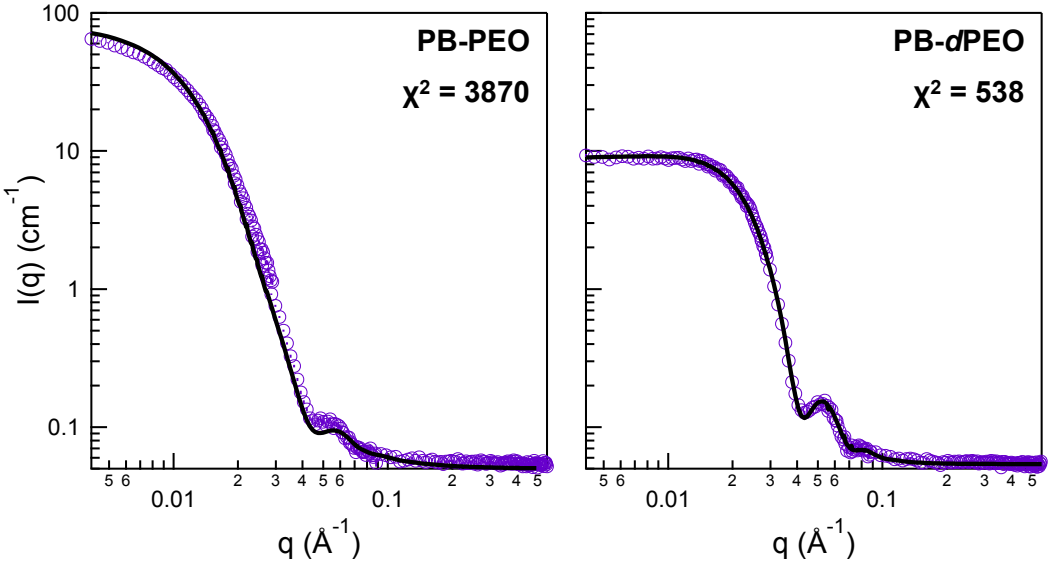

Figure C2 SANS data (points) and fits (lines) for PB-PEO and PB-*d*PEO micelles in a 2.5 vol% THF cosolvent mixture.

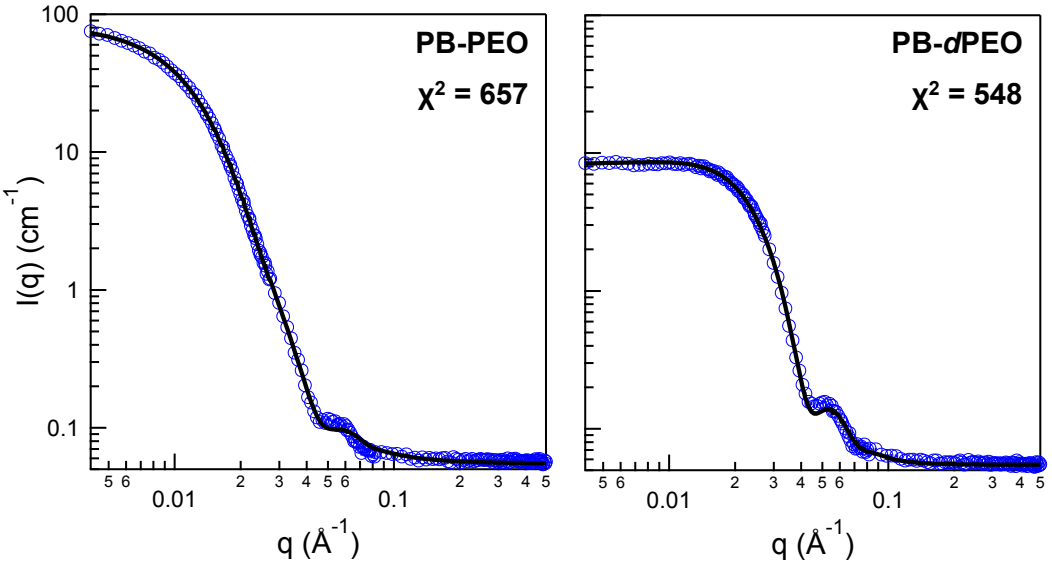

Figure C3 SANS data (points) and fits (lines) for PB-PEO and PB-*d*PEO micelles in a 5 vol% THF cosolvent mixture.

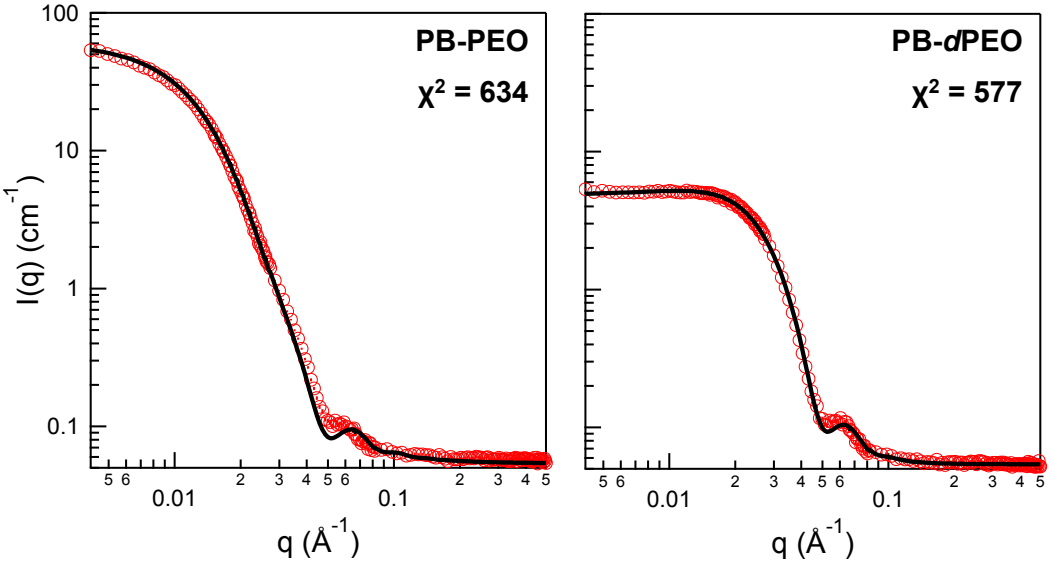

Figure C4 SANS data (points) and fits (lines) for PB-PEO and PB-*d*PEO micelles in a 10 vol% THF cosolvent mixture.

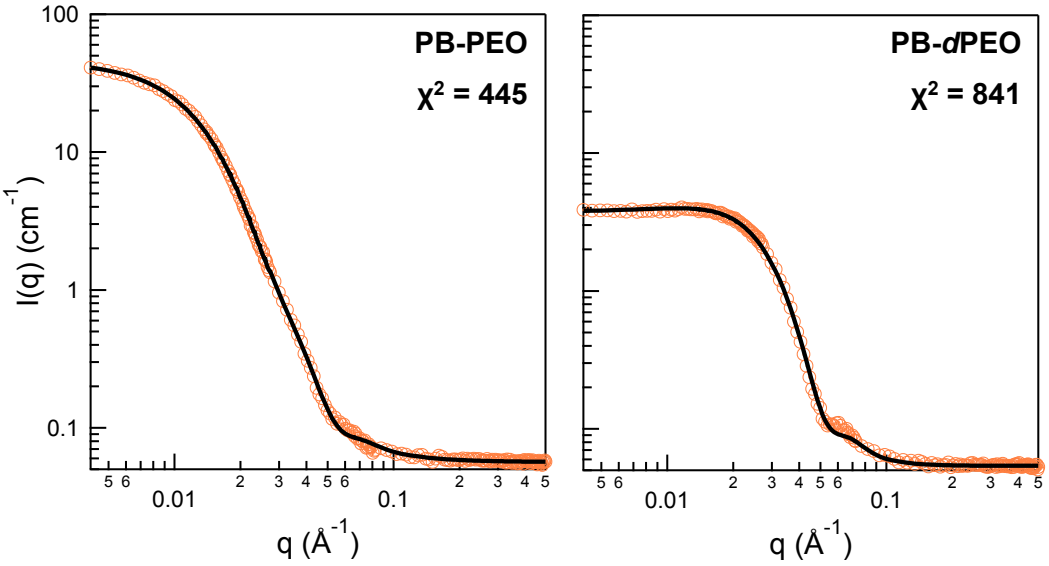

Figure C5 SANS data (points) and fits (lines) for PB-PEO and PB-*d*PEO micelles in a 15 vol% THF cosolvent mixture.

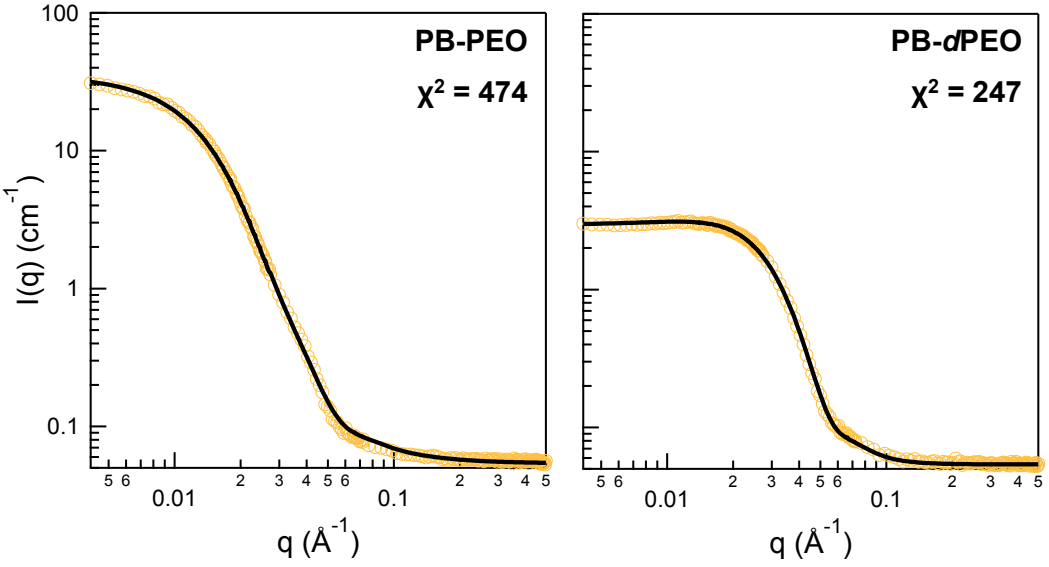

Figure C6 SANS data (points) and fits (lines) for PB-PEO and PB-*d*PEO micelles in a 20 vol% THF cosolvent mixture.

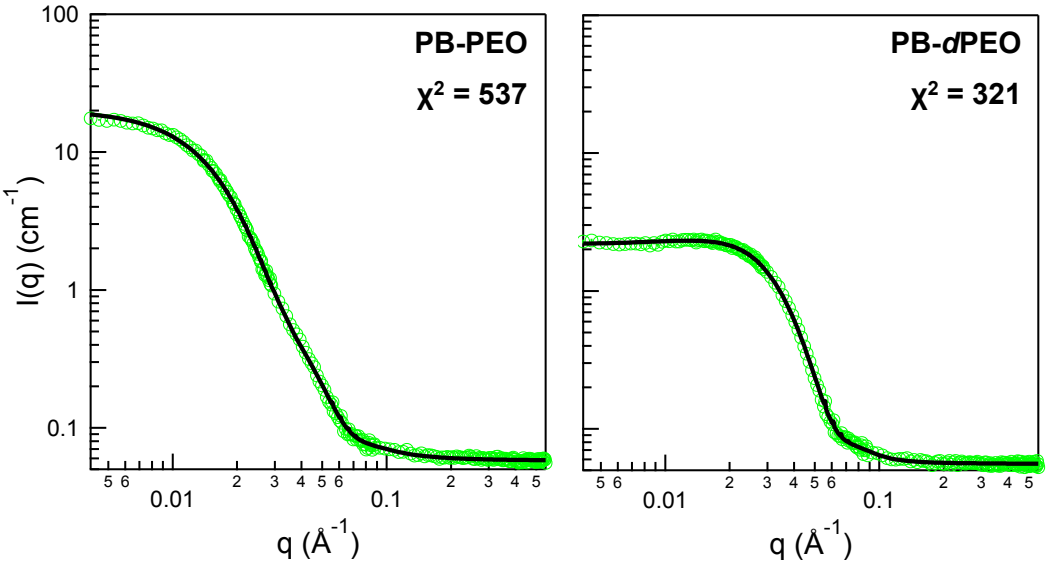

Figure C6 SANS data (points) and fits (lines) for PB-PEO and PB-*d*PEO micelles in a 30 vol% THF cosolvent mixture.

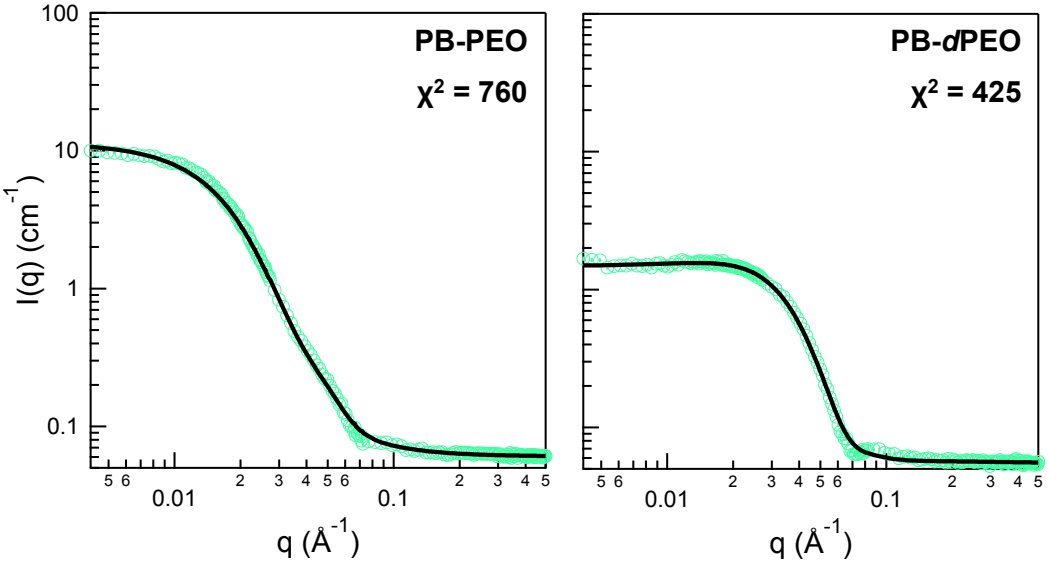

Figure C7 SANS data (points) and fits (lines) for PB-PEO and PB-*d*PEO micelles in a 40 vol% THF cosolvent mixture.

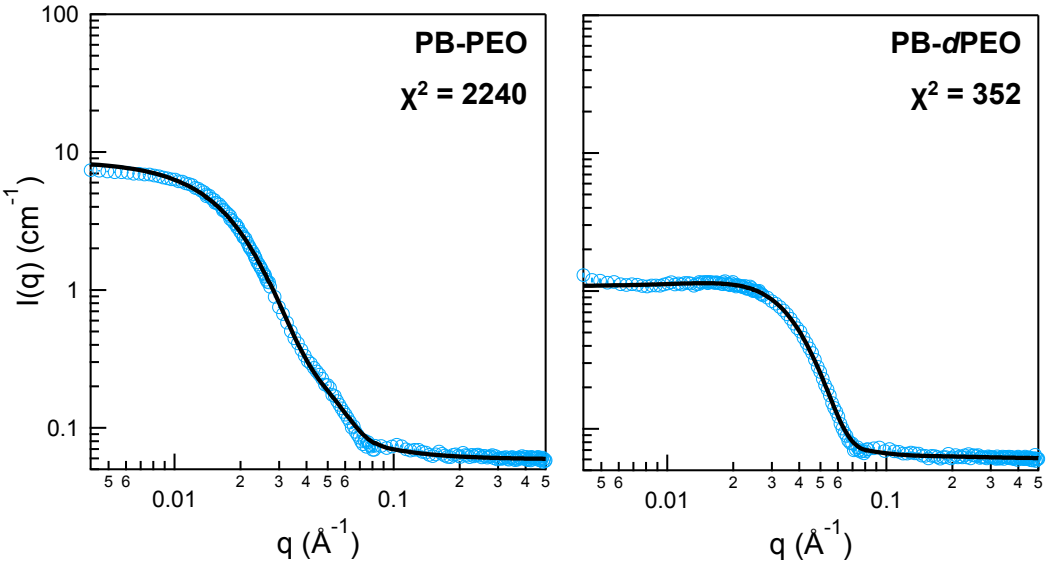

Figure C8 SANS data (points) and fits (lines) for PB-PEO and PB-*d*PEO micelles in a 50 vol% THF cosolvent mixture.

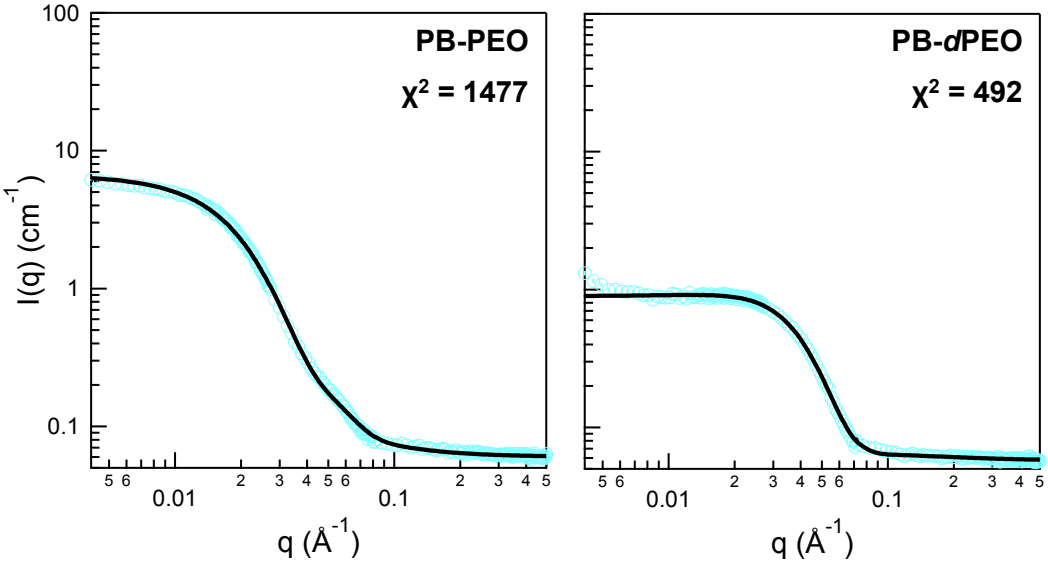

Figure C9 SANS data (points) and fits (lines) for PB-PEO and PB-*d*PEO micelles in a 60 vol% THF cosolvent mixture.

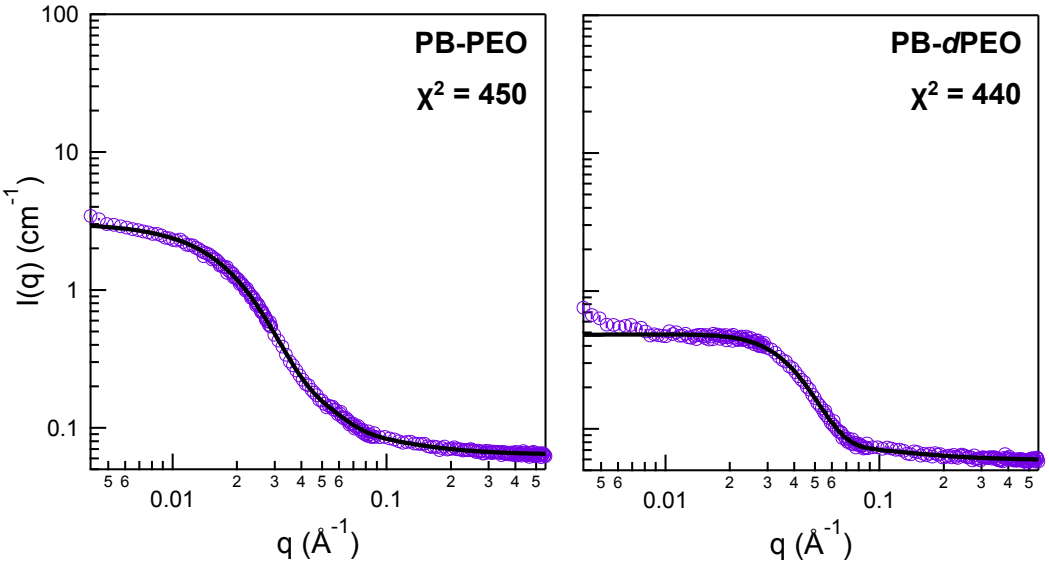

Figure C10 SANS data (points) and fits (lines) for PB-PEO and PB-*d*PEO micelles in a 70 vol% THF cosolvent mixture.

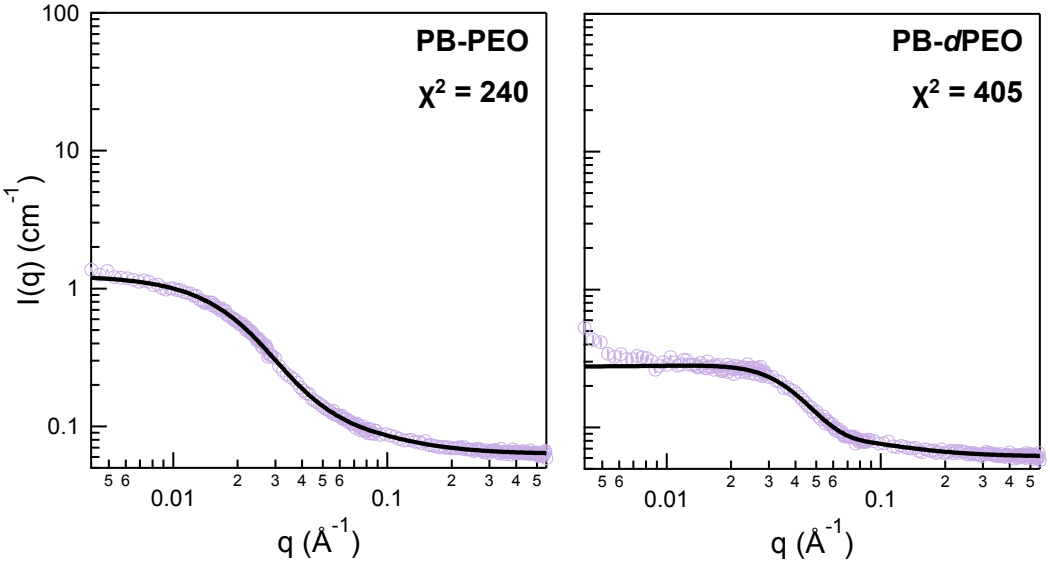

Figure C11 SANS data (points) and fits (lines) for PB-PEO and PB-*d*PEO micelles in a 72 vol% THF cosolvent mixture.

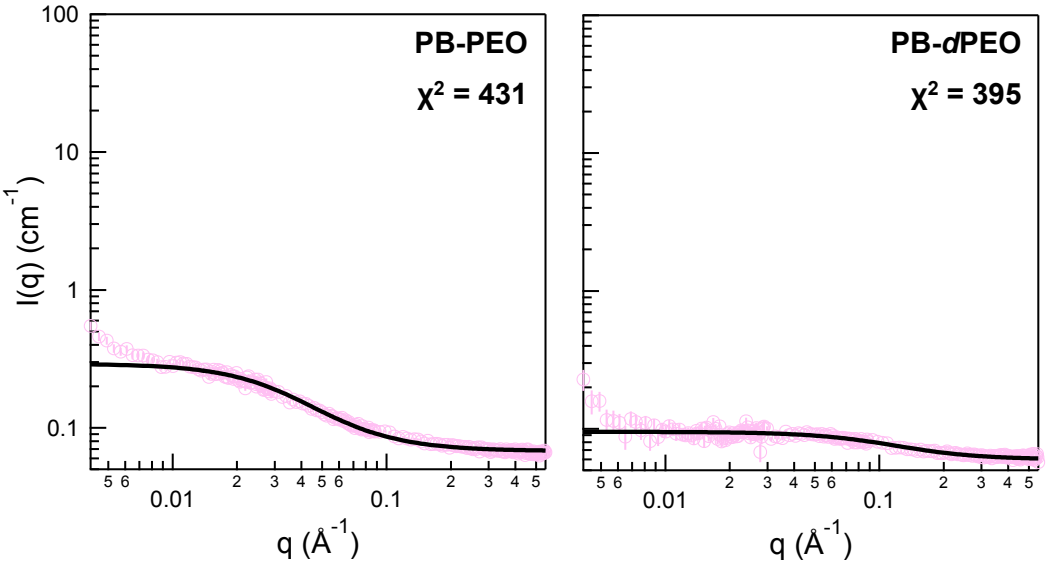

Figure C12 SANS data (points) and fits (lines) for PB-PEO and PB-*d*PEO micelles in a 75 vol% THF cosolvent mixture.

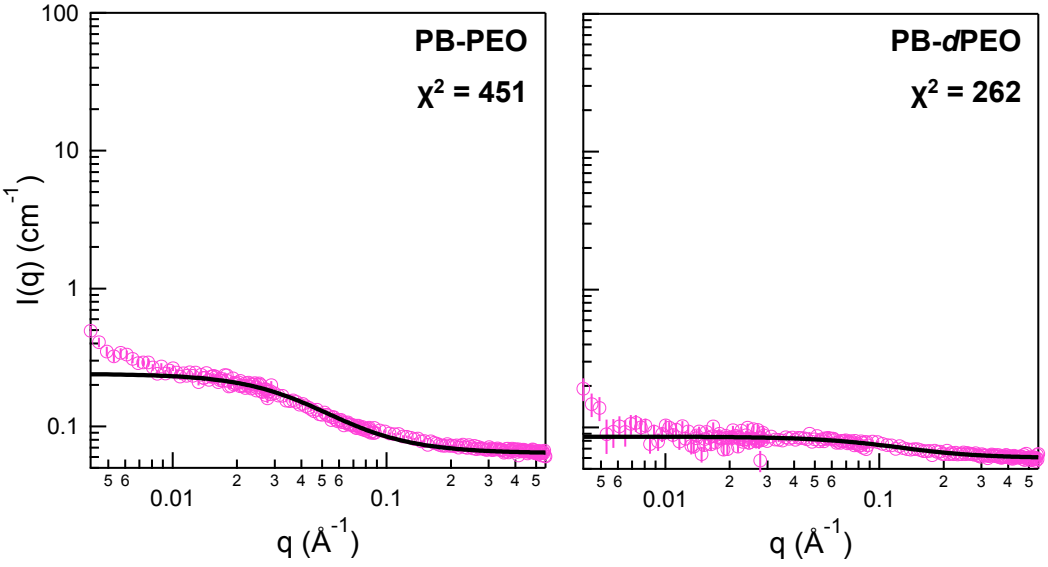

Figure C13 SANS data (points) and fits (lines) for PB-PEO and PB-*d*PEO micelles in a 77 vol% THF cosolvent mixture.

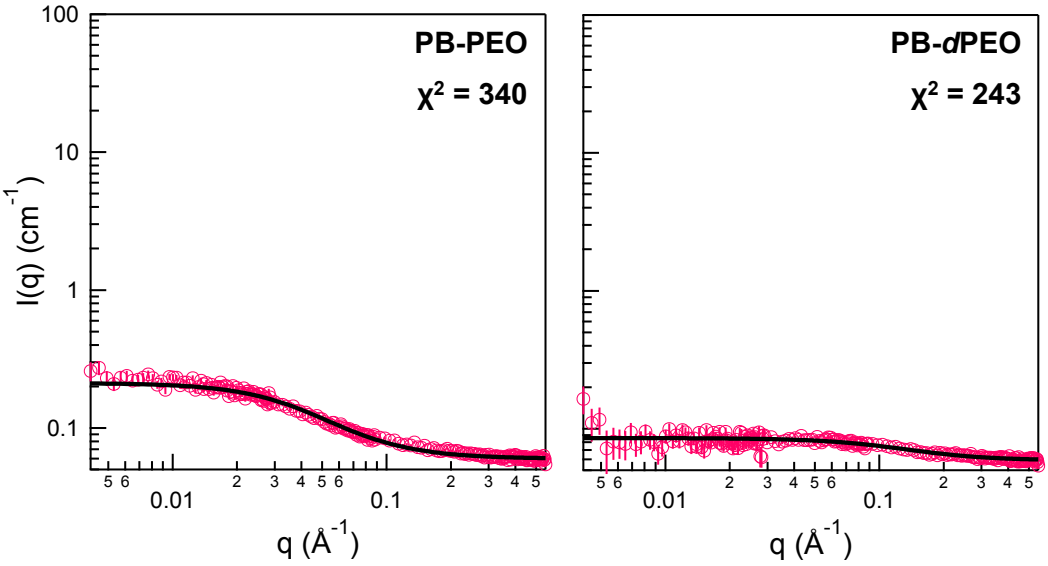

Figure C14 SANS data (points) and fits (lines) for PB-PEO and PB-*d*PEO micelles in an 80 vol% THF cosolvent mixture.

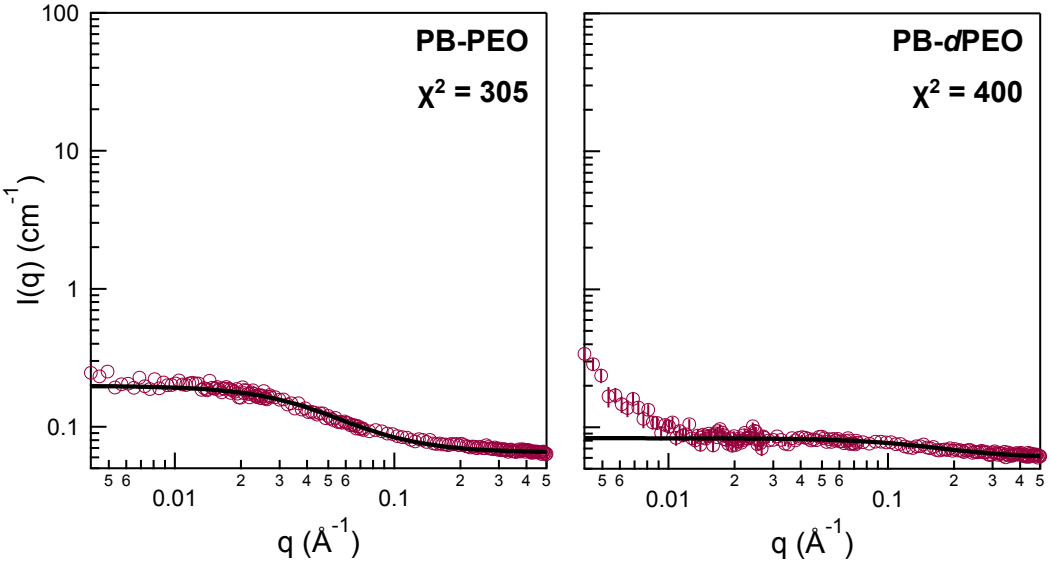

Figure C15 SANS data (points) and fits (lines) for PB-PEO and PB-*d*PEO micelles in a 90 vol% THF.

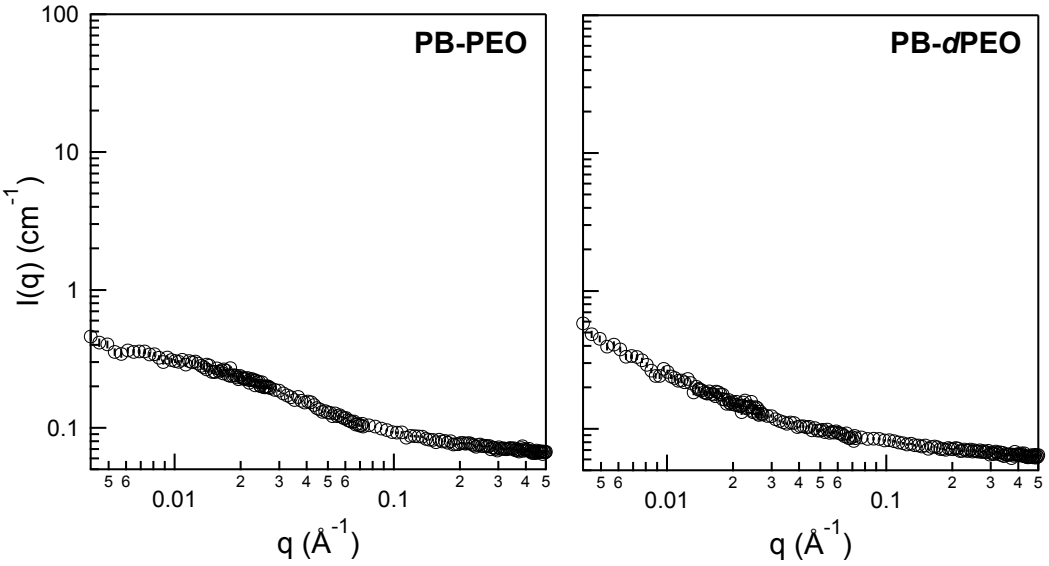

Figure C16 SANS data (points) and fits (lines) for PB-PEO and PB-*d*PEO micelles in pure THF cosolvent mixture.

Table C1 SANS model fit parameters for micelle corona profile

THF content (vol%)	Fit parameters	
	s[1]	a[2]
0	273.4	5E4
5	131.8	0.17
10	125.5	0.15
15	121.8	0.15
20	118.6	0.25
30	103.2	0.13
40	94.9	0.05
50	83.8	0.01
60	80.3	0.01
70	82.9	0.01
72	86.5	0.6

[1]Controls the width of the profile
[2]Controls the weighting of the *b* splines

Appendix D

PB HOMOPOLYMER SOLUBILITY IN COSOLVENT MIXTURES

The solubility of PB-OH homopolymer (3.2 kg mol^{-1}) in water/THF cosolvent mixtures was studied by UV-Vis absorbance. The final polymer concentration was 0.73 mg mL^{-1} polymer in solvent. The polymer was stirred in various H_2O/THF cosolvent mixtures for 3 days before analysis.

Plotted in Figure D1 is the measured absorbance at 600 nm *vs.* the THF content in the cosolvent mixture. The high absorbance values at lower THF contents ($\leq$75 vol% THF) indicated that the solution was turbid and that the polymer was not dissolved. The sharp decrease in absorbance supported that the homopolymer was soluble in cosolvent mixtures containing > 75 vol% THF.

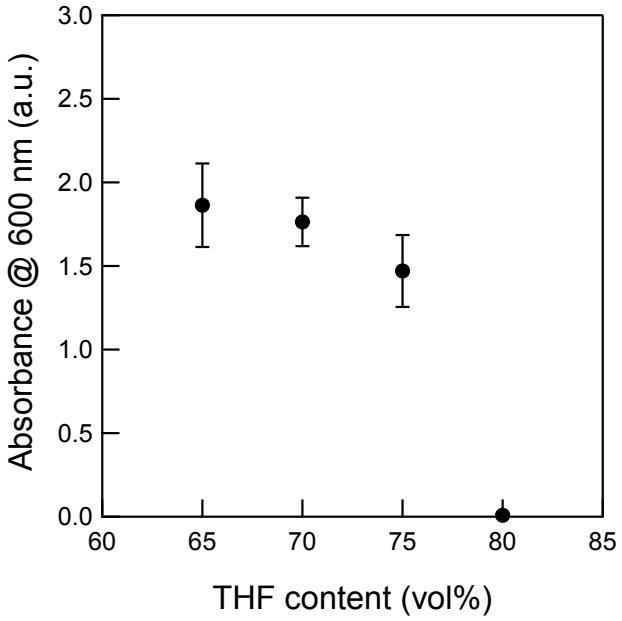

Figure D1 Absorbance measurements for PB homopolymer in H_2O/THF mixtures. Error bars represent the standard deviation of measurements from three different polymer solutions.

Appendix E

COMPARISON OF SANS DATA FITTING RESULTS FOR A BIMODAL DISTRIBUTION OF MICELLE SIZES

SANS experiments were performed to confirm the bimodal distributions noted in the cryo-TEM image analysis in Chapter 7. For the SANS experiments, the micelle coronas were contrast-matched to the solvent (D_2O) by blending PB-PEO and PB-*d*PEO polymers. Therefore, the scattering was only from the micelle cores, which simplified the data modeling and allowed for direct comparison with the cryo-TEM results. The data were fit with models for monomodal and bimodal distributions of Schulz spheres to determine which distribution better described the data (Figure E1). For both models, the sphere volume fractions, radii, and polydispersity in radii were fit, and the incoherent background and scattering length densities of the core block and solvent were held constant. The bimodal Schulz distribution was a better fit to all data sets, as demonstrated by the lower χ^2 values and the better agreement between the data and the model fits in the mid-q region ($0.02\ \text{Å}^{-1} \leq q \leq 0.1\ \text{Å}^{-1}$). The corresponding core radii distributions from the SANS data analysis were in good agreement with the distributions from cryo-TEM.

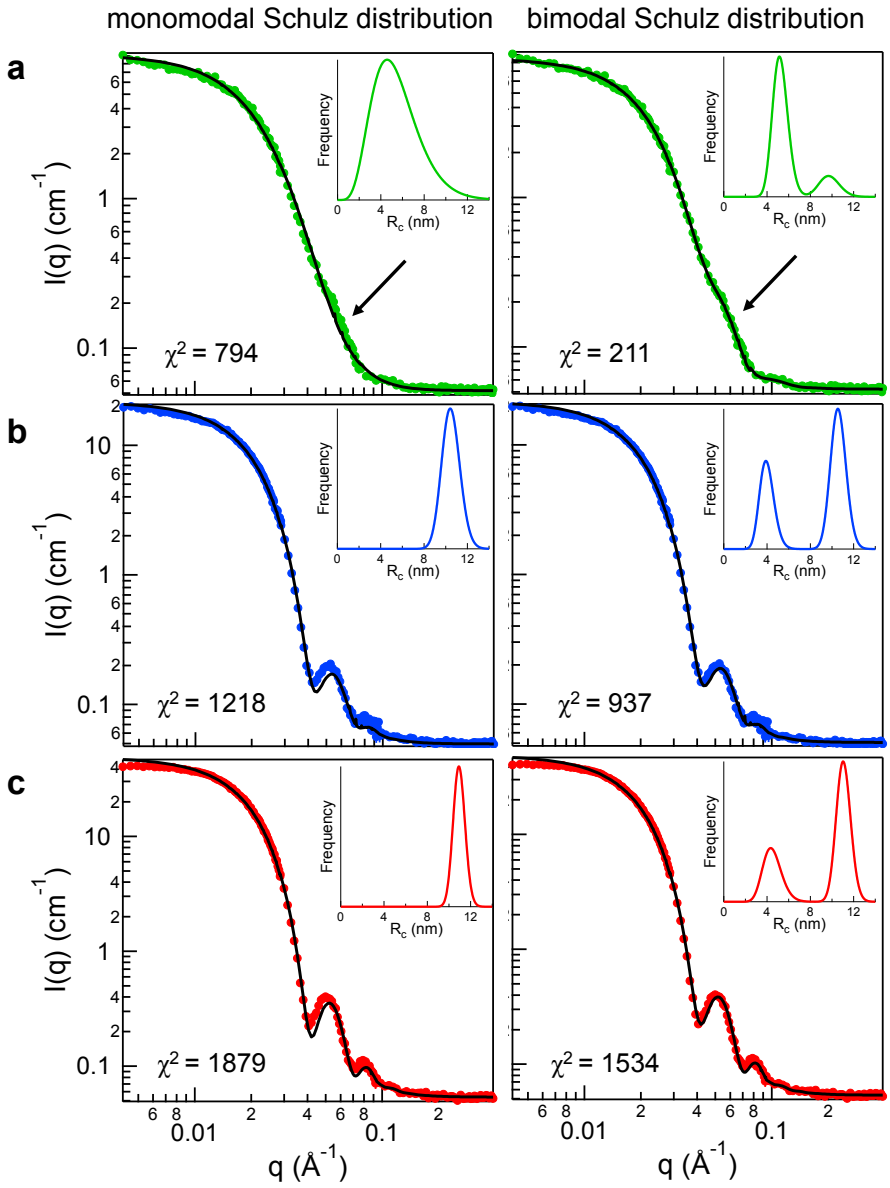

Figure E1 **SANS data and fits using a monomodal or bimodal distribution. SANS data (points) and monomodal or bimodal fits (solid lines) for micelle solutions at initial polymer concentrations of (a) 2 mg mL^{-1}, (b) 5 mg mL^{-1}, and (c) 10 mg mL^{-1}. Insets correspond to number frequency distributions of core radii for a monomodal (left) and bimodal (right) Schulz distribution of spheres. For each solution, THF content was 43 % by volume prior to dialysis into pure D_2O, and data were collected 11 d following dialysis. Arrows highlight distinguishing features between the monomodal and bimodal fits to the scattering curve.**

Appendix F

POLYMER END-GROUP CHEMISTRIES

Carboxylic Acid-Functionalized Poly(butadiene-*b*-ethylene oxide) [PB-PEO-COOH]

PB-PEO polymers were end-functionalized with a carboxylic acid by terminating the anionic polymerization with succinic anhydride as depicted in Figure F1.[1]

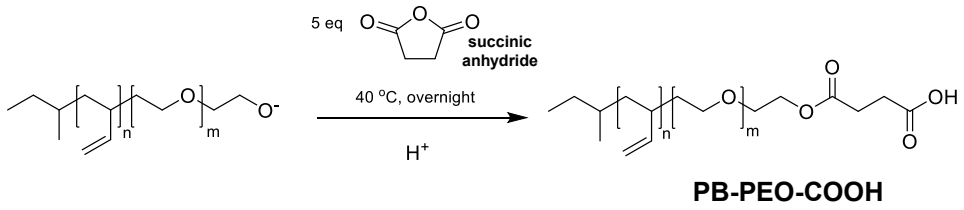

Figure F1 Synthetic scheme for PB-PEO-COOH.

Experimental

Before use, succinic anhydride (≥ 99%, Sigma Aldrich) was purified by recrystallization from chloroform. The crystals were recovered by filtration, rinsed with chloroform, and then vacuum dried.

PB-PEO polymers were synthesized using anionic polymerization as described in detail in Chapter 2. After polymerization of the ethylene oxide, 5 molar equivalents of succinic anhydride was dissolved in dry tetrahydrofuran and added to the living chain ends. The reaction was allowed to proceed overnight at 40 °C, during which time the reaction mixture changed from light blue/gray to deep blue/purple in color.

The reaction then was terminated with acidic methanol (~1M, 25 mL) and turned light yellow. The reactor was vented for 2 h to remove any residual ethylene oxide. Subsequently, the final polymer was purified as described in Chapter 2 and characterized using size exclusion chromatography (SEC) and proton nuclear magnetic resonance (^{1}H NMR) spectroscopy.

Results

The successful end-functionalization of PB-PEO-COOH was confirmed with ^{1}H NMR spectroscopy (Figure F2). Typically, the functionalized reaction was between 70 – 90% efficient.

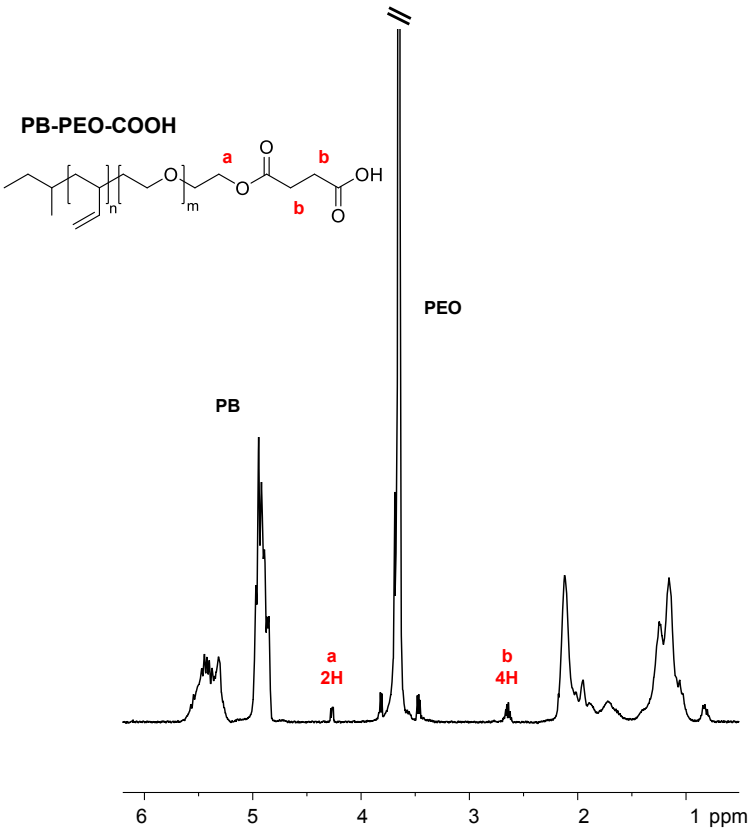

Figure F2 Representative ^{1}H NMR spectrum confirming successful synthesis of PB-PEO-COOH. Note that the PEO peak was clipped for clarity.

Bromide-Functionalized Poly(butadiene-*b*-ethylene oxide) [PB-PEO-Br]

PB-PEO polymers were end-functionalized with a bromide group using bromoisobutyryl bromide (BIBr), as depicted in Figure F3.[2]

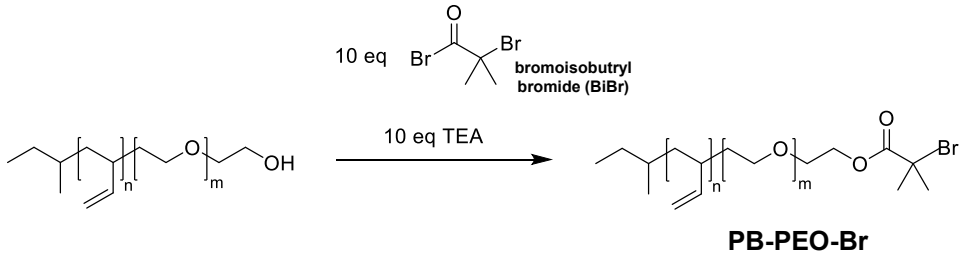

Figure F3 Synthetic scheme for PB-PEO-Br.

Experimental

Before use, dichloromethane (DCM) was sparged with argon, dried over calcium hydride overnight, filtered, and then vacuum distilled.

In a typical reaction, ~0.4 g of PB-PEO-OH polymer was dissolved in ~5 mL of dry DCM, and 10 molar equivalents of triethylamine (TEA) was added to the polymer solution. The solution was sparged with argon for ~20 min, and then cooled on an ice bath. Then, 10 molar equivalents of BIBr were dissolved in ~1 mL of dry DCM and were added to the polymer solution dropwise over 30 min. The ice bath was removed, and the reaction mixture was allowed to warm to room temperature. The reaction was stirred at room temperature for 24 h and then terminated by addition of H_2O. The solution was filtered to remove the amine-hydrobromide salt that formed during the reaction and then the polymer was washed with saturated sodium bicarbonate solution and water. DCM was removed by rotary evaporation and the polymer was analyzed with ^{1}H NMR spectroscopy.

Results

The successful bromination of PB-PEO was confirmed using ^{1}H NMR spectroscopy (Figure F4). Typically, the reaction efficiency was ~90%, which is consistent with reports in literature that range from 85-100%. *Note that it is important*

to use dry solvent and to slowly add the bromoisobutyryl bromide to increase the conversion.

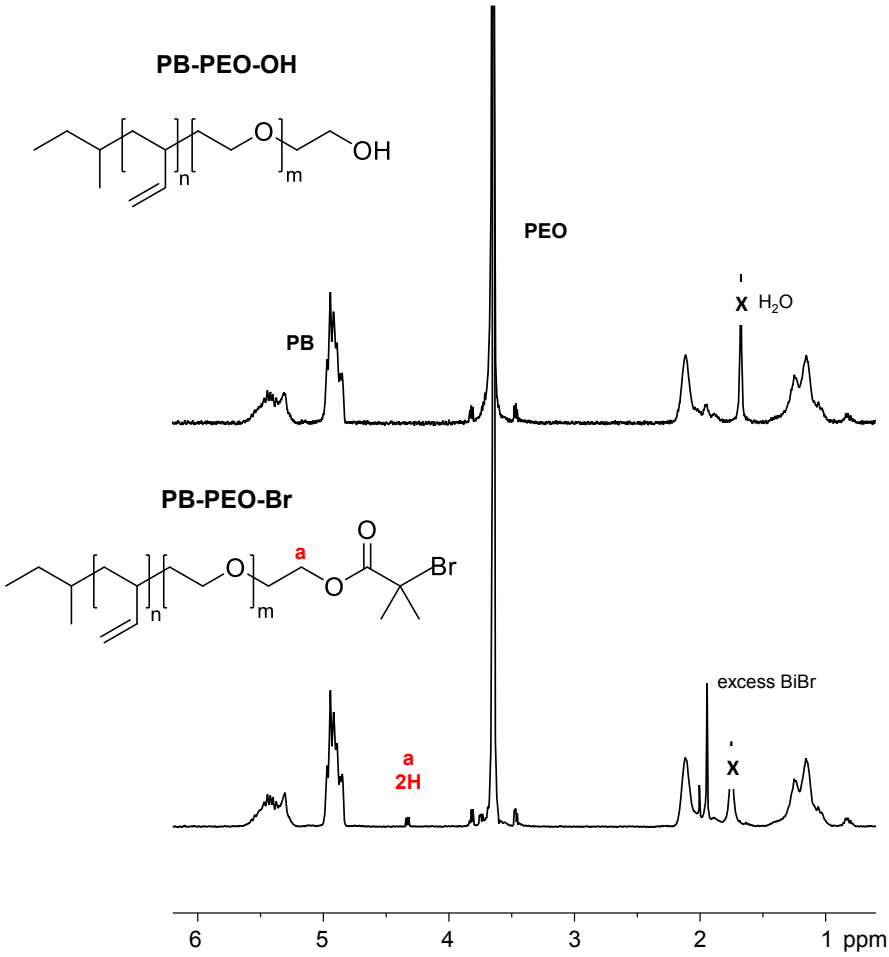

Figure F4 **^{1}H NMR spectra confirming successful synthesis of PB-PEO-Br. Note that the PEO peak was clipped for clarity.**

Azide-Functionalized Poly(butadiene-*b*-ethylene oxide) [PB-PEO-N_3]

PB-PEO-N_3 was synthesized using the two-step functionalization scheme presented in Figure F5 and described in Chapter 9. First the PB-PEO-OH was reacted

with methansulfonyl chloride (mesyl chloride) and subsequently sodium azide to fully end-functionalize the polymer with an azide. However, excess sodium azide could not be removed from the final product by precipitating the polymer into methanol (the polymer will not precipitate in alcohols); therefore, and additional reaction was performed to sequester the excess reagent.[3]

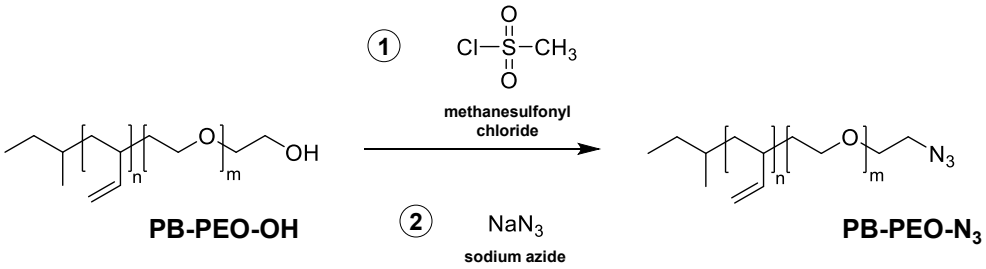

Figure F5 Scheme for two-step synthesis of PB-PEO-N_3.

Experimental

Reaction with mesyl chloride In a typical reaction, ~0.3 g of PB-PEO-OH was dissolved in ~2.5 mL of DCM, and 10 molar equivalents of TEA was added to the solution. The solution was sparged with argon for 20 min and then cooled on an ice bath. Subsequently, 10 molar equivalents of mesyl chloride was dissolved in ~0.5 mL of DCM, and this solution was added dropwise to the polymer solution over ~30 min. The reaction mixture was removed from the ice bath and allowed to warm to room temperature. The reaction was allowed to proceed overnight. The product was diluted with DCM and washed with cold water, dilute acid water, saturated sodium bicarbonate, and finally brine solution. The DCM was removed by rotary evaporation,

and the final polymer product was dissolved in benzene and freeze-dried to remove any residual solvent.

Reaction with sodium azide The dimethylformamide (DMF) for the reaction first was dried using standard procedures.[4] The solvent was by degassed with argon, stirred over calcium hydride overnight, filtered, and then vacuum distilled.

In a typical reaction, ~0.1 g of PB-PEO-mesyl and 5 molar equivalents of sodium azide were dissolved in ~1.2 mL of dry DMF. The solution was sparged with argon for 20 min and then heated to 50 °C. The reaction was allowed to proceed overnight. Subsequently, the excess sodium azide was sequestered by adding 10 molar equivalents of bromopropionic acid dissolved in dry DMF. The reaction was stirred overnight at room temperature. Subsequently, the DMF was removed by vacuum distillation at 50 °C. The polymer was dissolved in DCM and purified as described above.

Results

The successful synthesis of PB-PEO-N_3 (M_n = 12.0 kg mol^{-1}, w_{PEO} = 0.66) was determined by ^{1}H NMR spectroscopy and SEC, presented in Figures F6 and F7, respectively. Integration of the chemical shifts corresponding to the mesyl end-group (~4.4 ppm and ~3.2 ppm) indicated the hydroxyl end-group was completely converted to the mesyl. The complete disappearance of these peaks after the reaction with sodium azide indicated that the final functionalization reaction also was quantitative, and SEC supported that the functionalization reactions did not lead to cross-linking or degradation of the polymer.

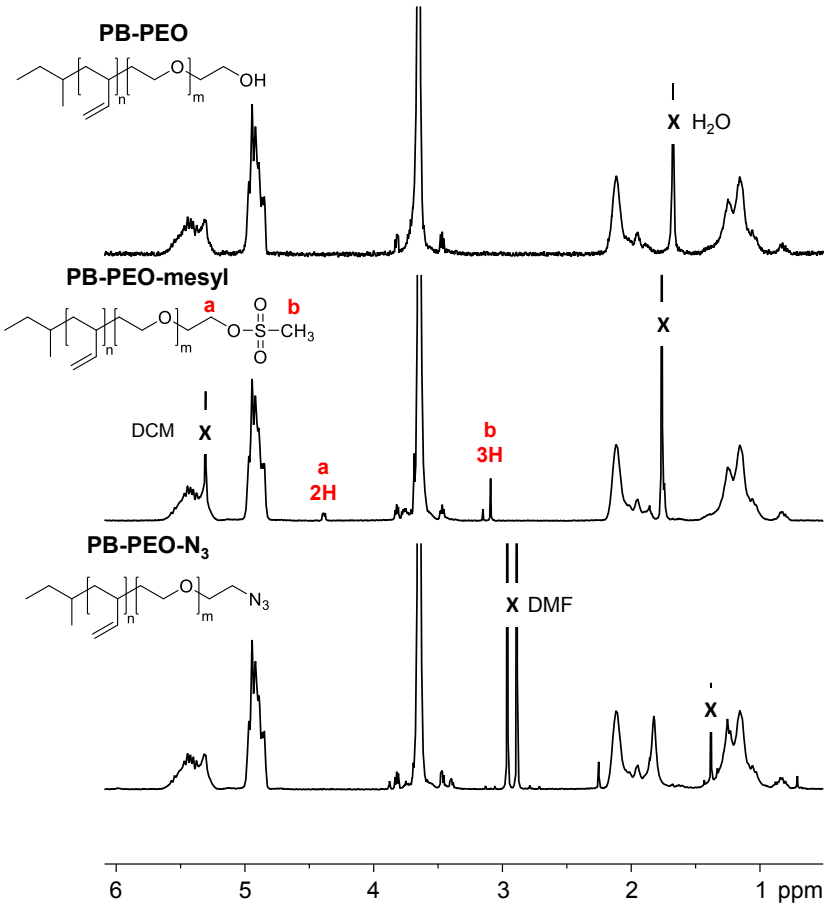

Figure F6 **^{1}H NMR of PB-PEO-OH, PB-PEO-mesyl intermediate, and PB-PEO-N_3 final product. Note that the PEO peak was clipped for clarity.**

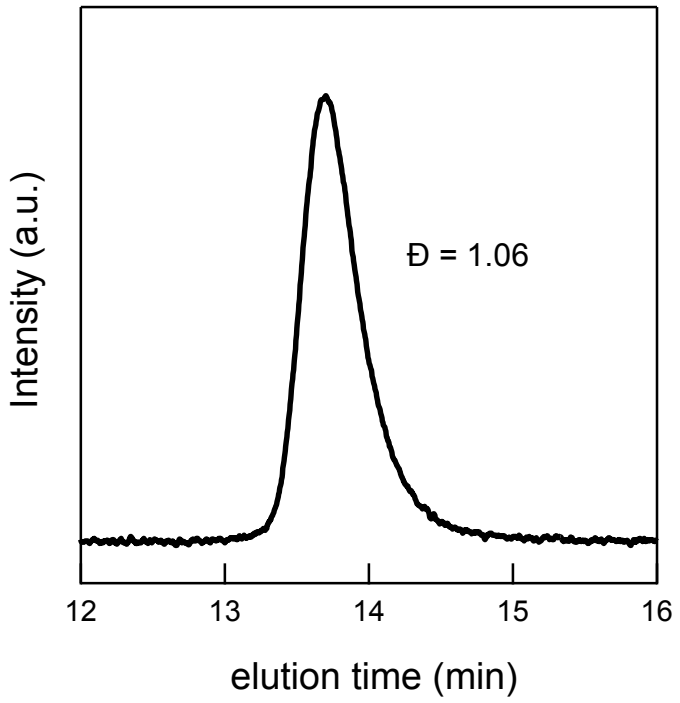

Figure F7 SEC trace for PB-PEO-N_3. Calculated dispersity is based on polystyrene standards.

REFERENCES

1 Maskos, M. (2006), *Polymer* **47**, 1172-1178

2 Kuan, W.-F., Roy, R., Rong, L., Hsiao, B. S. & Epps, T. H. (2012), *ACS Macro Letters* **1**, 519-523

3 Pangburn, T. O., Bates, F. S. & Kokkoli, E. (2012), *Soft Matter* **8**, 4449-4461

4 Armarego, W. L. F. & Chai, C. L. L. *Purification of laboratory chemicals*. Butterworth-Heinemann, 2003.

Appendix G

POLYMER-PEPTIDE CONJUGATION CHEMISTRIES

On-resin Synthesis of PB-PEO-Peptide Conjugates

Amphiphilic polymer-peptide conjugates were synthesized *via* an on-resin conjugation reaction as described in Chapter 9 and presented in Figure G1. While this scheme results in well-defined polymer-peptide conjugates, it is as less versatile method than the chemistries presented in Chapter 9 as it requires the synthesis and functionalization of multiple block polymers. Moreover, the on-resin conjugation efficiencies typically were low (< 30 %) for the high molecular weight block polymers.

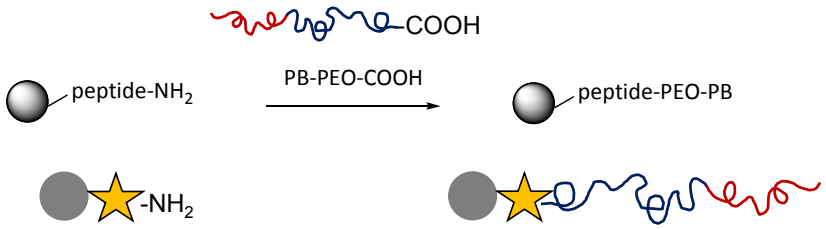

Figure G1 Schematic representation of PB-PEO-peptide synthesis *via* on-resin conjugation.

Experimental

PB-PEO-COOH (M_n = 11 kg mol^{-1}, w_{PEO} = 0.60, 87% end-functionalized) was synthesized as described in Appendix F, and was conjugated to the N-terminus of the

peptide on-resin as depicted in Figure G1. PB-PEO-COOH (2 eq) was activated with (benzotriazol-1-yloxy) tripyrrolidinophophonium hexafluorophosphate (PyBOP, 2 eq) and diisopropylethylamine (DIPEA, 4 eq) in a 5:1 (v:v) mixture of methylene chloride (DCM) and *N*-methyl-2-pyrrolidone (NMP). The polymer solution was added to peptide-loaded resin (peptide sequence: N-GRGDSPGGEGPQGIWGQKG-C), and the reaction was mixed for 96 h at room temperature. *Note that additional solvent was added every 12 h to keep the resin fully covered.* Then, the resin was filtered to remove the reaction solution and washed extensively with DCM to remove any unreacted polymer.

The on-resin conjugation reaction was monitored using the 2,4,6-trinitrobenzene sulfonic acid (TNBS) assay for primary amines, in which TNBS reacts with a primary amine to yield a trinitrophenyl derivative that is orange in color.[1-3] In this work, the amine content on the resin was quantified by first reacting the resin with a known excess of TNBS. The resin beads were removed from solution, and then the excess TNBS was reacted with an excess of glycine. The absorbance of this glycine solution was compared against a standard curve to determine the concentration of TNBS after reaction with the resin, and the amine content of the resin then was back-calculated.

Results

The on-resin polymer-peptide conjugation reaction was monitored using an adaptation of the TNBS assay for free amines. The successful polymer-peptide conjugation can be seen qualitatively in Figure G2, where the transition from dark orange resin beads before reaction to yellow after reaction with PB-PEO-COOH was

indicative of a decrease in free amine content. Quantification of this assay suggested the conjugation efficiency was ~ 30%.[1-3]

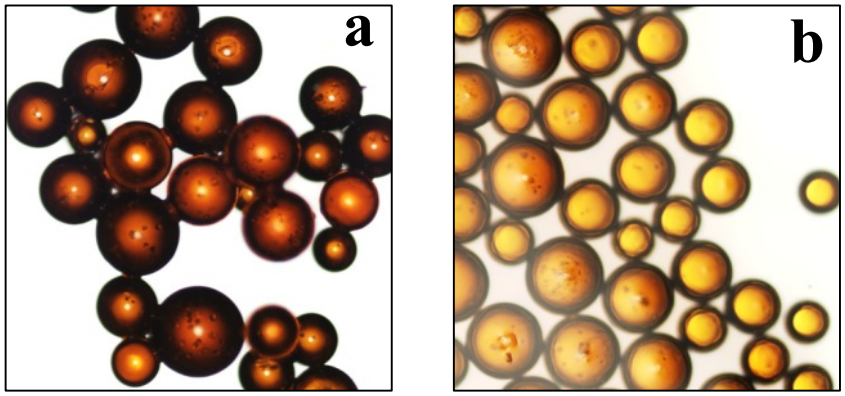

Figure G2 Images from the TNBS assay of the peptide-loaded resin beads (a) before and (b) after reaction with PB-PEO-COOH.

Micelle Functionalization Using Aqueous Click

Polymer micelles were functionalized with a targeting peptide using aqueous click as depicted in Figure G3.[4] Using this approach, a library of micelles with varying ligand densities is easily created, decoupling the effects of assembly size and ligand density on the performance as a drug delivery vehicle. However, this approach only allows for surface functionalization of the micelles and does not control the display of targeting ligands within the micelle corona.

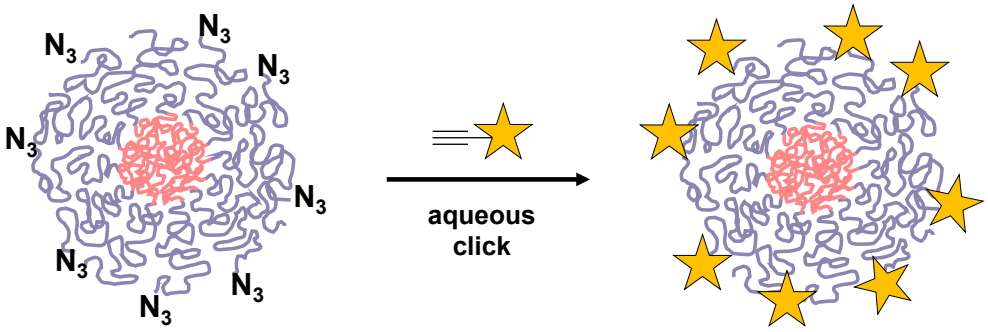

Figure G3 Schematic representation of micelle functionalization using an aqueous copper-catalyzed azide-alkyne cycloaddition (click) reaction.

Experimental

PB-PEO-N_3 (M_n = 12.5 kg mol^{-1}, w_{PEO} = 0.66, 100% functionalized) was synthesized as described in Appendix F. Micelles were formed by dissolving the dry polymer powder in water and stirring the resulting solution for 3 days. The final solution contained 5 mg mL^{-1} polymer in water.

Alkyne-functionalized peptide containing a matrix metalloproteinase cleavage site and RGD binding sequence (N-GEGPQGIWGQKGGRGDSPGG(alkyne)-C,

1934 g mol^{-1}, > 99% pure) was synthesized as described in Chapter 9. The peptide was dissolved in water and added to the micelle solution such that there was a 2:1 peptide to polymer ratio. Stock solutions of the copper salt and ligand were prepared in water and added to the micelle solution giving a final concentration of 1.1 mM copper sulfate and 5.5 mM sodium ascorbate in solution. The reaction was stirred for 24 h at room temperature. Subsequently, an excess of ethylenediaminetetraacetic acid (EDTA, final concentration ~ 6 mM) was added to the solution to chelate the copper. The micelle solution was transferred to dialysis tubing (12 – 14 kDa cutoff, Spectra Por) and extensively dialyzed against water to remove the excess peptide.

A portion of the final product was dried and for additional characterization using SEC and the TNBS assay. For the SEC experiments, the PB-PEO-peptide conjugate was dissolved in tetrahydrofuran (THF) at a concentration of 1 mg mL^{-1}. For the TNBS assay, the polymer-peptide conjugate was dissolved in 0.1 M sodium bicarbonate buffer, pH 8.5. The solution was stirred for 3 d before analysis.

Results

Following the functionalization reaction, the PB-PEO-peptide micelles were dried and resuspended in THF for SEC analysis. As seen in Figure G4, the SEC trace shows a clear shift to longer elution times for the PB-PEO-peptide conjugate compared to the polymer precursors. Functionalizing the polymer with a peptide would increase the molecular weight of the product, which should shift the peak to shorter elution times. The distinct shift to longer elution times seen here indicates that the peptide very strongly interacts with the column packing and suggests that successful polymer-peptide conjugate synthesis cannot be confirmed with SEC.

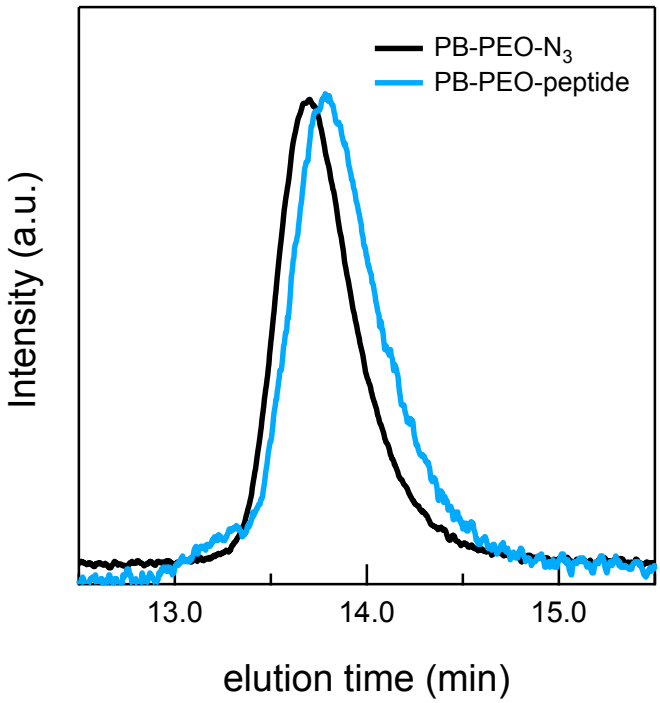

Figure G4 SEC data for PB-PEO-N_3 precursor and PB-PEO-peptide conjugates. SEC experiments were performed using THF as a mobile phase.

Because the SEC results were inconclusive, the polymer-peptide conjugates were characterized with the TNBS assay for primary amines. PB-PEO-N_3 and PB-PEO-peptide assemblies were prepared in 0.1 M sodium bicarbonate buffer (pH 8.5) for the assay and then incubated with TNBS. The maxima in the UV-Vis spectrum of the PB-PEO-peptide conjugate at ~350 nm and ~420 nm were characteristic of the trinitrophenyl derivative and confirmed the successful functionalization reaction (Figure G5). Moreover, the results suggested that the peptide was accessible to the small molecule and likely was not aggregated or buried within the assembly.

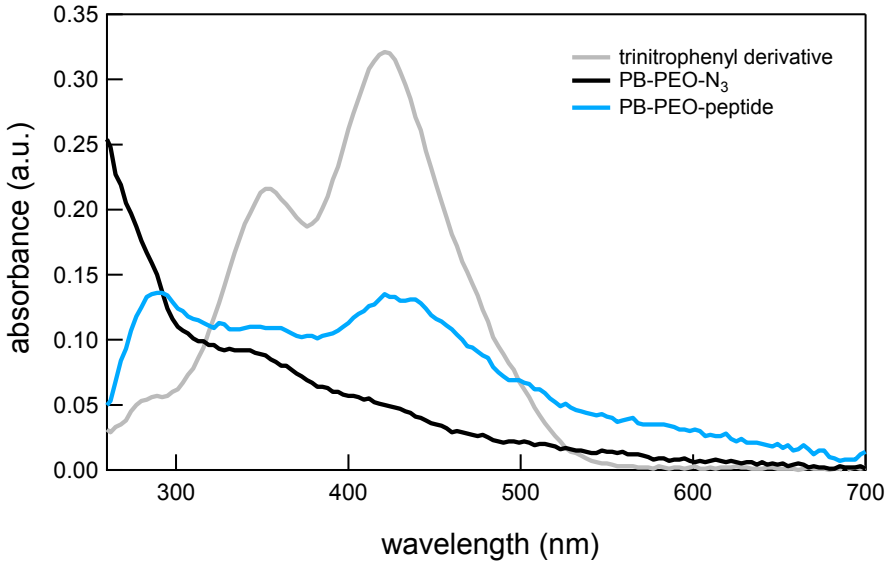

Figure G5 UV-Vis spectra from the TNBS assay of the PB-PEO-N3 precursor and the PB-PEO-peptide conjugate. The trinitrophenyl derivative control was prepared by incubating TNBS with a 200 µM glycine solution.

Aqueous solutions of PB-PEO-N_3 and PB-PEO-peptide conjugate assemblies also were characterized by dynamic light scattering (DLS). Before the functionalization reaction, the polymer formed relatively monodisperse micelles with an $\langle R_H \rangle \sim 63$ nm (PB-PEO-N_3 in water, Table G1). After the functionalization reaction, the micelle sizes were relatively unchanged (PB-PEO-peptide in water, Table G1). However, the amphiphilic polymers showed markedly different behavior after being dried and resuspended in a buffer solution. The PB-PEO-N_3 precursor still formed relatively monodisperse assemblies with $\langle R_H \rangle \sim 65$ nm, while the PB-PEO-peptide conjugates formed large, polydisperse assemblies. This result implies that the peptide significantly alters the self-assembly behavior of the amphiphilic block polymer, and suggests that both careful synthesis and detailed

structural characterization of polymer-peptide conjugates are necessary to create well-defined assemblies for drug delivery applications.[5]

Table G1 Summary of DLS characterization results for functionalized micelles

Sample	Solvent	$\langle R_H \rangle$ (nm)	Poly
PB-PEO-N_3	water	63	0.259
	buffer*	65	0.223
PB-PEO-peptide	water	58	0.235
	buffer*	192	0.349

*0.1 M sodium bicarbonate buffer at pH 8.5

REFERENCES

1 Antoni, G., Presentini, R. & Neri, P. (1983), *Analytical Biochemistry* **129**, 60-63

2 Chern, C. S., Lee, C. K. & Ho, C. C. (1999), *Journal of Polymer Science Part A: Polymer Chemistry* **37**, 1489-1499

3 Hancock, W. S. & Battersby, J. E. (1976), *Analytical Biochemistry* **71**, 260-264

4 Pangburn, T. O., Bates, F. S. & Kokkoli, E. (2012), *Soft Matter* **8**, 4449-4461

5 Zupancich, J. A., Bates, F. S. & Hillmyer, M. A. (2009), *Biomacromolecules* **10**, 1554-1563

Appendix H

COPYRIGHT PERSMISSIONS

Permissions for Figures 1.4 and 1.5

THE AMERICAN ASSOCIATION FOR THE ADVANCEMENT OF SCIENCE LICENSE TERMS AND CONDITIONS
Apr 23, 2014

This is a License Agreement between Elizabeth G Kelley ("You") and The American Association for the Advancement of Science ("The American Association for the Advancement of Science") provided by Copyright Clearance Center ("CCC"). The license consists of your order details, the terms and conditions provided by The American Association for the Advancement of Science, and the payment terms and conditions.

All payments must be made in full to CCC. For payment instructions, please see information listed at the bottom of this form.
License Number 3374860722368
License date Apr 23, 2014
Licensed content publisher The American Association for the Advancement of Science
Licensed content publication Science
Licensed content title On the Origins of Morphological Complexity in Block Copolymer Surfactants
Licensed content author Sumeet Jain, Frank S. Bates
Licensed content date Apr 18, 2003
Volume number 300
Issue number 5618
Type of Use Thesis / Dissertation
Requestor type Scientist/individual at a research institution
Format Print and electronic
Portion Figure
Number of figures/tables 2
Order reference number
Title of your thesis /dissertation Synthesis, solution assembly, and characterization of amphiphilic block polymers
Expected completion date May 2014
Estimated size(pages) 400
Total 0.00 USD
Terms and Conditions

This permission is not valid for the use of the AAAS and/or Science logos. AAAS makes no representations or warranties as to the accuracy of any information contained in the AAAS material covered by this permission, including any warranties of merchantability or fitness for a particular purpose. If permission fees for this use are waived, please note that AAAS reserves the right to charge for reproduction of this material in the future.
Permission is not valid unless payment is received within sixty (60) days of the issuance of this permission. If payment is not received within this time period then all rights granted herein shall be revoked and this permission will be considered null and void.
In the event of breach of any of the terms and conditions herein or any of CCC's Billing and Payment terms and conditions, all rights granted herein shall be revoked and this permission will be considered null and void.

AAAS reserves the right to terminate this permission and all rights granted herein at its discretion, for any purpose, at any time. In the event that AAAS elects to terminate this permission, you will have no further right to publish, publicly perform, publicly display, distribute or otherwise use any matter in which the AAAS content had been included, and all fees paid hereunder shall be fully refunded to you. Notification of termination will be sent to the contact information as supplied by you during the request process and termination shall be immediate upon sending the notice. Neither AAAS nor CCC shall be liable for any costs, expenses, or damages you may incur as a result of the termination of this permission, beyond the refund noted above.

This Permission may not be amended except by written document signed by both parties. The terms above are applicable to all permissions granted for the use of AAAS material. Below you will find additional conditions that apply to your particular type of use.

FOR A THESIS OR DISSERTATION
If you are using figure(s)/table(s), permission is granted for use in print and electronic versions of your dissertation or thesis. A full text article may be used in print versions only of a dissertation or thesis.

Permission covers the distribution of your dissertation or thesis on demand by ProQuest / UMI, provided the AAAS material covered by this permission remains in situ.

If you are an Original Author on the AAAS article being reproduced, please refer to your License to Publish for rules on reproducing your paper in a dissertation or thesis.

Questions about these terms can be directed to the AAAS Permissions department
permissions@aaas.org.
Other Terms and Conditions:
If you would like to pay for this license now, please remit this license along with your payment made payable to "COPYRIGHT CLEARANCE CENTER" otherwise you will be invoiced within 48 hours of the license date. Payment should be in the form of a check or money order referencing your account number and this invoice number RLNK501285431.
Once you receive your invoice for this order, you may pay your invoice by credit card. Please follow instructions provided at that time.

Make Payment To:
Copyright Clearance Center
Dept 001
P.O. Box 843006
Boston, MA 02284-3006
For suggestions or comments regarding this order, contact RightsLink Customer Support:
customercare@copyright.com or +1-877-622-5543 (toll free in the US) or +1-978-646-2777.
Gratis licenses (referencing $0 in the Total field) are free. Please retain this printable license for your reference. No payment is required.

Permissions for Chapter 4

Title: Structural Characterization of Amphiphilic Homopolymer Micelles Using Light Scattering, SANS, and Cryo-TEM

Author: Joseph P. Patterson, Elizabeth G. Kelley, Ryan P. Murphy, Adam O. Moughton, Mathew P. Robin, Annhelen Lu, Olivier Colombani, Christophe Chassenieux, David Cheung, Millicent O. Sullivan, Thomas H. Epps, III, and Rachel K. O'Reilly

Publication: Macromolecules

Publisher: American Chemical Society

Date: Aug 1, 2013

Copyright © 2013, American Chemical Society

Logged in as:
Elizabeth Kelley
Account #:
3000603378

LOGOUT

PERMISSION/LICENSE IS GRANTED FOR YOUR ORDER AT NO CHARGE

This type of permission/license, instead of the standard Terms & Conditions, is sent to you because no fee is being charged for your order. Please note the following:

- Permission is granted for your request in both print and electronic formats, and translations.
- If figures and/or tables were requested, they may be adapted or used in part.
- Please print this page for your records and send a copy of it to your publisher/graduate school.
- Appropriate credit for the requested material should be given as follows: "Reprinted (adapted) with permission from (COMPLETE REFERENCE CITATION). Copyright (YEAR) American Chemical Society." Insert appropriate information in place of the capitalized words.
- One-time permission is granted only for the use specified in your request. No additional uses are granted (such as derivative works or other editions). For any other uses, please submit a new request.

BACK CLOSE WINDOW

Permission for Chapter 7

Author Request

If you are the author of this content (or his/her designated agent) please read the following. If you are not the author of this content, please click the Back button and select an alternative Requestor Type to obtain a quick price or to place an order.

Ownership of copyright in the article remains with the Authors, and provided that, when reproducing the Contribution or extracts from it, the Authors acknowledge first and reference publication in the Journal, the Authors retain the following non-exclusive rights:

a) To reproduce the Contribution in whole or in part in any printed volume (book or thesis) of which they are the author(s).

b) They and any academic institution where they work at the time may reproduce the Contribution for the purpose of course teaching.

c) To reuse figures or tables created by them and contained in the Contribution in other works created by them.

d) To post a copy of the Contribution as accepted for publication after peer review (in Word or Text format) on the Author's own web site, or the Author's institutional repository, or the Author's funding body's archive, six months after publication of the printed or online edition of the Journal, provided that they also link to the Journal article on NPG's web site (eg through the DOI).

NPG encourages the self-archiving of the accepted version of your manuscript in your funding agency's or institution's repository, six months after publication. This policy complements the recently announced policies of the US National Institutes of Health, Wellcome Trust and other research funding bodies around the world. NPG recognises the efforts of funding bodies to increase access to the research they fund, and we strongly encourage authors to participate in such efforts.

Authors wishing to use the published version of their article for promotional use or on a web site must request in the normal way.

If you require further assistance please read NPG's online author reuse guidelines.

For full paper portion: Authors of original research papers published by NPG are encouraged to submit the author's version of the accepted, peer-reviewed manuscript to their relevant funding body's archive, for release six months after publication. In addition, authors are encouraged to archive their version of the manuscript in their institution's repositories (as well as their personal Web sites), also six months after original publication.